SLAC-446

ELECTROWEAK COUPLING MEASUREMENTS FROM POLARIZED BHABHA SCATTERING AT THE Z^0 RESONANCE

Kevin Pitts

SLAC-Report-446
March 1994

Prepared for the Department of Energy
under contract number DE-AC03-76SF00515

2/80

SLAC-446
UC-414
(E)

ELECTROWEAK COUPLING MEASUREMENTS FROM POLARIZED BHABHA SCATTERING AT THE Z^0 RESONANCE*

Kevin T. Pitts

Stanford Linear Accelerator Center
Stanford University
Stanford, CA 94309

March 1994

Prepared for the Department of Energy
under contract number DE-AC03-76SF00515

*Ph.D. thesis, University of Oregon

ABSTRACT

The cross section for Bhabha scattering ($e^+e^- \rightarrow e^+e^-$) with polarized electrons at the center of mass energy of the Z^0 resonance has been measured with the SLD experiment at the Stanford Linear Accelerator Center during the 1992 and 1993 runs. The electroweak couplings of the electron are extracted.

At small angles the measurement is done in the SLD Silicon/Tungsten Luminosity Monitor (LMSAT). A detailed description of the design, construction, commissioning and operation of the LMSAT is provided. The integrated luminosity for 1992 is measured to be $\mathcal{L} = 420.86 \pm 2.56$ (stat) ± 4.23 (sys) nb^{-1}. The luminosity asymmetry for polarized beams is measured to be $A_{LR}(LUM) = (1.7 \pm 6.4) \times 10^{-3}$.

The large angle polarized Bhabha scattering reveals the effective electron vector and axial vector couplings to the Z^0 through the measurement of the $Z^0 \rightarrow e^+e^-$ partial width, Γ_{ee}, and the parity violation parameter, A_e. From the combined 1992 and 1993 data the effective electron vector and axial vector couplings are measured to be $\overline{g}_v^e = -0.0495 \pm 0.0096 \pm 0.0030$, and $\overline{g}_a^e = -0.4977 \pm 0.0035 \pm 0.0064$ respectively. The effective weak mixing angle is measured to be $sin^2\theta_W^{eff} = 0.2251 \pm 0.0049 \pm 0.0015$. These results are compared with other experiments.

ACKNOWLEDGMENTS

First and foremost, thanks to my parents, William and Beverley Pitts, without whom none of this would have been possible. I will forever be in your debt. I am also very grateful to my brother, Rick, his wife Kathy and daughter Sarah for all their love and support. I would also like to acknowledge my grandparents, Howard and Thelma Miller and Gene and Bea Pitts.

Thanks very much to my advisor, Jim Brau, for his guidance, encouragement and friendship. I appreciate the friendship and support of my good friend and co-worker, Jenny Huber. Thanks also to Cary Zeitlin for his friendship and for his tremendous effort in making it all work.

Thanks to all of the physicists and support personnel of the SLD collaboration. This experiment is truly a team effort.
I would especially like to thank:

- the University of Oregon group: Ray Frey, David Strom, Koichiro Furuno, Hyun Hwang, Matt Langston, Anatoli Arodzero, Xiao Qing Yang, Hwanbae Park and David Mason for their contributions to the luminosity monitor and thoughtful discussions regarding my analysis.
- Bill Bugg and the University of Tennessee group: Steve Berridge, Achim Weidemann, Rob Kroeger, Peter Du, Joe Hargis and Sharon White for their contributions to the LMSAT/MASC.
- Iris Abt, Tony Waite, Eric Vella and Richard Dubois for their work on the calorimeter as well as their contribution and support to the luminosity monitor.
- John Yamartino and Saul González for their thoughtful insights and ideas, as well as their excellent work on calorimetry software.
- Peter Rowson, Morris Swartz and the Electroweak Physics group for their contribution and support of this analysis.
- Phil Seward and Behzad Sanii for their help, ideas and advice on the luminosity monitor hardware, as well as some stimulating conversations.

We are all grateful to the accelerator physicists and support personnel working on the SLC. Without luminosity and polarization, there would be no physics.

On behalf of the entire Luminosity group, thanks to Bernie Wendring and the University of Oregon machine shop for a tremendous job on the LMSAT hardware.

Last, but not least, special thanks to the members of the Jack Miller Roundtable: Jack Miller (the founder), Cary Zeitlin, Peter Rowson, Jim Grubb and the great John McGraw for their incredible insights into a plethora of topics.

This work was supported in part by U.S. Department of Energy grant number DE-FG06-85ER40224.

TABLE OF CONTENTS

LIST OF FIGURES

LIST OF TABLES

CHAPTER I

INTRODUCTION

This thesis will present a measurement of the electron electroweak couplings to the Z^0. The measurement is performed with the exclusive process of Bhabha scattering, $e^+e^- \rightarrow e^+e^-$, at a center of mass energy on the Z^0 resonance. The data presented in this thesis were acquired at the Stanford Linear Accelerator Center (SLAC) with the SLAC Large Detector (SLD) measuring electron-positron collisions produced by the SLAC Linear Collider (SLC) during the 1992 and 1993 runs. The 1992 SLC run was broken into two parts, one with an unpolarized electron beam and the bulk of the run with a polarized electron beam. Approximately 1,000 hadronic Z^0 decays were measured by the SLD during the unpolarized portion of the 1992 run. After the installation of the SLC polarized electron source, the SLD measured approximately 10,000 hadronic Z^0 decays with an electron beam polarization of $\sim 23\%$. The 1993 SLC run saw the SLC increase both luminosity and electron polarization. SLD accumulated approximately 50,000 hadronic Z^0 decays with a typical electron beam polarization of 60-65%.

The analysis presented here may be considered complementary to the SLD measurement of the left-right asymmetry, A_{LR}, which is a very sensitive test of the Standard Model of Electroweak Interactions [1]. In the measurement of A_{LR}, wide angle Bhabha events are discarded due to the dilution of the asymmetry introduced by the t-channel photon exchange (and, to a lesser extent, Z^0 and photon interference terms.) Although the t-channel photon exchange serves to complicate the behavior of the left-right asymmetry for $e^+e^- \rightarrow e^+e^-$, it provides a powerful method to calculate the overall normalization. Therefore, the cross section for the decay of the Z^0 in to electrons, $Z^0 \rightarrow e^+e^-$, and hence the partial width, Γ_{ee}, may also be measured. The combination of these measurements allows for the extraction of the effective electron vector and axial vector coupling to the Z^0, as well as the weak mixing angle, $sin^2\theta_W$.

To utilize the information contained in the data to its fullest, the polarized wide angle Bhabha distributions will be fit to theoretical calculations by the method of maximum likelihood. To protect against bias in the calculations and as a cross check, two separate fitting programs will be used. One calculation is based directly upon the Standard Model, while the other is based upon a model independent formulation of the $e^+e^- \rightarrow e^+e^-$ process in order to minimize Standard Model bias. The electroweak

couplings extracted from the best fit to the differential polarized Bhabha scattering distribution will be compared to other measurements of the electron couplings to the Z^0.

As stated above, the t-channel contribution to the $e^+e^- \rightarrow e^+e^-$ process at small angles provides an overall normalization for cross section measurements. The high event rate along with the ability to calculate the QED cross section with great precision makes this process ideally suited for luminosity monitoring. In addition, the left-right luminosity asymmetry may be directly monitored with small angle Bhabha scattering. Small angle Bhabha scattering is measured in the SLD with the Silicon/Tungsten Luminosity Monitor (LMSAT). Also presented in this thesis will be a detailed analysis of the luminosity measurement for the 1992 SLD run. The measurement of the absolute luminosity and the left-right luminosity asymmetry are both incorporated into the wide angle analysis to extract the electron couplings to the Z^0.

The Standard Model of Electroweak Interactions will be outlined in Chapter II, with special attention given to the aspects of Z^0 production and decay which are specifically addressed in this analysis. Chapter III will discuss the relevant aspects of Bhabha scattering near the Z^0 resonance, including a discussion of the angular regimes where different physics contributions dominate. The method of extracting the electron vector and axial vector couplings will then be outlined. Also discussed in Chapter III will be potential extensions to the Standard Model to which this analysis has some degree of sensitivity.

Chapter IV will describe the experimental apparatus, the SLC and the SLD. The description of the accelerator will pay particular attention to the production and transport of a polarized electron beam, due to the unique capability of the SLC to produce and accelerate a polarized electrons. The main subsystems of the SLD: calorimetry, tracking, particle identification, polarimetry and beam energy measurement will be introduced and outlined. Additional detail will be presented for the SLD Liquid Argon Calorimeter (LAC), as it is the aspect of the detector used for the identification and analysis of the wide angle Bhabha events.

The SLD Luminosity Monitor will be introduced in Chapter IV as a calorimetry subsystem in the SLD but discussed in detail in Chapter V. The design, construction, testing, commissioning and operation of the SLD Silicon/Tungsten Luminosity Monitor will be presented. The detector was designed and built at the University of Oregon then transferred to SLAC for installation onto the SLC beamline. The SLD LMSAT is considered to be the first generation of high precision silicon luminosity devices.

Chapter VI will describe the measurement of the luminosity for the SLD 1992 data run utilizing the LMSAT. Particular attention will be given to the systematic errors, as they are the limiting factor in the measurement of the luminosity. The result of the luminosity measurement for the 1993 SLD run, based upon the same analysis presented here, will also be presented in Chapter VI. The absolute luminosity measurement, as well as the measurement of the left-right luminosity asymmetry, will

be utilized in the extraction of the electron couplings to the Z^0.

Event selection and preparation for the wide angle Bhabha analysis will be presented in Chapter VII. This will include aspects of triggering and event selection, as well as corrections to the data due to contamination factors and detection inefficiencies. Also presented in Chapter VII will be the polarization and center of mass energy measurements which are necessary to completely characterize each selected event.

Chapter VIII will describe the procedure of fitting the corrected data distributions and present the results for the electroweak measurements. Systematic errors will be discussed and the results compared with other experiments. Some conclusions on the implications of this analysis and result will then be presented and discussed in the context of other precision electroweak measurements. Chapter VIII will conclude with some prospects and proposals for future improvements to this analysis.

Appendix A will provide some additional information on the probability functions for polarized scattering, which are used in the maximum likelihood fits to the wide angle Bhabha scattering distributions.

The entire SLD collaboration will be listed Appendix B. Without the hard work, inspiration and insight of all of these collaborators, this work would not have been possible.

CHAPTER II

THE STANDARD MODEL

History has shown that nature prefers simplicity over complexity. Nature does not act upon situations based upon context; nature plays by a very simple set of rules, and it plays by them consistently. When it takes many parameters and situational conditions to describe nature, it is time to look for the underlying symmetry that the physical processes demonstrate. The complexity on the surface can most likely be described by an underlying simplicity. This is exactly what has taken place with the unification first of electricity and magnetism, then with electromagnetism and the weak interaction. The following chapter will describe this electroweak unification.

The electromagnetic interaction has been studied in great detail over the past two centuries. Maxwell proved that two apparently distinct forces, electricity and magnetism, actually arose from the one interaction. In the 20th century, the electromagnetic field was quantized and it became understood that the photon is the carrier of the electromagnetic force. Nuclear beta decay was the first recognition of the weak interaction, which has now been under study for about 75 years. Fermi was the first to develop a working theory of beta decay, then Lee and Yang brilliantly determined that the weak interaction violates parity, a symmetry which was once believed always satisfied.

In the 1960's, Glashow, Weinberg and Salam developed a theory which unifies the weak and electromagnetic interactions [2]. At low interaction energies, the forces appear to be completely distinct. However, at energies around 100 GeV, the unification of these forces becomes apparent. The "Standard Model of Electroweak Interactions" has so far passed every high precision experimental test of its validity. However, there is the hope and expectation that the Standard Model is again a "low" energy approximation to a larger theory which unifies the electroweak, strong, and gravitational interactions. The job of the experimentalist is to measure the parameters of the Standard Model with as high precision as possible, looking for deviations from the theory which may provide further insight into the fundamental physics behind subatomic particles and their interactions.

2.1 Framework of the Standard Model

The Standard Model is a gauge theory based on the $SU(2)_L \times U(1)$ group, where the SU(2) symmetry arises in "weak isospin" space and the U(1) symmetry arises in "weak hypercharge" space. The SU(2) group is generated by a vector triplet, $\overline{W_\mu} = W_\mu^{(1)}, W_\mu^{(2)}, W_\mu^{(3)}$ and the U(1) group is generated by the singlet, B_μ. These generators may be thought of as massless vector bosons, which are not eigenstates of the electroweak interaction. A process known as spontaneous symmetry breaking is invoked by way of the "Higgs mechanism".[1] The broken symmetry gives rise to physical bosons which are linear combinations of the group generators,

$$W_\mu^{\pm} = \frac{1}{\sqrt{2}}(W_\mu^{(1)} \pm iW_\mu^{(2)}) \tag{2.1}$$

$$Z_\mu = \frac{gW_\mu^{(3)} - g'B_\mu}{\sqrt{g^2 + g'^2}}, \tag{2.2}$$

$$A_\mu = \frac{g'W_\mu^{(3)} + gB_\mu}{\sqrt{g^2 + g'^2}}, \tag{2.3}$$

where $W_\mu^{\pm}$ are charged massive bosons, Z_μ is a neutral massive boson and, A_μ is the massless photon. The $W^{\pm}$, Z^0 and all of the fermions acquire mass through self-interaction terms provided by the Higgs field. A consequence of the Higgs mechanism is the prediction of one or more massive Higgs bosons, which have yet to be seen experimentally.

The hypercharge and isospin fields are "mixed". The magnitude of the mixing is defined by the couplings g and g' in the following manner:

$$g = \frac{e}{sin\theta_W}, \quad g' = \frac{e}{cos\theta_W}, \tag{2.4}$$

where e is the magnitude of the charge of the electron and the parameter θ_W is known as the weak mixing angle. The weak mixing angle may be thought of as a parameter utilized to demonstrate a unitary transformation (rotation) in hypercharge/isospin space.

The portion of the electroweak Lagrangian which describes the interaction between fermions and the gauge bosons may then be written in the following manner:

$$\begin{aligned} \mathcal{L} = \; & \tfrac{e}{sin\theta_W cos\theta_W}(J_\mu^{(3)} - sin^2\theta_W J_\mu^{e.m.})Z_\mu + && \leftarrow (weak\ NC) \\ & \tfrac{e}{\sqrt{2}sin\theta_W}(J_\mu^- W_\mu^+ + J_\mu^+ W_\mu^-) + && \leftarrow (weak\ CC) \\ & eJ_\mu^{e.m.}A_\mu, && \leftarrow (electromagnetic\ NC) \end{aligned} \tag{2.5}$$

[1] Although the Higgs mechanism is part of the Standard Model, there are other possible origins of spontaneous symmetry breaking. Therefore the fact that spontaneous symmetry breaking occurs (hence the massive gauge bosons and fermions) is a more solid tenet of the Standard Model than is the mechanism responsible for the broken symmetry.

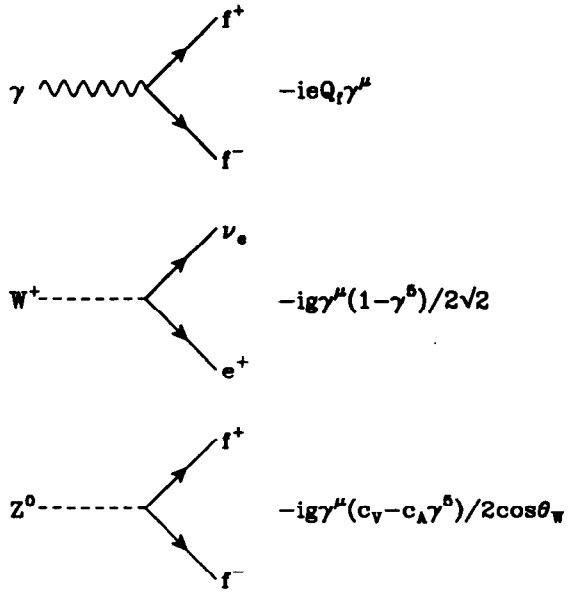

Figure 2.1: Electroweak vertex couplings.

where J_μ are the fermion currents. The first term of equation 2.5 is the weak neutral current interaction (Z^0 exchange), the second term is the weak charged current interaction ($W^\pm$ exchange) and the third term is the electromagnetic interaction (γ exchange). The Feynman vertices for each of these interactions is shown in Figure 2.1. The magnitude of each term depends upon θ_W and/or the charge of the fermions involved [3].

2.1.1 Bosons

A consequence of the broken symmetry is that three of the four gauge bosons gain mass. Since the boson propagator is proportional to $\frac{1}{q^2+m^2_{boson}}$, where q^2 is the square of the momentum transfer, the photon exchange of the electroweak neutral interaction dominates at low q^2. At $q^2 \gg m^2_{boson}$ the boson masses may be ignored altogether and the unified electroweak interaction behaves as a single force.

The mass of the charged gauge bosons (W^+, W^-) at tree level is given by:

$$M_W = \frac{1}{sin\theta_W}\sqrt{\frac{\pi\alpha}{\sqrt{2}G_F}} \simeq \frac{37.3}{sin\theta_W}\text{GeV}, \tag{2.6}$$

where α is the fine structure constant, $\alpha = \frac{e^2}{4\pi}$, and G_F is the Fermi constant. Both of these constants are very well measured, $\alpha = (137.0359895(61))^{-1}$ and $G_F = 1.16639(2) \times 10^{-5}\text{GeV}^{-2}$ [4]. The masses of the intermediate vector bosons are related

at tree level through the following expression:

$$M_W = M_Z \, cos\theta_W. \tag{2.7}$$

Both the W and the Z were discovered in 1983 by the UA1 experiment at the CERN $p\bar{p}$ collider [5]. Since then, the Z^0 factories at LEP and SLC have allowed for high precision study of Z^0 production and decay in the e^+e^- environment.

2.1.2 Fermions

In the Standard Model, fermions are broken into two categories: quarks and leptons. Leptons have integer charge and exist as fundamental particles. Quarks have fractional charge, couple to the color force of the strong interaction and are therefore always bound in quark-antiquark (meson) states or quark-quark-quark (baryon) states. Pairs of quarks and leptons are arranged into three generations of left-handed weak isodoublets:

$$\begin{array}{lccccc} quarks: & \begin{array}{c} Q=+2/3 \\ Q=-1/3 \end{array} & \begin{pmatrix} u \\ d \end{pmatrix}_L & \begin{pmatrix} c \\ s \end{pmatrix}_L & \begin{pmatrix} (t) \\ b \end{pmatrix}_L & \begin{array}{c} T_3=+1/2 \\ T_3=-1/2 \end{array} \\ leptons: & \begin{array}{c} Q=0 \\ Q=-1 \end{array} & \begin{pmatrix} \nu_e \\ e \end{pmatrix}_L & \begin{pmatrix} \nu_\mu \\ \mu \end{pmatrix}_L & \begin{pmatrix} (\nu_\tau) \\ \tau \end{pmatrix}_L & \begin{array}{c} T_3=+1/2 \\ T_3=-1/2 \end{array} \end{array} \tag{2.8}$$

where Q is the charge in units of the charge of the electron (e) and T_3 is the third component of weak isospin. All of the above fermions have an antiparticle counterpart which possesses the same mass and opposite charge. Massive right-handed fermions reside in isosinglet states, $T_3 = 0$, while right-handed neutrinos do not exist (see Table 2.1 and associated note). Neither the top quark nor the τ neutrino have been observed directly. However, the indirect evidence for their existence is overwhelming. In particular, the existence of the top quark is necessary to forbid flavor changing neutral currents (GIM mechanism). Furthermore, the couplings of both the τ lepton and the bottom quark to the Z^0 indicate that they are indeed members of weak isospin doublets.

As with gauge bosons, fermions gain mass through the Higgs mechanism. The three generations of quarks and leptons shown in equation 2.8 are listed by increasing mass. The Standard Model does not set the limit on the number of generations. Experimental evidence indicates that there are only three generations, based upon the number of light neutrinos [6].

2.1.3 Parameters of the Standard Model

The electroweak couplings and boson masses within the Standard Model may be completely specified by three parameters. Typically, those parameters are chosen to be the fine structure constant, $\alpha = e^2/4\pi$, the Fermi constant, $G_F = \sqrt{2}g^2/8M_W^2$, and the mass of the Z^0 boson, M_Z. The first two are chosen due to the high precision

with which they have been measured, leaving M_Z as the single parameter which is characteristic of electroweak unification to be measured with high precision. However, from the relationships listed above, as well as equations 2.4, 2.6 and 2.7, it is clear that a different set of parameters could be chosen without any loss of information. For example, e, $sin^2\theta_W$, and M_W also specify the Standard Model couplings.

Complete calculation of observables, however, requires the additional information of the fermion masses, and the Higgs boson mass, the number of fermion generations and the Cabbibo-Kobayashi-Maskawa (CKM) mixing angles. The particle masses and number of generations enter into seemingly unrelated processes by way of radiative corrections, discussed in Section 2.4. The CKM mixing angles relate the quark mass eigenstates and electroweak eigenstates.

2.1.4 Couplings

Figure 2.1 shows diagrammatically how the fermions couple to gauge bosons in the electroweak theory. The electromagnetic interaction preserves parity, insuring that left- and right-handed fermions couple identically to the photon. The V-A ("V minus A") nature of the charge current interaction couples exclusively to left-handed fermions.

Only in the case of the Z^0 are the couplings to left- and right-handed fermions different and nonzero. Left- and right-handed fermions couple to the Z^0 with the following strengths:

$$\begin{aligned} g_L &= T_3 - Qsin^2\theta_W, \\ g_R &= -Qsin^2\theta_W, \end{aligned} \tag{2.9}$$

where $g_L(g_R)$ is the left-(right-)handed fermion coupling to the Z^0. The corresponding vector and axial vector couplings follow from this:

$$\begin{aligned} g_v &= g_L + g_R = T_3 - 2Qsin^2\theta_W, \\ g_a &= g_L - g_R = T_3. \end{aligned} \tag{2.10}$$

The differences in the left- and right-handed couplings provide for some very interesting physics effects such as the forward-backward asymmetry and the left-right asymmetry (see Section 2.3). Table 2.1 summarizes the fermion quantum numbers and left and right handed couplings to the Z^0. Vector and axial vector couplings are summarized in Table 2.2.

The couplings g and g' and, hence, e and $sin^2\theta_W$ are "running" coupling constants. This means that the magnitude of the parameters depends upon the momentum scale of the interaction involving these parameters (see Section 2.4).

Table 2.1: Table of fermion couplings to the Z^0.

fermion	helicity $(h)^2$	charge (Q)	T_3	g_h^f
ν_e, ν_μ, ν_τ	$-\frac{1}{2}$	0	$+\frac{1}{2}$	$\frac{1}{2}$
	$(+\frac{1}{2})$	0	0	0
e^-, μ^-, τ^-	$-\frac{1}{2}$	-1	$-\frac{1}{2}$	$-\frac{1}{2} + sin^2\theta_W$
	$+\frac{1}{2}$	-1	0	$sin^2\theta_W$
u, c, t	$-\frac{1}{2}$	$+\frac{2}{3}$	$+\frac{1}{2}$	$\frac{1}{2} - \frac{2}{3}sin^2\theta_W$
	$+\frac{1}{2}$	$+\frac{2}{3}$	0	$-\frac{2}{3}sin^2\theta_W$
d, s, b	$-\frac{1}{2}$	$-\frac{1}{3}$	$-\frac{1}{2}$	$-\frac{1}{2} + \frac{1}{3}sin^2\theta_W$
	$+\frac{1}{2}$	$-\frac{1}{3}$	0	$\frac{1}{3}sin^2\theta_W$

2.2 Z^0 Production in e^+e^- Collisions

Although the Z^0 was discovered at a $p\overline{p}$ collider, high precision study of the Z^0 is best performed in the e^+e^- environment.

Near the Z^0 resonance, the photon contribution may be ignored in the $e^+e^- \rightarrow \gamma/Z^0 \rightarrow f\overline{f}$ ($f \neq$ electron) process. In the case of a polarized electron beam, the tree-level differential cross section for a fermion-antifermion (except e^+e^-) final state is given by:

$$\begin{aligned}\frac{d\sigma}{d\Omega} = & \frac{N_c\alpha^2}{2} \times \frac{s}{(s-M_Z)^2 + M_Z^2\Gamma_Z^2} \times \\ & \frac{(g_v^{e2} + g_a^{e2})}{sin^2 2\theta_W} \times \frac{(g_v^{f2} + g_a^{f2})}{sin^2 2\theta_W} \times \\ & [(1+cos^2\theta)(1+\mathcal{P}_e A_e) + 2A_f cos\theta(A_e + \mathcal{P}_e)], \end{aligned} \tag{2.11}$$

where N_c is a color factor (1 for leptons, 3 for quarks), and Γ_Z is the width of the Z^0 resonance.

The kinematics of this process is seen in Figure 2.2, where p_1, p_2, k_1, and k_2 are the four-momenta of the incoming and outgoing particles. The center of mass energy squared is defined as $s = (p_1+p_2)^2$ and is Lorentz invariant. Another Lorentz invariant variable which will be utilized in this discussion is the square of the momentum

[2]In the Standard Model, neutrinos are massless and exclusively left-handed. However, if neutrinos do have mass, then the right-handed neutrinos would exist but not couple to any of the four gauge bosons of the electroweak theory. Right handed neutrinos are included in the table for completeness.

Table 2.2: Table vector and axial vector couplings to the Z^0. The approximate values for A_f given in column 4 assume $sin^2\theta_W = 0.23$.

fermion	g_v^f	g_a^f	A_f
ν_e, ν_μ, ν_τ	$\frac{1}{2}$	$\frac{1}{2}$	1
e^-, μ^-, τ^-	$-\frac{1}{2} + 2sin^2\theta_W \simeq -0.04$	$-\frac{1}{2}$	$\frac{2[1-4sin^2\theta_W]}{1+[1-4sin^2\theta_W]^2} \simeq 0.15$
u, c, t	$\frac{1}{2} - \frac{4}{3}sin^2\theta_W \simeq 0.19$	$\frac{1}{2}$	$\frac{2[1-\frac{8}{3}sin^2\theta_W]}{1+[1-\frac{8}{3}sin^2\theta_W]^2} \simeq 0.67$
d, s, b	$-\frac{1}{2} + \frac{2}{3}sin^2\theta_W \simeq -0.35$	$-\frac{1}{2}$	$\frac{2[1-\frac{4}{3}sin^2\theta_W]}{1+[1-\frac{4}{3}sin^2\theta_W]^2} \simeq 0.94$

transfer, $t = (\mathrm{p_1} - \mathrm{k_1})^2$. The scattering angle, θ, is defined as the angle between the final state fermion (f) and axis of the outgoing electron beam.

The electron beam polarization, $\mathcal{P}_e$, is defined as

$$\mathcal{P}_e = \frac{N_L^{e^-} - N_R^{e^-}}{N_L^{e^-} + N_R^{e^-}}, \tag{2.12}$$

where $N_L^{e^-}$ ($N_R^{e^-}$) is the number of left-(right-)handed electrons in the beam [7]. The quantity A_f is a measure of the degree of parity violation in the neutral current:

$$A_f = \frac{g_L^{f\,2} - g_R^{f\,2}}{g_L^{f\,2} + g_R^{f\,2}} = \frac{2g_v^f g_a^f}{g_v^{f\,2} + g_a^{f\,2}}. \tag{2.13}$$

It is also convenient to define the partial width for Z^0 decaying into fermions:

$$\Gamma_{f\bar{f}} = \frac{G_F M_Z^3}{6\sqrt{2}\pi}(g_v^{f\,2} + g_a^{f\,2})N_c(1 + \delta_f), \tag{2.14}$$

where δ_f is the correction for final state radiation, defined as $\delta_f = \frac{3\alpha}{4\pi}Q_f^2$ for leptons and $\delta_f = \frac{3\alpha}{4\pi}Q_f^2 + \frac{\alpha_s}{4\pi}$ for quarks, where α_s is the strong coupling constant. The total width of the Z^0 is the sum of the partial widths, $\Gamma_Z = \sum \Gamma_{f\bar{f}}$.

Equation 2.11 may be utilized in several different ways to extract the electroweak parameters. Some of the methods require identification and isolation of a specific final state, known as an exclusive measurement, while others simply require a sum over final states, known as inclusive measurements. The following methods isolate specific terms in Equation 2.11:

- With unpolarized beams, measure the inclusive and exclusive differential and/or total cross section while scanning the center of mass energy, $\sqrt{s}$. This yields M_Z, Γ_Z and $\Gamma_{f\bar{f}}$.

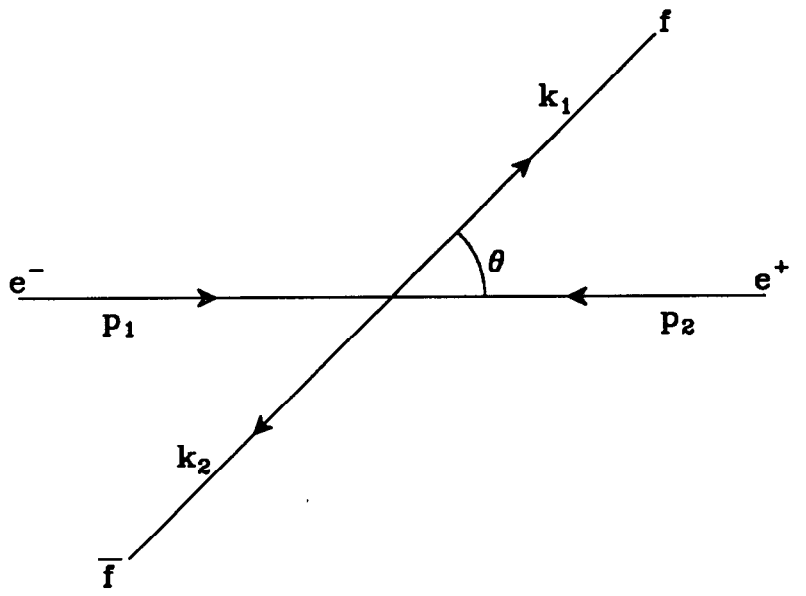

Figure 2.2: Kinematics of electron-positron annihilation.

- With unpolarized beams, measure the forward-backward asymmetry for exclusive final states:

$$A_{fb} = \frac{\int_0^1 \frac{d\sigma}{dcos\theta} dcos\theta - \int_{-1}^0 \frac{d\sigma}{dcos\theta} dcos\theta}{\int_0^1 \frac{d\sigma}{dcos\theta} dcos\theta + \int_{-1}^0 \frac{d\sigma}{dcos\theta} dcos\theta} = \frac{3}{4} A_e A_f. \tag{2.15}$$

- With a polarized electron beam, measure the total cross section for beams with each helicity, known as the left-right asymmetry:

$$A_{LR} = \frac{\sigma_L - \sigma_R}{\sigma_L + \sigma_R} = A_e. \tag{2.16}$$

- With a polarized electron beam, measure the polarized forward-backward asymmetry for exclusive final states:

$$\tilde{A}_{fb} = \frac{[\int_0^1 \frac{d\sigma}{dz} dz - \int_{-1}^0 \frac{d\sigma}{dz} dz]_L - [\int_0^1 \frac{d\sigma}{dz} dz - \int_{-1}^0 \frac{d\sigma}{dz} dz]_R}{[\int_0^1 \frac{d\sigma}{dz} dz - \int_{-1}^0 \frac{d\sigma}{dz} dz]_L + [\int_0^1 \frac{d\sigma}{dz} dz - \int_{-1}^0 \frac{d\sigma}{dz} dz]_R} = \frac{3}{4} A_f, \tag{2.17}$$

where $z \equiv cos\theta$.

The first method listed above allows for high precision measurement of the Z^0 mass and width, as well as the partial widths. The partial widths, $\Gamma_{f\bar{f}}$, are primarily sensitive to the axial vector coupling between the fermion and the Z^0. The final three methods listed above are sensitive to the fermion vector coupling to the Z^0 and, therefore more sensitive to $sin^2\theta_W$. These different sensitivities make all of the above measurements complementary [8].

2.3 The Left-Right Asymmetry

The left-right asymmetry, A_{LR}, is an especially robust, high precision method for measuring the electroweak mixing angle [9, 10]. By forming the cross section asymmetry in this manner, the dependence on the final state couplings is completely removed. A_{LR} is a measure of the electron coupling to the Z^0 in the initial state.

The asymmetry is related to the weak mixing angle in the following way:

$$A_{LR} = \frac{2[1 - 4sin^2\theta_W]}{1 + [1 - 4sin^2\theta_W]^2}. \tag{2.18}$$

The error on $sin^2\theta_W$ is approximately 1/8th the error on the left-right asymmetry.

Since A_{LR} is independent of the final state couplings, a statistical advantage is gained by using all final states from the Z^0 with the exception of the e^+e^- final state, which is removed due to the complication of the t-channel photon contribution (see Section 3.1.2). In addition, the A_{LR} measurement does not require knowledge of the absolute luminosity or the detector acceptance and efficiency.

The quantity actually measured is the experimental asymmetry, A_{LR}^{exp}:

$$A_{LR}^{exp} = \frac{N_L - N_R}{N_L + N_R} = \mathcal{P}_e A_{LR}. \tag{2.19}$$

where N_L (N_R) is the number of Z^0 decays found with a left-(right-)handed electron beam. Equation 2.19 is valid provided that both the luminosity and polarization of the left-handed beam is the same as that of right-handed beam. The two dominant experimental errors on A_{LR} are the statistical error and the error on the measure of the beam polarization:

$$\delta A_{LR} = \sqrt{\frac{1}{\mathcal{P}_e^2 N_{tot}} + A_{LR}^2 \left(\frac{\delta \mathcal{P}_e}{\mathcal{P}_e}\right)^2}, \tag{2.20}$$

where $N_{tot} = N_L + N_R$ and $\delta\mathcal{P}_e$ is the uncertainty on the electron beam polarization measurement. Figure 2.3 shows the error on A_{LR} and $sin^2\theta_W$ as a function of the number of Z^0 decays for different errors on the polarization measurement. With low statistics, the first term of equation 2.20 dominates. As statistics grow, the error on the polarization becomes the limiting factor.

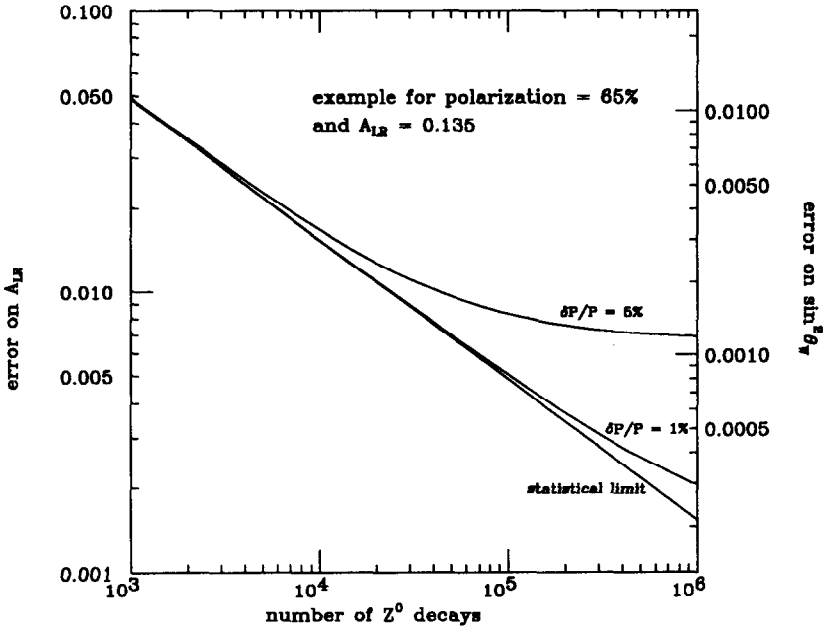

Figure 2.3: Error on A_{LR} and $sin^2\theta_W$.

It may also be seen from equation 2.20 that the statistical error on the left-right is reduced as $1/\mathcal{P}_e\sqrt{N}$. Therefore, doubling the beam polarization is equivalent to increasing the number of Z^0 decays fourfold, demonstrating the large gain in analyzing power that high polarization provides.

2.4 Radiative Corrections

All electroweak observables are modified from their Born level expectations by way of radiative corrections. Radiative corrections are especially important in electron-positron annihilation near the Z^0 resonance, due to the large Breit-Wigner Z^0 contribution.

Radiative corrections are typically handled by perturbation theory. This method is accurate due to the small value of the coupling constants. For electromagnetic radiative corrections, the perturbation expansion is in terms of α, yielding fast convergence.

There are four major classes of lowest order radiative corrections: bremsstrahlung, vertex corrections, box diagrams and oblique corrections. Examples of these four processes are shown in Figure 2.4. Initial state photon bremsstrahlung is usually the dominant correction, which produces the effect of lowering the center of mass energy in the e^+e^- system, while boosting the center of mass along the beam axis. Also important are the oblique corrections, which must be summed over all fermions and

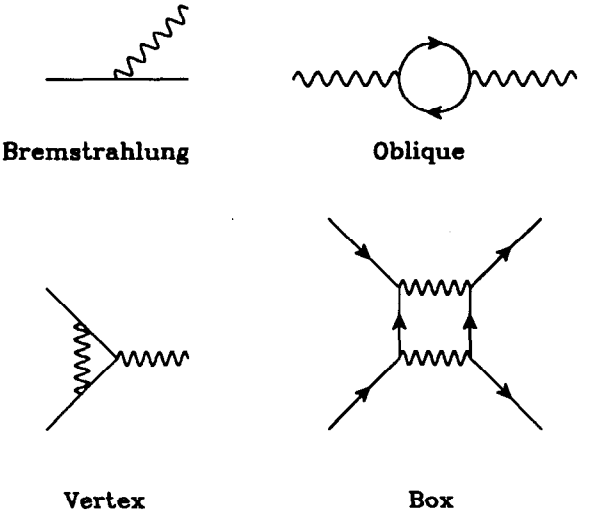

Figure 2.4: Examples of processes contributing to first-order radiative diagrams.

bosons, rendering them sensitive to massive particles, such as a heavy top quark. Oblique corrections are also sensitive to new heavy particles which couple to the gauge bosons.

Different processes are affected by radiative corrections in different ways. The Z^0 cross section is lowered by 30% and shifted by 100 MeV due primarily to initial state bremsstrahlung. The left-right asymmetry is very sensitive to the masses of heavy fermions through oblique and initial weak vertex corrections [9, 11, 12].

The parameters of the Standard Model can be redefined to absorb the running couplings and radiative corrections. These parameters correspond to quantities which can be accessed experimentally. Effective couplings will be defined with a bar over them. The effective electron vector and axial vector couplings to the Z^0 (evaluated at $\sqrt{s} = M_Z$) will be denoted as $\overline{g}_v^e$ and $\overline{g}_a^e$ respectively.

There are a number of ways in which to define the weak mixing angle. The definition chosen here follows from equation 2.10:

$$sin^2\theta_W^{eff} = \frac{1}{4}(1 - \frac{\overline{g}_v^e}{\overline{g}_a^e}). \tag{2.21}$$

This definition allows corrections to the weak mixing angle to be absorbed directly through the effective coupling constants [13].

CHAPTER III

BHABHA SCATTERING NEAR THE Z^0 RESONANCE

The Bhabha process [14], $e^+e^- \rightarrow e^+e^-$, is particularly interesting in that it exhibits both neutral current processes (Z^0 and photon exchange) at magnitudes which are non-negligible. This means that not only the direct contributions, but also the interference between the photon and Z^0 contribute to the total cross section in an appreciable manner. At the Z^0 resonance, the QED contribution may be used as a reference point, allowing the electron couplings to the neutral current to be extracted from the Bhabha process.

3.1 Born Level Contributions to $e^+e^- \rightarrow e^+e^-$

At lowest order near the Z^0 resonance, four diagrams (shown in Figure 3.1) contribute to the $e^+e^- \rightarrow e^+e^-$ cross section in the Standard Model. The square of these contribution gives rise to 10 lowest order terms [15]:

$$d\sigma_0[\gamma(s),\gamma(s)] = \frac{\alpha^2}{4s}(1+z^2) \equiv d\sigma_0(1), \tag{3.1}$$

$$d\sigma_0[\gamma(s),\gamma(t)] = -\frac{\alpha^2}{4s}2\frac{(1+z)^2}{(1-z)} \equiv d\sigma_0(2), \tag{3.2}$$

$$d\sigma_0[\gamma(t),\gamma(t)] = \frac{\alpha^2}{4s}2\frac{(1+z)^2+4}{(1-z)^2} \equiv d\sigma_0(3), \tag{3.3}$$

$$d\sigma_0[\gamma(s),Z(t)] = -\frac{\alpha^2}{4s}\left[\frac{2R'(t)}{sin^2 2\theta_W}\right](1+z)^2(g_v^{e2}+g_a^{e2}) \equiv d\sigma_0(4), \tag{3.4}$$

$$d\sigma_0[\gamma(t),Z(t)] = \frac{\alpha^2}{4s}\left[\frac{2}{(1-z)}\right]\left[\frac{2R'(t)}{sin^2 2\theta_W}\right] \times [(g_v^{e2}+g_a^{e2})(1+z)^2+4(g_v^{e2}-g_a^{e2})] \equiv d\sigma_0(5), \tag{3.5}$$

$$d\sigma_0[Z(t),Z(t)] = \frac{\alpha^2}{4s}\left[\frac{2R'(t)}{sin^4 2\theta_W}\right]\left\{(1+z)^2\left[(g_v^{e2}+g_a^{e2})^2+4g_v^{e2}g_a^{e2}\right]+\right.$$

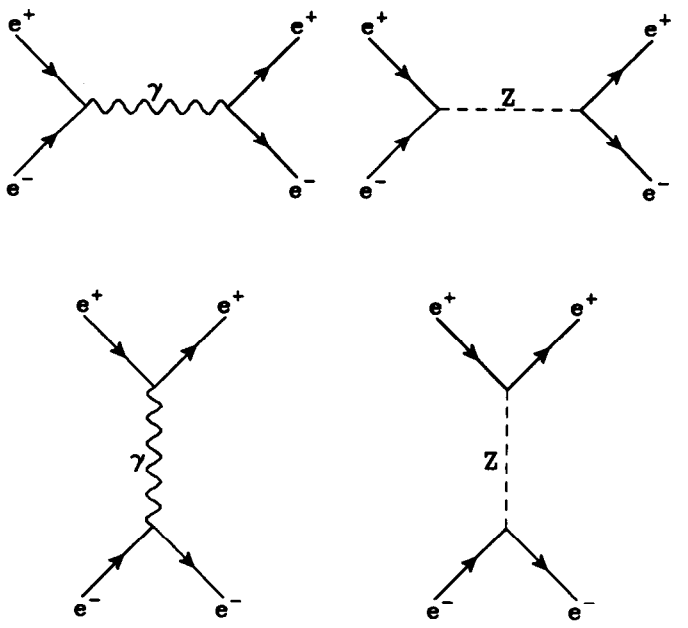

Figure 3.1: Born Level contributions to $e^+e^- \rightarrow e^+e^-$.

$$4\Big[(g_v^{e2}+g_a^{e2})^2 - 4g_v^{e2}g_a^{e2}\Big]\Big\} \equiv d\sigma_0(6), \tag{3.6}$$

$$d\sigma_0[Z(s),\gamma(s)] = \frac{\alpha^2}{4s}\Big[\frac{2R'(s)}{sin^2 2\theta_W}\Big][g_v^{e2}(1+z^2)+2zg_v^{e2}] \equiv d\sigma_0(7), \tag{3.7}$$

$$d\sigma_0[Z(s),\gamma(t)] = -\frac{\alpha^2}{4s}\Big[\frac{2R'(s)}{sin^2 2\theta_W}\Big]\Big[\frac{(1+z)^2}{(1-z)}\Big](g_v^{e2}+g_a^{e2}) \equiv d\sigma_0(8), \tag{3.8}$$

$$d\sigma_0[Z(s),Z(t)] = -\frac{\alpha^2}{4s}\Big[\frac{2R'(s)R'(t)}{sin^4 2\theta_W}\Big](1+z)^2 \times$$
$$[(g_v^{e2}+g_a^{e2})^2 + 4g_v^{e2}g_a^{e2}] \equiv d\sigma_0(9), \tag{3.9}$$

$$d\sigma_0[Z(s),Z(s)] = \frac{\alpha^2}{4s}[R'^2(s)+I'^2(s)]\frac{(g_v^{e2}+g_a^{e2})^2}{sin^4 2\theta_W} \times$$
$$\Big\{(1+z^2)+\Big[\frac{4g_v^{e2}g_a^{e2}}{(g_v^{e2}+g_a^{e2})^2}\Big]2z\Big\} \equiv d\sigma_0(10), \tag{3.10}$$

where $z = cos\theta$ (θ the angle between the initial and final electron), M_Z and Γ_Z are the mass and width of the Z^0 and

$$R'(t) = \frac{s}{2(M_Z - t)} \qquad \text{and} \qquad R'(s) + iI'(s) \equiv \frac{s}{(s-(M_Z - iM_Z\Gamma_Z)^2)}$$

are the Z^0 propagator terms. The lowest order differential $e^+e^- \rightarrow e^+e^-$ cross section is the sum of these terms:

$$\frac{d\sigma}{d\Omega} = \sum_{i=1}^{10} d\sigma_0(i). \tag{3.11}$$

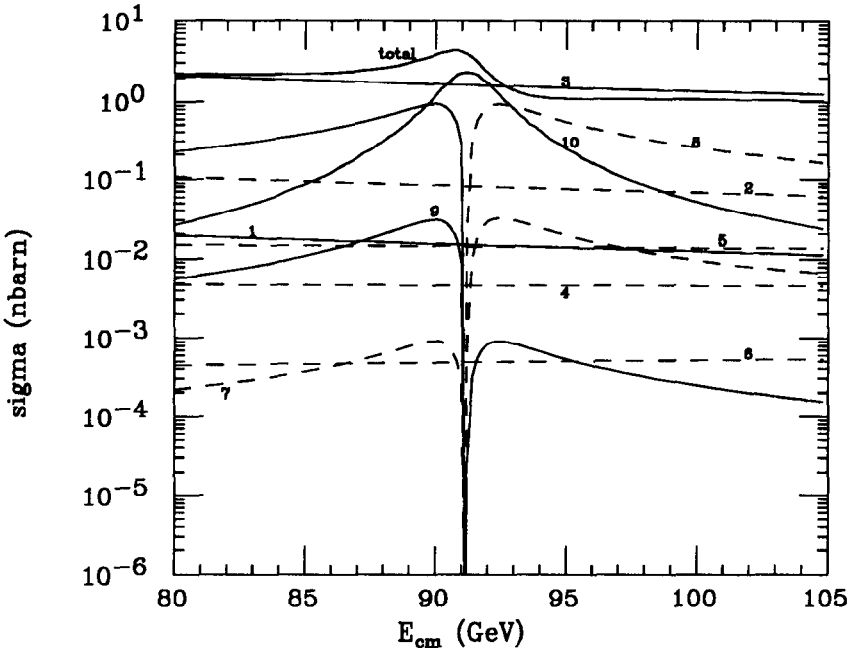

Figure 3.2: Contributions to the $e^+e^- \rightarrow e^+e^-$ cross section as a function of center of mass energy. See text for definitions. Terms with a negative contribution are denoted by a dashed curve.

Figure 3.2 shows the contribution of each of these ten terms as a function of center of mass energy. The cross sections presented in this figure are integrated from 0 to 2π in azimuth and from 15° to 165° in polar angle. Negative contributions are denoted by dashed lines. Terms which interfere with the s-channel Z^0 exchange possess a very steep slope near the Z^0 pole and pass through zero at $\sqrt{s} = M_Z$.

The angular dependence of each of the terms is shown in Figure 3.3. Again, terms with a contribution less than zero are show as dashed lines. The center of mass energy for this plot is 91.29 GeV and the Z^0 mass is set to be 91.187 GeV. At large angles ($\cos\theta < 0.7$) the s-channel Z^0 exchange term $[Z(s), Z(s)]$ dominates and the cross section looks similar to that of any other $Z^0 \rightarrow f\bar{f}$ process (with an additional t-channel photon contribution of a few percent). The t-channel photon exchange $[\gamma(t), \gamma(t)]$ begins to dominate at small angles ($\cos\theta > 0.85$). Since this is a pure quantum electrodynamics interaction, the cross section for $e^+e^- \rightarrow e^+e^-$ at small angles can be calculated with great precision.[1] This fact coupled with the large event rate makes the small angle e^+e^- process ideal for luminosity monitoring at e^+e^- colliders.

Above the the Z^0 pole in this case, the largest interference contribution comes

[1]The $[\gamma(t), \gamma(t)]$ contribution diverges more quickly as $\cos\theta \rightarrow 1$ than do the $[Z(s), \gamma(t)]$ and $[\gamma(s), \gamma(t)]$ terms, so it continues to dominate as the scattering angle goes to zero.

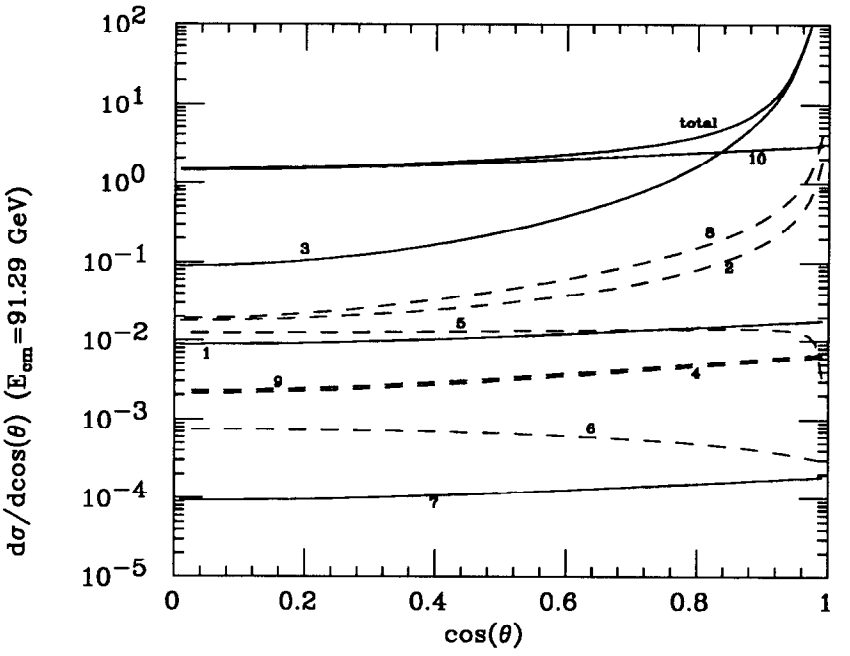

Figure 3.3: Contribution to the differential $e^+e^- \rightarrow e^+e^-$ cross section as a function of scattering angle. Terms with a negative contribution are denoted by a dashed curve. See text for definitions.

from the $[Z(s), \gamma(t)]$ term, which subtracts from the total cross section. The behavior of the interference terms very near the Z^0 pole have prompted some to consider using the large angle e^+e^- process as a high precision, luminosity independent measurement of M_Z [16].

The discussion so far has been restricted to the tree-level behavior of the terms contributing to the differential Bhabha cross section. The measured cross section is modified somewhat by radiative corrections, which affect different contributions in different ways. The trends discussed here still hold, but to compare theory with observation, the radiative corrections must be included. A great of work has gone into the radiative corrections of $e^+e^- \rightarrow e^+e^-$ at large and small angles [15, 17].

3.1.1 Bhabha Scattering at Small Angles

As stated above, the small angle $e^+e^- \rightarrow e^+e^-$ process is ideal for luminosity monitoring due to the large event rate and dominance of the QED t-channel photon exchange. The SLD Luminosity Monitor covers an angular region between 28 and 65 milliradians. The e^+e^- cross section into this region is approximately 120 nanobarns, which is four times the hadronic Z^0 cross section at the peak. The steep behavior of the differential cross section, $\frac{d\sigma}{d\theta} \sim \frac{1}{\theta^3}$, makes knowledge of the acceptance region important when measuring the luminosity.

In addition, the QED dominance at small angles renders the cross section largely polarization independent. Therefore, the small angle e^+e^- process may also be used to measure the luminosity asymmetry between the left and right handed polarized electron beam. This is an important systematic effect in the measurement of the left-right asymmetry, A_{LR}.

3.1.2 Bhabha Scattering at Wide Angles

At larger angles ($\theta > 15°$) the $e^+e^- \rightarrow e^+e^-$ process is an interesting interplay between the s-channel Z^0 exchange, $[Z(s), Z(s)]$, the t-channel photon exchange, $[\gamma(t), \gamma(t)]$, and the interference between these two, $[\gamma(t), Z(s)]$, which depends on both angle and energy. At $cos\theta < 0.6$ the contribution is virtually all through the s-channel Z^0 exchange. The region is typically used when measuring the $Z^0 \rightarrow e^+e^-$ cross section. Corrections must be performed to either add the remaining contributions from the other terms to the partial width or subtract them from the data [18].

The $[\gamma(t), Z(s)]$ interference term contributes its largest amount in the angular range $10° < \theta < 25°$. Depending on the center of mass energy, this contribution can be as large as 25% of the differential cross section in that region.

In the standard analysis of A_{LR}, the e^+e^- final state is discarded due to the dilution which arises from the photon exchange. However, it is possible to form a left-right quantity for $e^+e^- \rightarrow e^+e^-$ which is directly analogous to A_{LR}:

$$A_{LR}^{e^+e^-}(|cos\theta|) = \frac{\left(\frac{d\sigma}{d|cos\theta|}\right)_L - \left(\frac{d\sigma}{d|cos\theta|}\right)_R}{\left(\frac{d\sigma}{d|cos\theta|}\right)_L + \left(\frac{d\sigma}{d|cos\theta|}\right)_R}. \tag{3.12}$$

The quantity $A_{LR}^{e^+e^-}$ can be measured by binning the data as a function of $|cos\theta|$ for left- and right-handed polarized beams. The behavior of $A_{LR}^{e^+e^-}$ as a function of $|cos\theta|$ depends on the initial state electron couplings to the Z^0 as well as the magnitude of the QED contributions relative to the Z^0. The portion of the cross section from $[Z(s), Z(s)]$ contributes an amount $A_{LR}(=A_e)$ to the $A_{LR}^{e^+e^-}$, while the QED terms contribute zero to $A_{LR}^{e^+e^-}$. Figure 3.4 shows $A_{LR}^{e^+e^-}$ as a function of $|cos\theta|$ at the Born level for five different center of mass energies. The difference in these curves reflects the difference in relative contributions. At $\sim$800 MeV above the Z^0 peak, the $[\gamma(t), Z(s)]$ interference subtracts enough from the sum to force $A_{LR}^{e^+e^-} < 0$ at $|cos\theta| \sim 0.95$. By defining the quantity $A_{LR}^{e^+e^-}$ in terms of $|cos\theta|$, the forward-backward asymmetry is explicitly removed.

3.2 Extracting $\overline{g}_v^e$ and $\overline{g}_a^e$ with Polarized Bhabha Scattering

The Bhabha process provides an opportunity to simultaneously extract both the electron vector and axial vector couplings to the Z^0. The partial width, Γ_{ee}, can

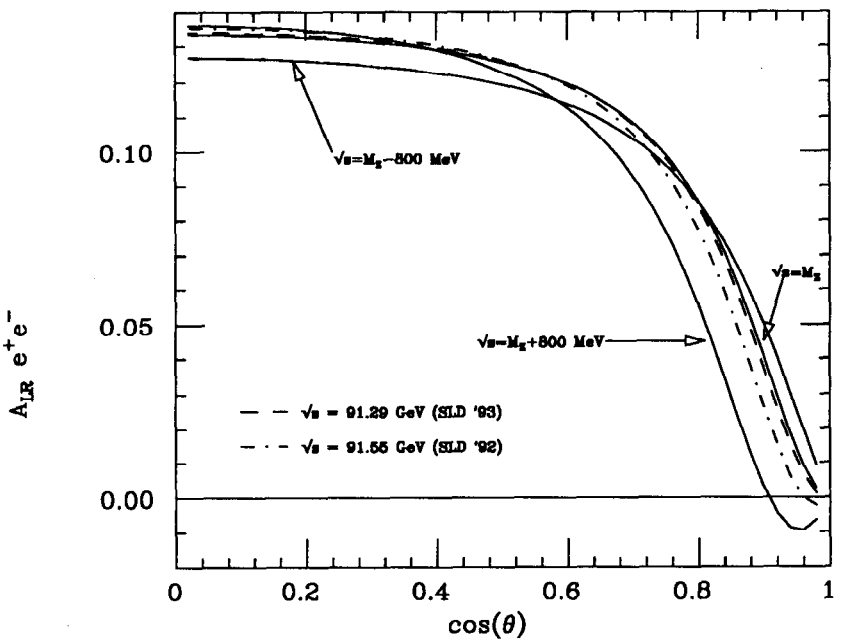

Figure 3.4: $A_{LR}^{e^+e^-}$ as a function of scattering angle.

be related to the cross section for $Z^0 \rightarrow e^+e^-$ in the following way (for unpolarized beams):

$$\frac{d\sigma}{d\phi d|cos\theta|} = \frac{9\Gamma_{ee}^2}{2M_Z^2\Gamma_Z^2}\Big(1 + cos^2\theta\Big). \tag{3.13}$$

A measurement of the differential or total cross section for $Z^0 \rightarrow e^+e^-$ can be related to the partial width, assuming knowledge of the Z^0 mass and total width.

Both Γ_{ee} (equation 2.14) and A_e (equation 2.13) are functions of $\overline{g}_v^e$ and $\overline{g}_a^e$. Measuring Γ_{ee} and A_e yields two equations with the couplings as the two unknowns. Figure 3.5 shows the expression for Γ_{ee} and A_e plotted in the vector–axial vector plane. The solution for Γ_{ee} is circle of radius $\sqrt{\frac{\Gamma_{ee}}{C_{SM}}}$, where $C_{SM} = \frac{G_F M_Z^3}{6\sqrt{2}\pi}(1 + \frac{3\alpha}{4\pi}) = 332.34 \pm 0.08$ MeV. The expression for A_e is seen to be a line in the vector–axial vector plane, with the solution: $\overline{g}_v^e \simeq (\frac{1}{2}A_e)\overline{g}_a^e$, where we have made use of the the fact that $A_e^2 \ll 1$. The quadratic nature of equation 2.13 provides two solutions, one in which the axial vector coupling is dominant and one where the vector coupling is dominant. Results from measurements of Γ_{ee} at LEP, as well as ν_e scattering experiments allow us to exclude the vector dominated solution, which is shown as a dashed line. In addition, ν_e scattering is used to prove that the proper solution is for both the vector and axial vector coupling to be negative, indicating that the solution must lie in the third quadrant [19].

The smallness of the vector coupling (due to $sin^2\theta_W$ near 1/4) greatly reduces the correlation between $\overline{g}_v^e$ and $\overline{g}_a^e$. Consequently, Γ_{ee} depends almost exclusively upon

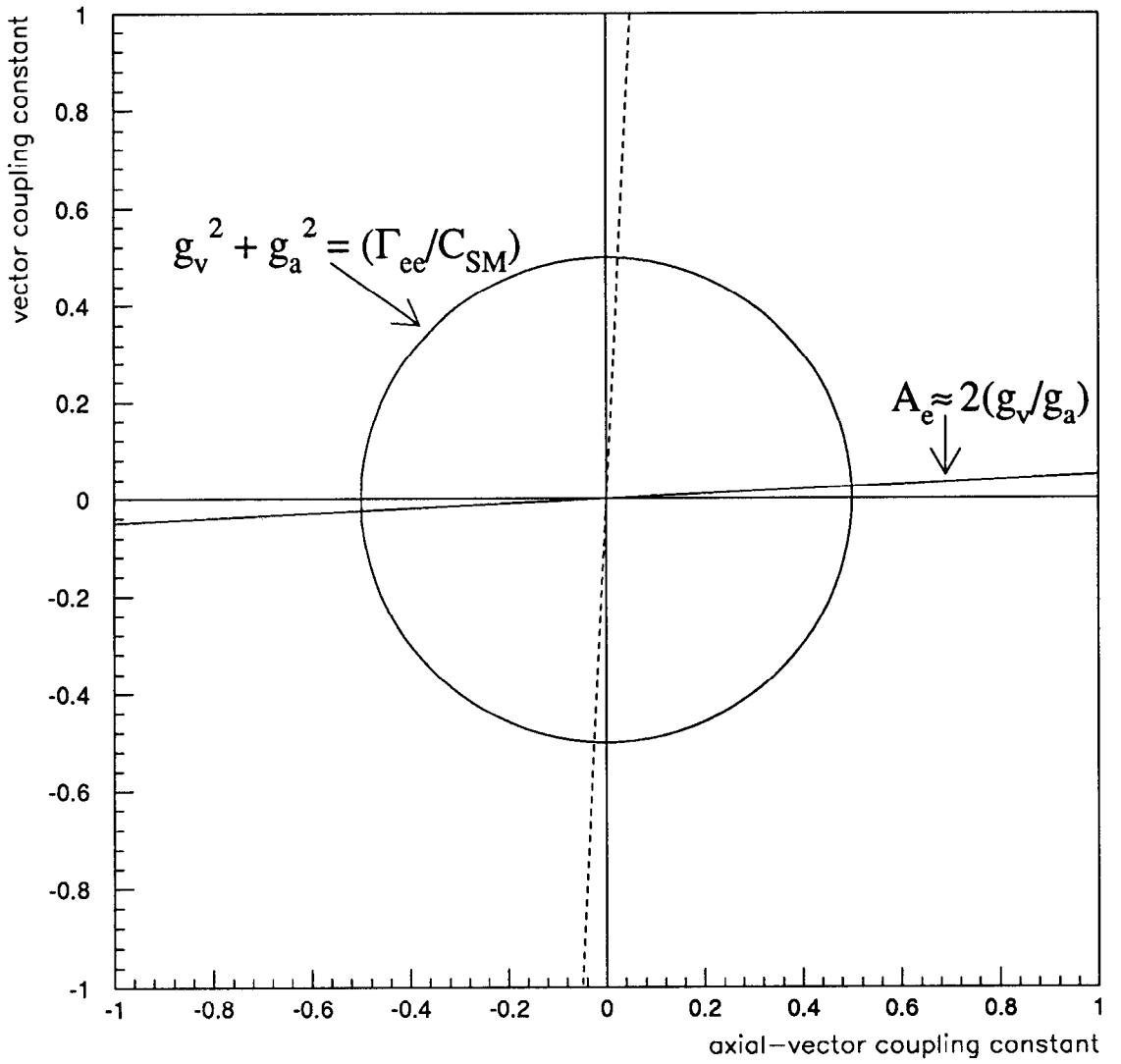

Figure 3.5: Γ_{ee} and A_e in the axial vector–vector coupling plane.

$\overline{g}_a^e$, while A_e depends almost exclusively upon $\overline{g}_v^e$. Since the the vector coupling is the one which depends upon $sin^2\theta_W$ in the Standard Model, A_e yields much greater sensitivity to the weak mixing angle than does Γ_{ee}.

To summarize, it can be said that Γ_{ee} is sensitive primarily to the axial vector coupling, while A_e is sensitive primarily to the vector coupling. However, *both* measurements are required to extract the two couplings. By fitting the polarized wide angle Bhabha distribution, it is possible to simultaneously extract both $\overline{g}_v^e$ and $\overline{g}_a^e$.

3.3 Beyond the Standard Model

The Bhabha scattering process has been calculated with high precision within the framework of the Standard Model. Any deviation from the expected differential cross section may be an indication of physics beyond the Standard Model.[2] Since direct searches at e^+e^- and $p\overline{p}$ machines have ruled out physics beyond the Standard Model at or below the mass of the Z^0, deviations seen at the Z^0 resonance would most likely be low energy manifestations of new physics at higher energy.

Several possible Standard Model extensions have been proposed which may be recognized through deviations in the differential Bhabha scattering distribution with a polarized electron beam. This section will discuss three of these topics: the existence of one or more additional gauge bosons, contact interactions, and the existence of a fourth generation.

3.3.1 Additional Gauge Bosons (Z')

Many extensions to the standard $SU(2)_L \times U(1)$ symmetry group include the existence of one or more additional neutral gauge bosons (Z'). These theories include the $SU(2)_L \times U(1)$ group as a subgroup to a larger unified group. Among these are the E_6, $SO(10)$ and $SU(2)_L \times SU(2)_R \times U(1)$ theories [20]. The models typically specify the strengths of the couplings of the Z' to quarks and leptons but make no predictions for the Z' mass.

To date, there is no experimental evidence for the existence of any Z' bosons. The experimental limit on the mass of the Z', $m_{Z'}$, is 412 GeV. This limit assumes Standard Model coupling strengths between the Z' and leptons [21].

The Z^0 and Z' would arise from a mixing of the $SU(2)_L \times U(1)$ group of the Standard Model and the additional U(1) or $SU(2)_R$ group which extends the model. The mass eigenstates of the bosons could then be different from the interaction eigenstates:

$$\begin{pmatrix} Z \\ Z' \end{pmatrix} = \begin{pmatrix} cos\theta_M & sin\theta_M \\ -sin\theta_M & cos\theta_M \end{pmatrix} \begin{pmatrix} Z^0 \\ Z^{0\prime} \end{pmatrix} \tag{3.14}$$

[2] "Physics beyond the Standard Model" is a phrase often used to summarize all particles and couplings which are not explicitly present within the Standard Model.

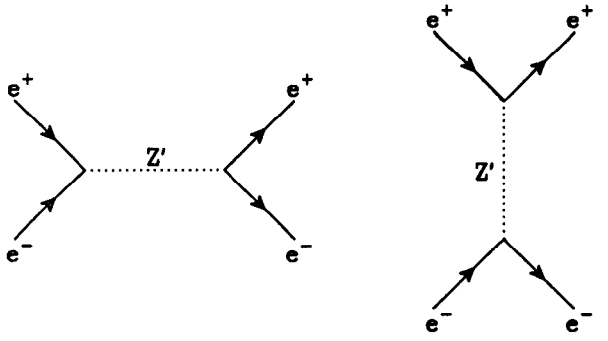

Figure 3.6: Born level Z' contributions to e^+e^- scattering.

where Z^0 and $Z^{0\prime}$ are the symmetry eigenstates and Z and Z' are the mass eigenstates. The boson masses are related to the mixing angle, θ_M, by:

$$tan^2\theta_M = \frac{m_0^2 - m_Z^2}{m_{Z'}^2 - m_0^2}, \tag{3.15}$$

where m_0 is the mass of the standard Z boson in the absence of mixing. An analysis performed at the Z^0 resonance limits the Z-Z' mixing angle to the range: $-0.05 \lesssim \theta_M \lesssim 0.015$ [22].[3] For a 500 GeV Z' with a mixing angle of $\theta_M = 0.005$, the measured Z^0 mass would be shifted from its unmixed value by approximately 34 MeV.

In the case of $e^+e^- \rightarrow f\overline{f}$, where $f \neq e$, the Z' would contribute an s-channel term and interfere with the s-channel photon and s-channel Z^0. In the case of Bhabha scattering, the Z' would contribute both an s and t channel term to the differential cross section [23, 24]. The Feynman diagrams for the Z' contribution to the $e^+e^- \rightarrow e^+e^-$ process are shown in Figure 3.6. These terms would exist in addition to and therefore interfere with those shown in Figure 3.1. Due to the proximity of the large Z^0 resonance, the effect of a Z' is expected to be very small in the case of polarized $e^+e^- \rightarrow e^+e^-$ near the Z^0.

3.3.2 Contact Interactions

Based on past successes of uncovering underlying structure in matter as well as the symmetries and mass structure displayed by quarks and leptons has led some to hypothesize the existence of quark and lepton substructure. These theories are known as composite theories, where the bosons and fermions of the standard model are comprised of subconstituents, sometimes called 'preons' [25].

Substructure may manifest itself in two ways. First, excited states of leptons and quarks may exist which have large masses and possibly exotic quantum numbers

[3]The exact results depend upon the model and may be found in [22].

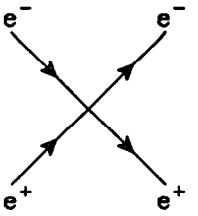

Figure 3.7: The Feynman diagram for a contact interaction in e^+e^- scattering.

[26]. Secondly, the composite bound state would arise from an interaction beyond the Standard Model [27]. In both cases, the energy scale of the composite system, set by the parameter Λ, is greater than or of order of that of electroweak symmetry breaking, $\lesssim 1$ TeV.

Direct searches for excited quarks and leptons have been undertaken elsewhere. To date, there is no experimental evidence for composite particles. The current limit on the mass of an excited electron is 225 GeV [28].

Since the energy scale, Λ is much larger than the scattering energy at the Z^0 resonance, the momentum of the propagator may be ignored relative to the mass, rendering the interaction point-like, or a contact interaction. The fermion currents in this interaction are helicity conserving and flavor diagonal, but do not necessarily conserve parity.

Polarized Bhabha scattering is a desirable method for searching for contact interactions for two reasons: first, the $e^+e^- \rightarrow e^+e^-$ process probes exclusively the composite structure of the electron. Secondly, electron polarization allows for additional sensitivity to the helicity conserving nature of the contact interaction if it is indeed parity violating. Figure 3.7 shows the Feynman diagram for the contact interaction. This term must be considered in addition to those of Figure 3.1. Several other experiments have searched for contact interactions in $e^+e^- \rightarrow e^+e^-$ [29] and have set limits on the different types of interactions. This search has yet to be undertaken with a polarized electron beam.

3.3.3 Fourth Generation

The Standard Model places no limit upon the number of generations of quarks and leptons. The number of light neutrino generations is set stringently to three by the LEP scans of the Z^0 resonance [6]. While this evidence is compelling, it does not rule out the existence of a massive fourth generation. Direct searches at LEP and SLC have ruled out the existence of charged or neutral heavy leptons below a mass of

approximately one-half the mass of the Z^0 [30].[4] In the quark sector, direct searches have ruled out the existence of a fourth generation down-type quark with a mass less than 72 GeV [31].

However, if a additional generations do exist, they would manifest themselves in the radiative corrections to measurements at the Z^0. In particular, a fourth generation would drastically modify the contributions of the vertex and oblique radiative corrections, which A_{LR} are very sensitive to. Therefore, if the top quark is found at the TeVatron, a discrepancy between A_{LR} and the standard model might arise from the existence of additional heavy fermions [32]. Clearly, the measurement of A_{LR} is the best low-energy test for additional heavy fermions. However, since $A_{LR}^{e^+e^-}$ is complementary to A_{LR}, it too, is sensitive to massive fermions from additional generations.

[4]The exact limit depends upon the assumptions made about the type of lepton and its stability or decay modes.

CHAPTER IV

APPARATUS

The measurements described in this thesis were performed with the SLAC Large Detector (SLD) operating at the SLAC Linear Collider (SLC). The SLC is capable of colliding polarized or unpolarized electrons with unpolarized positrons at a center of mass energy at or near the Z^0 resonance.

The SLC was conceived as an upgrade to the existing linear accelerator at SLAC. The first Z^0 boson was produced by the collider in the Spring of 1989 and measured by the Mark II detector. The SLD detector was designed and constructed specifically for Z^0 physics at the SLC. The SLD collaboration consists of approximately 150 active physicists from 34 institutions. (A complete list of SLD collaborators and institutions may be found in Appendix B.) The SLD was first moved onto the SLC beamline in February of 1991 and underwent an "engineering run" from June through August of that year.

The 1992 SLC run began with an unpolarized electron beam. Roughly 1000 hadronic Z^0 decays were measured with the SLD detector. In April of 1992, a polarized electron source was installed and commissioned. From May through August, SLC produced approximately 10,000 Z^0 events with an average electron beam polarization of 23%. Both luminosity and polarization were improved for the 1993 run. SLD logged approximately 50,000 Z^0 events to tape with an electron beam polarization of 63% from March through August of 1993.

4.1 The SLAC Linear Collider

The SLC is the first ever linear collider [33] and shown schematically in Figure 4.1. Linear colliders are unique in that electrons and positrons must be accumulated, accelerated and brought into collision on each machine cycle. While this environment offers a set of challenges very different from that of storage rings, it also offers unique opportunities in both electroweak and heavy flavor physics. The SLC parameters are given in Table 4.1. These numbers, along with an uptime of 65-75%, allowed SLC to deliver over 50,000 Z^0s to SLD with high polarization in 1993.

The following sections will describe the main aspects of the SLC, with particular

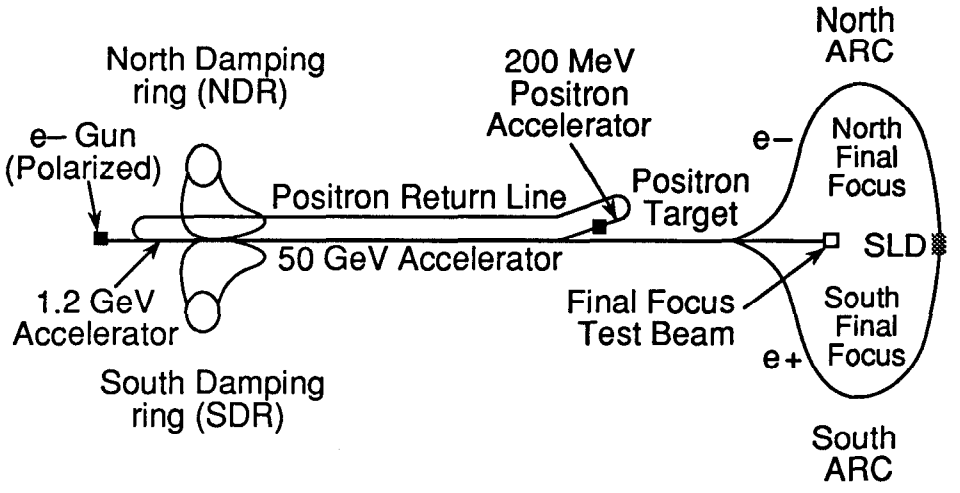

Figure 4.1: The SLAC Linear Collider (SLC).

attention given to the aspects which involve the creation and transport of a polarized electron beam.

4.1.1 Polarized Electron Source

A longitudinally polarized electron beam may be created by irradiating a GaAs semiconductor cathode with a circularly polarized laser [34]. The energy of the photons must be slightly greater than the band gap energy for photoemission to take place. Angular momentum conservation is responsible for the electron polarization, as $P_{\frac{3}{2}}$ valence band electrons are promoted to the $S_{\frac{1}{2}}$ conduction band by the circularly polarized photons in a 3:1 ratio. Therefore, the maximum polarization possible in conventional bulk GaAs cathodes is $\mathcal{P}_e = (3-1)/(3+1) = 50\%$. The true polarization is always below this limit due to excitation of conduction band electrons.

More recently, strained GaAs cathodes have been shown to produce polarizations well over 50% [35]. The strained lattice removes the degeneracy of the $m_j = 3/2$ and $m_j = 1/2$ levels of the $P_{\frac{3}{2}}$ valence state and theoretically allows for 100% polarization.

Figure 4.2 shows the electron polarization for different types of cathodes as a function of laser wavelength. In 1992, SLC ran with a bulk GaAs cathode and a laser wavelength of 715 nm. This produced an electron beam with $\sim$28% polarization. In 1993, the cathode used was a strained GaAs wafer. For the first portion of the 1993 run, the laser wavelength was 850 nm, producing a polarization of $\sim$55-60%. For the remaining 80% of the 1993 run, the laser wavelength was 865 nm, yielding an electron beam polarization of $\sim$62-67%.

The photo-emitted electrons are accumulated into a "bunch" by a 178 MHz RF

Table 4.1: Table of SLC parameters.

parameter	symbol	design goal	achieved[1]
frequency	f	180 Hz	120 Hz
beam spot size at the IP	σ_x, σ_y	$2\mu m \times 2\,\mu m$	$2.2\mu m \times 1.7\mu m$ (1992) $2.6\ \mu m \times 0.8\mu m$ (1993)
bunch intensity	N_{e+}, N_{e-}	$5 \times 10^{10}, 5 \times 10^{10}$	$3 \times 10^{10}, 3 \times 10^{10}$
polarization	$\mathcal{P}_e$	50%	63%
luminosity	$\mathcal{L}$	$10^{30}/cm^2/sec$	$3.8 \times 10^{29}/cm^2/sec$ $\simeq 40Z°/hr$

field. The electrons are then accelerated through a high-gradient field to an energy of 50 MeV. Figure 4.3 shows the layout of the polarized electron gun and laser. The laser strikes the cathode two times per 120 Hz machine cycle. One bunch of electrons will eventually comes into collision with positrons at the interaction point, while the other electron bunch is used to create positrons. Typically, between 6 and 10×10^{10} electrons are liberated from the cathode per pulse.

After reaching an energy of 50 MeV, the electrons enter the first section of the linear accelerator (LINAC) where they, along with one positron bunch from the positron target, are accelerated to an energy of 1.19 GeV. The electrons and positrons are then diverted from the LINAC into two different damping rings.

4.1.2 Damping Rings

The damping rings serve to "cool" the beams so that they may be accelerated. The smaller the spread in both momentum and position space allows for fewer losses during acceleration as well as lower backgrounds in the detector. Both electron and positron beams are stored at 1.19 GeV. Since the positrons have a larger energy spread as they are captured from the positron target (see Section 4.1.3), they must be damped for two machine cycles ($\sim$ 16.6 ms), while the electrons are damped for only 1 cycle ($\sim$8.3 ms).

In order to preserve polarization in the damping ring, the electron spin vector must be pointing parallel to the magnetic field direction of the bending magnets. This is achieved by passing the beam through a solenoid field as it enters the damping ring. The spin vector is flipped from along the direction of motion to perpendicular to the plane of the damping ring.

[1]The parameters listed in this column were achieved during or before the 1993 SLC run. Improvements on bunch intensity and spot sizes are planned for subsequent SLC runs.

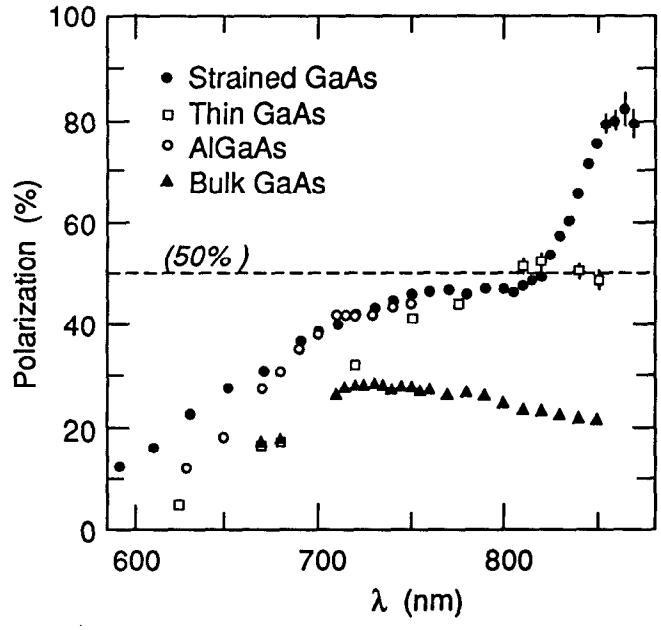

Figure 4.2: Electron polarization as a function of source laser wavelength (λ). SLC utilized a bulk GaAs cathode in 1992 and a strained GaAs cathode in 1993.

If the SLC is running round beams ($\epsilon_x \simeq \epsilon_y$) the beams have their spin vector oriented in the horizontal plane while being accelerated. Spin procession in the arcs brings the electron spin longitudinal at the interaction point. This means that another solenoid, the ring-to-linac solenoid (RTL) must be used to flip the spins back to longitudinal after the electrons exit the damping ring. When SLC is running in "flat" beam mode ($\epsilon_x \simeq 10\epsilon_y$), the RTL solenoid disrupts the beam by coupling the horizontal and vertical emittance (the flat beam passing through the solenoidal field gets rotated in the transverse plane) and must be turned off. The electrons are accelerated with their spins pointing up and the spin is made longitudinal through a series of "spin bumps" in the arcs (see Section 4.1.5).

The SLC was designed to run with round beams and did so for the entire 1992 run. Late in the 1992 run, some tests were performed with the SLC in flat beam mode for the Final Focus Test Beam Facility, which performs research and development for a future high energy linear collider. Flat beam acceleration and transport down the LINAC was so successful that it was decided to bring the beams through the arcs and into collision. Record specific luminosities were set almost immediately and it was determined that transport of flat beams through the arcs was not as difficult as once anticipated. The smaller spot size, as well as lower emittance in the vertical plane allowed for higher luminosity with lower backgrounds in the SLD. Consequently, the SLC ran in flat beam mode for the bulk of the 1993 run and plans to continue to do so in future runs [36].

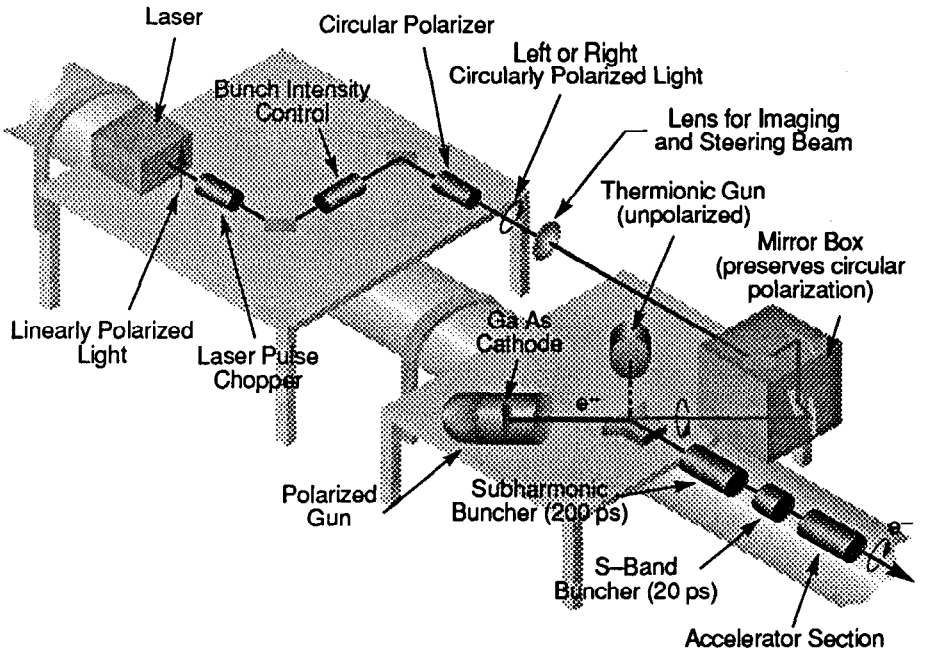

Figure 4.3: The SLC Polarized Electron Source.

4.1.3 Positron Production

Three bunches of particles are accelerated during each machine cycle. The first two bunches are the positrons and electrons (respectively) which are to be brought into collision. The third bunch is known as the "scavenger" electron bunch. This bunch is diverted from the linear accelerator at approximately 2/3 the way down its length and steered into a tungsten positron production target. The resulting electromagnetic showers produce both electrons and positrons. Positrons in the energy range 2-20 MeV are captured and returned to the front end of the LINAC where they are accelerated and stored in the damping ring. Typical yields from the positron target are one positron per incident electron.

4.1.4 Linear Accelerator

The bunches are accelerated down approximately 3 kilometers of linear accelerator (LINAC). The beams gain energy from radiofrequency cavities which are pumped with energy from klystrons. The accelerating gradient is 17 MeV/m. In typical running conditions, $\sim 3 \times 10^{10}$ particles per bunch are accelerated down the linear accelerator.

4.1.5 Arcs

After being accelerated to ~ 0.9 GeV above collision energy in the linac, the electrons and positrons are steered through two opposing arcs of 1 km in length. The beams "coast" through the arcs, losing energy by synchrotron radiation. The arcs do not lie in the horizontal plane, so the beam transport is complicated by motion in both dimensions perpendicular to the momentum of the electrons.

In flat beam mode, the electron arc is utilized to flip the spin vector from transverse to longitudinal by way of "spin bumps" [37], which utilize a strong resonance between the vertical betatron tune and the spin tune. Spin bumps are vertical orbit distortions which a separated by a fixed spin rotation around the vertical axis. The net effect of the spin bumps in the arc is to bring the electron spin from transverse entering the arcs to longitudinal exiting the arcs (entering the final focus).

4.1.6 Final Focus

To make up for the relatively low repetition rate of a linear collider, the beams must be focused very strongly at the interaction point. This is achieved at the SLC via three superconducting quadrupole magnets. The final quadrupole is approximately 1.5 meters from the interaction point (IP). At the point of collision, the dimensions of the beams (in flat-beam mode) are $\sim 3\,\mu$m in the horizontal, $\sim 0.8\,\mu$m in the vertical and ~ 1 mm along the beam axis. The size and location of the IP is very stable over time (see Section 6.6.3).

4.2 The SLAC Large Detector

Collisions are measured by a single multipurpose detector, the SLAC Large Detector [38]. The SLD, shown in Figure 4.5, combines excellent tracking, calorimetry and particle identification into a state-of-the-art high energy physics apparatus.

The SLD is a cylindrically symmetric detector with a 0.6 Tesla solenoidal magnetic field to momentum analyze charge particles. The detector has a central "barrel" system that surrounds the interaction point and two "endcaps" which cover the forward angles. During down times, the endcaps may be withdrawn for access to the interior components of the detector.

The right-handed coordinate system used by the SLD is a normal spherical polar system:

- the z axis is defined by the positron beam (pointing North)
- azimuthal angle (ϕ) runs from 0 to 2π, the x-axis (ϕ=0) points to the West.
- polar angle (θ) runs from 0 (North) to π (South).

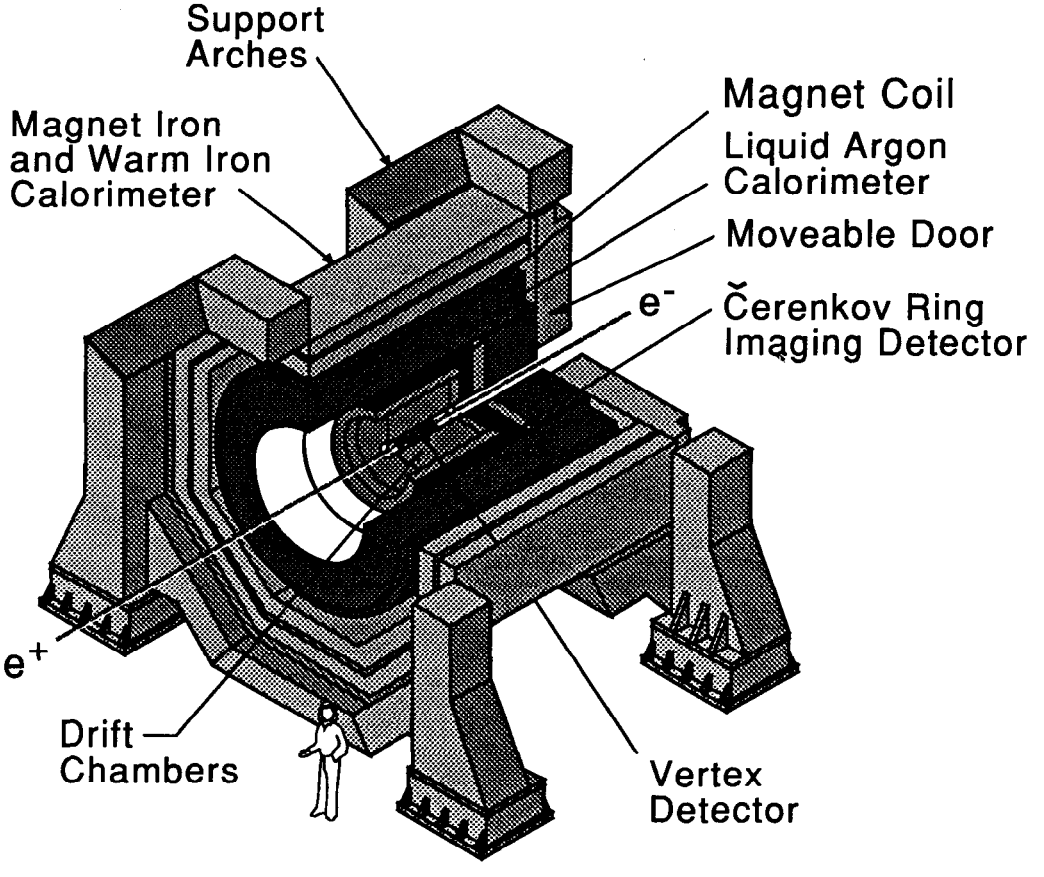

Figure 4.4: Cutaway view of the SLAC Large Detector.

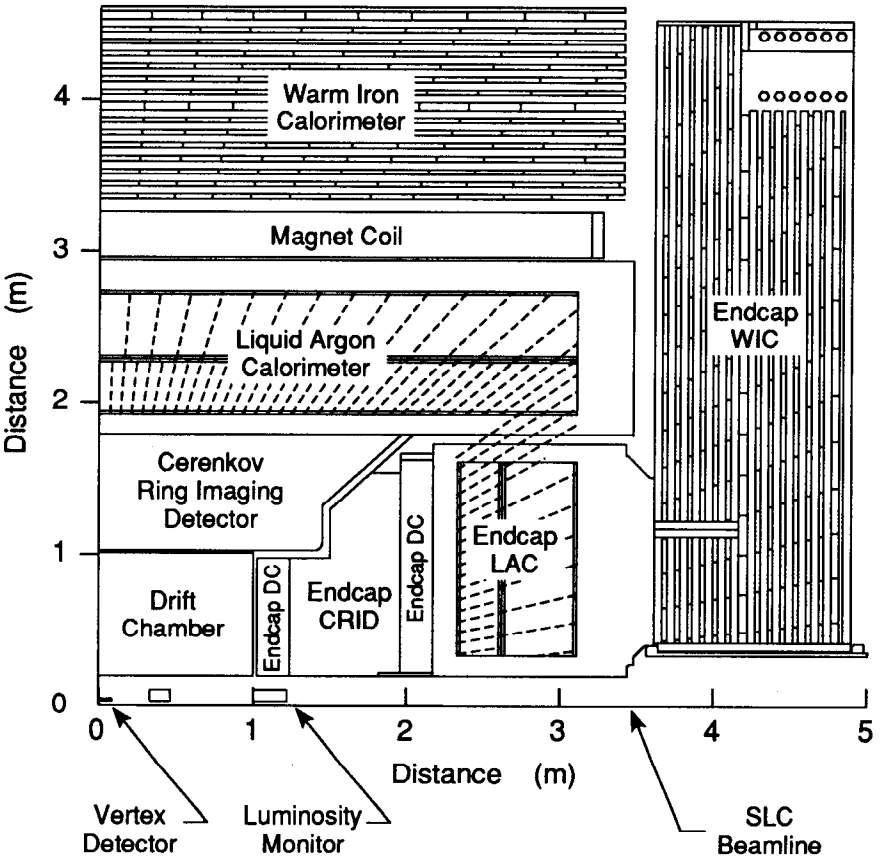

Figure 4.5: Quadrant view of the SLD.

The analyses discussed in this thesis make use of the SLD calorimetry systems: the liquid argon calorimeter and the luminosity monitor. The following sections will describe all of the major subsystems of the SLD. However, calorimetry will be emphasized.

4.2.1 Tracking

SLD possesses three major tracking systems, the Vertex Detector, the Drift Chambers and the Warm Iron Calorimeter (WIC) Strips.

Vertex Detector

Taking advantage of the small beampipe at the interaction point and the low repetition rate of the SLC, the SLD Vertex Detector utilizes charge coupled devices to make high resolution space point measurements of charged particle tracks. When

track points are linked with tracks reconstructed by the Central Drift Chamber, secondary vertices from heavy quark and tau lepton decays can be resolved with high precision.

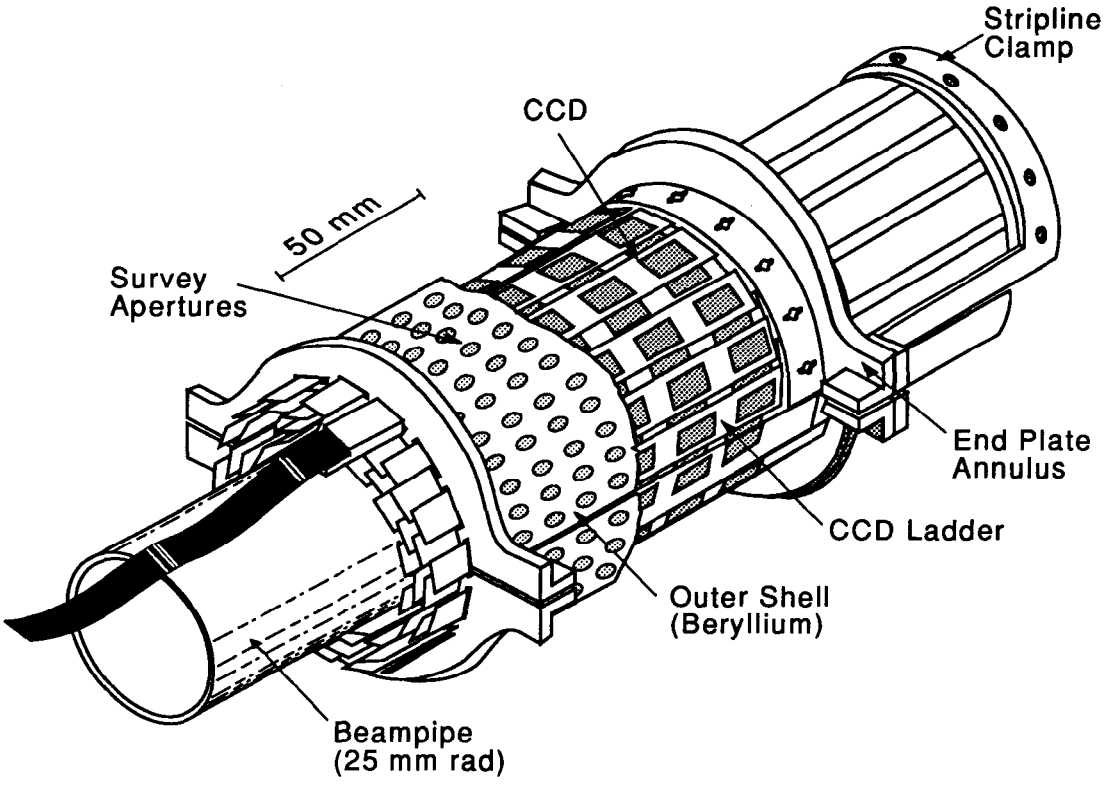

Figure 4.6: The SLD Vertex Detector.

The Vertex Detector (shown in Figure 4.6) is comprised of 480 CCDs which surround the interaction point in four concentric barrels. Each CCD contains approximately 400×600 pixels each of size 22×22 microns. The data from 120 Mpixels is read out and condensed to approximately 50-80 Kbytes per event [39].

Drift Chambers

Before linking tracks with hits in the Vertex Detector, tracks are found and fitted with the Central Drift Chamber (CDC) and the Endcap Drift Chambers (EDC). The drift chambers are gas-wire tracking systems. The CDC contains a cylindrical arrangement of wires which run approximately parallel to the beam line. Ionization from charged particles passing through the chamber drifts to the wires in the presence of large electrostatic fields. The wires are instrumented on both ends, so the z component of the tracks may be found via charge division.

The Endcap Drift Chambers have wires running perpendicular to the beamline for track reconstruction at smaller angles. The chambers are divided into an inner and outer chamber which are separated by the Endcap CRID (see Section 4.2.2). Backgrounds from the SLC as well as material in front of the EDCs have thus far hampered their ability to find charged tracks.

4.2.2 Particle Identification

When the velocity of a particle exceeds the speed of light in a medium, the particle emits Čerenkov radiation. The Čerenkov angle is related to the velocity of the particle. From the measurement of the Čerenkov angle, coupled with momentum information from the drift chamber, the mass of the particle and hence the identity of the particle can be ascertained. The Čerenkov Ring Imaging Detector (CRID) is designed to measure the Čerenkov angle of tracks and therefore perform particle identification [40].

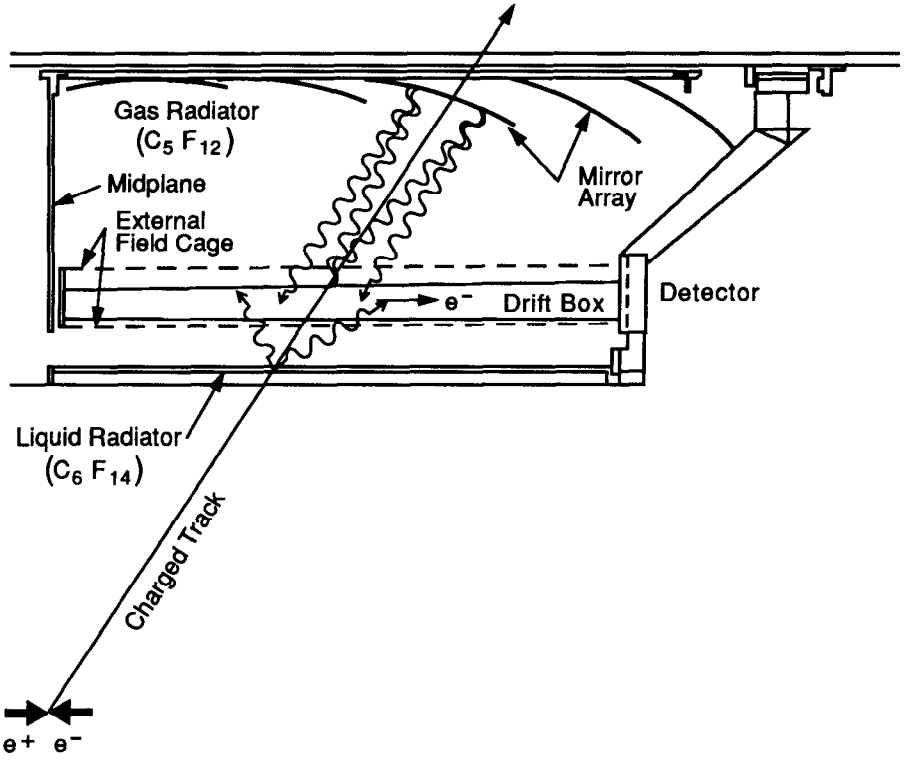

Figure 4.7: The SLD Čerenkov Ring Imaging Detector (CRID).

The CRID is shown schematically in Figure 4.7. The barrel CRID sits between the CDC and the Liquid Argon Calorimeter (LAC). In the case of the endcap, the

CRID is sandwiched between layers of the endcap drift chamber.

Particles emit Čerenkov radiation in both a liquid and gas radiator. The photons are converted by photo-ionization in gas. The photo-electrons then drift to the end of the detector where they are measured by proportional wires. The drift time yields information regarding the conversion depth. From this information, photon rings may be reconstructed and the Čerenkov angle measured.

4.2.3 Calorimetry

The SLD calorimetry is comprised of three complementary systems. The bulk of the electromagnetic and hadronic energy measurement is performed with the lead-liquid argon calorimeter (LAC). The warm iron calorimeter (WIC) provides measurement of the remainder of hadronic showers. The Luminosity Monitor and Medium Angle Silicon Calorimeter complete the electromagnetic coverage at small angles.

Liquid Argon Calorimeter

The SLD LAC design is based on a new understanding of the compensation mechanism for sampling calorimeters [41, 42]. For liquid argon devices, equalization of electromagnetic and hadronic response can be achieved by using a high Z absorber such as lead or uranium. This leads to an overall improvement in hadronic energy resolution due to the minimization of fluctuations of the electromagnetic components of the shower.

Liquid argon is advantageous in that it allows for arbitrary transverse segmentation, can be designed for minimal dead regions, can reside inside the 0.6 T magnetic field of the SLD solenoid, is radiation hard and a unity gain sampling medium. Since the argon is a dense sampling medium, it can be used with thin absorber layers to achieve excellent electromagnetic energy resolution.

As with other subsystems, the LAC is divided into a barrel detector and two endcap detectors. The barrel LAC (shown schematically in Figure 4.8) covers roughly 80% of the solid angle. The aluminum dewar structure is suspended inside the SLD solenoid. The dewar contains one large liquid argon volume in which all of the lead plates and tiles reside. The full azimuth of the cylinder is spanned by 48 modules of width $\sim$30 cm. Along the z axis, three modules comprise the length of the spool, two end modules and one center module.

The endcap LAC covers the angular region between $8° < \theta < 35°$ and is mounted on the endcap warm iron structure. An exploded view of the endcap assembly is shown in Figure 4.9. Like the barrel, the dewar contains a single argon volume. Inside the dewar, 16 wedge shaped modules surround the beam axis.

The structure of the endcap and barrel modules is very similar. Figure 4.11 shows a LAC barrel electromagnetic and hadronic module. A single endcap module contains both the electromagnetic and hadronic section (see Figure 4.12). Both barrel and endcap modules are comprised of an alternating array of lead plates and tiles.

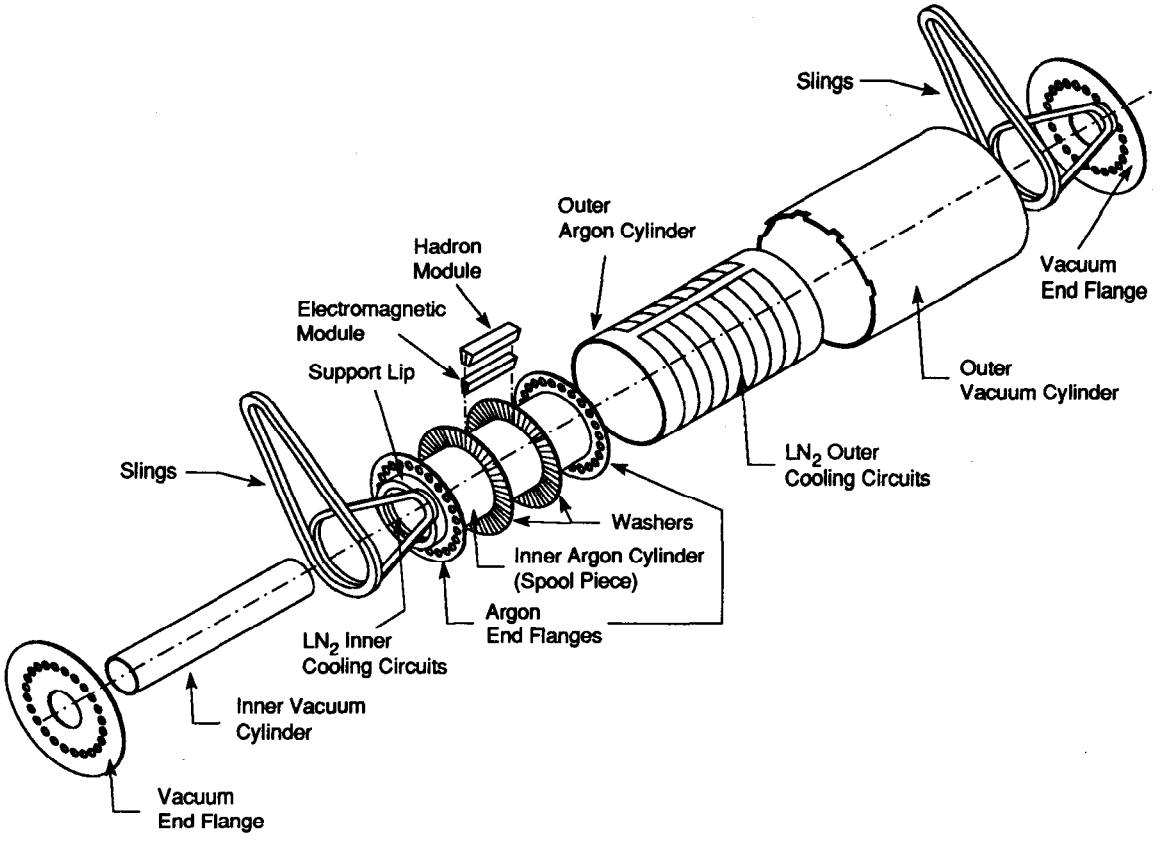

Figure 4.8: The barrel LAC assembly. The calorimeter is suspended inside the SLD magnet.

Figure 4.10 shows the plate and tile structure. The plates are held at ground; the tiles are held at negative high voltage and serve as the charge collecting electrodes. Structure and electrical isolation is maintained with a series of plastic spacers. The tiles are projective and joined longitudinally to form towers. Charge deposited in the liquid argon is collected on the tiles which is then passed outside the cryostat to the electronics.

The lead plates and tiles in the electromagnetic (EM) section are 2.00 mm thick and are separated by 2.75 mm liquid argon gaps. The first 16 layers (EM1) are readout in parallel, as are the last 40 layers (EM2). The EM1 section is roughly 6 radiation lengths of material and the EM2 section is 15 radiation lengths deep. The EM section contains 98-99% of a 50 GeV electromagnetic shower.

The hadronic section resides directly behind electromagnetic calorimeter. For the hadronic sections, the 2.75 mm argon gap thickness is maintained, but the lead plate and tile thickness is increased to 6.00 mm. The hadronic calorimeter is also divided into a front and back section (HAD1 and HAD2). The total thickness of the LAC (EM + HAD) is 2.8 nuclear absorption lengths and contains 80-90% of the hadronic shower energy.

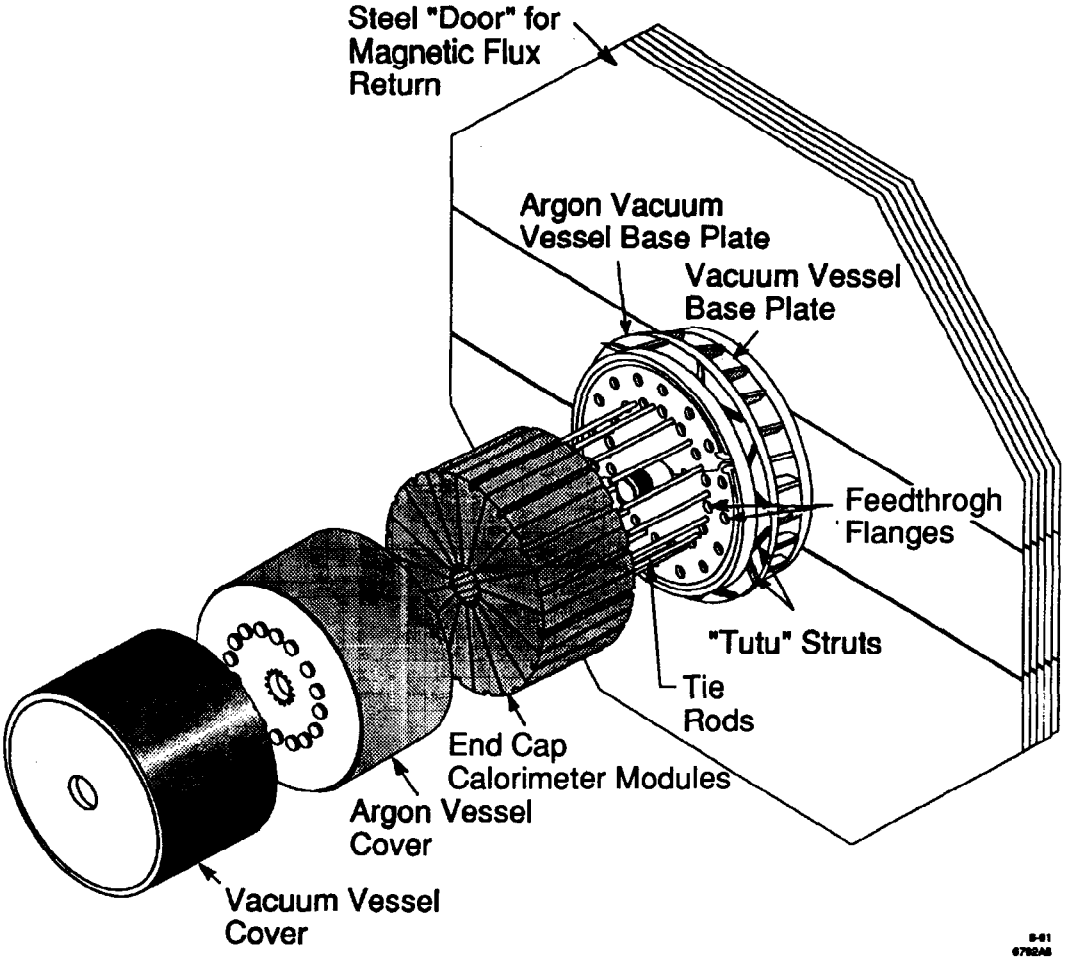

Figure 4.9: The endcap LAC assembly. The calorimeter is attached to the endcap iron door structure.

The barrel and endcap tower structure is projective. In the barrel, 192 EM towers span the azimuth, each with an opening angle of $\delta\phi = 33$mr. The polar angle of the barrel is divided into 34 EM towers on each side of the midpoint. Azimuthal coverage in the endcap is 192 towers at large angles, falling to 96 and then 48 at angles nearer the beamline. The polar angle is divided into 17 EM segments in the endcap. The total tower count is 32448 for the barrel and 8640 for the endcaps.

The design electromagnetic energy resolution is $10-12\%/\sqrt{E}$ and is dominated by the presence of the aluminum dewar in front of the calorimeter and shower fluctuations. The resolution is worse than this near module gaps due to charge collection inefficiency. Also the resolution is poor in the endcap region, where additional material in front of the calorimeter from the inner detectors and associated electronics causes preshowering.

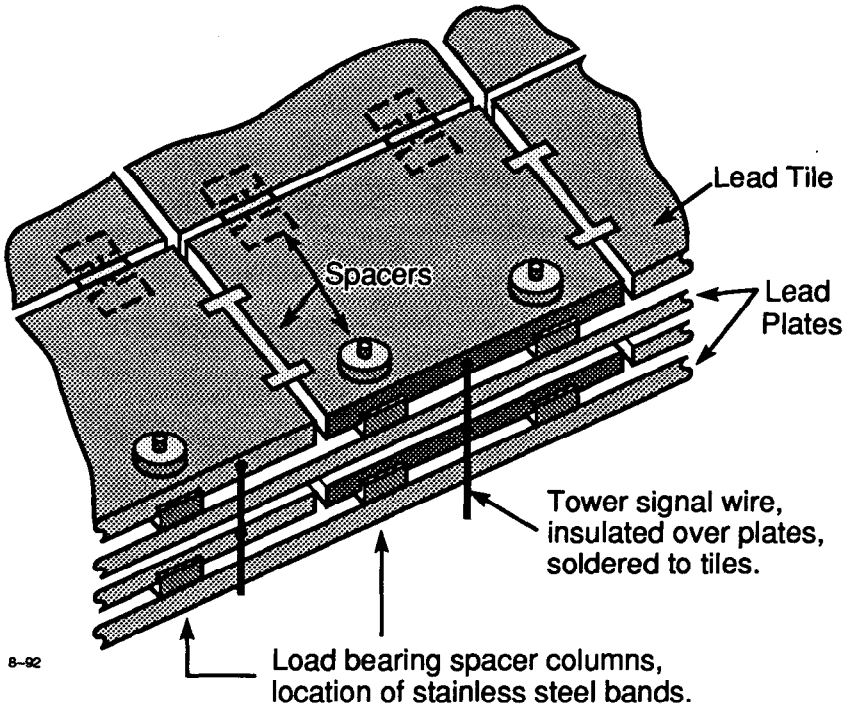

Figure 4.10: One cell from the barrel LAC.

Data Acquisition and Trigger

Signals are bussed out of the aluminum argon vessel and into "tophats", which perform the tasks of amplification, digitization and data multiplexing. Electronics and data acquisition for the LAC is almost identical to that of the Luminosity Monitor. The data acquisition and trigger will be briefly outlined here and discussed in detail in Chapter V. Signals are sent from the tophats via optical fiber to custom Fastbus Calorimeter Data Modules (CDMs).

The CDMs perform the trigger calculations at 120 Hz. If a trigger condition is satisfied, the data from the CDMs is sent to the AEB and eventually written to tape. The processors within the CDMs perform several trigger tasks at 120 Hz in addition to performing baseline subtraction and application of the proper calibration constants.

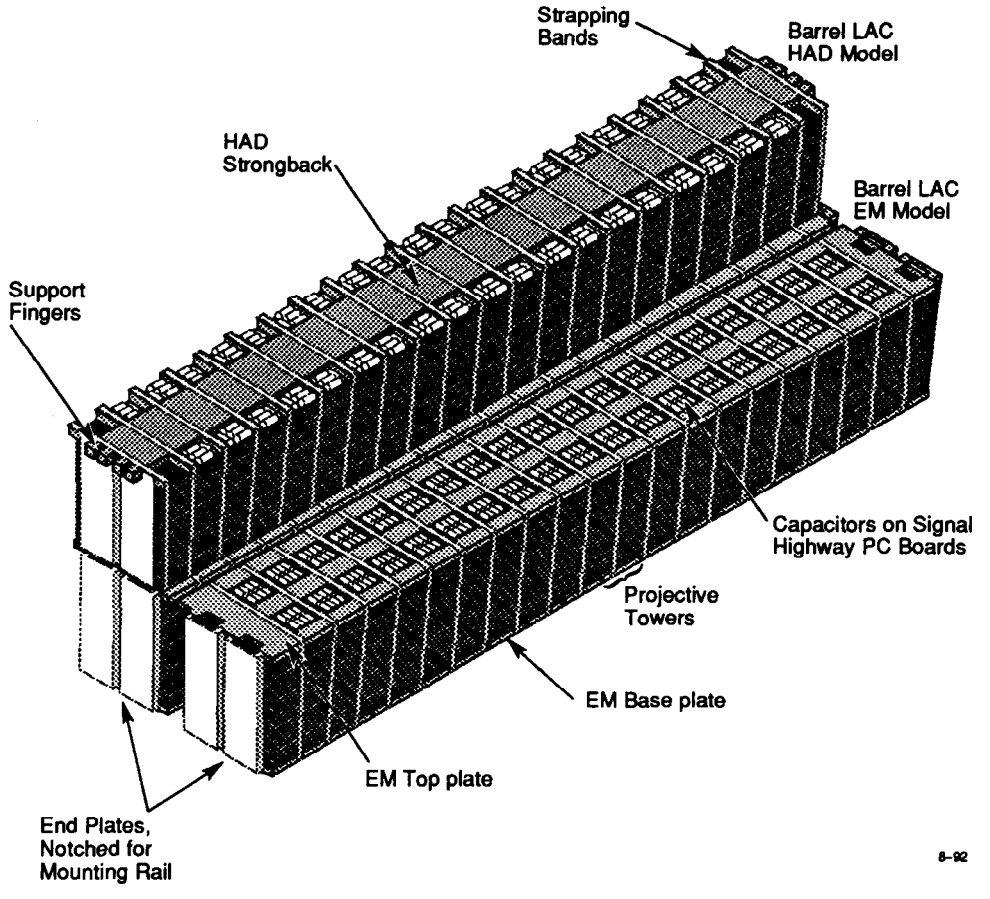

Figure 4.11: A LAC barrel module.

Luminosity Monitor

Electromagnetic calorimetry at small angles is performed with two silicon sampling calorimeters: the Luminosity Monitor and Small Angle Tagger (LMSAT) and the Medium Angle Silicon Calorimeter (MASC). The compact size of these detectors make them ideal for the tight space constraints of the beamline region. In addition, the fine transverse segmentation which silicon allows makes it ideal for luminosity monitoring by means of the $e^+e^- \rightarrow e^+e^-$ process.

The LMSAT will be discussed in detail in Chapter V.

Warm Iron Calorimeter

The WIC is a steel-limited streamer tube sampling calorimeter and muon tracker [43]. It also acts as a magnet flux return, as well as an octagonal superstructure which supports the remainder of the SLD. The total thickness of the WIC is 4.2 nuclear interaction lengths (λ), comprised of 14 steel plates 5 cm thick. In addition, there

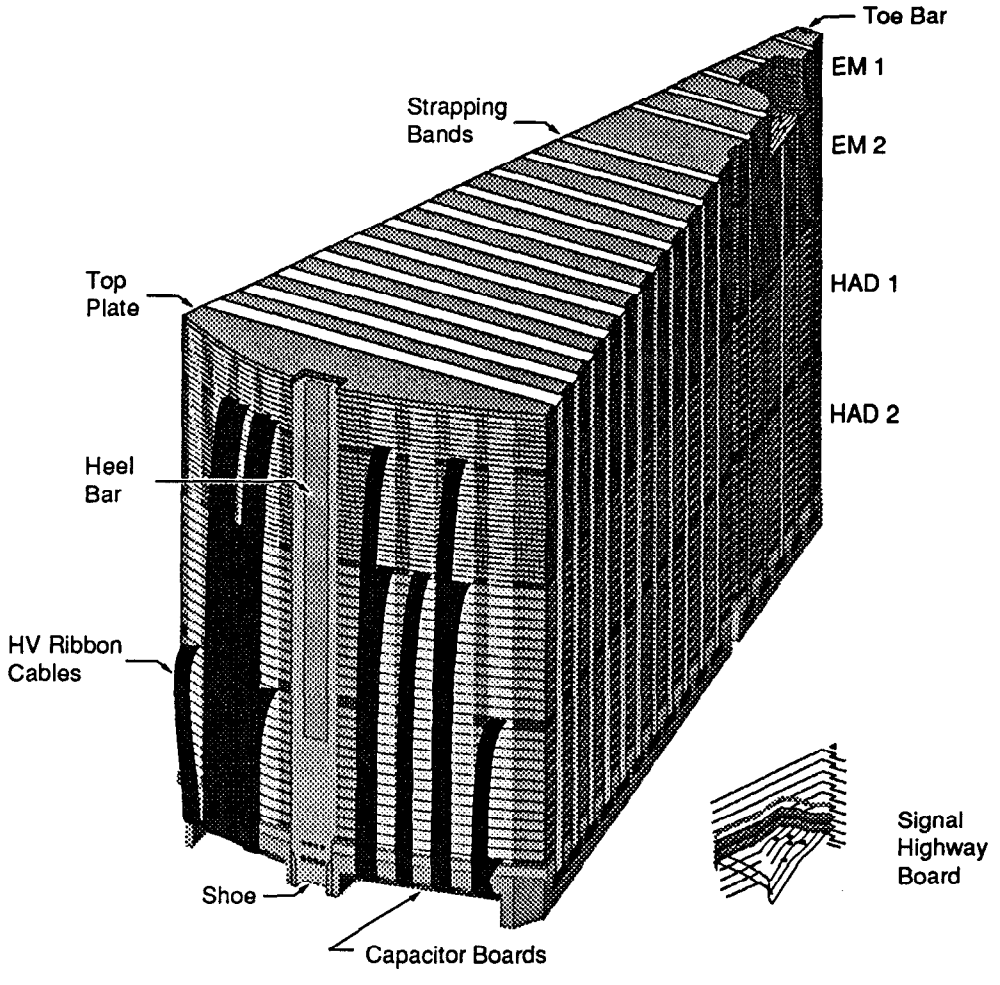

Figure 4.12: A LAC endcap module.

are two iron endcaps which support the remainder of the endcap components.

Wire planes between the steel layers are plastic streamer tubes bundled together to form planar chambers. The WIC tower segmentation follows that of the LAC.

Muon tracking is also performed with the WIC. The chambers contain copper strips which are 1 cm wide and run the length of the chamber. These are read out digitally. Muon tracks are identified by matching extrapolated CDC tracks with hits in the WIC strips.

4.2.4 The WISRD

The energy of both the electron and positron beams are measured on a pulse by pulse basis by the Wire Imaging Synchrotron Detector (WISRD) [44]. One detector sits in each extraction line and is able to measure the beam energy by the profile of synchrotron radiation the beam emits as it is passed through an analyzing magnet.

This is shown in Figure 4.13.

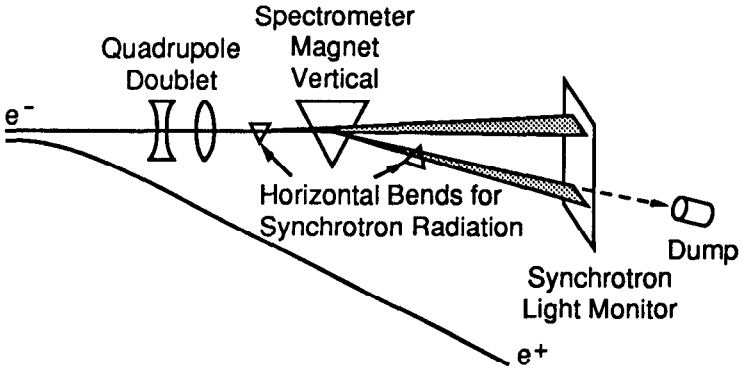

Figure 4.13: The Wire Imaging Synchrotron Detector (WISRD) Energy Spectrometer.

4.3 Polarimetry

In all electroweak measurements involving a polarized electron beam, the magnitude of the polarization enters linearly into the measured quantity. Therefore, it is crucial to measure and monitor the magnitude of the electron beam polarization as accurately as possible.

The primary electron beam polarization measurements are undertaken with the Compton Polarimeter [45]. This device makes use of the cross section asymmetry in electron-photon scattering. The Compton scattering process is shown in Figure 4.14. Circularly polarized photons are backscattered off of the electrons in the center of momentum frame. The scattered electrons are momentum analyzed by means of a bending magnet and then detected in both a Čerenkov detector and proportional tube detector. By measuring the Compton asymmetry and the photon polarization, the electron polarization can be extracted.

The layout of the Compton polarimeter is shown in Figure 4.15. The electrons are brought into collision with the laser approximately 40 meters after the e^+e^- collision point. The laser fires at a rate of 10.9 Hz, coinciding with every eleventh SLC pulse. Data from every laser-beam crossing are used to measure the electron beam polarization. A statistical error of 1-2% is achieved in a three minute run. The Compton data is shipped to the SLD data acquisition system and written to tape asynchronously with the triggered data from the other subsystems.

It should be noted that the helicity of each pulse is transmitted by means of redundant lines from the Polarized Electron Source directly to both the SLD acquisition system and the Compton polarimeter on a pulse-by-pulse basis. The magnitude of

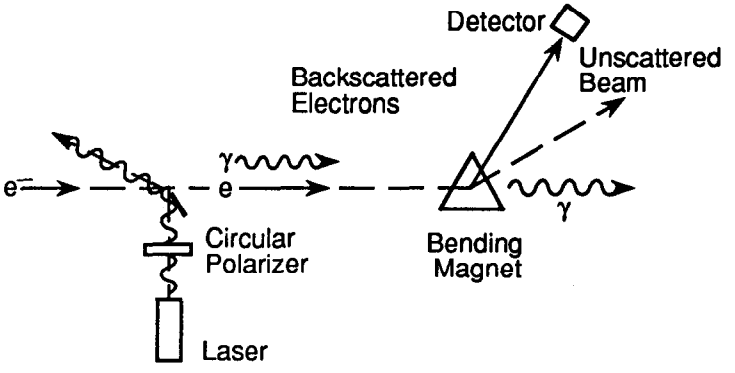

Figure 4.14: The Compton Scattering Process.

the electron beam polarization is measured every few minutes [46]. The beam polarization assigned to each event is a combination of the helicity from that beam crossing along with the polarization magnitude from the nearest polarimeter measurement in time.

In addition to the primary Compton polarimeter, two other polarimeters utilize Moller scattering ($e^-e^- \rightarrow e^-e^-$) to measure beam polarization. Both detectors make use of a foil target in an external magnetic field. The polarized beam is then incident upon a target of polarized electrons. The Moller asymmetry is small and more difficult to extract than is the Compton asymmetry. The Linac Moller polarimeter is stationed at the end of the linear accelerator. Beam must be diverted from the arc to the Linac Moller target. The Extraction Line Moller has only been used sparingly due to high backgrounds in the extraction line area. Also, the location of the Extraction Line Moller is incompatible with the normal operation of the WISRD.

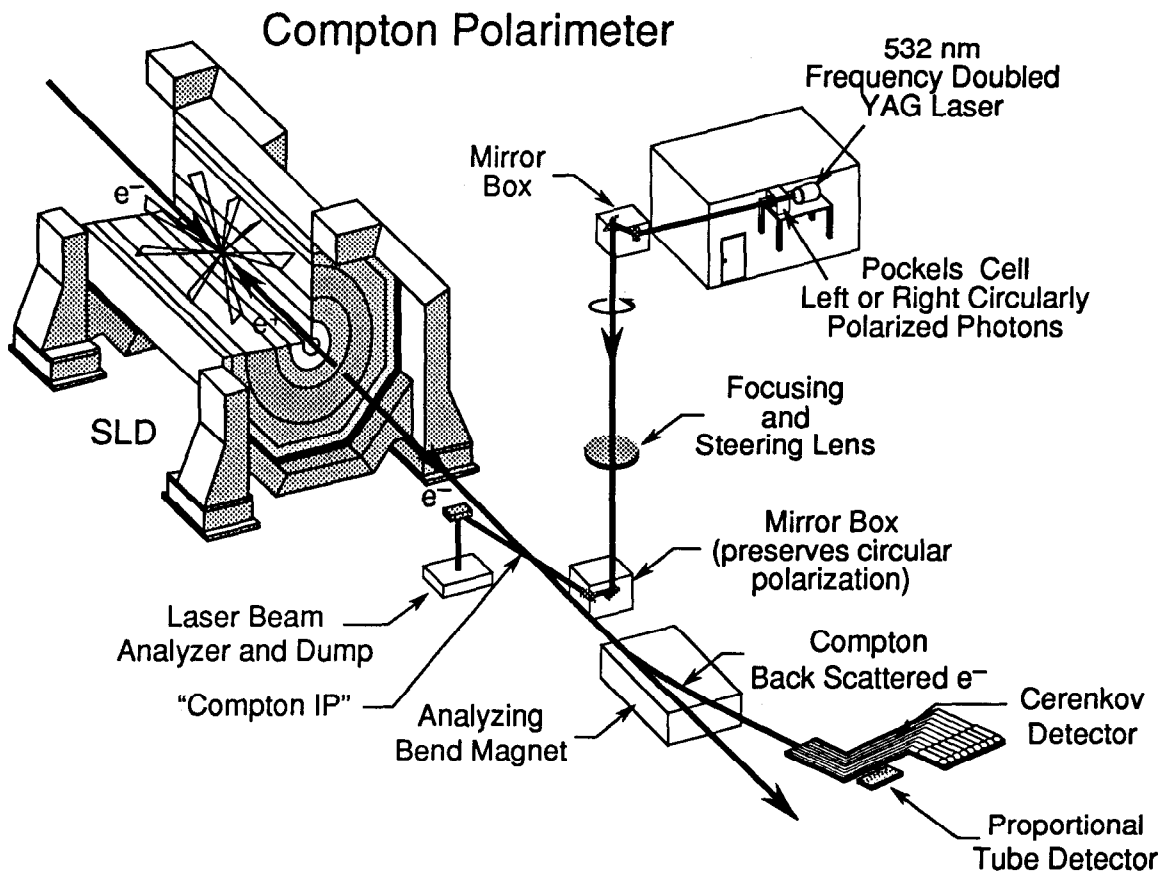

Figure 4.15: The Compton Polarimeter. Polarized photons are scattered off the extracted electrons. The electrons are momentum analyzed to determine the beam polarization.

CHAPTER V

THE SLD LUMINOSITY MONITOR

5.1 Introduction

The SLD is a nearly-hermetic detector, with the Liquid Argon Calorimeter providing electromagnetic coverage for 98% of the solid angle. To complete the angular coverage, the small angle calorimetry was designed with the following priorities [38]:

- provide a high precision measurement of the absolute luminosity
- provide a measure of the luminosity difference between left- and right-handed polarized beams
- extend the electromagnetic calorimetry coverage down to small angles
- tag electrons for two-photon physics.

To achieve these goals, the small angle calorimeters employ silicon sampling detectors with a pseudo-projective pad readout. This chapter will discuss the design, construction, electronics and operation of the SLD Luminosity Monitor and associated Medium Angle Silicon Calorimeter.[1]

Two luminosity monitors have been built for the SLD. The first set of detectors was designed and built for a beampipe with a radius of 16 mm at the interaction point. Due to synchrotron radiation concerns, the beamline was redesigned to have a 25 mm radius at the interaction point. The first Luminosity Lonitor (LMSAT-16) was too far along in construction to be modified. Therefore a second Luminosity Monitor (LMSAT-25) was designed and built. The following sections will discuss the construction of the second Luminosity Monitor, which is currently in operation in the SLD [47].[2]

[1] Portions of this Chapter are taken from references [47], [49], and [56], documents on which I was coauthor.

[2] For simplicity, the following sections will use the acronym LMSAT in reference to the LMSAT-25. The first Luminosity Monitor will continue to be referred to as LMSAT-16.

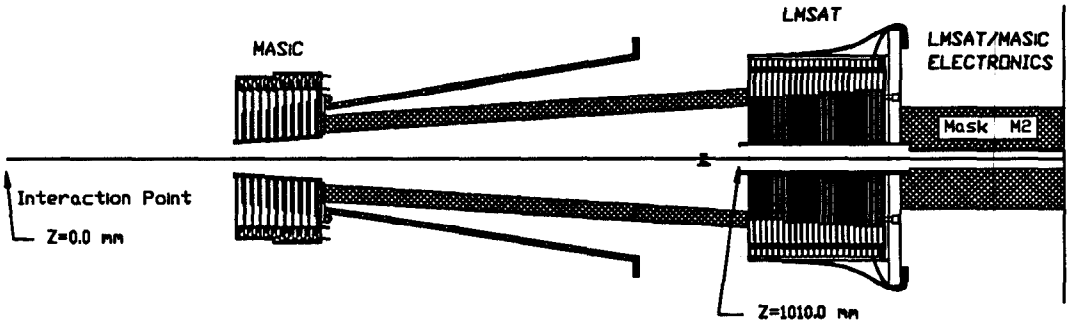

Figure 5.1: The SLD Luminosity Monitor (LMSAT) and Medium Angle Silicon Calorimeter (MASC).

5.2 Design

The small angle calorimetry is divided into two separate detector modules illustrated in Figure 5.1. The Luminosity Monitor/Small-Angle Tagger (LMSAT) mounts directly on the Superconducting Final Focus triplet assembly and provides coverage between 28 and 68 mrad. The Medium Angle Silicon Calorimeter (MASC) mounts onto the R20 assembly, provides coverage from 68 to 200 mrad, and also defines the outer acceptance of the LMSAT. The endcap Liquid Argon Calorimeter (LAC) coverage extends slightly below 200 mrad, insuring full electromagnetic coverage.[3] Readout electronics for both the LMSAT and MASC are contained in one "tophat"[4] (Section 5.5) which mounts behind the Luminosity Monitor on the Final Focus triplet.

The LMSAT detectors encircle the beam pipe on both ends of the interaction point.[5] The inner acceptance is defined by a tungsten snout which is 10 cm long and extends forward from the front face of the Luminosity Monitor. The outer acceptance is defined by the inner edge of the MASC. A cutaway picture of one Luminosity Monitor is shown in Figure 5.2. The detector and electronics fit within a region of 45 mm along the beamline. A beam position monitor and the final quadrupole focusing magnet reside immediately behind the Luminosity Monitor electronics (looking out from the interaction point).

The module structure consists of 23 layers of alternating silicon detectors and tungsten radiator plates. Electromagnetic showers which develop in the tungsten create electron/hole pairs in the fully depleted silicon detectors which are then collected by charge sensitive preamplifiers. The silicon samples 1.54% of the shower, based on the dE/dx sampling fraction for minimum ionizing particles. The total depth of the

[3]The endcap LAC is occluded by the MASC out to 200 mrad. The additional LAC coverage below 200 mrad insures that showers beyond 200 mrad are fully contained.

[4]The term "tophat" comes from the LAC electronics packages, which are cylindrical in shape and surrounded by a black anodized cooling assembly. Consequently, the packages very much resemble a gentleman's tophat.

[5]The beamline runs North/South at the interaction point, so the detectors are sometimes referred to as "North" and "South" for convenience.

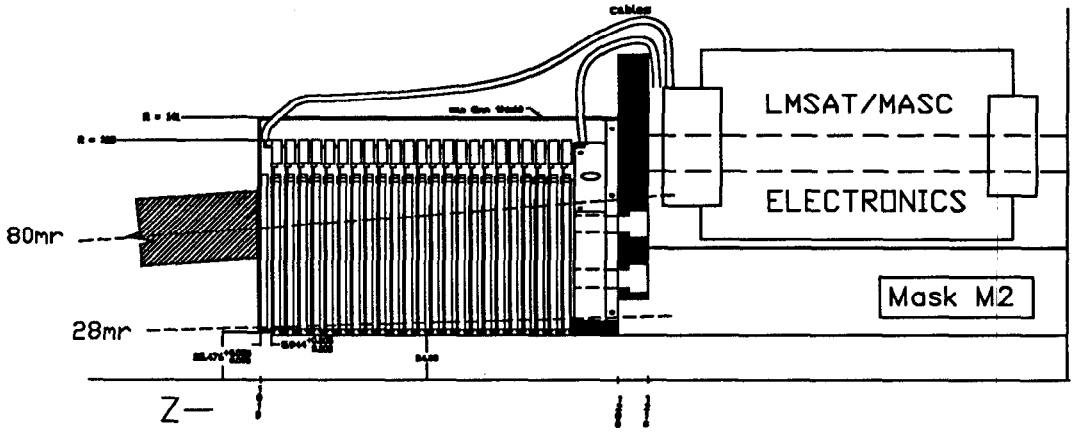

Figure 5.2: Side view of the SLD Luminosity Monitor (LMSAT). The alternating silicon/tungsten structure encircles the beam pipe on both sides of the interaction point. Readout electronics for both the LMSAT and MASC reside directly behind the LMSAT.

calorimeter is 21 X_0, containing >99.5% of a 45 GeV electromagnetic shower. The design energy resolution is 3% at 50 GeV.

Readout is divided longitudinally into two sections. The first six layers are connected in parallel and defined to be Layer 0 (EM1). The depth of EM1 is 5.5 X_0. Layer 1 (EM2) is the last seventeen layers connected in parallel, with a depth of 15.6 X_0. There is very little material between the first layer of tungsten and the interaction point (< 0.10 X_0), therefore little preshowering occurs.

The transverse segmentation may be seen in Figure 5.3. There are sixteen towers[6] in azimuth in the two rings closest to the beampipe, corresponding to 22.5° coverage per tower. For the four outermost rings, there are 32 towers, corresponding to an azimuthal coverage of 11.25° per tower. The structure of the detector towers form a pseudo–projective geometry. This is achieved by having four different types of detectors (L1-L4), each type with larger pad dimensions than the previous type. The first six layers (counting away from the interaction point) are L1 detectors, the second six are L2 detectors, the third six L3 detectors and the last five layers are L4 detectors. Towers cover approximately 9 mrad in polar angle,[7] extending out to 80 mrad. The outer acceptance is defined by the MASC to be 68 mrad, so the additional silicon coverage out to 80 mrad insures that showers are fully contained.

The radiator plates are made of a 90% W, 10% Cu-Ni "heavy met" alloy. The material is non-magnetic to protect against adverse effects in the presence of the 0.6 Tesla SLD magnetic field. The Cu-Ni binders allow for ease of machining. Pure

[6]Detector cells ganged together longitudinally are referred to as "towers".

[7]In the case of the Luminosity Monitor, the polar angle, θ is defined to be the angle to the nearest beamline. For the remainder of the SLD, polar angle is defined as the angle from a point to the positron beam axis.

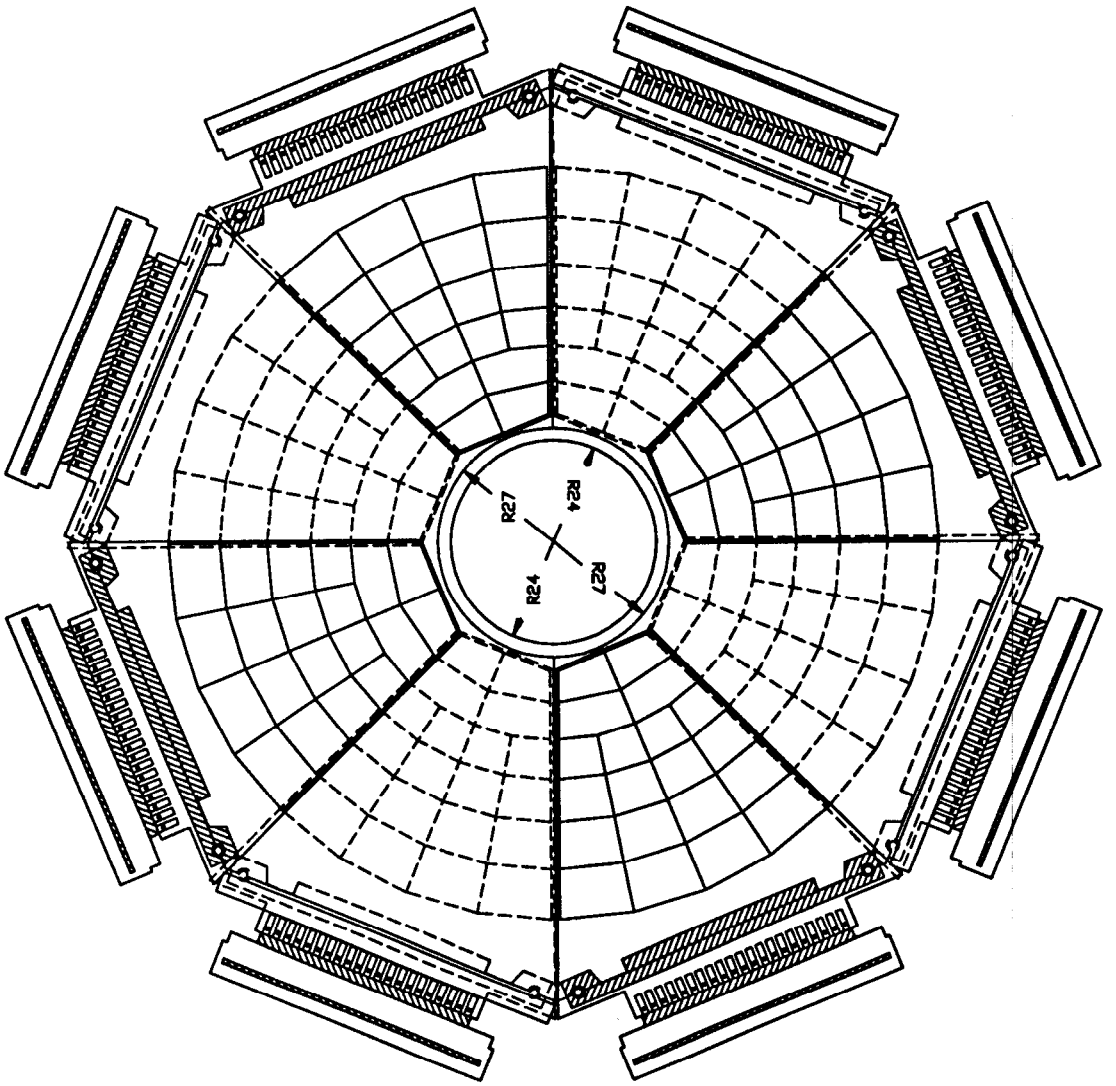

Figure 5.3: One silicon plane of the SLD Luminosity Monitor (LMSAT) as seen from the interaction point. The connectors are shown attached to the daughterboards.

tungsten has a radiation length (X_0) of 3.5 mm. The addition of the binders increases the radiation length to 3.8 mm. The plates are 3.5 mm thick, with 3.5 mm gaps between the plates. The detectors are mounted on opposing faces of the tungsten so that the active regions overlap in azimuth. A 2 mm gap in silicon coverage does occur in the vertical plane (see Figure 5.3) where the two halves of the calorimeter come together (for installation and removal). Electrons entering the gap still shower in the tungsten, which has a Molière radius ~ 1 cm [48]. Therefore $\sim 90\%$ of the shower enters the active region for an electron incident upon the gap.

The channel count for the Luminosity Monitor is 20 pads/detector $\times$ 8 detectors/layer $\times$ 2 layers (EM1, EM2) $\times$ 2 sides (N, S) = 640 channels. The MASC contributes 384 channels, for a total of 1024 channels for the entire subsystem.

5.3 Silicon Detector Tests

The silicon detectors were made by Hamamatsu Photonics. Upon receipt at the University of Oregon, every detector was tested for capacitance and leakage current at -65, -75 and -150 V DC. The results of these tests were compared to the Hamamatsu test results which accompanied each detector.

The layout of an individual detector may be seen in figure 5.4. The detectors arrays were constructed from 300 (± 10) μm high resistivity n-type silicon wafers with a p-type ion-implantation from the front surface to form the junction diode. The physical gap between adjacent pads on one silicon chip is less than 300 μm. The actual inactive gap is much smaller than this.

After the silicon wafers were trimmed, Hamamatsu mounted the 20 cell detector on a printed circuit daughterboard with conductive epoxy. The daughterboard provides increased mechanical strength and the necessary electrical contact areas. The epoxy also provides connection to feed-through holes on the daughterboards [49]. The daughterboards are approximately 0.8 mm thick with card-edge connections.

Direct card-edge connectors were too bulky to use, so modified insulation displacement connectors (IDC) were chosen instead. For this, header pins were soldered directly onto each detector daughterboard at the University of Oregon.

The detectors were originally received from Hamamatsu in March, 1990. However, all detectors had to be returned because the stainless steel bars for mounting each detector were found to be inadequately attached. Upon slight pressure the bars fell off. All detectors were shipped back to Hamamatsu to correct this problem.

Upon return in early June, 1990, the mounting bars were deemed to be securely attached and testing began. Four hundred forty-four detectors were received, 368 to be used in the LMSAT with $\sim 20\%$ spares.

Individual detector testing consisted of two visual tests and three electrical tests. Visually, the detectors were inspected for defects, as well as surveyed for proper positioning relative to the mounting bars. Electrically, the capacitance and leakage current of each cell was tested, as well as the continuity of the ground plane.

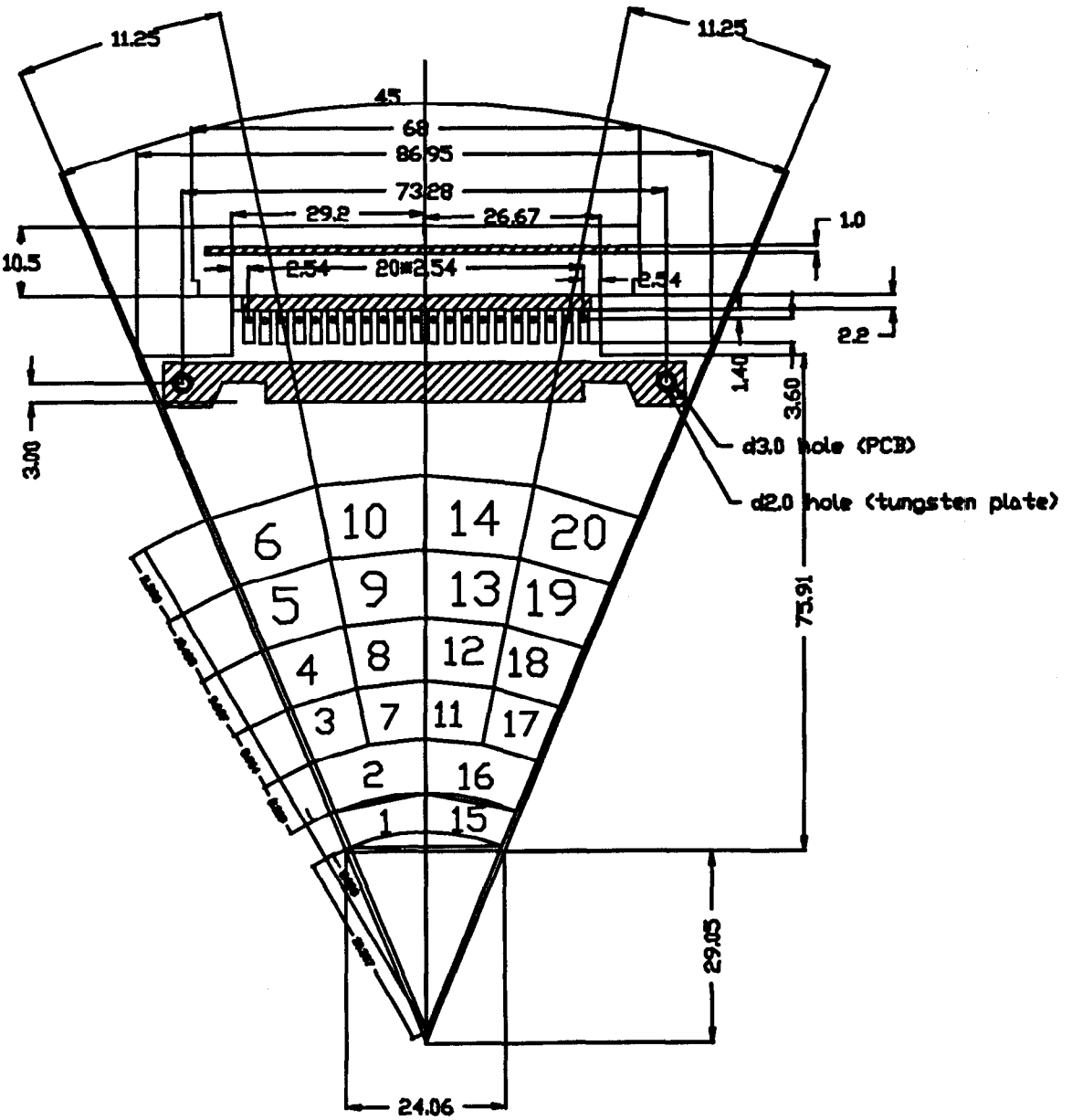

Figure 5.4: Diagram of an L1 detector (divided into 20 cells) mounted on the daughterboard. (Dimensions are in millimeters.)

5.3.1 Visual Test

Upon arrival, all detectors were inspected visually and submitted to a checklist of ten items. This was to assure that the detectors were numbered consistently and were not physically damaged before or during shipment. The metal mounting bars were also checked to make sure they were refastened securely.

Since the visual tests were subjective, only detectors which possessed obvious defects, such as chipped silicon, were failed. Detectors with subtle problems like slight bowing were noted for grading purposes, but not failed.

5.3.2 Ground Plane Resistance

The front face of the detectors is covered by a one-half to one micron thick layer of aluminum, which forms a common ground for all cells in the detector. At the time of the visual test, continuity from the ground pin to aluminum ground plane was tested by a hand held Fluke 8020B digital multimeter. A detector failed if the resistance to the ground plane was found to be greater than 1 kΩ. Detectors with ground plane resistance greater than 100 Ω were graded accordingly and only used as spares.

5.3.3 Visual Survey

The Bhabha cross section falls rapidly with increasing theta ($d\sigma/d\theta \sim 1/\theta^3$). It is therefore important to have good angular resolution. This means that the locations of the towers must be known to high precision. To verify that the silicon wafers were mounted properly on the daughterboard with respect to the mounting bar, the detectors were visually surveyed.

A plate for consistently mounting the detectors was made by the University of Oregon machine shop. Etchings on this plate near two corners of the detector allowed for the position of the two corners of the chip to be measured relative to the mounting bar. The actual measurement was done with a Baush & Lomb microscope and reticle. It is estimated that the accuracy of this process was $\sim 50\mu$m.

Detectors failed the visual survey if they were more than 150μm from the correct location. Only one detector failed the position survey. That detector also had a chipped corner and failed the visual test.

5.3.4 Leakage Current

Full depletion of the 300μm high-resistivity silicon requires approximately -30 V DC. The slight current that persists is defined as leakage current. Specifications for the detectors was that the leakage current could not exceed 100 nanoAmps at full depletion voltage, which is -75 V DC.

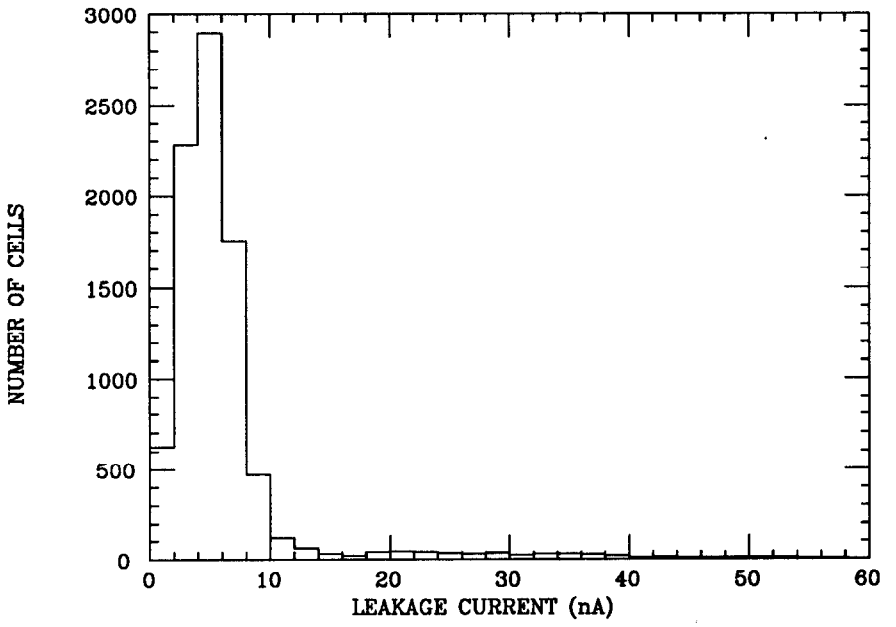

Figure 5.5: Distribution of cell leakage currents for all detectors after headers were attached (see text). Bias voltage was –75 VDC. The cell areas range from 0.8 to 2 cm^2.

A single silicon detector contains 20 electrically isolated cells. A test of one detector is actually a test of all 20 individual cells. As specified, Hamamatsu tested all detectors before shipment and included a cell-by-cell production data sheet for each detector. To confirm these results, the tests were repeated at the University of Oregon.

The testing was controlled by a PC clone AST–286 computer. The bias voltage was provided by a Tennelec TC954 power supply, which was set from the PC. In order to test all 20 cells in a detector without operator intervention, a Keithley Instruments 705 Scanner was used. This allowed the PC to read data from one cell at a time in a sequential manner.

A 100 kΩ resistor was placed in series with the detector. The voltage drop across the resistor was measured with a Keithley 197 digital multimeter. This method was preferable to direct current measurement due to the small values of leakage current.

Leakage current measurements were made for each cell at –65, –75 and –150 V DC bias. In addition, all detectors were retested at –75 V DC after the headers were soldered on them, to verify that the soldering process did not damage the silicon.

To compare the measurements with those provided by Hamamatsu, the difference in temperature at the time of the two tests was taken into account.

A detector failed the leakage current test if one cell had leakage current greater than 500 nanoAmps, or two cells had leakage current greater than 100 nanoAmps.

In addition, if the measurements taken at the University of Oregon differed from the Hamamatsu measurements by more than 20 nanoAmps, the detector was first retested to verify the results, and then deemed a failure. These requirements were very conservative since typical leakage currents were less than 10 nA per cell (Figure 5.5).

The detectors were tested at Hamamatsu before shipping, once at the University of Oregon upon receipt and again at the University of Oregon after the headers had been soldered onto the daughterboards. No detectors failed the initial leakage current tests at the University of Oregon. There was about 2% failure rate on post–soldering retests.

5.3.5 Capacitance

The purpose of capacitance testing is to verify depletion depth and cell isolation. As with leakage current, capacitance of each cell was measured at –65, –75, and –150 V DC bias, as well as –75 V after the headers were soldered.

In addition to the equipment discussed previously, a Keithley 590 CV Analyzer meter was used to measure capacitance. To understand the stray capacitances introduced by the automatic switch, a manual switch was used. The additional capacitance was then accounted for in the software.

A detector was considered a failure if one cell had a capacitance value greater than 10 pF different from the mean value for that type of cell. This constraint also forced the capacitance values to be consistent with the Hamamatsu pre–test values. With this requirement, less than 0.5% of all detectors failed on the test of capacitance.

5.3.6 Detector Test Summary

All 444 detectors were submitted to the battery of tests discussed above. Three detectors failed the initial tests: one had two cells shorted together (flagged in capacitance test) and two failed the visual test because the silicon was chipped. Four detectors failed the electrical tests after soldering: one due to an anomalously large capacitance in a single cell and three due to large leakage current in a single cell. It is not known why one cell on each of these detectors was affected by the soldering process. In addition, 25 detectors passed the tests but were graded as spares, primarily due to slightly high current in one cell or large ground plane resistance. This left 410 grade A detectors, 356 of which were initially installed in the LMSAT–25. The design of this Luminosity Monitor makes it possible to easily replace bad detectors during times of access (see Section 5.4), although this has not occurred often.

5.3.7 Multiple Detector Tests

To verify that a 7 mm per layer spacing was physically achievable, a seven layer aluminum mock-up was built. Originally, this was used to check spacings and test the mounting procedure. Seven layers of aluminum were chosen so that six detector

layers could be mounted, making it an EM1 mock-up. In addition, leakage currents and capacitance of six detectors could be tested together in this arrangement. Tests for noise and response to an alpha source were also performed with the mock-up, to insure that nothing unexpected would occur when the detectors were mounted into the tungsten structure.

5.4 Construction

As seen in Figure 5.3, the tungsten radiator structure is octagonal. This is to allow the silicon detectors to be mounted directly to the structure. Delrin pins are used to fix the location of the detectors on the tungsten plate. A brass bar is then screwed over the pins and they are held into place by compression.

The modules are attached to the Final Focus triplet by way of five 3/8 inch bolts directly into the aluminum backplate of the luminosity monitor assembly. The tungsten inner cylinder is attached to the backplate with a set of radial screws. The tungsten plates are then attached to the inner cylinder. To allow for a tight fit and no gaps in the radiation shielding, the two halves of the inner cylinder are keyed.

5.4.1 Mechanical Components

The inner cylinder is also made of a 90% W, 10% Cu-Ni "heavy met" alloy. The cylinder acts as both a support for the radiator plates and a radiation mask. The radial thickness of the cylinder is 3 mm. Northwest Industries in Albany, Oregon was responsible for the heavy met inner cylinder.

Each radiator plate is secured to the cylinder by three screws radially through the inner cylinder. The machining of the heavy met radiator plates was done at the University of Oregon machine shop. The heavy met material was made by Teledyne Powder Allows of New Jersey. The plates were ground to the proper 3.5 mm thickness by Double Disk Grinding of Vancouver, Washington.

To maintain proper spacing between tungsten layers, an additional bracket assembly was added to the outside of the plates. This also allowed for the modules to be placed on their backplates to take cosmic rays (Section 5.6.2) without worry of undue stress on the screws holding the plates into place.

5.4.2 Module Assembly

The four LMSAT modules were assembled at the University of Oregon in April of 1991. The assembly procedure is shown in Figure 5.6. A special assembly table was built which let the tungsten plates sit flat on the table while allowing access to the inner cylinder to screw-in the tungsten plates. The table also insured proper alignment of the plates.

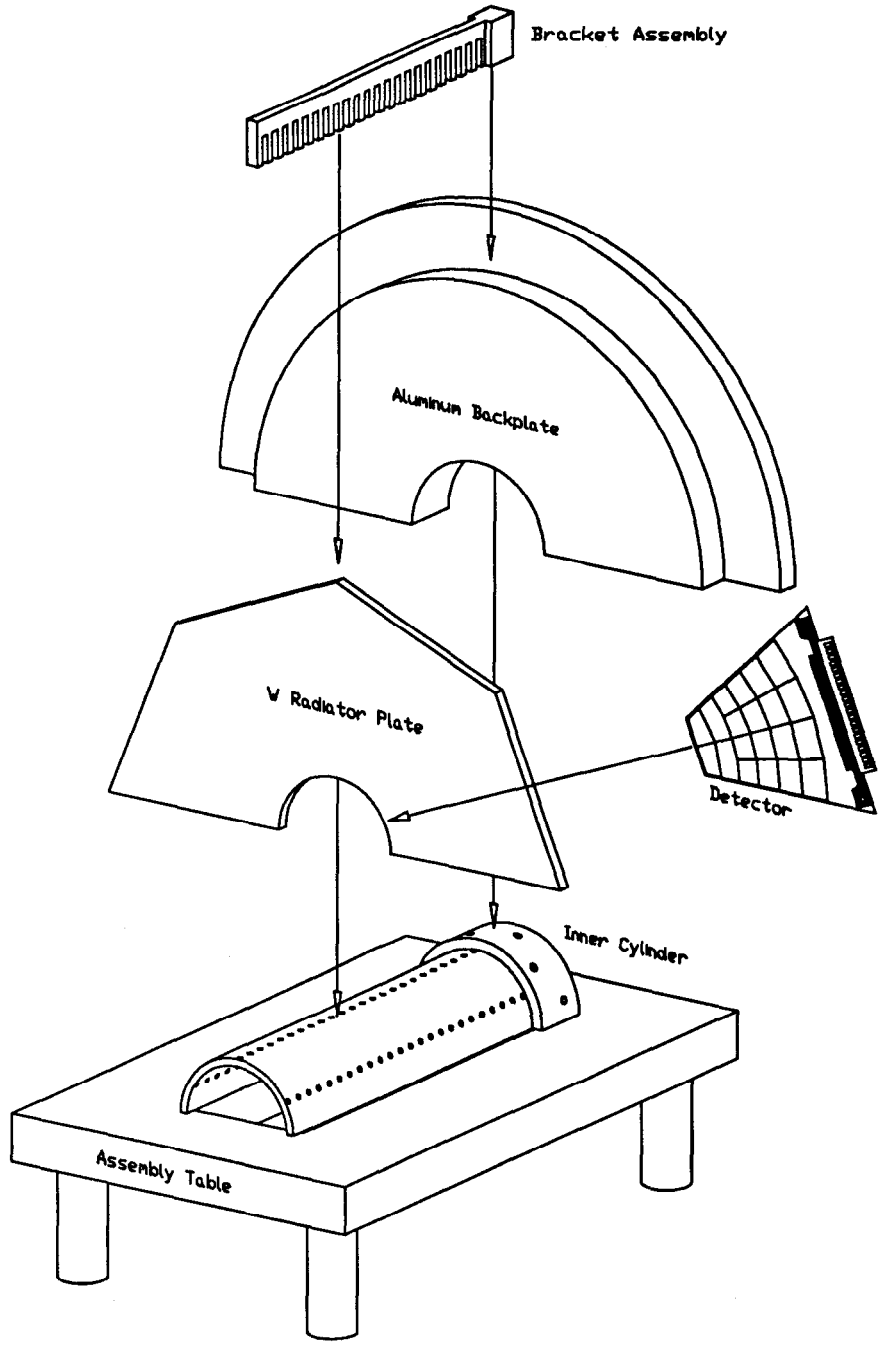

Figure 5.6: An exploded view of one Luminosity Monitor module assembly. The inner cylinder rests upon the assembly table while the the backplate and 23 tungsten radiator plates (only one is shown here) are attached with screws extending outward radially through the cylinder. The bracket assembly is then attached for additional strength and to maintain proper spacing. The detectors are inserted between the radiator plates and secured into place with a brass bar which holds the delrin pins by compression. (The bar and pins are not shown in this picture.)

After the backplate and radiator plates were secured to the inner cylinder, the detectors were inserted with the delrin pins already in place. To keep electrical isolation between the tungsten and the printed circuit board (the silicon always faces away from the plate which it is mounted on) a layer of 100 μm thick mylar was placed between the plate and the circuit board. In addition, a layer of mylar was also placed between opposing detectors to insure that their ground planes were not shorted together.

The completed modules were flown to SLAC. Upon arrival at SLAC, the capacitance and leakage currents of the towers were again measured to insure that no damage occurred during transport.

5.4.3 Installation onto Beamline

Since the Luminosity Monitor mounts onto the Superconducting Final Focus, it must be installed after access to all beamline components is completed. It must be removed before any subsequent access as well.

Both Luminosity Monitors were installed onto beamline for the first time in May of 1991, with a full complement of electronics. The detectors were then removed after the 1991 engineering run to allow installation of the CCD Vertex Detector. The detectors were reinstalled onto beamline in January of 1992 and have remained in place through two successful SLD physics runs in 1992 and 1993.

Tower capacitances were measured after the 1991 and 1992 runs to verify that the silicon is still functioning properly. After the 1992 run, an access to the detectors was made to disconnect three pads which were drawing high current. In one case, it appeared as though the silicon was damaged due to impact (chipped) during installation. The other two wafers showed no visible damage, although it is possible that they were damaged due to impact as well. Two disconnected pads were L4 detectors and moved to layer 23 to minimize the effect of having one less layer contributing to the EM2 signal. Since much less than 1% of the energy from a 50 GeV electron reaches 21 X_0, the effect is negligible. The third disconnected pad was an L1 detector which was left in layer 2.

5.5 Readout Electronics

The electronics packages used to read out the LMSAT and MASC are mounted immediately behind the LMSAT on each side of the IP. The design is very similar to that of the SLD Liquid Argon Calorimeter (LAC) electronics, described in Reference [50]. (Many elements, including the custom preamplifier hybrids, are identical.) Each LMSAT/MASC package, known as a "tophat" (see Section 5.2), reads out 512 channels. Ribbon and twisted pair cables carry the signals from the detectors to the preamp boards, each of which carries four eight-channel preamps. A tophat consists of sixteen preamp boards ($16 \times 32 = 512$), a fiber optic receiver/transmitter board,

Table 5.1: Table of Acronyms and Abbreviations.

acronym	proper name
LMSAT	Luminosity Monitor Small Angle Tagger
MASC	Medium Angle Silicon Calorimeter
LAC	Liquid Argon Calorimeter
TCM	Fastbus Timing and Control Module
CDM	Fastbus Calorimeter Data Module
AEB	Aleph Event Builder
CDU	Calorimeter Data Unit
A to D	Analog to Digital Converter

a controller board, an Analog-to-Digital converter board, a depletion voltage filter board, and an instrumentation board used for various monitoring functions. These boards all mount upon a motherboard which provides the interconnections between boards. The motherboard is split into an upper and lower half so it may be assembled around the beampipe.

The tophats receive commands from, and send data out to, custom Fastbus modules. A block diagram of tophat functionality is shown in Figure 5.7. The scheme is as follows: Signals from a Fastbus Timing and Control Module (TCM) are transmitted on optical fibers using a three-wire protocol; these signals are received and converted to TTL on the fiber optic board, and then used to generate the appropriate strobes and logic levels by the controller board. Output from the preamps is sampled immediately before and after the beam crossing in gates of width 3.75 to provide a baseline and signal.

Amplified outputs from the preamps are passed on to the 16 channel Calorimeter Data Unit (CDU) which performs a sample-and-hold function. Signals are split into two paths in the CDU, one path with unity gain (beyond the gain of the preamp) and the other with a factor of 8 gain. Each CDU services two preamps. The high and low gain signals are multiplexed and passed on to the Analog-to-Digital conversion board.

The signal is digitized and transmitted to the Fastbus Calorimeter Data Module (CDM) in a serial stream via optical fiber. The use of optical fibers results in lower noise and greater immunity from ground loops. Each signal is carried on a redundant pair of optical fibers.

In order to minimize heat dissipation, the power to the preamps is pulsed at the SLC repetition rate of 120 Hz: the power cycles on 1 ms prior to the beam crossing, to allow time for settling, and then turns off approximately 100 μs after the beam crossing, resulting in a duty cycle of 13%. The tophat is surrounded by an aluminum housing with a water cooling loop for temperature stability.

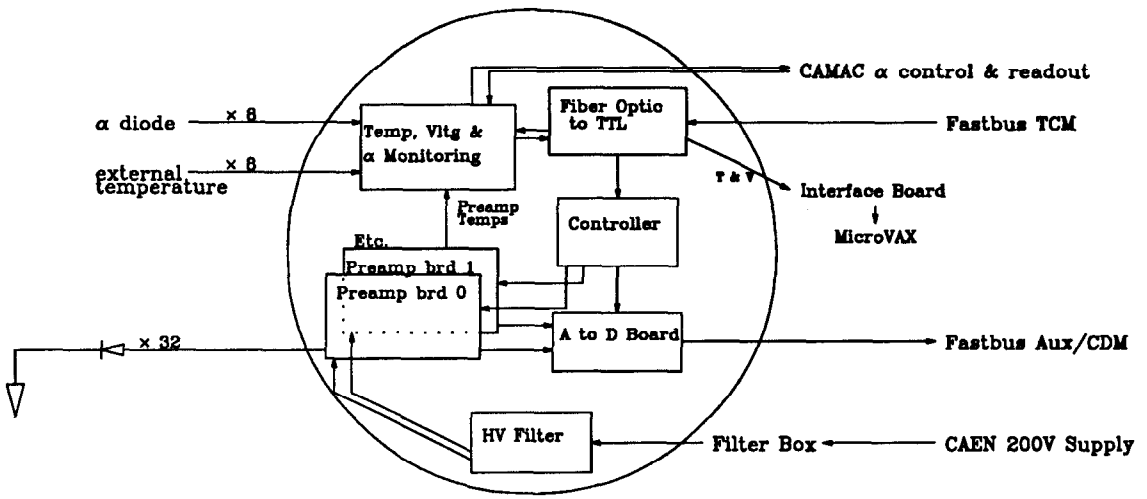

Figure 5.7: Block diagram of the LMSAT/MASC electronics.

The Vertex Detector cables and electronics are in close proximity to the LMSAT. The presence of the 10 V high frequency drive signals which readout the CCDs could cause pickup in the Luminosity Monitor readout. To avoid this, the Vertex Detector drive pulses are gated off for a few hundred microseconds around each SLC beam crossing [39].

The voltages used to deplete the silicon are supplied by special 200 V, 200 μA CAEN supplies which are controlled by the online Vax 8800. They are typically run at -75 V. Each CAEN channel services one LMSAT preamp board (32 channels). Currents on the order of a few microAmps per CAEN channel in the absence of shorted detector towers is seen. The voltages are passed through a filter box containing RC elements to remove any residual AC components. Multiconductor cables bring the voltages from the sources to the filter board on the tophat; the voltages then go through the motherboards to the preamp boards, where for each tower a 1 $M\Omega$ current-limiting resistor lies between the voltage source and the silicon.

A special circuit (shown in Figure 5.8) was added ahead of the preamp for each channel which enables us to measure the voltage drop across the 1 $M\Omega$ resistor due to leakage current out of the silicon. The strobe used to pulse this circuit is activated by toggling a single bit on the controller. Thus the leakage current for every tower can in principle be measured online, although currents below a few hundred nanoamps cannot be measured reliably.

The electronics is calibrated using circuitry built into the preamps. A precision DAC on the controller board generates a voltage in the range 0–5 V which charges laser-trimmed 8.4 pF capacitors (one per channel) in the preamp hybrid. The resulting

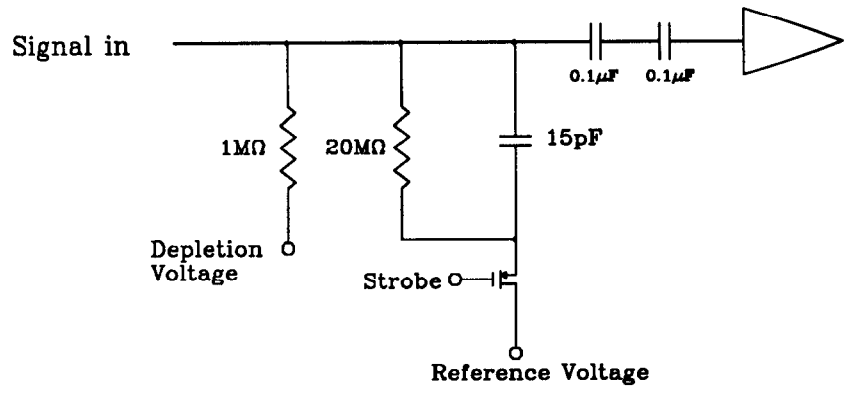

Figure 5.8: The leakage current measurement circuit.

charge is injected into the amplifier section of the hybrid, which is read out in the normal way. The CDM calculates and stores the constants obtained from a 16-point linear fit to the calibration data for each channel. Data taken during normal running are corrected using these constants to produce a "calibrated ADC" value for each channel, with 390 counts per pC of deposited charge. The CDM also applies a threshold cut before passing its data on to the Aleph Event Builder (AEB) [51]. In normal running mode, the CDM also performs the baseline subtraction function, so data passed to the AEB has been corrected for gain and pedestal.

5.5.1 Trigger

Readout of the LMSAT/MASC is closely coupled to readout of the SLD LAC. Both systems share a single TCM and AEB. (This particular AEB is dedicated to the calorimeter subsystems and hence is known as the KAL AEB. Other subsystems, e.g. CRID, have separate AEBs.) Since each CDM handles two tophats, the LMSAT/MASC requires only a single CDM, compared to 32 CDMs for the LAC. The TCM and CDM functions have been described above. The KAL AEB buffers data from all the CDMs and passes its data on to the Trigger AEB, which receives data from all the subsystem AEBs and distributes the trigger on the Fastbus backplane [52].

The slow (120 Hz) repetition rate of the SLC allows the CDM to acquire data and calculate the trigger quantities on every beam crossing. This information is buffered up to the online Vax every few minutes, allowing for monitoring of trigger rates and associated trigger quantities. Energy sums performed in the CDM at 120 Hz are also passed back to the SLC in the form of an oscilloscope signal which allows the operators to see a real time noise signal and tune the accelerator to reduce backgrounds [53].

The typical Bhabha trigger (see Section 6.4.1) for the LMSAT requires a total energy above some threshold (9.4-12.5 GeV) in both the North and South, with towers having less than 1.25 GeVsuppressed. To minimize detector deadtime, only the

calorimetry systems (KAL AEB) are read out for Bhabha triggers. It takes roughly 12 SLC beam crossings to read out the calorimetry systems. When the entire detector (tracking systems included) are read out the SLD is dead for approximately 25-35 SLC beam crossings, depending on event size [54]. In normal running conditions, the Bhabha trigger dead time is roughly 6%, while triggers reading out the entire detector have dead times of approximately 10-15%. Over the entire span of the 1992 data run, the Bhabha trigger rate was roughly 0.25 Hz, with approximately 4% of the triggers caused by physics events.

Beam backgrounds tend to give low-energy hits in many towers, which motivated the 1.25 GeV threshold. Since higher backgrounds may be unavoidable in future SLC running (due to higher currents and stronger focusing of the beam near the IP), more sophisticated trigger algorithms may be necessary to minimize deadtime. The SLD trigger hardware was designed with these possibilities in mind, and can accommodate a wide variety of specifications. Current plans are to implement an improved trigger algorithm for the 1994 run [55].

5.6 Operation

The first Luminosity Monitor (LMSAT-16) was put in a test beam at Brookhaven in the Spring of 1990. Before installation into the SLD, cosmic ray data was taken with the LMSAT-25. Since the Spring of 1991, the detectors have been operating as a part of the SLD detector collecting colliding beam data.

5.6.1 BNL Beam Test

One LMSAT-16 module was tested at the A2 test beam at the Brookhaven National Laboratory Alternating Gradient Synchrotron [56]. The A2 test beam delivers hadrons with a few percent electrons at 2 GeV/c, falling to less than one percent at 7 GeV/c.

The trigger was implemented in a simple fashion. It is illustrated in Figure 5.9. One 3×2 in^2 plastic scintillator, S1, was positioned about 3 meters upstream of the detector, and a second 2×1.5 in^2 scintillator, S2, was positioned immediately in front of the detector. A 7 foot gas Čerenkov counter, located 7 meters upstream of the detector, was operated with air at ambient temperature and pressure, to select electrons and reject hadrons.

The signals were amplified with electronics developed by SLD for earlier liquid argon calorimetry prototype tests. The final preamps, cables, and readout system were not available for the beam test. The system used for the beam test was much more susceptible to crosstalk and electronic noise than that used in the SLD experiment.

Event readout was performed on an IBM PC/AT which was used to drive standard LeCroy Research Corporation FASTBUS data acquisition modules via CAMAC. The CAMAC system was interfaced to the host PC/AT by means of a DSP PC004

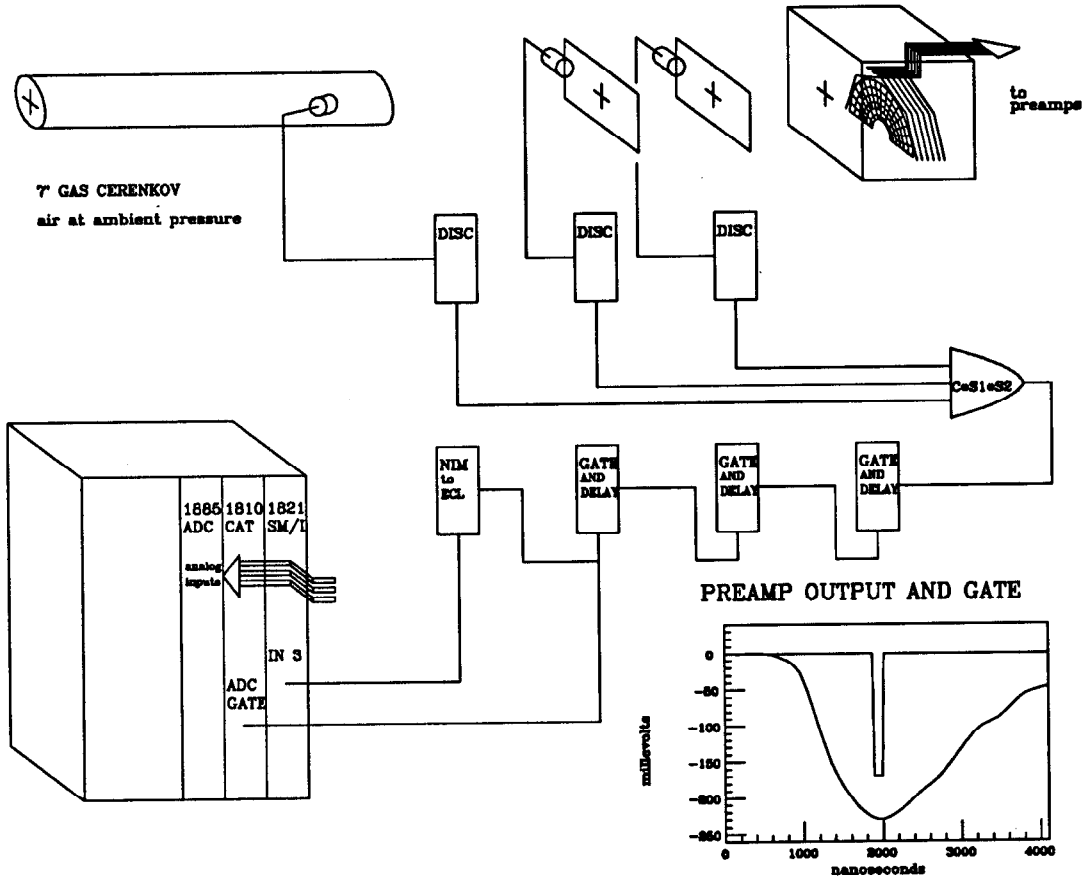

Figure 5.9: Logic diagram for beam test data acquisition.

interface card and a DSP 6001 crate controller. Analog signals from the calorimeter were digitized by a LeCroy 1885F charge sensing FASTBUS ADC, used in conjunction with an 1810 calibration and timing (CAT) module and an 1821 segment manager and interface module (SM/I). The 1821 is interfaced to the CAMAC crate by means of an 2891A FASTBUS/CAMAC interface module. The fastbus modules operated in a Dr. B. Struck FASTBUS mini-crate.

The ADC gate was formed by delaying the trigger coincidence by 1700 ns and sampling a 120 ns gate at the pulse peak (see Figure 5.9.) The gate width was selected to be much shorter than the pulse duration in order to bring the integrated charge down within the range of the ADC. Offline pulser tests showed that this practice did not adversely affect the linearity of the measured charge.

The ADC gate was brought to the NIM ADC GATE input on the front panel of the 1810 CAT module and distributed to the ADC via the crate backplane. The autoranging feature of the ADC was disabled and the ADC's high range was used exclusively. In high range the ADC has a sensitivity of 0.4 picocoulombs/count and a full scale of 1350 picocoulombs.

Data were taken for beam momenta of 2.0, 4.0, 5.42, and 7.0 GeV/c for several placements of the calorimeter relative to the beam. The muon threshold for the Čerenkov counter was 4.5 GeV/c and the pion threshold was 5.9 GeV/c. Data were taken both with and without the Čerenkov coincidence.

The 7.0 GeV/c data with Čerenkov trigger provides channel to channel muon calibration. The data was collected for muons incident upon a fraction of the total cross section of the calorimeter. This data was used to determine the gains for 13 towers in EM1 and 16 towers in EM2. Events in which the muon was contained in 1 EM1 tower and 2 EM2 towers were used to obtain the gains. Events in the Landau tail of the energy deposition were not included in the gain determination. Although the tail events were not used in the gain determination, they are plotted in figure 5.10.

Figure 5.11 presents the energy distributions for 2, 4, and 5.42 GeV/c electrons based on these muon calibrations. The fitted Gaussian curves to these distributions yield energy resolutions of $\sigma_E/E = 0.174 \pm 0.004, 0.116 \pm 0.003$, and 0.102 ± 0.003 at 2, 4, and 5.42 GeV/c, respectively. The electron energy distribution, being calibrated by the muons, indicated the e/μ response of the system to be 0.75 ± 0.01, 0.78 ± 0.01, and 0.77 ± 0.01 at 2, 4, and 5.42 GeV/c.

The test beam data was also used to show the EGS Monte Carlo accurately reproduces the features of electromagnetic showers in thin silicon. This is important in understanding the position resolution of the calorimeter, which is an important aspect of the luminosity determination. From this data and EGS studies at higher energy, the position resolution at 46 GeV is 300 μm.

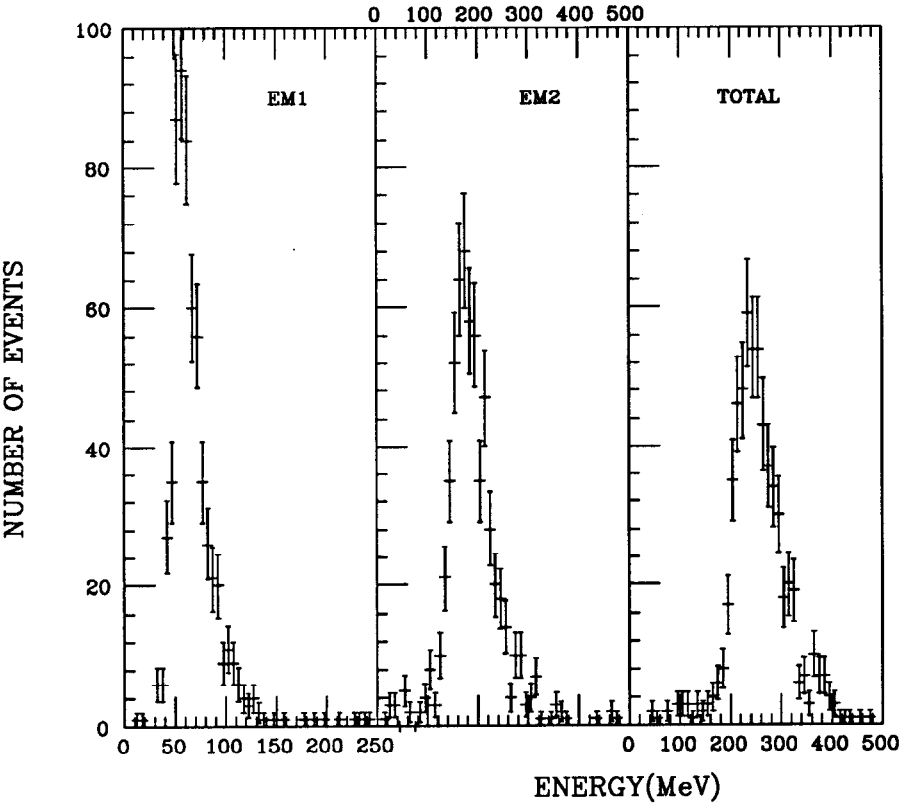

Figure 5.10: Test beam response to 7 GeV muons. Events in the tail were not used in the gain determination.

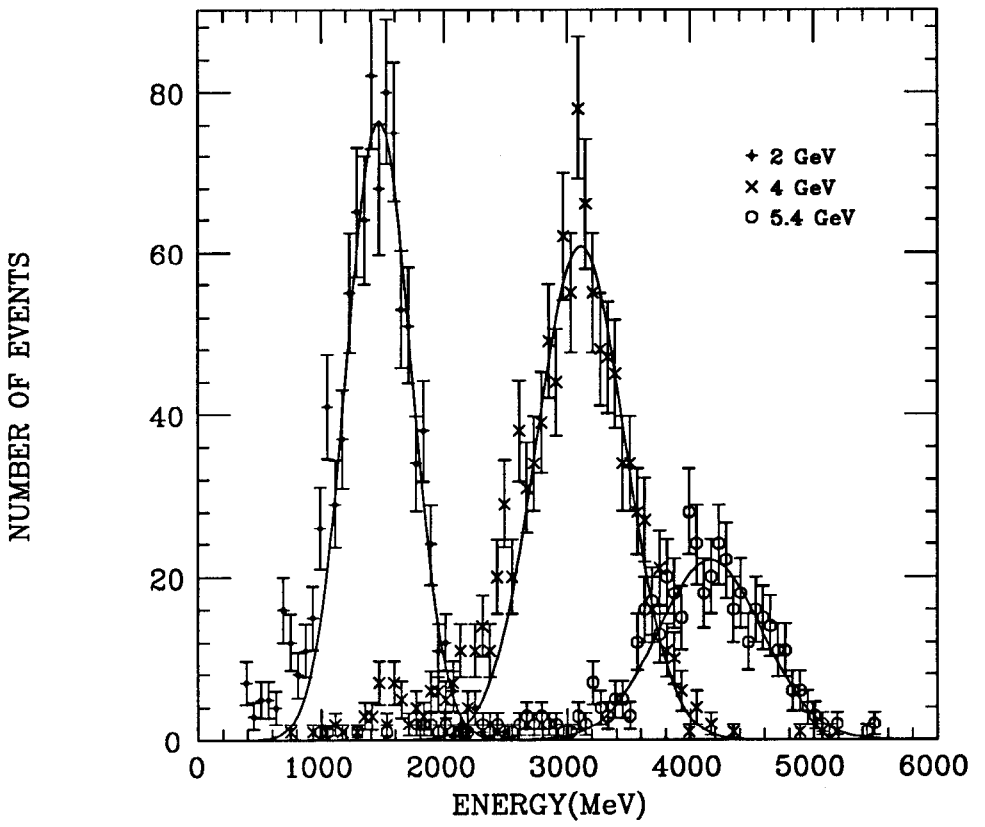

Figure 5.11: Response to 2, 4 and 5.42 GeV/c electrons based on the minimum ionizing energy scale.

5.6.2 Cosmic Ray Test

One LMSAT detector was placed on its back to accumulate cosmic ray data.[8] This was done prior to installation onto beamline at SLAC, in order to test the detector and exercise the electronics with the SLD data acquisition system.

To trigger on cosmic rays, scintillator paddles slightly larger than the surface of the LMSAT were placed above and below the detector. The trigger was simply an AND of hits in the two scintillators. To increase the event rate, the TCM timing was modified so that the active portion of the power-on cycle was increased from the nominal 100 μs to 500 μs.

Figure 5.12 shows the raw ADC spectrum for accepted cosmic events. The expected ADC values for minimum ionizing particles may be calculated based on knowledge of the electronics gain and digitization factors. The expected values are 12 ADC counts for EM1 and 34 ADC counts for EM2, for a total of 46 ADC counts. Although the cosmic ray statistics are low, the mean ADC values are consistent with expectation [57].

5.6.3 Colliding Beams

The first small angle Bhabha event was recorded in the LMSAT on July 6, 1991. Roughly 1000 events were recorded throughout the 1991 engineering run [47]. In 1992, over 25000 events were recorded [58]. The detailed analysis of the 1992 data is discussed in Chapter VI. The experimental systematic error on the luminosity measurement is found to be less than 0.9%. The 1993 run saw a factor of five increase in statistics over the 1992 run.

Radiation damage is not expected to be an issue in the low repetition, low luminosity e^+e^- environment of the SLC for two reasons. First, the beamline radiation produced by the SLC is primarily low energy ($\sim$1 MeV) electrons and photons, which are very inefficient for displacing silicon atoms [59]. Secondly, it has been shown that silicon radiation damage is highly dependent upon the period of time the dose is received [60]. The low repetition rate of the SLC (coupled with running a fraction of the year) and the type of beamline radiation involved led to the conclusion that the radiation damage will not be an issue [38].

The radiation dose is monitored by inserting thermoluminescent dosimeters (TLD) at various locations around the detectors and electronics. These TLDs are removed and the integrated dose is measured. Space constraints render it impossible to place and retrieve TLDs from the front face of the detector without removing the LMSAT completely. Since this was done after the 1991 run, rough estimates of the maximum integrated dose on any of the silicon can be made for later runs based upon the doses measured in other accessible locations. In 1991, the silicon pads in the first layer nearest the beamline received a dose of order 2 kiloRads. This is the maximum dose

[8]The orientation for cosmics was such that the silicon detector planes were parallel to the ground.

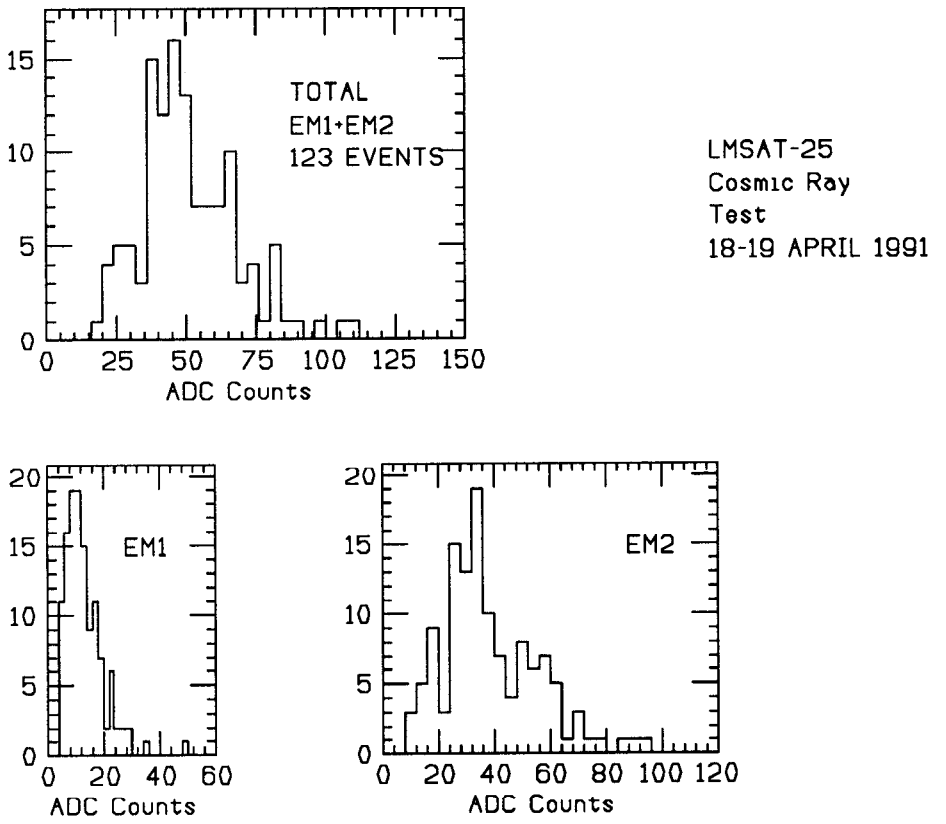

Figure 5.12: ADC distributions for cosmic ray events in the Luminosity Monitor.

any of the detectors received. In 1992, the same region received roughly 3 kiloRads. The radiation dose in the electronics region was roughly a factor of 20 to 30 less than this.

In addition, 1 cm^2 diode detectors with an α source implanted on the ground plane are placed inside the detector region. The α particles produced in nuclear decays range out in the first $25\mu m$ of silicon. Therefore, the alpha signal is an excellent way to monitor depletion depth. While it is possible to read out the diode detectors in situ, they are removed and returned to the University of Oregon after each run for complete analysis. To date, no degradation of depletion depth has been seen.

5.7 Summary

The SLD Luminosity Monitor has been operating successfully at the SLC Z^0 factory since turn-on. Extensive testing and preparation made it possible to acquire data originally through beam test and cosmic ray running, and eventually in the collider environment. All design goals have been met or exceeded. The following chapter will present an analysis of the luminosity measurement performed with the SLD Silicon/Tungsten Luminosity Monitor. In addition, electronics have been very reliable, with no major failures in three years of operation. This detector should be able to perform very well throughout the lifespan of the SLD experiment.

CHAPTER VI

MEASUREMENT OF LUMINOSITY

The luminosity at e^+e^- machines is determined by measuring the rate of Bhabha scattering, $e^+e^- \rightarrow e^+e^-$, at small angles. Since this process is dominated by t-channel photon exchange, the cross section can be calculated to great precision. To achieve the lowest systematic errors possible, experiments rely primarily on small angle calorimeters to measure the Bhabha events. By simply counting the number of events within a well-defined region and knowing the accepted cross section for that region, the luminosity can then be calculated.

This chapter will describe the measurement of the luminosity for the 1992 SLD data run. This analysis relies on the Luminosity Monitor/Small Angle Tagger (LMSAT), which is a finely segmented silicon/tungsten calorimeter and described in Chapter V. The preliminary luminosity measurement for the 1993 run will also be presented here. The analysis of the 1993 data is nearly identical to the analysis detailed in this chapter [61].

6.1 Overview

The dominance of the QED interaction in Bhabha scattering at small angles allows for the cross section to be calculated to a high degree of precision even near the Z^0 resonance. The process of calculating the luminosity involves triggering, identifying and classifying $e^+e^- \rightarrow e^+e^-$ events with a high efficiency and small contamination from background sources. By counting the number of Bhabha events incident on a well defined region of the detector and calculating the cross section for the Bhabha process in that region, the luminosity may be extracted.

The high energy electrons deposit virtually all of their energy in a very localized region of the detector. The trigger and event selection algorithms utilize this property to identify Bhabhas with a very high efficiency.

6.2 Measured Quantities

An electron or positron incident on a luminosity monitor will create an electromagnetic shower in the tungsten radiator. Since the calorimeter will fully contain the shower, the amount of charge collected in the silicon is directly proportional to the incident energy. The relative amount of charge collected in towers near one another may be used to calculate an effective position of the incident particle.

For each event that is a potential Bhabha candidate, a cluster is found in each layer (EM1, EM2) of both sides. First, the most energetic tower is found and considered the cluster initiator. The main tower and all adjacent towers are included in the cluster.

The cluster energy is simply the sum of the energy deposited in all towers of the cluster. The cluster position is calculated as an effective polar angle and azimuthal angle. Both of these quantities are calculated using an energy-weighted-mean. The narrowness of the electromagnetic showers is known to give too much weight to the most energetic tower of the cluster [62]. While it is possible to correct for this effect, the correction is unnecessary as long as all pertinent cuts are placed along tower boundaries. The correction will not move any positions across tower boundaries. Therefore, the energy-weighted-mean is sufficient for calculating an effective shower position so long as the cuts are placed at the boundaries of adjacent towers. A second motivation for placing cuts at tower boundaries arises from the fact that the boundary is where the optimal position resolution may be found.

The clusters from layer EM1 and layer EM2 are then combined if they are correlated (see below). The shower position is then the energy-weighted-mean of the clusters of the two layers. Cluster position quantities in this chapter are all calculated using an energy-weighted-mean and are effective positions.

6.3 Method of Measuring Luminosity

To reduce the sensitivity of the luminosity measurement to calorimeter alignment and interaction point location, we make use of the gross-precise method [63]. The gross-precise method uses the two luminosity monitors as single arm spectrometers. Although Bhabha events are identified by using information from both detectors, the events themselves are counted based on the location of each of the two showers in the respective detector. In each detector, a tight fiducial region and loose fiducial region are defined. For the SLD LMSAT, the tight fiducial region is defined as the second through fourth rings of towers (counting away from the beam line, see Figure 5.3). The loose fiducial region is the entire LMSAT.

Events in which both the electron and positron showers are within the tight fiducial region are labeled as "precise" Bhabhas and counted with weight 1. Events in which one of the two showers is inside the tight fiducial region and the other shower is inside the loose fiducial region (but not the tight region) are labeled as

"gross" events and given weight 1/2. An effective number of events can then be calculated:

$$n_{eff} = n_{precise} + \frac{n_{gross}}{2}. \tag{6.1}$$

The gross-precise method is advantageous because the effects of misalignment cancel to first order. Events near the inner edge of the tight fiducial region are allowed a "fuzzy" region of acceptance on the other side. If only the "precise" events are counted, then any misalignment causes a net loss of events. (The loss is roughly 3% per mm.) However, using gross-precise, one gains very nearly as many events as are lost.

For the gross-precise method to be valid, the transverse displacements must remain small compared to the distance of the inner acceptance to the beam line. In the case of the LMSAT, the inner acceptance is $\sim 35\,\mathrm{mm}$ from the beam line. Therefore, the gross-precise method is valid for transverse displacements of $\sim 2\,\mathrm{mm}$ or less. Displacements along the beam axis enter the acceptance in higher order.

In the Born limit with perfect alignment of the calorimeters and the beam, as well as perfect angular resolution, $n_{gross} = 0$. With perfect alignment, radiation and the intrinsic resolution of the LMSAT yields $n_{precise} \sim 8n_{gross}$. A misalignment of order 1 mm reduces that ratio to about 4.

The effective cross section (σ_{eff}) is calculated by Monte Carlo simulation of the Bhabha process and simulation of the electromagnetic shower in the detector. The knowledge of σ_{eff} and the measurement of n_{eff} may then be used to calculate the integrated luminosity:

$$\int \mathcal{L}\mathrm{dt} = \frac{n_{eff}}{\sigma_{eff}}. \tag{6.2}$$

6.4 Event Selection

The Bhabha event selection makes use of the narrowness of electromagnetic showers, as well as the fact that the two-body final state will be collinear. Although physics processes such as two-photon and Z^0 decays are potential contaminants, the dominant source of background comes from synchrotron radiation and off-energy beam particles produced by the SLC.

The selection criteria listed below are designed to be very efficient in finding Bhabhas while rejecting background. The typical background profile produced by the SLC falls rapidly with increasing theta. Background events tend to be mostly inner-ring events, where neither shower enters into the tight fiducial region.

6.4.1 Trigger

The Bhabha trigger energy sum is formed separately for the North and South detectors. Only towers containing more than 1.25 GeV (electromagnetic energy scale

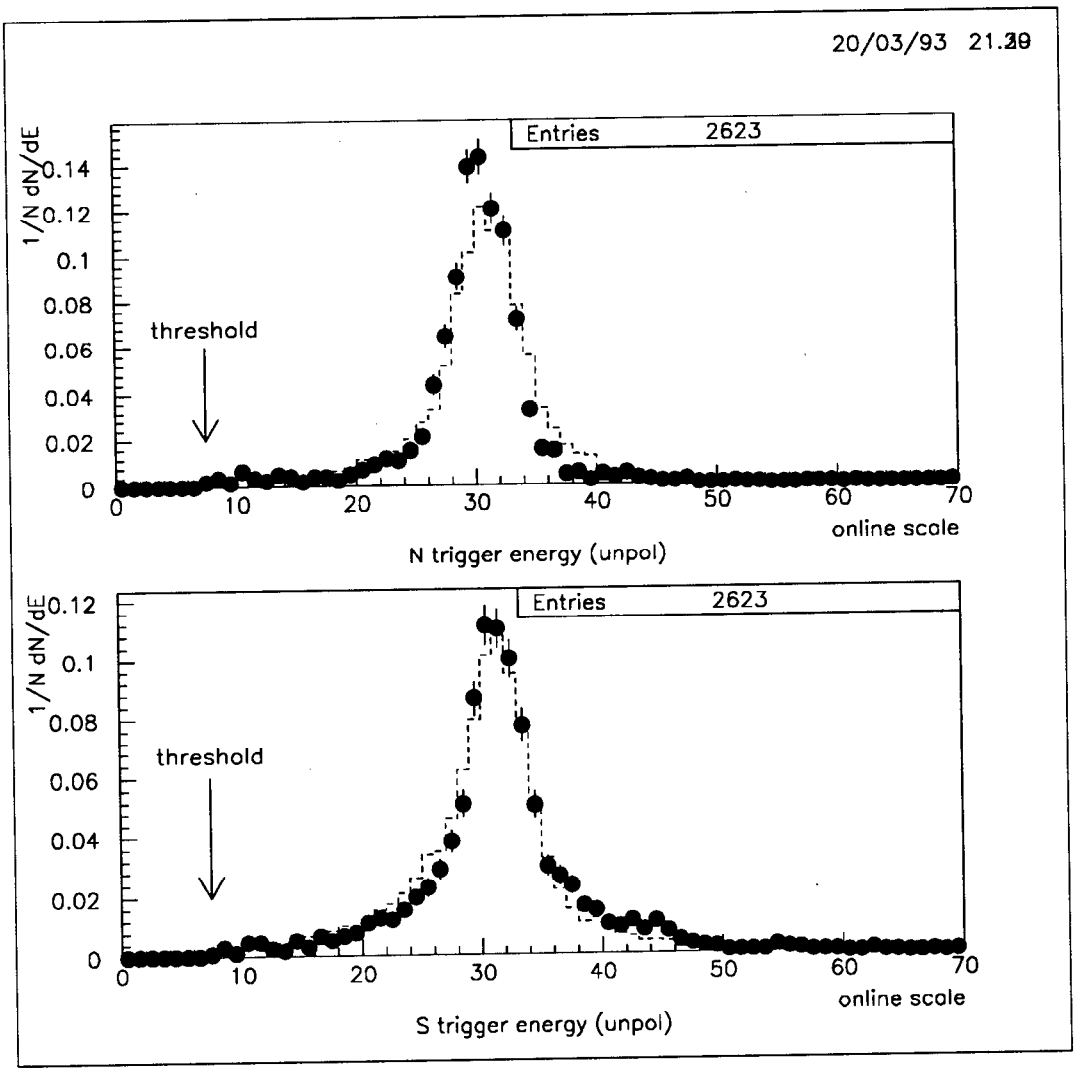

Figure 6.1: Trigger energy, unpolarized running, for selected Bhabha events. The points are data and the dashed line is Monte Carlo. The energy scale used by the trigger is approximately 20% below the true energy scale.

used throughout) contribute to the sum. Both the North and South energy sum must be above the trigger threshold energy.

Two different versions of the Bhabha trigger were used during the 1992 run. For unpolarized running, the energy sums were formed over all LMSAT towers. The trigger threshold energy was 9.4 GeV per side. This trigger was tightened for polarized running, so that the energy sums were formed over EM2 towers only. In addition, the threshold energy was raised to 12.5 GeV per side. The polarized trigger caused a slight reduction in efficiency while greatly reducing background, which is predominantly deposited in EM1 towers.

The trigger efficiency is estimated with the Monte Carlo simulation. (The simulation will be described in greater detail in Section 6.5.3). Any additional events which pass the event selection cuts while failing the trigger simulation indicate a trigger inefficiency. Figures 6.1 and 6.2 shows the trigger energy plots for both North and South for both data and Monte Carlo. For unpolarized running, the trigger was greater than 99.9% efficient. For polarized running the efficiency dropped to 99.6%. The failure of one path on the A to D board serving the South LMSAT (see Section 6.5.2) led to an additional 0.2% inefficiency.

Although it is possible to fit the trigger energy using data only to estimate the area under the curve falling below trigger threshold, this is not a reliable way to estimate the trigger efficiency. The energy cut imposed on the clusters (Section 6.4.2) artificially cuts out the low end of the trigger energy spectrum. Any fit of the data to a Gaussian or sum of two Gaussians will overestimate the trigger efficiency.

6.4.2 Selection

The event selection cuts are very loose, as the Bhabha events are very well separated from the background. Event selection criteria make use of the localized energy deposition of a single 46 GeV electron shower, as well as collinearity of the Bhabha events. These qualities are demonstrated in the typical Bhabha event shown in Figure 6.3.

Only events which pass the Bhabha trigger (Section 6.4.1) are submitted for further filtering. Calling the trigger filter stage 1, filter stage 2 is a fast pre-filter which is based on the online Bhabha filter algorithm that samples the data as it is being written to tape. While the online filter is set to find Bhabhas, the offline version is only used to cut out obvious background events. Any event which has a potential cluster well above the average energy per tower is passed on for full filtering. When the data is run without the stage 2 pre-filter, no additional events are tagged as Bhabhas. The stage 2 filter only serves to cut down processing time.

Events passing the stage 2 filter are sent to the clustering algorithm. Unlike the calorimetry reconstruction, Bhabha-finding clusters are of fixed size, which is a 3x3 array of towers surrounding the largest hit tower. Monte Carlo studies with EGS and GEANT show that 90% of the Bhabha energy on average is contained within a 3x3 cluster. Clusters which are wider than three bins in azimuth cover too much of the

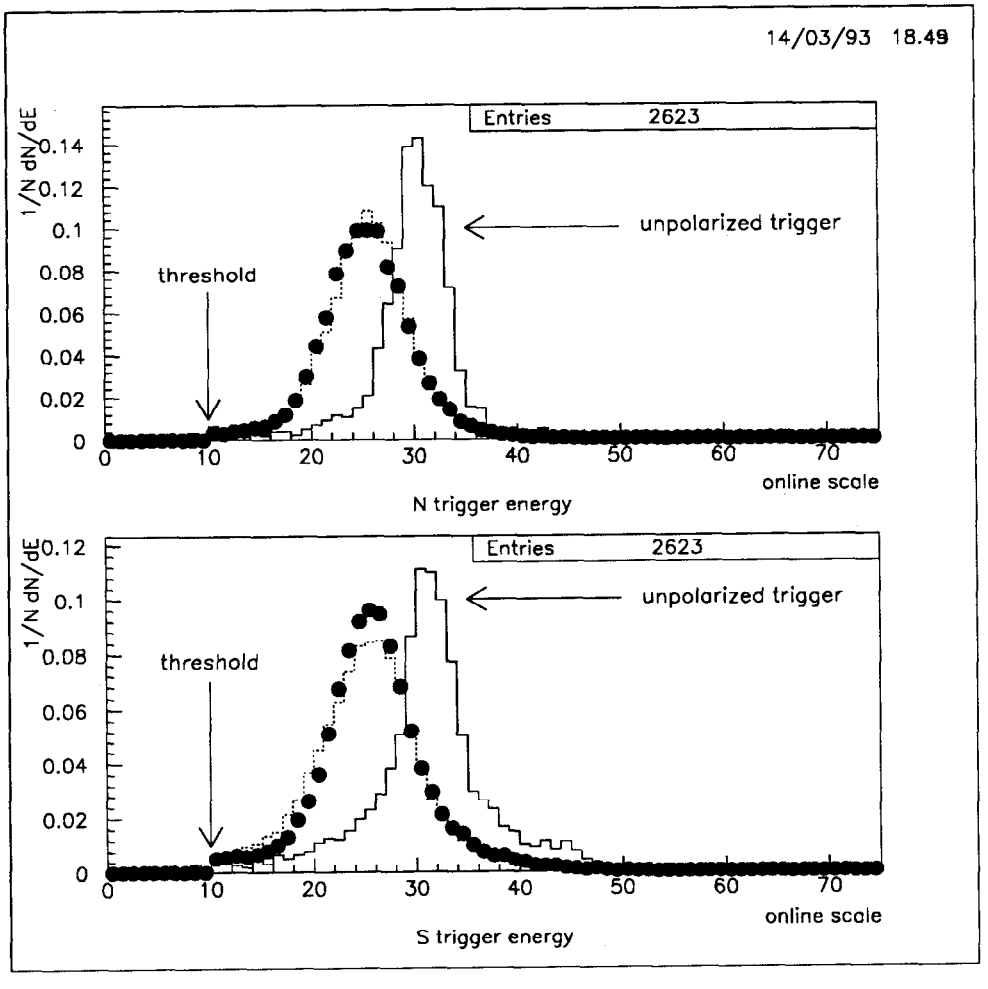

Figure 6.2: Trigger energy, polarized running, for selected Bhabha events. The points are data and the dashed line is Monte Carlo. The energy scale used by the trigger is approximately 20% below the true energy scale. For reference, the solid curve demonstrates the trigger energy sum for the same Monte Carlo sample using the unpolarized trigger cuts.

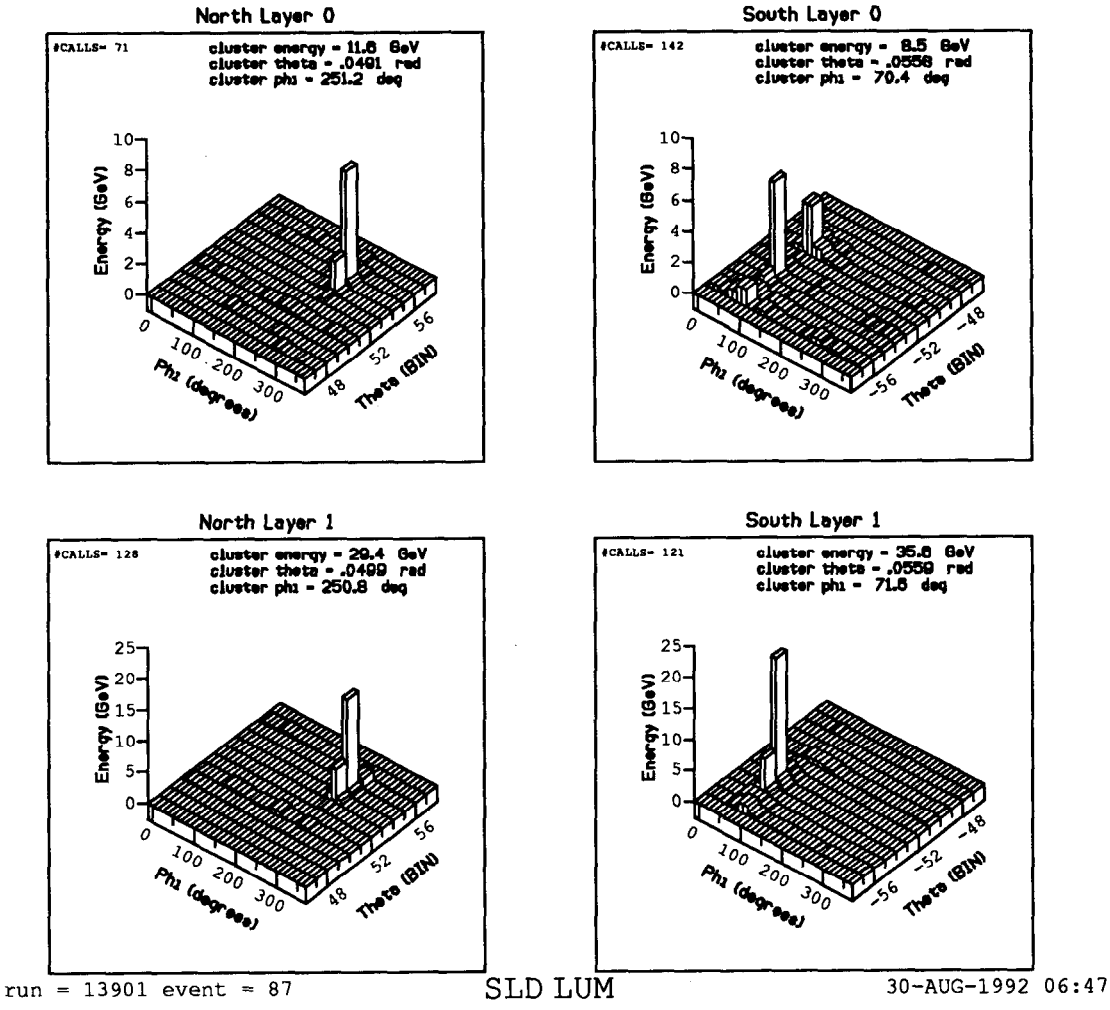

Figure 6.3: A typical Bhabha event from the 1992 run. Each entry in the energy deposition plot (a.k.a. Lego) corresponds to one LMSAT tower. Polar angle is shown in units of "bin," where the bin nearest the beamline is bin 56, with decreasing bin number with increasing theta. Layer 0 is EM1, Layer 1 is EM2. Notice the splash of background in South layer 0 on both the inner ring of the luminosity and also MASC. The MASC spans theta bins 47 through 50.

solid angle and tend to add more background than signal to the cluster. For example, a cluster which was 5 bins wide in phi would cover 56.25 degrees in azimuth. Larger clusters also lead to uneven cluster sizes and increase the cluster energy spread.

One cluster is found in each layer (EM1 and EM2) of each side (N and S). EM1 clusters below 1.25 GeV and EM2 clusters below 2.50 GeV are rejected and not included in the subsequent cuts. This does not mean, however, the event is not a Bhabha. This cluster energy threshold is to insure that random noise clusters are not included in any calculation of the shower position.

The cuts are then made on the cluster quantities and are as follows:

$$E_N > 20\,\mathrm{GeV} \quad \text{and} \quad E_S > 20\,\mathrm{GeV} \tag{6.3}$$

$$E_N < 125\,\mathrm{GeV} \quad \text{and} \quad E_S < 125\,\mathrm{GeV} \tag{6.4}$$

where $E_{N,S} = E_{EM1\,clus(N,S)} + E_{EM2\,clus(N,S)}$, and

$$|\pi - \delta\phi| < 0.5\,rad \tag{6.5}$$

where $\delta\phi = \phi_N - \phi_S$. Cluster position ($\phi$ and θ) is calculated by energy weighted mean. If the EM1 cluster and EM2 cluster are separated by more than 67.5 degrees in azimuth, the position of the shower is taken to be the centroid of the EM2 cluster.

The "low" energy cut (equation 6.3) rejects background triggers which have diffuse energy deposition. The "high" energy cut (equation 6.4) was implemented to protect against very poor beam conditions, where saturation effects can cause false clusters to be made. LMSAT towers saturate at around 60 GeV. The azimuthal cut (equation 6.5) makes use of the fact that the Bhabhas are collinear. There is no specific cut on polar angle, that variable is used for classification of event type.

The "cut" ("classification" is more accurate) which strongly rejects background is the gross/precise requirement. In other words, events in which the centroids of BOTH N AND S clusters are on the inner ring are rejected because neither cluster is located inside the tight fiducial region. This is exactly where the dominant background lies. Backgrounds in the LMSAT are mainly caused by electromagnetic radiation along the beam line. The background profile is continuous and falls steeply with radius ($\sim 1/r - 1/r^2$) from the beam line. The localized energy distribution of Bhabha events is very well separated from this continuous background distribution except in the ring of towers nearest the beam line. Therefore, accepting events where at least one of the clusters is located outside the inner ring rejects the background very efficiently. While the gross/precise method yields by far the lowest systematic error, approximately half of the Bhabhas into the luminosity monitor are in the inner ring. These inner ring events are useful for measuring the left-right luminosity asymmetry, as well as short term luminosity monitoring, (e.g. 24 hour Bhabha and Z^0 totals) where the statistical error dominates. Event selection of inner ring Bhabhas and the potential benefit has been investigated and was implemented for the 1993 run [64].

Table 6.1: Run blocks for luminosity measurement.

block no.	runs	dates (approx)	change in condition
1	5023-10141	2-Feb - 10-Mar	begin run
2	10142-10179	10-Mar - 13-Mar	db 15S dead
3	10180-10221	13-Mar - 17-Mar	4 channels no trig
4	10222-10355	17-Mar - 23-Mar	db 15S no trig
5	10356-10402	23-Mar - 24-Mar	multiple event problem
6	10437-10746	25-Mar - 6-Apr	same as block 4
7	11157-11366	1-May - 11-May	begin of polarization
8	11367-11555	11-May - 19-May	correct notrig channels
9	11556-11825	19-May - 6-Jun	db 12S dead
10	11978-12089	6-Jun - 12-Jun	SLC timing off, IP=(0.,0.,5.3cm)
11	12093-12430	12-Jun - 28-Jun	same as block 9
12	12431-12455	28-Jun - 29-Jun	LMSAT CPUs truncate
13	12456-13962	29-Jun - 17-Aug	same as block 9

6.5 1992 Luminosity

Since changes in the trigger and hardware lead to a different effective cross section for the gross-precise acceptance, it is useful to break the run into blocks. The beginning of a new block is determined by a change in running conditions (e.g. the begin of polarization) or a change in the LMSAT hardware (e.g. dead towers).

The 1992 is broken into thirteen separate blocks. Table 6.1 shows the run numbers which span the blocks. The blocks continue through in chronological order, therefore some conditions are repeated in more than one block. The blocks will be discussed below.

6.5.1 Unpolarized Run Blocks

The break-up of the unpolarized running into blocks was primarily due to shifting some noisy channels in and out of the trigger and acquisition system. The noise was caused by an oscillation in the daughterboard temperature monitoring circuitry and was corrected for polarized running. These differences lead to minor changes in the accepted cross section. Some of the blocks are rather small and 80% of the unpolarized logged luminosity falls in blocks 4 and 6.

The luminosity cannot be calculated directly for block 5 because the data acquisition system was putting single events on tape multiple times. Runs 10022 and 10048-10080 cannot be used because the Bhabha trigger was not active for those runs.

For the measurement of the total luminosity logged in 1992, the hadronic Z^0

count and effective hadronic cross section will be used to estimate the luminosity logged in runs in which the LMSAT data cannot be used.

6.5.2 Polarized Run Blocks

The dominant problem of the polarized run was the failure of the A to D path serving preamp board 12 in the South. This rendered roughly 10% of the South LMSAT dead. This condition covers blocks 9-13, which contain approximately 92% of the polarized data.

Block 10 contains the runs during which the SLC timing caused the interaction point to be off 5.3 cm in z. During this period, the electron bunch was being accelerated one RF cycle sooner than it is during proper running conditions. The electrons therefore arrived at the interaction point sooner than the positrons did. The effect was a shift of the interaction point along the beam axis.

Block 12 can not be used in the luminosity analysis because the data was truncated in the 4 CDM CPUs which acquire the LMSAT data. The origin of this problem is unknown, and did not reappear. In addition, runs 11306-11335 can not be used in the luminosity analysis because the Bhabha trigger was not active for those runs. Run 13285 in block 13 also can not be used due to acquisition problems.

6.5.3 Cross Section Calculation

The Bhabha cross sections are calculated from Monte Carlo generation and simulation of the physics and the detector. Two Monte Carlo generators are used, one written by Jadach and Ward, BHLUMI [65], and another written by Berends, Kleiss, and Hollik, BABAMC [66]. The BABAMC program includes single initial and final state Bremsstrahlung, while the BHLUMI program uses the exponentiation of the YFS calculation to include higher order effects.

Simulation of the LMSAT is done with GEANT [67]. The fast shower simulation GFLASH [68] accurately reproduces the data and is used here. Previous studies have been done with EGS3 [69] and accurately simulate the data.

The conditions of each block were put into the Monte Carlo to determine an effective cross section for that block. Blocks 1-4, 6-11 and 13 can all be simulated with the same Monte Carlo data set, by appropriate zeroing out of dead towers and turning off the appropriate towers in the trigger simulation. Block 10 (SLC timing) uses the same generated four-vectors, but must be resimulated with the appropriate interaction point location. Blocks 5 and 12 can not be simulated.

The data is uncorrected before being passed through the cuts. Therefore, all known effects are put into the simulation so that simulated data matches the uncorrected real data. The simulated data may then be passed through the same set of cuts that are imposed upon the real data. The two most dominant effects are due to local hardening and the blocking capacitors.

Table 6.2: Effective cross sections by run block.

block number	runs	σ_{eff} (nb)	$\frac{\sigma_{block}}{\sigma_{block\#1}}$
1	5023-10141	66.44	100%
2	10142-10179	66.20	99.6
3	10180-10221	66.00	99.3
4	10222-10355	66.19	99.6
5	10356-10402	-	-
6	10437-10746	66.10	99.6
7	11157-11366	63.65	95.8
8	11367-11555	66.16	99.6
9	11556-11825	60.98	91.8
10	11978-12089	57.81	87.0
11	12093-12430	60.98	91.8
12	12431-12455	-	-
13	12456-13962	60.98	91.8

The local hardening effect comes from the fact that low-Z materials within the calorimeter will suppress the soft component of the electromagnetic shower. The location of the low-Z material relative to the active region will affect the response differently [70]. In the LMSAT, alternate octants of silicon are mounted such that the active areas overlap in phi. To achieve this, the detectors are oriented so that the G10 board on which the silicon is mounted alternately facing toward and away from the interaction point. The response for octants facing toward the IP is about 6% less than it is for those facing away.

The daughterboards have blocking capacitors which protect the preamp inputs from the detector bias voltage [47]. Two blocking capacitors are in series, each with a capacitance of 56 pF. There is an effective charge division between the preamp and the detector itself, based on the capacitance of the tower. LMSAT towers range in capacitance from 270 pF to 1.45 nF. This leads to a charge correction ranging from 0.9% to 4.9%. Since nearby towers have similar capacitance, the effect of correcting the data shows up only slightly in the resolution, and much more strongly in the energy scale. Upon correcting the data, the relative resolution improves by 2%, while the mean energy increases by 3.5%.

Table 6.2 shows the effective gross-precise cross section for each run block. Errors on these cross sections will be discussed in Section 6.6.

6.5.4 Accounting

Table 6.3 shows the number of gross and precise events, for each run block.

Table 6.3: 1992 luminosity by block (error is statistical only).

block number	n_{gross}	$n_{precise}$	n_{eff}	nz	$\mathcal{L}(nb^{-1})$ (meas)	$\mathcal{L}(nb^{-1})$ (est)
1L	4	19	21.	15	0.32 ± 0.07	-
1N	-	-	-	19		0.70 ± 0.16
2	2	4	5.	8	0.08± 0.03	
3	71	359	394.5	183	5.98 ± 0.29	
4	147	680	753.5	333	11.38 ± 0.40	
5	-	-	-	36		1.32±0.22
6	238	922	1041.	419	15.73 ± 0.47	
unpol total	462	1984				
7L	105	567	619.5	283	9.73 ± 0.38	
7N	-	-	-	49		1.80±0.26
8	2	7	8.	2	0.12 ± 0.04	
9	369	1588	1772.5	753	29.07 ± 0.67	
10	387	921	1114.5	525	19.28 ± 0.55	
11	561	2654	2934.5	1316	48.12 ± 0.87	
12	-	-	-	187		6.88±0.50
13L	3256	14823	16451	7306	269.78 ± 2.05	
13N	-	-	-	16		0.59±0.15
polarized total	4680	20560				
1992 total	5142	22544				

Table 6.4: 1992 Luminosity. First error is statistical, second is systematic.

	1992 Luminosity		
	measured (nb^{-1})	estimated (nb^{-1})	total (nb^{-1})
unpolarized	$33.49 \pm 0.69 \pm 0.34$	2.02 ± 0.27	$35.51 \pm 0.68 \pm 0.36$
polarized	$376.10 \pm 2.42 \pm 3.80$	9.27 ± 0.58	$385.37 \pm 2.47 \pm 3.89$
total	$409.59 \pm 2.52 \pm 4.14$	11.29 ± 0.53	$420.86 \pm 2.56 \pm 4.23$

Applying equation 6.1, the effective number of events is found. From equation 6.2, the luminosity for that run block is then calculated. The statistical error on the luminosity can also be calculated from equations 6.1 and 6.2,

$$\frac{\Delta\mathcal{L}}{\mathcal{L}} = \frac{\sqrt{n_p + n_g/4}}{n_p + n_g/2}. \tag{4}$$

The errors on the luminosity in Table 6.3 are statistical only.

The number of hadronic Z^0s are also listed by block and are broken into whether or not the luminosity can be measured directly for that block. The Z^0 count used here is the "official" calorimeter-based selection used for the A_{LR} analysis [71]. The far right column of Table 6.3 includes luminosity estimates based on the number of Z^0s found for runs in which the luminosity cannot be measured directly. These sub-blocks are labeled "N" for "no LUM data." The portions of those blocks for which the luminosity is measured directly are labeled "L" for "using LUM data." The errors on the numbers in the "N" sub-blocks are dominated by the statistical error on the number of found Z^0s. From all runs where luminosity and Z^0 information are available (excluding block 10), an effective Z^0 cross section is calculated to be 27.17 nb [72]. This number is then used to estimate the luminosity for periods where small angle Bhabha data is not available.

The final results are shown in Table 6.4, and are broken down by polarized and unpolarized running. As can be seen from the table, the portion of the 1992 luminosity which has to be estimated is very small. The total luminosity logged by SLD in 1992 is 420.88 ± 4.94 nb^{-1}. Systematic errors will be discussed in detail in Section 6.6.

6.5.5 Left-Right Luminosity Asymmetry

For polarized running the number of polarized Bhabhas were counted for each beam helicity. Including gross and precise events, there were 12395 Bhabhas created with a left-handed beam and 12353 Bhabhas created with a right-handed beam. This gives the following left-right luminosity asymmetry:

$$A_{LR}^{exp}(LUM) = (1.7 \pm 6.4) \times 10^{-3}, \tag{6.6}$$

where the error is purely statistical. As in the measurement of A_{LR}, the random flipping of beam helicity states causes all detector and background related systematics to cancel. The expected asymmetry for small angle Bhabhas is $\sim 3 \times 10^{-4} \mathcal{P}_e$. It should be noted that the number of both left- and right-handed Bhabhas are slightly less in this report than the numbers quoted in the SLD A_{LR} paper [1]. In that document, the number of Bhabhas created with a left-handed beam was 12832 and the number of Bhabhas created with a right-handed beam was 12783. The luminosity asymmetry was $A_{LR}^{exp}(LUM) = (1.9 \pm 6.2) \times 10^{-3}$. The $\sim 3\%$ reduction in events is due exclusively to the tighter energy cut imposed here.

6.6 Systematic Errors in the Luminosity Measurement

The systematic effects can most conveniently be broken into seven categories: contamination, energy cuts, beam parameters, Monte Carlo generation, accuracy of simulation, phi cut and theta cut. As will be seen, there is some overlap between the categories. The sources listed above will be tackled in succession in the following sections. Table 6.5 will show the systematic error contributions by type.

6.6.1 Contamination

The effect of non-Bhabha contamination can be broken into two categories: physics and SLC beam background.

Three physics processes could potentially pass the filter cuts: two-photon ($e^+e^- \rightarrow e^+e^-X$), $e^+e^- \rightarrow \gamma\gamma$, and Z^0 decays.

For the two-photon process, approximately 10 times the 1992 dataset was generated using a two-photon generator imported from Mark II and TPC [73]. The events were simulated and overlayed on a sample of luminosity weighted random triggers. The contamination is found to be less than two events ($< 0.01\%$). Likewise, for Z^0 decays, roughly 5 times the 1992 dataset was filtered through the Bhabha cuts. No events pass, leaving the contamination to be the less than 0.22 events ($< 0.001\%$). The process $e^+e^- \rightarrow \gamma\gamma$ is directly calculable [74] and has a cross section into the luminosity acceptance region of approximately 30 pb. This contributes less than 0.05%.

Electromagnetic radiation produced by the SLC along the beamline is a much larger source of background. This contamination can be estimated by looking at triggers which pass all Bhabha cuts except the opening angle between the N and S cluster is near zero radians instead of π. This method will over estimate the background, because the SLC background is actually correlated. For example, if the beam is misteered so that energy is deposited in the top of the North LMSAT, there is a high probability that more energy will be deposited near the top of the South LMSAT, too.

For 1992 running, this method yields 1 precise event and 162 gross events. Upon inspection, the 1 precise event is actually a radiative Bhabha event. (That event has a well defined third cluster in the endcap LAC which balances energy and momentum). Therefore, the upper limit on the effective number of contaminant events is 81. Taking this as the error due to SLC contamination, the systematic effect is 0.32%.

It should be noted that backgrounds produced by the SLC affect other aspects of the luminosity measurement. To account for these effects, all Monte Carlo simulations are overlayed on a luminosity weighted set of random triggers.

The contributions to the systematic error from contamination can be summarized as follows: 0.01% from the two-photon process, 0.001% from the hadronic Z^0 process, 0.05% from the process $e^+e^- \rightarrow \gamma\gamma$, and 0.32% from SLC background. The total systematic error caused by contamination is 0.32%.

6.6.2 Energy Cuts

There are actually three energy-related cuts: trigger (Section 6.4.1), energy cut low (equation 6.3) and energy cut high (equation 6.4). The effects which lead to error in the cross section are the energy scale, the energy resolution, unaccounted dead towers and tower-to-tower calibration errors.

Figure 6.4 shows the energy distributions for both data and Monte Carlo. The data has been corrected for clustering, local hardening and the blocking capacitors. The resolution of the Monte Carlo is worse than that of the data. Although this leads to an error in the cross section, this error is minimized by placing the energy cut down on the tail of the distribution. The shape of the tail on the low end is dominated by radiation, clustering and dead towers.

The overall energy scale is set by the Bhabha events themselves, after correcting the data for known effects such as clustering, local hardening and tower capacitance. The energy scale is seen to be correct to within 1%. Variation of the overall energy scale by 2% leads to a change in the luminosity of 0.17%.

The upper energy cut of 125 GeV per side is only to guard against bad-beam saturated background events. The effect of this cut is less than 5 events out of 25k Bhabhas (0.02%).

Several effects contribute to the tower-to-tower calibration errors. The laser-trimmed calibration capacitors are good to 0.25%. The LAC hybrid preamp and CDU combination have a temperature dependence of about 0.3% per degree C. While temperatures are very stable inside the detector during data acquisition, drifts of up to 1° C have been observed. In addition, the degradation of the Monte Carlo for the capacitive charge division is done by using an average tower capacitance for each cell type. Also, all channels are pulsed simultaneously during calibration, causing a different crosstalk effect than is seen in normal running. The magnitude of the crosstalk has been measured to be less than 0.3%. The combination these effects leads to a calibration error of roughly 0.5% [50].

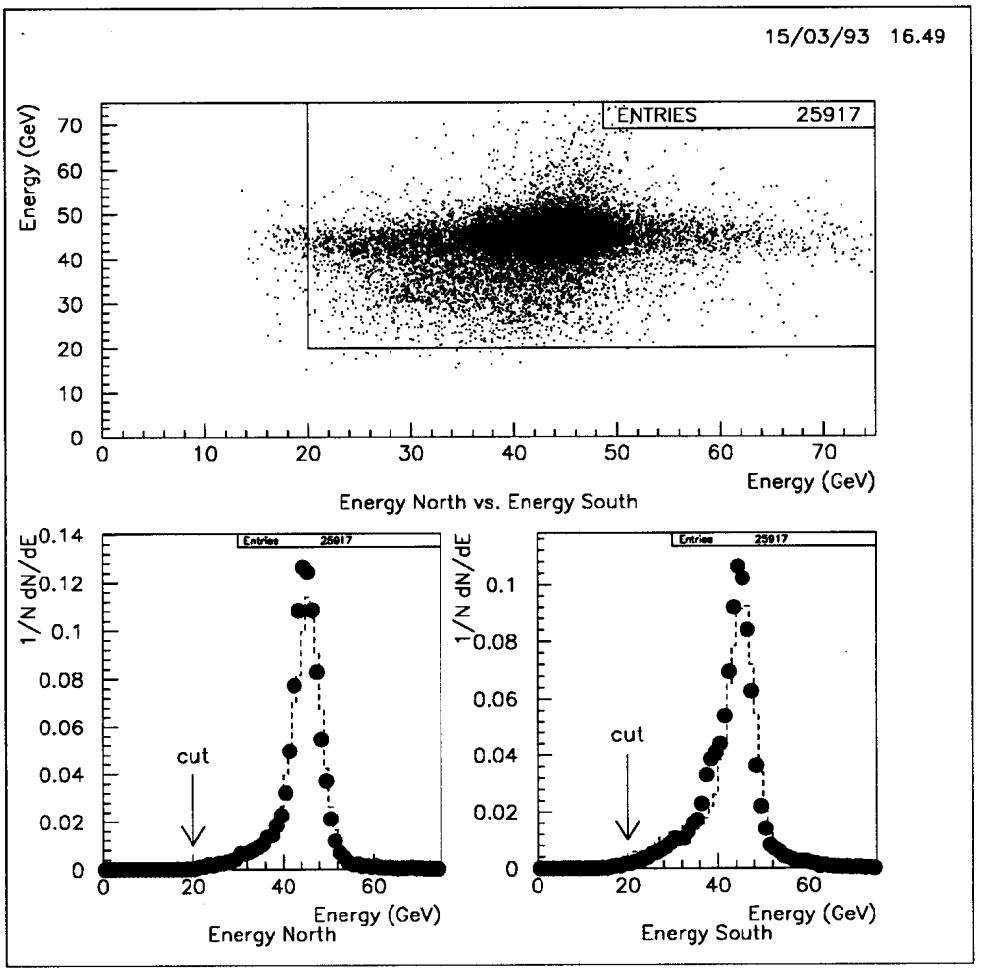

Figure 6.4: The top figure shows North energy vs. South energy for the 1992 polarized data. The points in the lower two figures are the projections onto each of the two axes of the top figure. The dashed lines are Monte Carlo.

To simulate tower-to-tower calibration effects, the Monte Carlo was run with a gaussian smearing of the tower energies with a root-mean-square deviation of 1%. This leads to a 0.22% increase in the accepted cross section.

Calibrations are run on varying intervals. The towers which calibrate dead are tracked offline. However, it is possible that single towers could calibrate as dead and get missed for single blocks. Most Bhabhas are unaffected even if they strike a dead tower directly, because enough energy is captured in the surrounding towers to pass the cuts. To estimate the absolute upper limit on the energy cut due to dead towers, one tower was randomly zeroed out in every tenth Monte Carlo event. The reduction in acceptance was 0.05%.

Two other potential effects of the energy cuts are the effect of clustering and leakage. These effects are both implicit in the Monte Carlo simulation, and will be handled in Section 6.6.5.

The contributions to the systematic error from the energy cuts can be summarized as follows: 0.17% from the absolute energy scale, 0.02% from the "high" energy cut, 0.22% from tower-to- tower calibration uncertainty, and 0.05% from unaccounted dead towers. The total systematic error from the energy cuts is 0.28%.

6.6.3 Beam Parameters

Five effects fall under the category of beam parameters: beam energy, energy spread, interaction point location, interaction point spread and the pitch of the beam at the interaction point.

The absolute center of mass energy measurement comes from the WISRD energy spectrometer. For the 1992 run, the average center of mass energy was 91.57 GeV. The absolute error on the center of mass energy is 35 MeV [44, 75]. The energy spread of the beams were typically 150 MeV. The absolute calibration error leads to an error of 0.08% in the Bhabha cross section. The error induced by the energy spread is negligible as long as the distribution is symmetric. Figure 6.5 shows that while this is indeed the case for the electron beam, the positron beam exhibits an asymmetry about the mean energy. From the two-gaussian fit shown in Figure 6.5, there is a 12% excess on the high side of the most likely value. If we estimate the mean of the tail to be 200 MeV above the mean of the main distribution, this leads to an error in the cross section of 0.06%.

The SLC ran with asymmetric beam energies during 1992. The electron beam was on average approximately 120 MeV more energetic than the positron beam. For the luminosity acceptance, this is equivalent to displacing the IP along the beam axis by about 1 mm. The gross-precise method renders this effect negligible.

The Vertex Detector along with the Central Drift Chamber provide excellent resolution of the position and spread of the interaction point. Since the luminosity monitors are mounted on the final focus triplet array while the Central Drift Chamber and Vertex Detector are mounted from the SLD solenoid, there is also a relative misalignment between these systems.

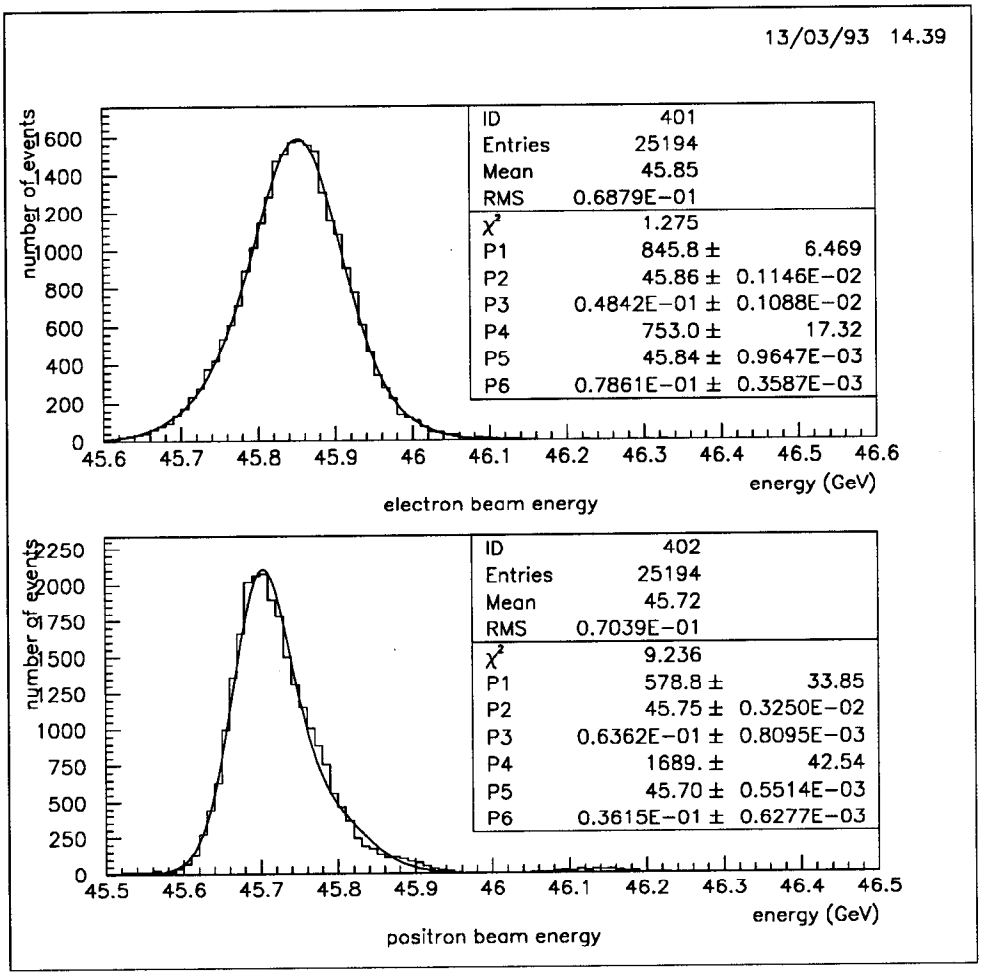

Figure 6.5: Beam energy distributions for Bhabha events.

Figure 6.6 shows the x and y spatial coordinates of the interaction point, as measured by the Vertex Detector. The variation of the interaction point in x is less than 300 μm. In y, the variation is less than 100 μm for the entire run. This means that the variation in the $x-y$ plane was less than 320 μm. Figure 6.13 shows the error on the luminosity as a function of beam position in the transverse plane. This translates into an error of less than 0.01% if the initial alignment is perfect, and an error of less than 0.03% if the absolute position of the IP is off center by 1.0 mm. The variation in z of the IP, as well as the $\sim$0.5 mm beam size in z are negligible effects on the luminosity measurement. The exception, of course, is when the IP shifts by 5.3 cm.

The absolute position of the interaction point will be handled in the discussion of alignment, since the two topics are inextricably linked.

Any nonzero beam crossing angle is equivalent to a displacement of the opposing detector. The upper limit on each beam crossing angle is 100 μrad [76], which corresponds to a displacement of 100 μm for each LMSAT module. For a perfectly aligned system, this would add an error of less than 0.007%. If the absolute position of the IP is off by 1.0 mm, the error from the crossing angle is less than 0.06%.

The contributions to the systematic error from the beam parameters can be summarized as follows: 0.08% from the absolute calibration of the WISRD, 0.06% from the asymmetry in the positron energy distribution, 0.03% from the uncertainty of the interaction point location, and 0.06% from the maximum beam crossing angle. The total systematic error from the beam parameters is 0.12%.

6.6.4 Monte Carlo

Three sources of systematic error arise from the Monte Carlo generation of events and cross section calculation: 1) the statistical error on the number of events which are generated, simulated and pass the cuts, 2) the "technical precision" or numerical precision of the generators, and 3) the physics which is not included in the Monte Carlo calculation.

For the different blocks, different numbers of Monte Carlo events pass the cuts after simulation. To be conservative and for simplicity, we use the smallest number of events to pass the cuts of any block as the systematic error due to Monte Carlo statistics for the entire run. The error due to 41953 Monte Carlo events is 0.50%.

A detailed comparison of the Berends-Kleiss-Hollik and Jadach-Ward generators has been undertaken elsewhere. Since the two generators can be made to calculate the cross section to the same order, comparison of the two relatively independent generators yields the "technical precision." The two programs are found to agree to within 0.1% [77].

Higher order physics effects which are not calculated completely or not present in the generators include terms proportional to $(\frac{\alpha}{\pi})^2 \times (ln(\frac{t}{m_e^2}))^2$ (where the typical momentum transfer squared t $\sim$4 GeV^2), vacuum polarization effects, and production

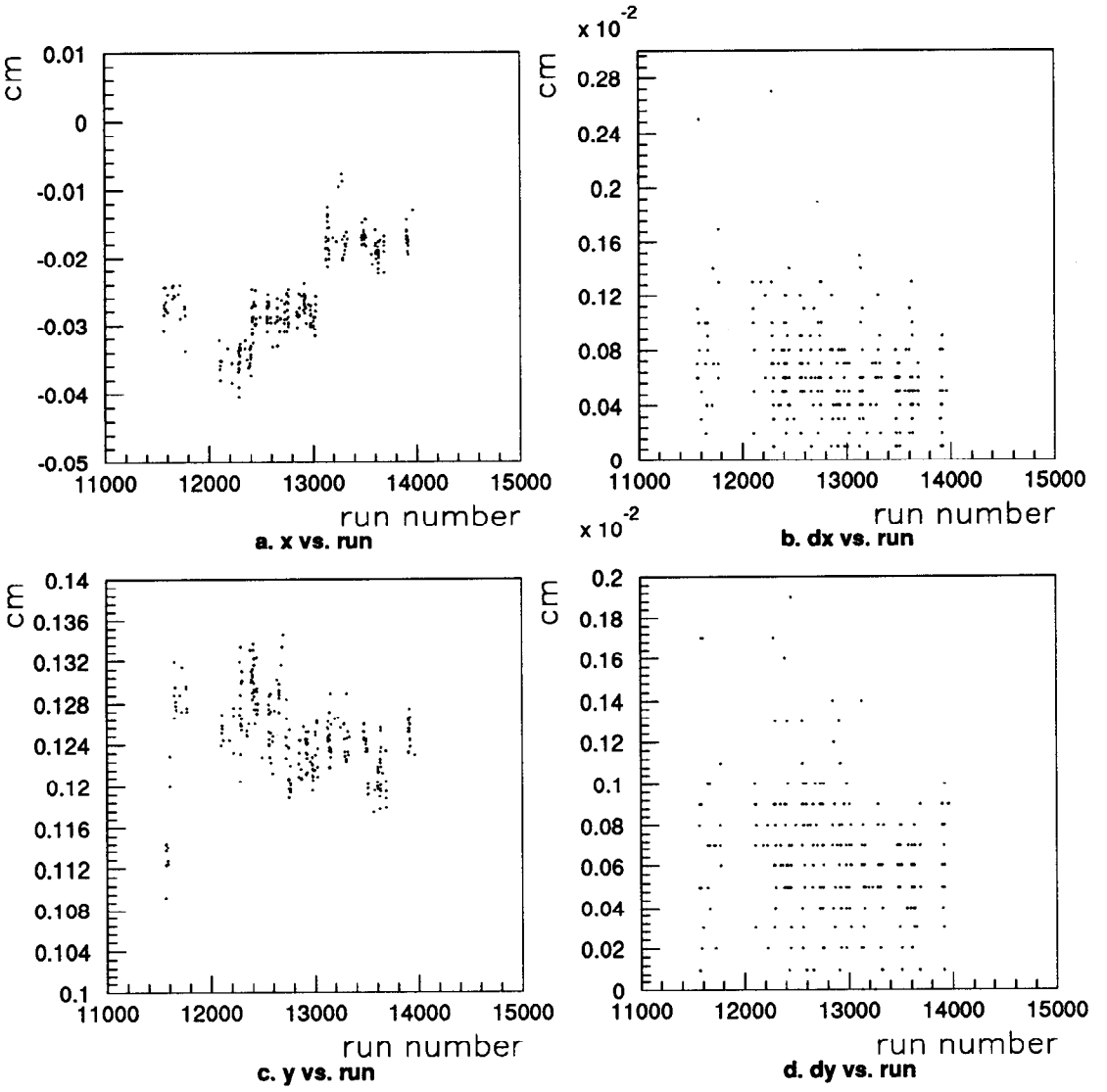

Figure 6.6: Interaction point location as a function of run number. The IP location is measured by the SLD CCD Vertex detector along with the Central Drift Chamber.

of light fermion pairs from radiated photons. Others have estimated these effects to be 0.5% or less [77, 78, 79, 80, 81].

The contributions to the systematic error from the Monte Carlo can be summarized as follows: 0.50% from the Monte Carlo statistics, 0.10% from the technical precision of the generators, and 0.5% due to theoretical uncertainty. The total systematic error from the Monte Carlo is 0.71%.

6.6.5 Simulation

The accuracy of the GEANT/GFLASH Monte Carlo can be estimated by comparison of data and Monte Carlo, as well as by variation of the simulation parameters.

The cluster energy resolution is dominated by the transverse shower size and not sampling fluctuations. For example, the cluster energy resolution for 46 GeV electrons from Monte Carlo is $\frac{44\%}{\sqrt{E}}$. While 90% of the incident energy is collected in a cluster on average, the fluctuation on this number is much greater than the intrinsic resolution due to sampling fluctuations.

The shower width, and fluctuations on that width also affect the position resolution. Since the cuts only rely on energy depositions within a specific 3x3 tower array of the maximum tower, energy lost beyond this array is not included in the cluster energy.

One effect which warrants specific study is the modeling of energy leakage out of the active area. This might affect the acceptance in two ways. First, there is a charge collection inefficiency in the vertical plane, where the two module halves meet. This can be seen by comparing the cluster energy as a function of azimuthal angle for data (figure 6.7) with Monte Carlo (figure 6.8). Also, inefficiency due to dead towers may be seen in Figures 6.7 and 6.8. The favorable comparison between data and Monte Carlo demonstrates that these effects are indeed well modeled.

Secondly, the amount of charge collected for Bhabhas which shower near the inner edge of the acceptance is degraded due to energy leakage back into the beam pipe. This may be seen graphically in Figures 6.9 and 6.10, where cluster energy is plotted as a function of polar angle for data and Monte Carlo. Moving toward smaller θ, less charge is collected. This will not have any effect on the classification of event type, because the events are categorized only by the location of the most energetic tower. It will, however, lead to an inefficiency in the trigger and energy cuts.

To verify that the simulation is handling both of these effects properly, modified gross-precise regions can be defined. For example, by shrinking the precise fiducial region by an additional bin, we move the acceptance away from the area of interest. The change in acceptance for data and Monte Carlo are then compared. Likewise, a precise region can be defined which excludes the towers nearest the vertical gap in phi. Again, by comparing the change in acceptance in the Monte Carlo to the change in acceptance in the data, we may estimate the integrity of the simulation.

This maximum discrepancy between data and Monte Carlo for any of these modified fiducial regions is 0.43%.

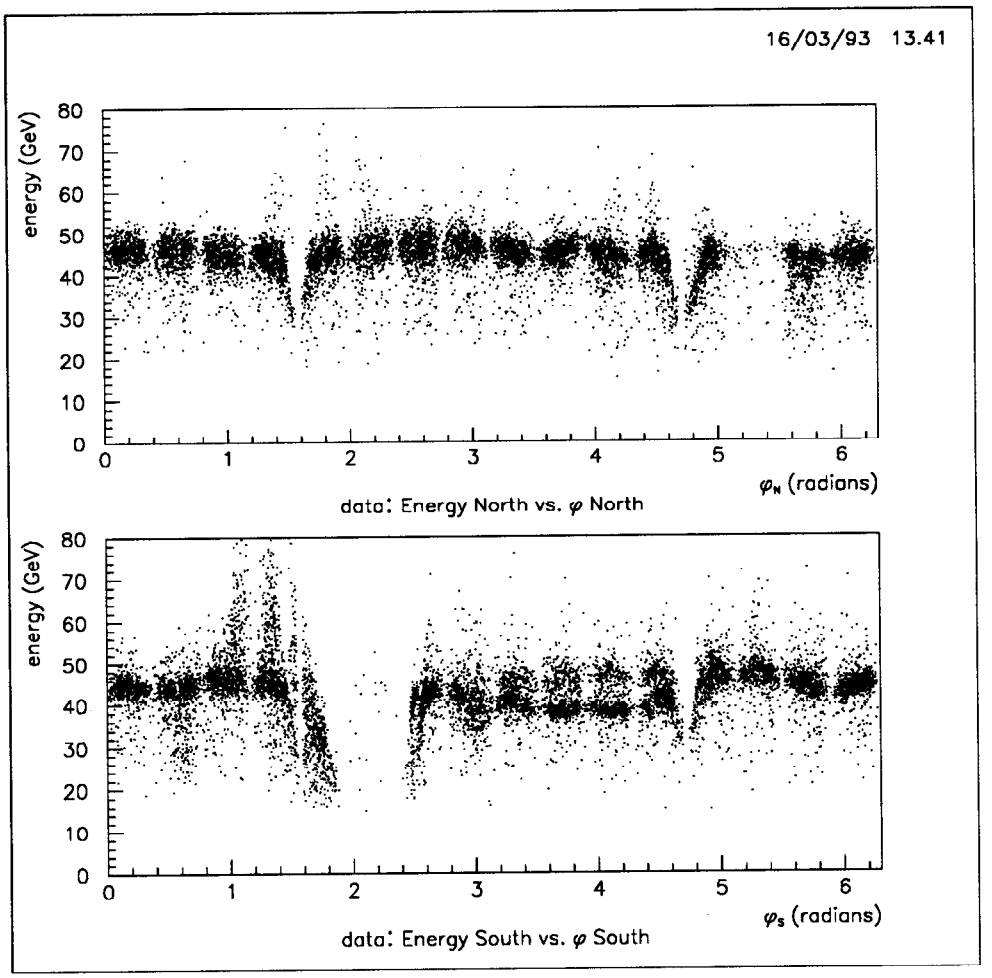

Figure 6.7: Energy vs. azimuthal angle for data. Features such as dead towers and the vertical gap between the two modules are apparent.

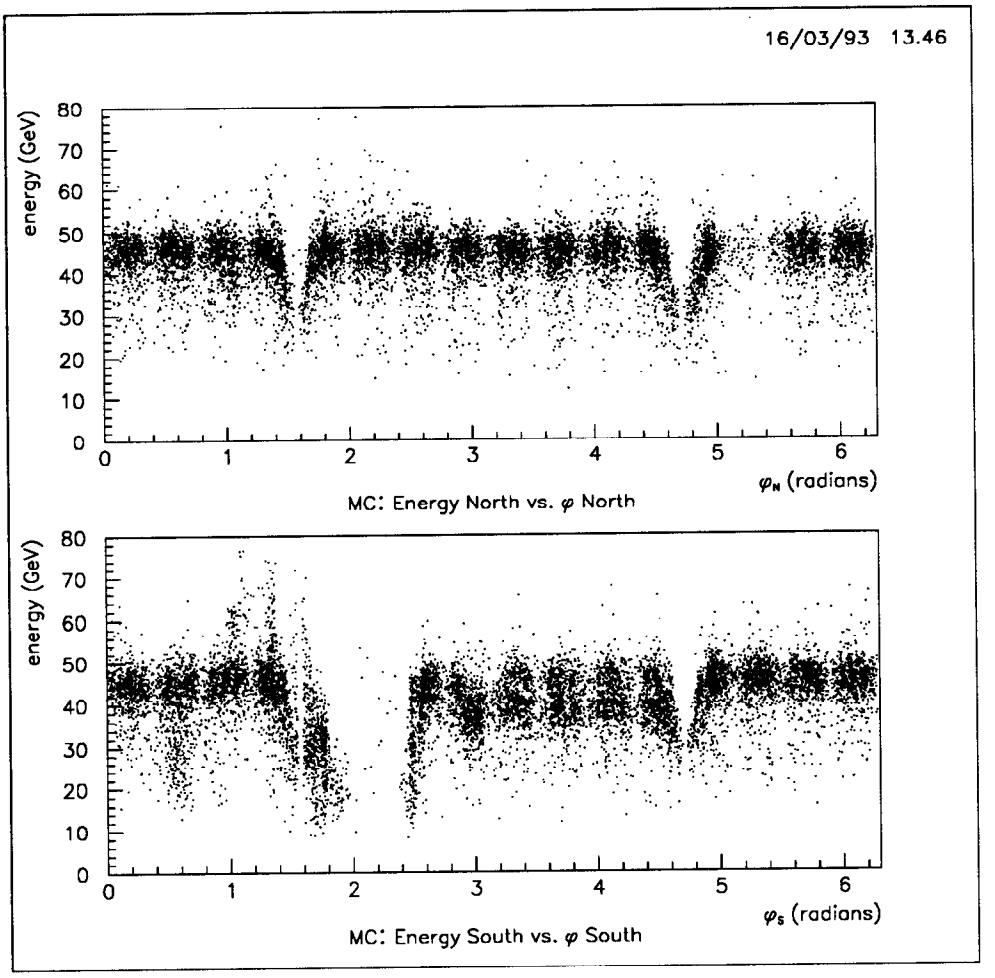

Figure 6.8: Energy vs. azimuthal angle for Monte Carlo. Features visible in Figure 6.7 are also see here, indicating that they are well modeled.

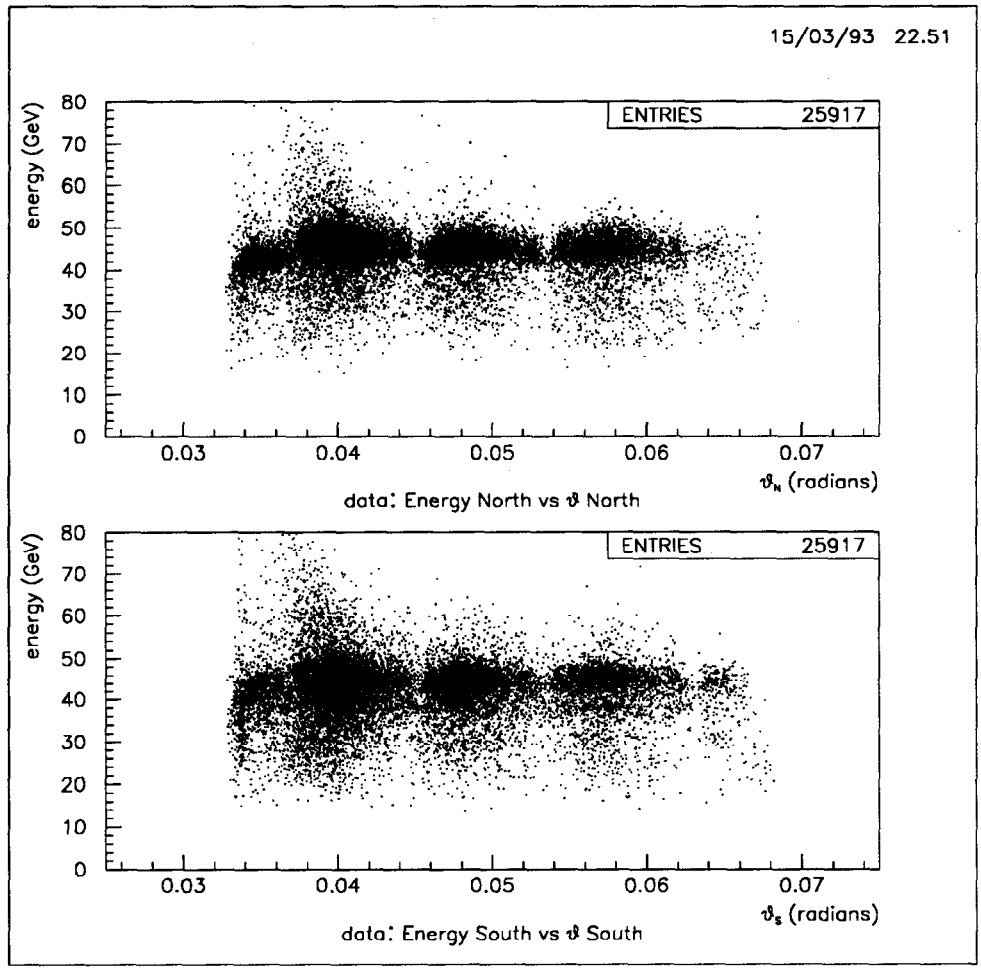

Figure 6.9: Energy vs. polar angle (data). Less energy is collected for showers into the ring of silicon nearest to the beam pipe. This is because energy leaking back into the beam pipe is not recovered.

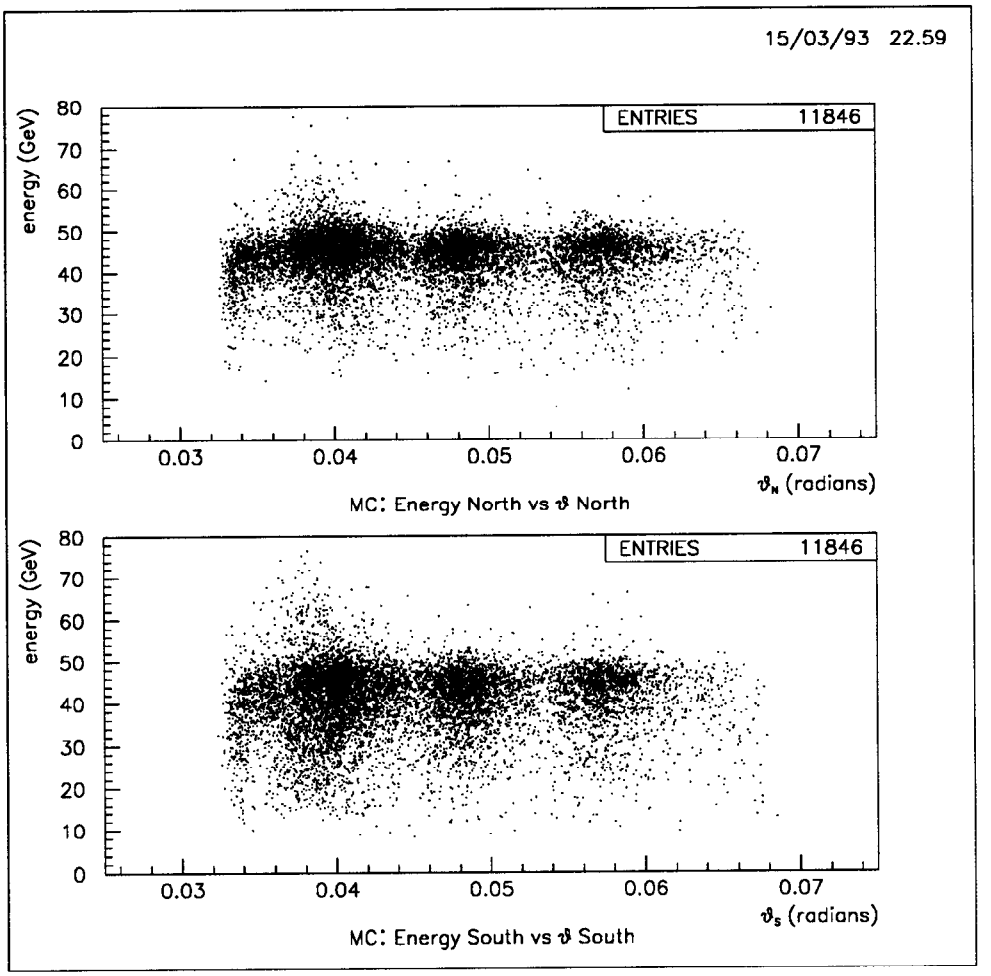

Figure 6.10: Energy vs. polar angle (Monte Carlo). The agreement with Figure 6.9 demonstrates that the leakage is well modeled.

Some studies of relative luminosity changes due to small displacements have made use of four-vector information at the generator level. This is a necessity due to the high statistics required to map out the error as a function of various alignment configurations.

Electrons and photons which strike the snout are discarded in the generator-level simulation. EGS studies previously have shown that less than 2% of 50 GeV electrons striking the snout may still form a good cluster in the LMSAT. The effect of running the simulation with no snout is 0.20% different than the result seen when the snout is included. Therefore, we estimate the upper limit of the error due to snout modeling to be 2% of the 0.20%, which is 0.004%.

The pseudo-projective nature of the towers is not modeled in the generator-level simulation. This could effect events very near the edge of the inner acceptance. For a transverse displacement of 1 mm, the shower axis will be off by 100 μm at a depth of 10 cm into the calorimeter (although incident at the proper location of the LMSAT). Most of the shower energy has already been lost at this depth. The maximum error in the simulation would occur if all events within 100 μm of the cut were classified incorrectly. When convoluted with the position resolution of 300 μm at the tower boundary, there is a 26% probability that an event which falls within this region will be classified incorrectly. This leads to an error of 0.19% in the generator-level simulation due to incomplete modeling of the pseudo-projective towers.

The contributions to the systematic error from the simulation can be summarized as follows: 0.43% from the largest discrepancy between the calculated luminosity and that which is derived from modified geometrical acceptance, 0.04% from incomplete modeling of the snout in the generator-level simulation and 0.19% from incomplete modeling of the pseudo-projective nature of the towers in the generator-level simulation. The total systematic error due to the simulation is 0.47%.

6.6.6 Theta Cut

As discussed in Section 6.3, the gross-precise method serves to greatly reduce the sensitivity of the luminosity measurement to misalignment. The measured luminosity does not need to be corrected for small displacements. The magnitude of any misalignment must be estimated in order to calculate the systematic error due to the cut on polar angle.

The pad to pad alignment of the towers is accurate to 200 μm. This is dominated by the accuracy of the silicon mount upon the G10 board, which is accurate to 150 μm. The next largest effect is the accuracy of the tungsten plates, which not only serve as a radiator structure, but also as the device on which the detectors are directly mounted.

The position resolution at the cut boundary is 300 μm. This was determined using EGS as well as test beam data [56]. Figure 6.11 shows the distribution of events in polar angle. The position is calculated by energy-weighted-mean and gives too much weight to the central tower. As discussed in Section 6.2, it is not necessary

to correct for this effect, since the theta cut is placed at a tower boundary where the resolution is the best. Any correction to the theta calculation will not push any events across a tower boundary. The theta cut is therefore unaffected by this method of position calculation.

The location of the interaction point with respect to both the Central Drift Chamber and the Vertex Detector was measured to be 1 mm high during unpolarized running. Due to this, the R20 module was moved up by 1 mm at the beginning of the polarized run. From that point onward, the beam was found to be well-centered within the Vertex Detector. Since the luminosity monitors are mounted on the triplets, they did not undergo such a move. Initial surveys indicated that the R20 and triplets were well aligned. This indicates that the beam was actually 1 mm high relative to the triplets, too.

The strongest indication of the alignment comes from the shadow cast upon the luminosity monitor by the Medium Angle Silicon Calorimeter (MASC). Figure 6.12 shows the distribution of events with the maximum tower energy in the fifth ring of towers (counting out from the beamline). For perfect alignment, approximately 40% of the tower has an unobstructed view of the interaction point. If the triplet is misaligned relative to the R20 module and/or the interaction point, the shadow cast by the MASC will no longer be a constant function of phi. The structure shown in Figure 6.12 shows a large excess of events in the upper hemisphere of both modules. This is consistent with the IP being 1 mm too high or the triplets being 1 mm too low.

The position of the triplets is very stable over time, therefore, we expect no drift in the location of the detectors during running. The SLC beam based alignment program is run every time the SLD doors are open, to realign the triplets.

For the alignment, then, the displacement of the interaction point is taken to be up 1.0 mm in the vertical plane. The uncertainty on location of the modules is then conservatively taken to be 0.5 mm. The error on the luminosity from the IP displacement is 0.08%. The effect of the uncertainty in x is negligible since the modules and beam are well aligned in that direction. The effect of a displacement in y of 0.5 mm would lead to an error on the luminosity of 0.06%. Errors from individual detector alignments come into the systematic error once per side, while the IP location enters the systematic only once.

The other potential effect of alignment is the distance between the North and South detectors. Figure 6.13 shows how the luminosity changes as a function of misalignment in z. While the effect of the IP being displaced in z is negligible (out to several cm) the distance between detectors is not. This can be estimated by using survey information from the triplets. The triplets were originally measured to be 1.8 mm further apart than the design separation. However, the field produced by the SLD solenoid was found to pull both triplets toward the IP. The North moves in 2 mm; the South moves in 1 mm. This means that the triplets are actually 1.2 mm closer together than design when the field is on. Since the luminosity monitors mount

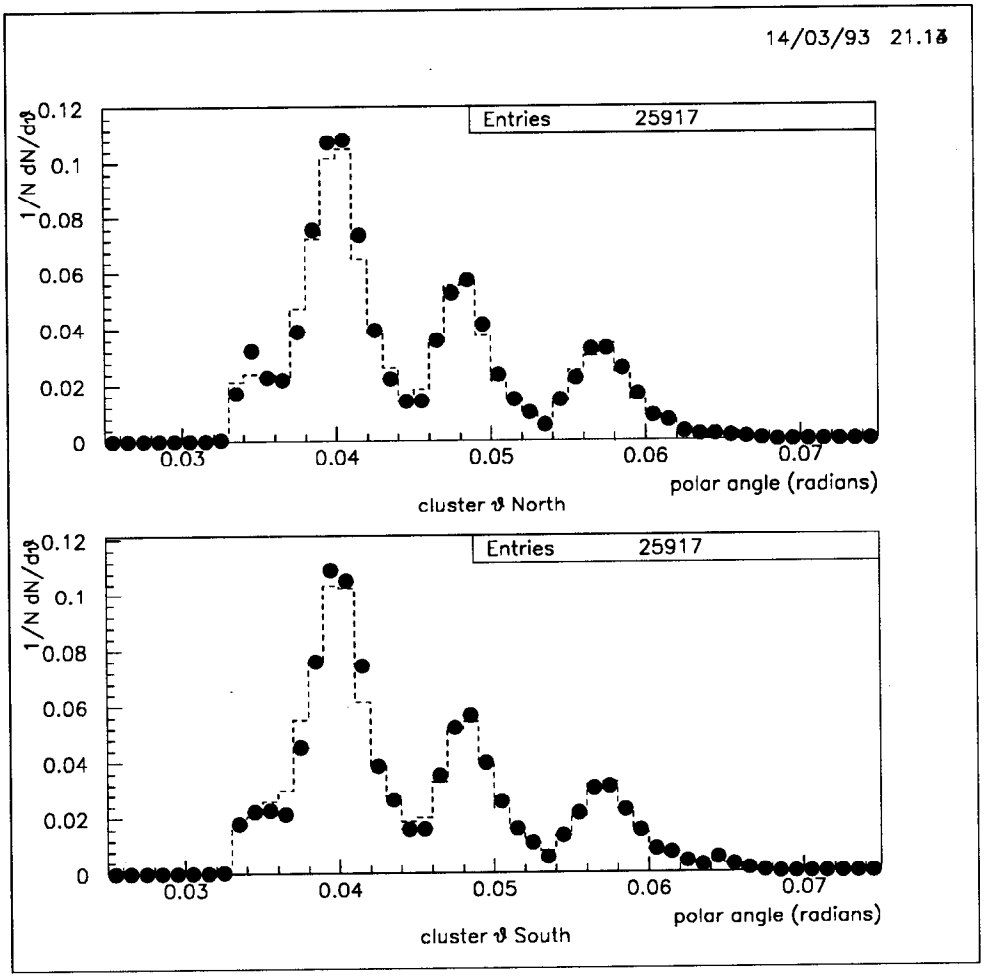

Figure 6.11: Polar angle distribution as calculated by energy weighted mean. The points are data, the dashed line is Monte Carlo. Since the showers are non-gaussian in the transverse plane, the central tower is given too much weight in the calculation. While it is possible to correct for this effect, it is not necessary. No shower position will be corrected across a tower boundary. The cut is placed at the tower boundary because that is where the best resolution is achieved. Therefore, correcting the theta distribution will not change the number of accepted events.

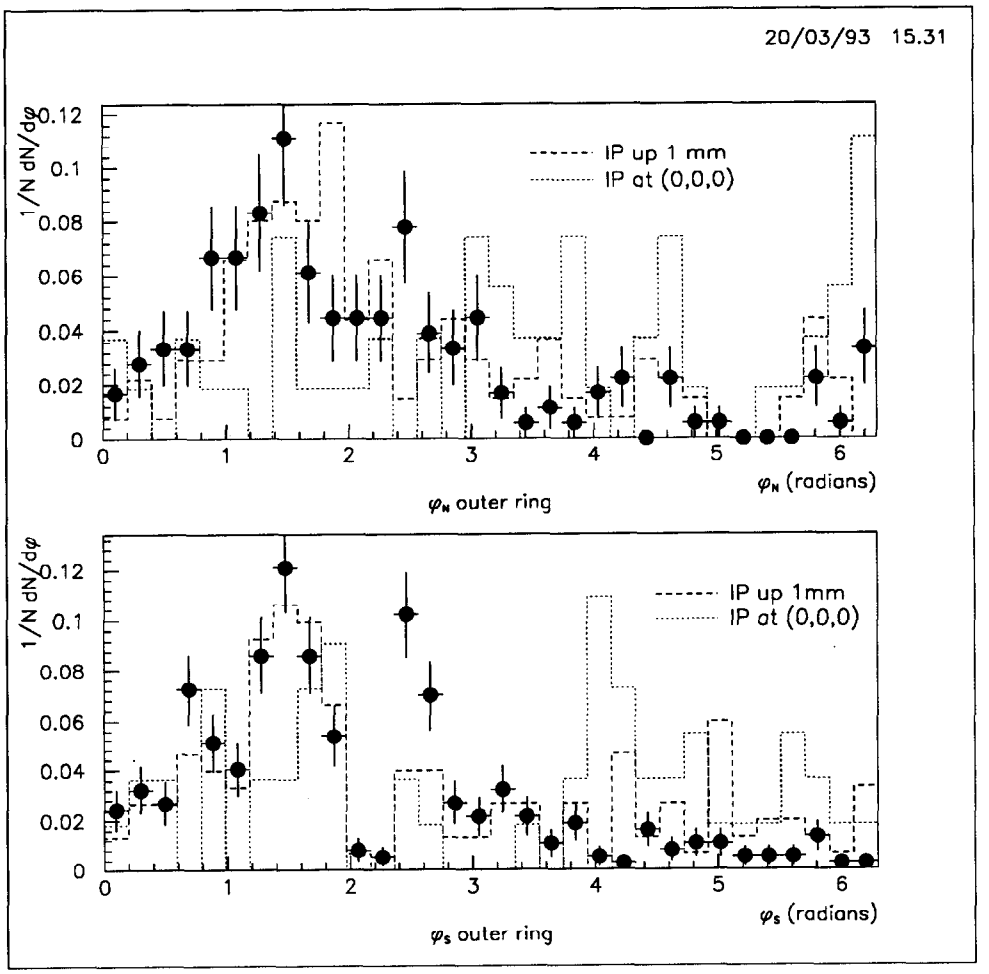

Figure 6.12: Phi distribution for Bhabha clusters in the North (a) and South (b) where the main tower of the cluster resides in the fifth tower (counting away from the beamline). This ring of towers is partially occluded by the MASC. The points are data. Monte Carlo is shown with perfect alignment and the interaction point 1 mm high.

directly onto the ends of the triplets, only machine tolerances are added to the errors of the triplet survey, which are very small. Since the deviation from the design separation of the luminosity monitors is measured to be less than 2 mm, we conservatively take an error on this distance to be 3 mm. From figure 6.13, this leads to an error in the luminosity measurement of 0.30% [82].

The contributions to the systematic error from the theta cut can be summarized as follows: 0.08% from the absolute offset of the interaction point, $0.06\% \times \sqrt{2}$ due to module misalignment, and 0.30% due to the absolute distance between luminosity modules along the beam line. The total systematic error due to the theta cut is 0.32%.

6.6.7 Phi Cut

By plotting $\pi - (\phi_N - \phi_S)$ by octant, it can be seen that there is no systematic shift away from zero, which would be caused by a relative rotation of the two modules. If the two halves of each luminosity monitor were sagging, this would also be apparent in these plots.

The cut on δ_ϕ ($\delta_\phi = \phi_N - \phi_S$, equation 6.5) is very conservative and has little effect on the luminosity. Figure 6.14 shows the collinearity for both Monte Carlo and data. If the cut is turned off altogether, the change in luminosity is 0.46%. Beyond the cut value of 0.5 radians, the distribution is relatively flat, caused by radiative events. A variation of the δ_ϕ cut by 80% (= 22.5°, or 1 wide bin width) leads to a systematic error of 0.07%.

6.6.8 Systematic Error Summary

Table 6.5 shows the systematic error by type. The total systematic error on the luminosity measurement is 1.01%. If the error due to theoretical uncertainty is excluded, the experimental systematic error is 0.88%.

6.7 Systematic Error Comparison

With a systematic error of 1.01% on the 1992 luminosity determination, SLD compares favorably with the four LEP luminosity determinations. This is summarized in Table 6.6.

Two LEP experiments are currently pursuing ultra-high precision luminosity devices in order to push the invisible width measurement down to less than 1%. To do so, the error on the luminosity measurements must approach 0.1%. To achieve this, both OPAL and ALEPH have chosen to build silicon/tungsten luminosity monitors [83]. The main improvements over the SLD silicon/tungsten device are finer

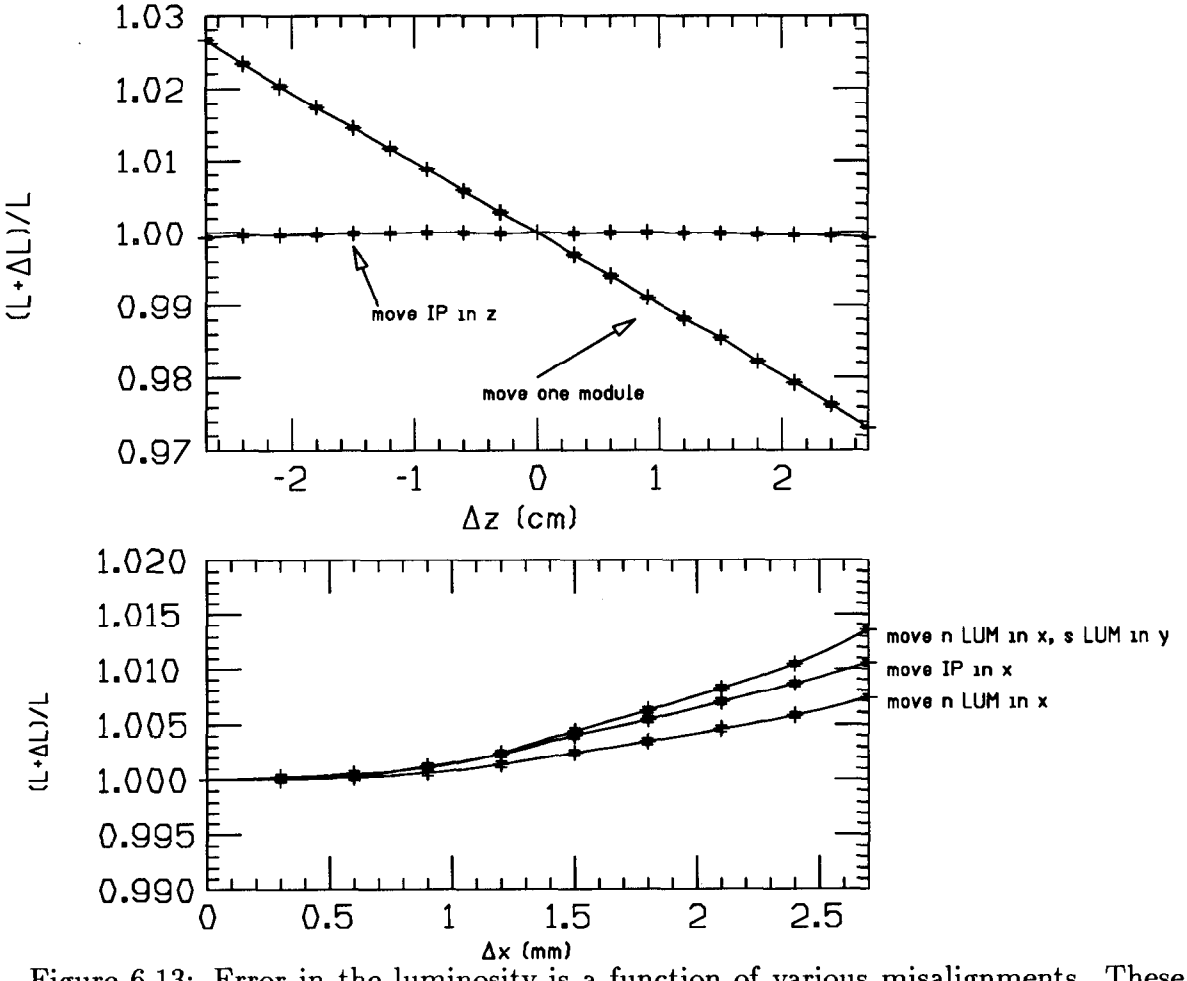

Figure 6.13: Error in the luminosity is a function of various misalignments. These errors are so small, it is not necessary to correct for any misalignments. For reference, if one only uses events within a defined fiducial region on both sides of the interaction point, the error is roughly 3% per mm of displacement.

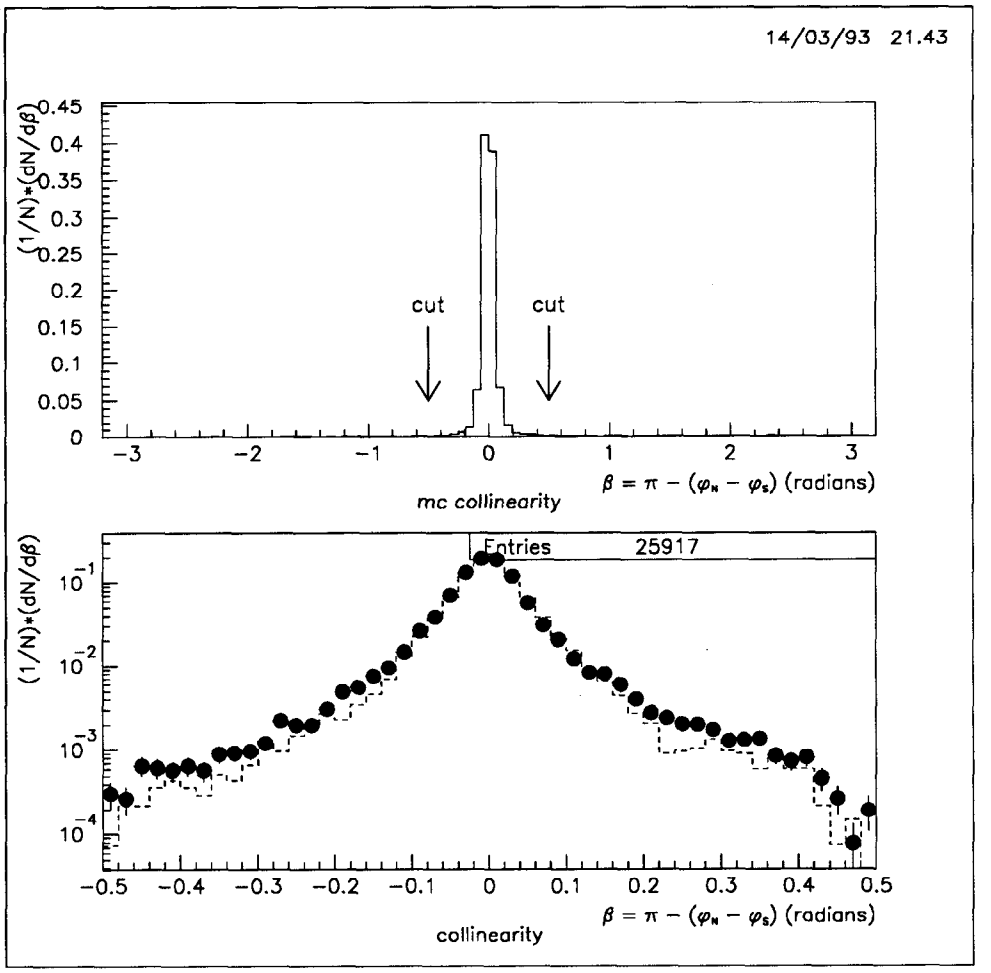

Figure 6.14: Collinearity distribution. The top plot shows Monte Carlo Bhabhas with no cut on $\phi_N - \phi_S$. The lower plot shows the data (as points) and Monte Carlo (dashed line) after the collinearity cut has been performed.

Table 6.5: Systematic errors in the luminosity determination.

systematic effect	error (%)	section
contamination	0.32	7.a
energy cuts	0.28	7.b
beam	0.12	7.c
Monte Carlo	0.51	7.d
simulation	0.47	7.e
θ cut	0.32	7.f
ϕ cut	0.07	7.g
total experimental	0.88	
theoretical uncertainty	0.5	7.d
total systematic error	1.01	

segmentation of the silicon, readout of every silicon pad independently, and very precise ($\sim 20\mu$m) silicon chip alignment. The SLD luminosity monitor reads out 640 channels, the OPAL device reads out roughly 40,000 channels.

6.8 1993 Luminosity

For the 1993 run, 110,226 precise events and 18,583 gross events were tagged using the same method described in this chapter. The preliminary cross section for the 1993 run is $\sigma_{eff} = 67.49$ nb, yielding a luminosity of $\mathcal{L} = 1770.9 \pm 5.1$ (stat)± 17.7 (sys) nb^{-1} [61]. The luminosity accumulated after the polarized source wavelength was increased to 865 nm (see Section 4.1.1) was $\mathcal{L} = 1541.6 \pm 4.6$ (stat) ± 15.4 (sys) nb^{-1}.

Since the systematic uncertainties cancel for the luminosity asymmetry, the fiducial restriction used for the absolute luminosity determination is not used in the calculation of the left-right luminosity asymmetry measurement for the 1993 run. Bhabha

Table 6.6: Comparison of systematic errors in the luminosity determination.

experiment	systematic error (%)	reference
ALEPH	0.7	[77]
DELPHI	0.9	[78]
L3	0.9	[79]
OPAL	0.67	[80]
SLD	1.0	-

events tagged anywhere within the luminosity detectors are included in this measurement. Improved beam conditions and hardware performance made this analysis improvement possible. For the 1993 run, 93,727 events were tagged with a left-handed electron beam and 94,319 events tagged with a right-handed electron beam, therefore $A_{LR}^{exp}(LUM) = (-3.2 \pm 2.3) \times 10^{-3}$, where the error is statistical only. The expected small angle Bhabha asymmetry is $\sim -2 \times 10^{-4} \mathcal{P}_e$ for a center of mass energy of 91.26 GeV.

6.9 Conclusion

Using the SLD silicon/tungsten luminosity monitor, we have measured the 1992 luminosity to be 35.51 $\pm$ 0.68 (stat) $\pm$ 0.36 (sys) nb^{-1} for unpolarized running and 385.37 $\pm$ 2.47 (stat) $\pm$ 3.89 (sys) nb^{-1} for polarized running. The systematic error of 1.01% is comprised of 0.88% experimental error and 0.5% theoretical uncertainty.

There are several aspects of this analysis which may be improved upon in the future. The dominant error in this measurement comes from the Monte Carlo. The Monte Carlo statistical error is simply a function of cpu time. There is also definitely room for improvement in the tuning of the GFLASH simulation. In addition, better understanding of the higher order contributions will lead to a smaller contribution from the theoretical uncertainty. With more data, it should be possible to measure and correct for any offsets in calorimeter alignment or interaction point location, therefore reducing the error on both the beam position and the theta cut.

With more data, the SLD luminosity systematic error should become less than 1%. This luminosity measurement demonstrates the ability of the SLD luminosity monitor to measure small angle Bhabha scattering with excellent precision.

CHAPTER VII

WIDE ANGLE BHABHA EVENT SELECTION

This chapter will describe the data processing and selection algorithm used to identify wide angle Bhabha events. The Monte Carlo simulation of the SLD detector will be described in the context of calculating the correction factors to be applied to the data due to selection inefficiency and contamination from other processes. Also presented in this chapter will be the center of mass energy and electron beam polarization for the 1993 SLD run.

The wide angle Bhabha selection algorithm makes use of the distinct topology of the e^+e^- final state. Events will be required to have two large clusters of electromagnetic energy which are nearly back-to-back in the detector. These clusters will be required to have deposited very little energy in the hadronic calorimeter, as well as very little energy beyond the two primary clusters. Figure 7.1 shows a typical Bhabha event. The top view is along the e^+e^- beam axis, the lower-right view is looking down on the detector from above and the lower-left view is looking at the detector from the side. This event shows to large energy clusters nearly back-to-back with virtually no energy elsewhere in the calorimeter. The strings of hits running nearly parallel to the beam line are muons produced by the SLC upstream collimation. Steps are taken to identify these patterns of hits from events and exclude them from the analysis.

7.1 Trigger

The trigger and data acquisition system for the LAC (see Section 4.2.3) evaluate data on every SLC beam crossing (120 Hz). The trigger performs several sets of energy sums and tower counts based on two thresholds, defined as the "low" and "high" thresholds. The high threshold requires the energy in a tower to be above the energy deposited by a minimum ionizing particle, while the low threshold is placed slightly above the typical electronics noise.

The conversion from ADC to energy for the LAC is 524 MeV/128 ADC ($\simeq 4$ MeV/ADC) in the EM sections and 1384 MeV/128 ADC in the HAD sections.[1] The

[1]The energy scale used here is the minimum ionizing energy scale, which means no e/μ or π/μ correction factor has been applied.

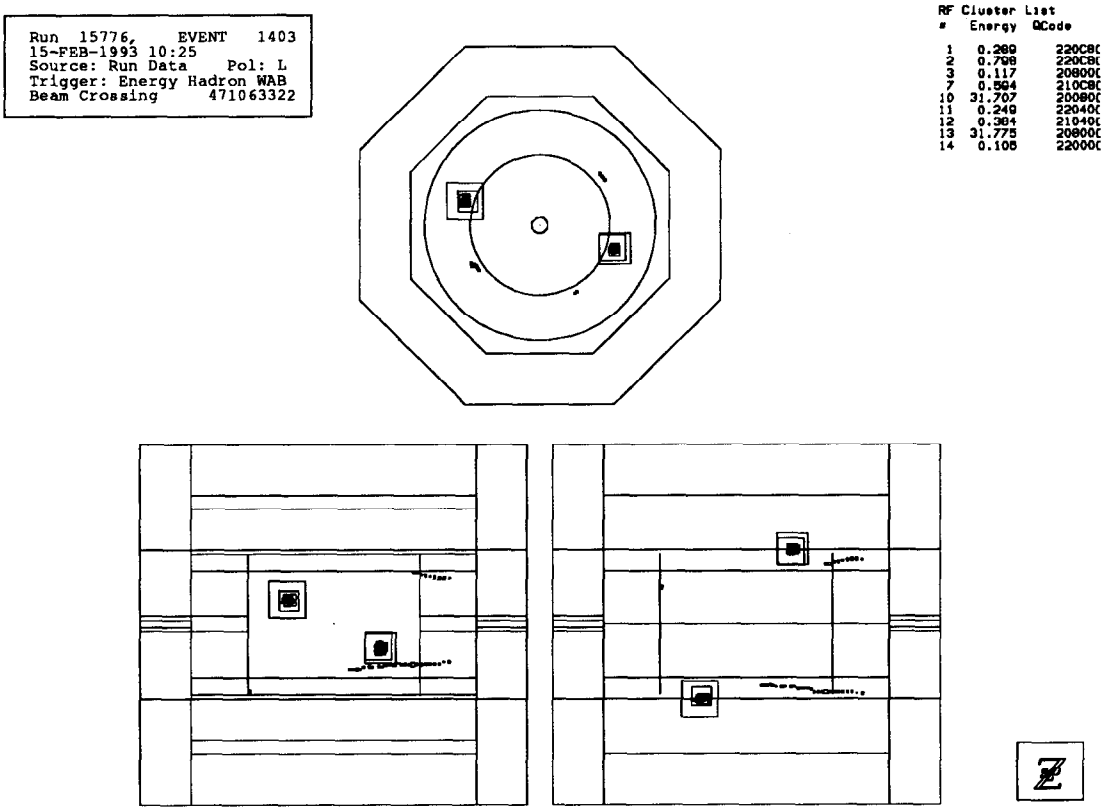

Figure 7.1: A typical wide angle Bhabha event. The top view is along the beam axis, the lower-left view is a side-view and the lower-right view is looking down upon the detector from above. The Bhabha produces two high energy electromagnetic clusters nearly back-to-back in the calorimeter. The strings of hits running nearly parallel to the beamline are muons produced by SLC upstream collimation. Steps are taken to remove these (see text).

low threshold is 8 ADC in the EM sections and 12 ADC in the HAD sections. The high threshold is 60 ADC in the EM and 120 ADC in the HAD. When a trigger is taken, data from towers above 2 ADC in EM1, 3 ADC in EM2 and 6 ADC in the HAD sections are written to tape [84].

The following sums are made in the trigger:

- ELO = the sum of the energy in all towers above the low threshold
- EHI = the sum of the energy in all towers above the high threshold
- NLO = the number of towers above the low threshold
- NEMHI = the number of towers in the EM section above the high threshold.

The trigger requirement is such that the sum of energy in towers above the high threshold be greater or equal to 8 GeV (EHI $\geq$ 8 GeV) for the 1992 run. This trigger was made more stringent for the 1993 run, as the requirement was increased to EHI $\geq$ 12 GeV. This trigger is very efficient for e^+e^- events, where virtually all of the energy is deposited into a few towers, which means that the low and high energy sums are nearly identical. It is also very robust against the muon background caused by upstream beam collimation in the SLC, as towers which only have a minimum ionizing signal will not contribute to the trigger energy sum. The trigger is vetoed if more than 1000 towers contribute to the low threshold sum (NLO $<$ 1000). This veto protects against particularly bad pulses.

7.2 PASS 1 Filter

Events which satisfy the trigger are written to tape. Before reconstruction, these events are subjected to the the PASS 1 filter, which greatly enriches the hadronic and e^+e^- sample. The PASS 1 filter is based exclusively on sums which are performed at the trigger level. The PASS 1 requirements are as follows:

- NEMHI $\geq$ 10 towers
- EHI $>$ 15 GeV
- ELO $<$ 140 GeV
- ELO $<$ $\frac{2}{3}$ EHI + 70 GeV

PASS 1 is effectively a tightening of the trigger. Events satisfying PASS 1 have localized energy deposition with at least some of that energy deposited in the electromagnetic section of the calorimeter. The PASS 1 requirement of EHI $>$ 15 GeV insures that the difference in the trigger level for the 1992 and 1993 runs does not

change the selection efficiency. Figure 7.2[2] shows the quantity EHI plotted against ELO. The number of towers contributing to the EHI sum is always less than or equal to the number of towers contributing to the ELO sum, making the region EHI > ELO forbidden. Events in the region centered at roughly 60 GeV on the ELO axis and 40 GeV on the EHI axis are primarily hadronic decays of the Z^0, while events with ELO > 60 GeV and EHI $\simeq$ ELO are the wide angle Bhabha events, where most of the energy is deposited in relatively few towers [85].

7.3 Reconstruction

Events which satisfy the PASS 1 filter are passed through the calorimeter reconstruction. The reconstruction forms "clusters" of localized energy based on the UCLUS algorithm [86]. The WIC PADs, Luminosity Monitor and the Medium Angle Silicon Calorimeter are not included in the reconstruction. Also, LAC towers below 7 ADC in the EM section and 9 ADC in the HAD section are excluded from clusters. The effect of this on the energy response is virtually nil, while drastically cutting the number of clusters in each event. These single-hit clusters arise from beam background and electronics noise.

The reconstruction also attempts to separate clusters if it appears the cluster was formed by more than one incident particle. This primarily affects the response in the jet environment of the hadronic events, as the algorithm tries to break-off hadronic and electromagnetic showers which partially overlap.

Cluster position is calculated as an energy weighted mean summed over all towers in the cluster. Each cluster is then defined by four energy values (one per layer), ϕ and $\cos\theta$.

Clusters are subjected to a pattern recognition routine which looks for strings of calorimeter hits which run approximately parallel to the beam line and deposit minimum ionizing energy into the liquid argon [87]. These clusters are flagged as muons produced by the tails of the beam hitting the SLC upstream collimation [88] (see Figure 7.1). The SLC muon background is the dominant form of background for the LAC. This is in sharp contrast with the dominant synchrotron radiation background seen in the Luminosity Monitor (Section 6.4). There is enough material between the beamline and the LAC to stop most of the low energy radiation coming from the final focusing of the beams. The only exception to this is the ring of LAC towers which surround the beamline. To model the effects of beam background, Monte Carlo events are "overlayed" on a set of luminosity weighted random triggers, which will be described in Section 7.5.1.

[2]There were 18393 PASS 1 events in 1992 and 63546 PASS 1 events in 1993. To make the plots legible and to demonstrate the trends, Figures 7.2 and 7.3 show a sample of 20,000 PASS 1 events from the 1993 run. The trends seen in the full sample are identical to those displayed in the figures.

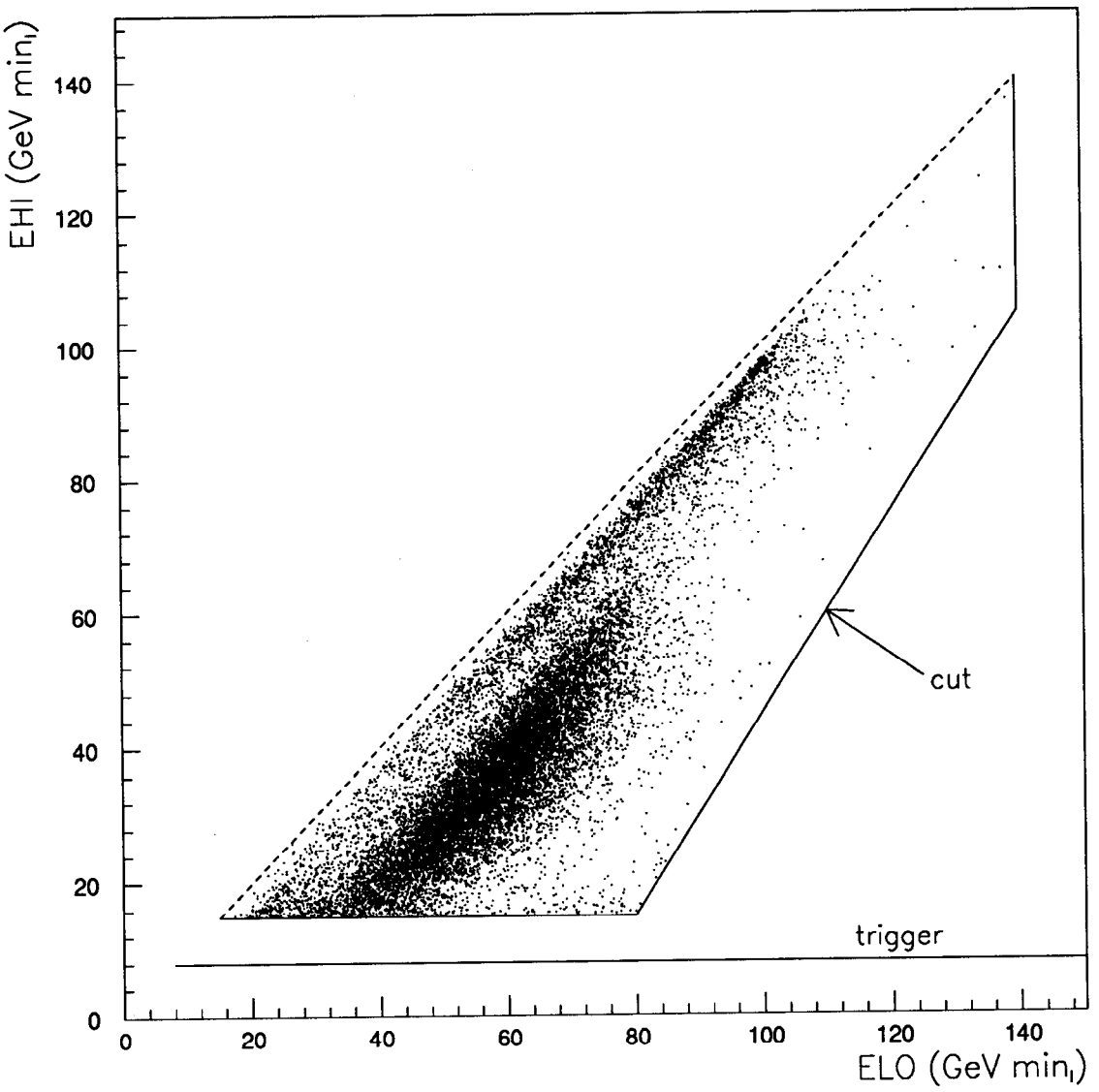

Figure 7.2: PASS 1 energy sums (EHI vs. ELO).

7.4 Selection

The $e^+e^- \rightarrow e^+e^-$ selection criteria make use of the low multiplicity and high energy deposition in the EM calorimeter expected from e^+e^- final states. In the limit of no radiation, an event will deposit the center of mass energy into two clusters in the calorimeter which will be back to back. In addition, virtually all of the energy will be deposited in the EM section of the LAC.

At the reconstruction stage, clusters are required to have the following properties:

- $E_{EM} > 0.0$ GeV
- $E_{clus} > 1.0$ GeV
- not flagged as an SLC μ.

Clusters failing any of these criteria are not included in the following analysis.

The imbalance (I) and total reconstructed energy (E_{tot}) are calculated:

$$E_{tot} = \sum_{i=1}^{N_{cl}} |\vec{k}|, \tag{7.1}$$

$$I = \frac{|\sum_{i=1}^{N_{cl}} \vec{k}|}{E_{tot}}. \tag{7.2}$$

where $\vec{k}$ may be thought of as a three-vector for a massless particle derived from the cluster quantities and N_{cl} is the number of clusters. E_{tot} is the total energy of the reconstructed event, while the imbalance (I) is a measure of how symmetric the energy is deposited. Events with uniform energy deposition will have low imbalance, while events with all of the energy deposited in one location will have an imbalance near unity. Also calculated at this time is the thrust

$$T = max\left(\frac{\sum_{i=1}^{N_{cl}} |\vec{k}_i \cdot \hat{n}|}{\sum_{i=1}^{N_{cl}} |\vec{k}_i|}\right), \tag{7.3}$$

where $\hat{n}$ is a unit vector chosen to maximize the numerator and defines the thrust axis. In the limit of no radiation, the thrust axis is parallel to the axis defined by the final state fermions.

Events are then required to have:

- $E_{tot} > 15$ GeV
- $I < 0.6$
- $N_{cl} < 9$.

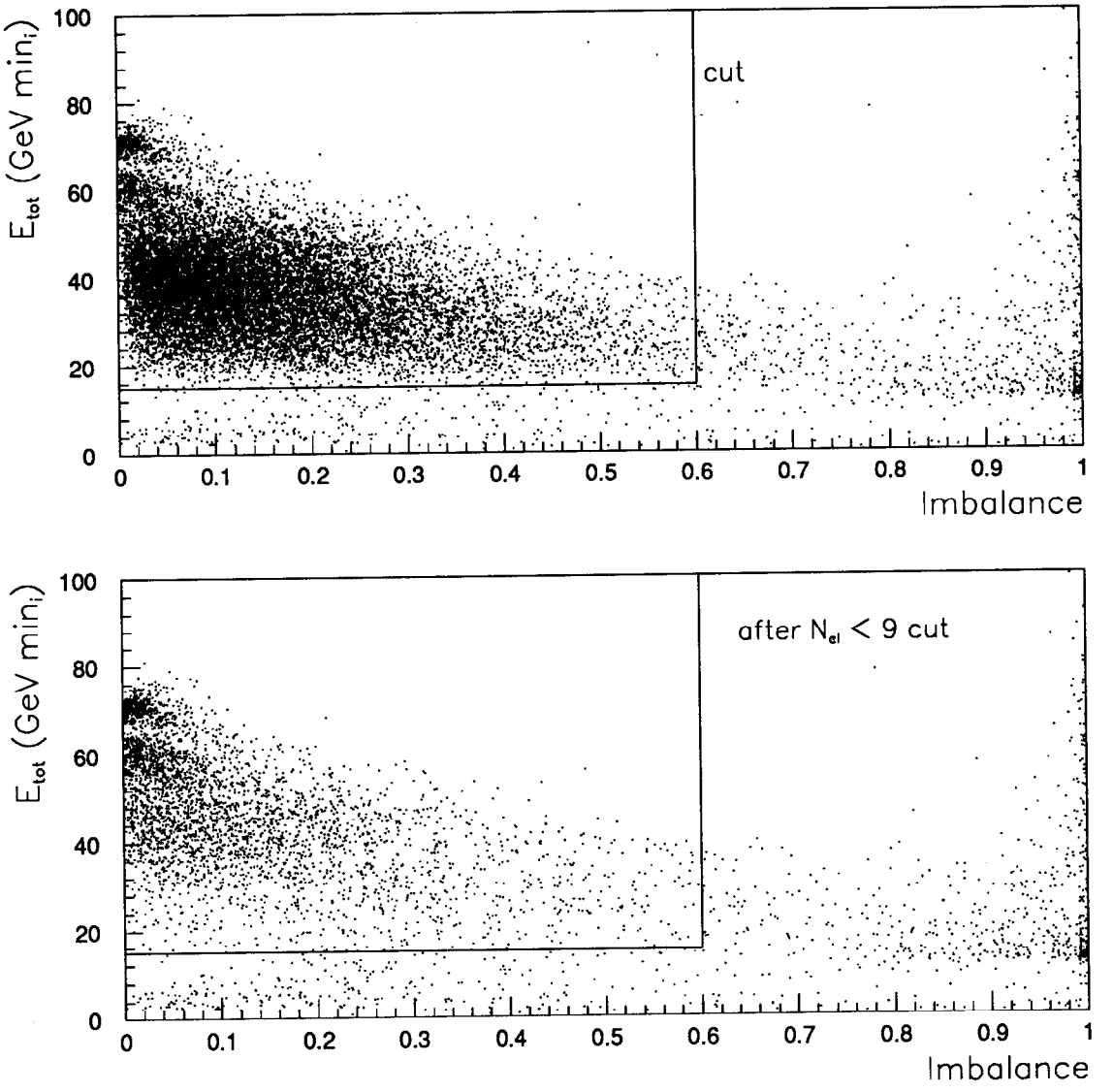

Figure 7.3: Reconstructed energy vs. imbalance. The top plot shows a sample of PASS1 events. The lower plot shows the same event sample subjected to the additional requirement that there be less than nine clusters within the event.

Figure 7.3 shows the energy vs. the imbalance before either of these cuts has been applied. Events with very high imbalance are beam-related background. The large grouping of events with low imbalance ($I < 0.3$) and E_{tot} near 40 GeV are hadronic Z^0 decays. The Bhabha events are seen at higher E_{tot} with an imbalance near zero. The lower figure shows the energy vs. the imbalance after the cluster requirement has been applied. The hadronic sample is greatly reduced, while the Bhabha sample is left unchanged. The combination of the energy E_{tot} and imbalance (I) cuts reduces the sample to e^+e^- final states, hadronic and τ decays of the Z^0, and $e^+e^- \rightarrow \gamma\gamma$ events.

Figure 7.4 shows the separation between low- and high-multiplicity events. The N_{cl} cut selects low multiplicity events, removing a large fraction of the hadronic decays. This may also be seen in the lower plot of Figure 7.3, which shows the energy versus the imbalance after the cluster cut is applied. The hadronic contribution is seen to be greatly reduced, while the Bhabha contribution remains unchanged.

The cuts which follow are designed to further reduce the hadronic and $Z^0 \rightarrow \tau^+\tau^-$ channels. The two largest energy clusters are selected from the event and tested to match the hypothesis of a high energy electromagnetic shower:

- $E_{EM}(1) > 10$ GeV , $E_{EM}(2) > 10$ GeV
- $E_{HAD1}(1) < 3$ GeV, $E_{HAD1}(2) < 3$ GeV
- $E_{HAD2}(1) < 0.5$ GeV, $E_{HAD2}(2) < 0.5$ GeV,

where E_{EM} is the cluster energy in EM1 + EM2 and $E_{HAD1}(E_{HAD2})$ is the cluster energy in HAD1(HAD2). The (1) and (2) denote that the two clusters evaluated are the two clusters with the largest total energy within the event.

Figure 7.5 shows the effect of cluster energy cuts for both clusters. Clearly, the requirement that the second most energetic cluster within the event have greater than 10 GeV in the electromagnetic portion of the cluster is the strictest cut. Virtually all of the inefficiency of this cut comes from the poor response in the endcap calorimeter. This may be see in the most energetic cluster, too. The peak near 36 GeV arises from Bhabha events in the barrel calorimeter, while the broad peak at lower energy comes from the Bhabha events into the endcap.

In place of the traditional cut on collinearity, a cut is placed on the longitudinal rapidity of the center of mass, which is defined as:

$$y = ln\sqrt{\frac{E+p_z}{E-p_z}} = ln\sqrt{\frac{sin\theta_+(1+cos\theta_-)+sin\theta_-(1+cos\theta_+)}{sin\theta_+(1-cos\theta_-)+sin\theta_-(1-cos\theta_+)}}. \qquad (7.4)$$

The rapidity is written in terms of the final state electron and positron scattering angles (θ_-, θ_+) in the laboratory frame. The cut placed on the rapidity is:

- $|y| < 0.3$.

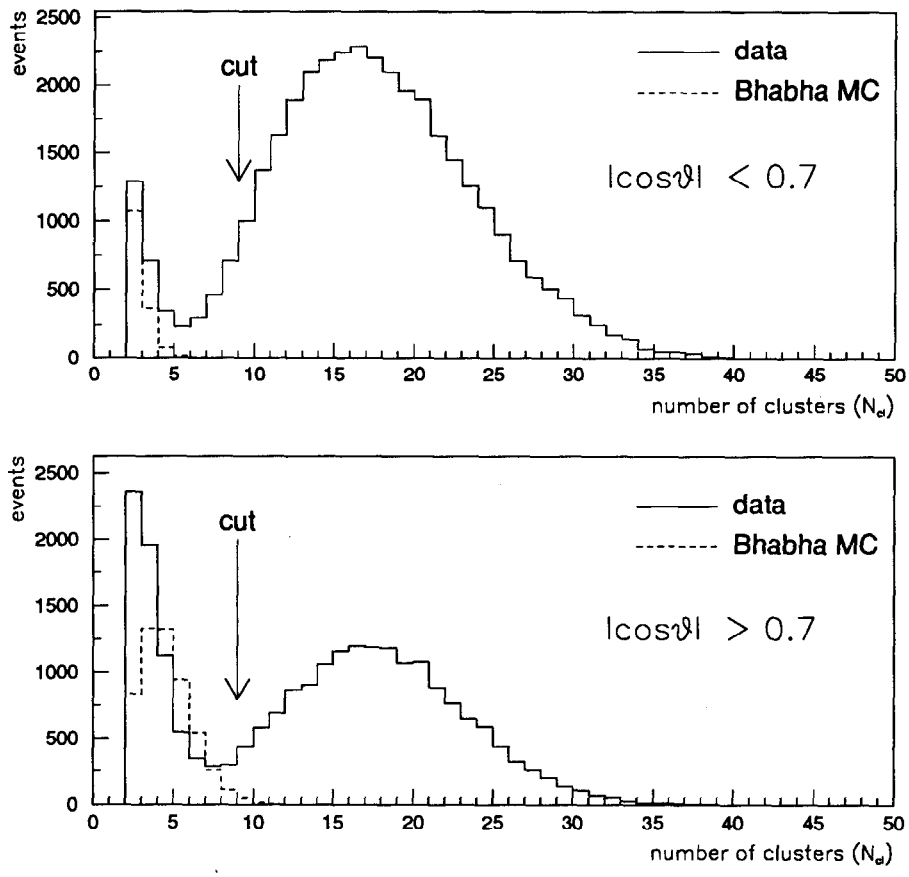

Figure 7.4: Number of reconstructed clusters after the energy and imbalance cuts have been applied. The top plot shows events with $|cos\theta_{thrust}| < 0.7$, the bottom plot shows events with $|cos\theta_{thrust}| > 0.7$. The peak at low cluster multiplicity comes primarily from Bhabha events. The dashed curve is Monte Carlo Bhabha events subjected to the same cuts.

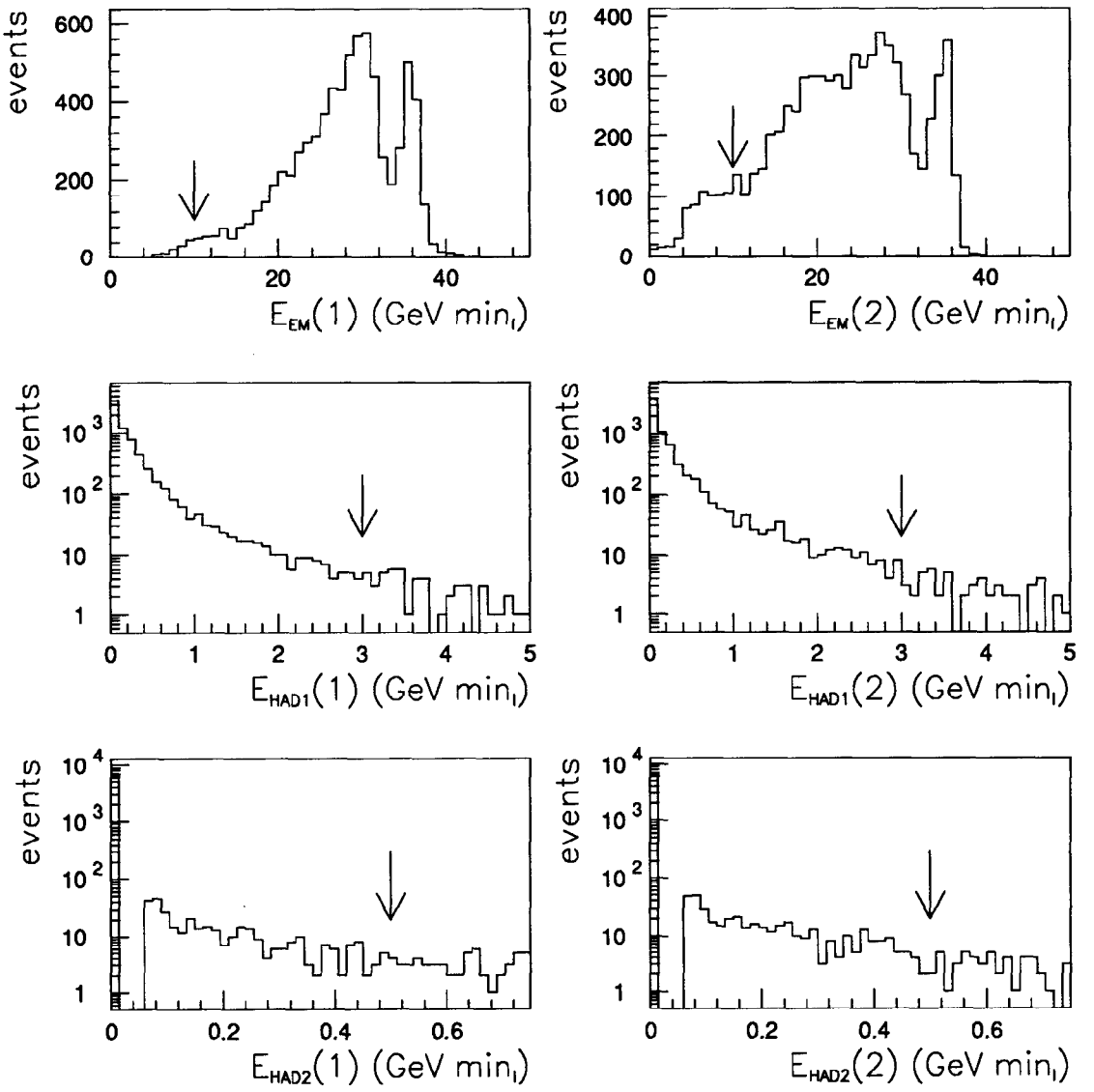

Figure 7.5: Cluster energy cuts by layer. Each of the three cluster energy quantities ($E_{EM}, E_{HAD1}, E_{HAD2}$) is plotted for both selected clusters. In each case, the cut pertaining to that quantity has NOT been applied. For example, $E_{EM}(1)$ and $E_{EM}(2)$ are both plotted with all cuts except the requirements on $E_{EM}(1)$ and $E_{EM}(2)$. The gap seen in the HAD2 energy plots arises from the readout threshold.

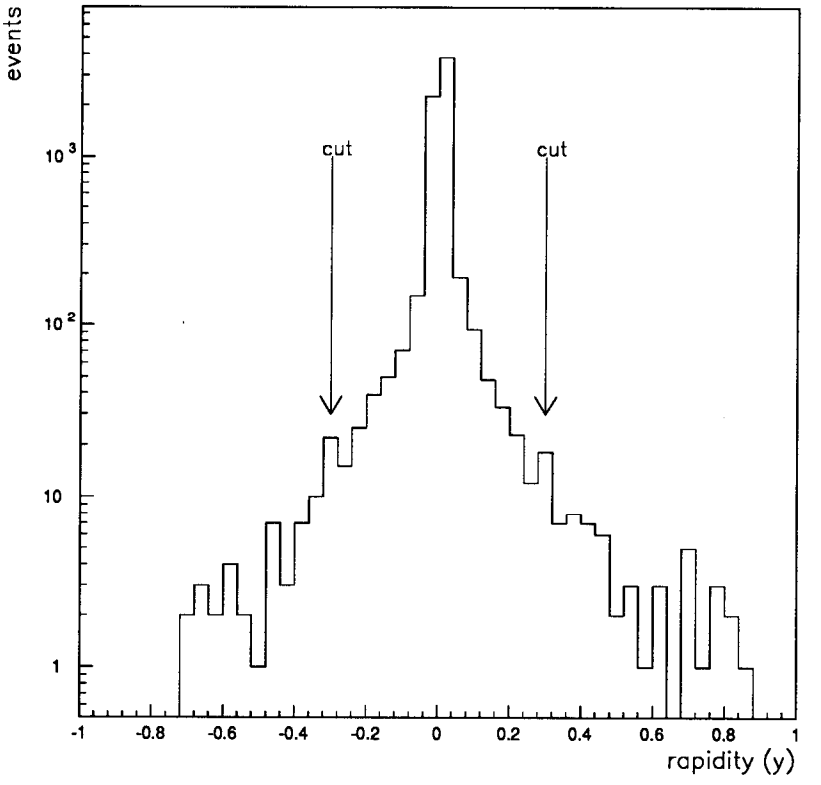

Figure 7.6: Rapidity cut. The distribution includes all cuts except the cut on the rapidity.

The longitudinal rapidity of the center of mass along is a measure of the amount of initial state radiation within the event. This may be thought of as an angle dependent collinearity cut, as it takes more radiation to change the collinearity by an amount $\delta\theta$ at small θ than it does at large θ. Figure 7.6 shows the effect of the rapidity cut.

The final selection criteria is chosen to reduce tau contamination at large angles and to put the barrel and endcap LAC response onto similar footing (see Section 7.5.1):

- for $cos\theta_{thrust} > 0.80$: no cut
- for $0.68 < cos\theta_{thrust} < 0.80$: $E_{clus}(1) + E_{clus}(2) > 168.3 - 166.7 cos\theta_{thrust}$
- for $cos\theta_{thrust} < 0.68$: $E_{clus}(1) + E_{clus}(2) > 55.$

where $E_{clus}(1) + E_{clus}(2)$ is the sum of the energy in the two most energetic clusters in the event. This cut is shown graphically in Figure 7.7.

The corrections to the cuts outlined in this section will be discussed in the following section. In general, it may be said that the selection criteria is very efficient for finding wide angle e^+e^- events while substantially reducing the background from other processes. Overall, the selection is about 87% efficient, with a 0.3% contamination from $Z^\circ \rightarrow \tau^+\tau^-$ events and about 1% contamination from $e^+e^- \rightarrow \gamma\gamma$ events.

7.5 Correction Factors

In fitting the e^+e^- distribution, it is necessary to know the "bin-to-bin" efficiency and contamination. These factors will be calculated from Monte Carlo simulation of the relevant physics processes and detector simulation. As a consequence, the overall efficiency factors are calculated as well. However, this information is only necessary when the fit to the wide angle e^+e^- distribution is constrained by the luminosity measurement provided by the small angle Bhabha process (see Chapter VI and Section 8.2.3).

7.5.1 Detector Simulation

Physics Monte Carlos simulate the processes of interest and pass the final state particles over to the simulation of the detector. The detector simulation is done with GEANT [67]. Electromagnetic and hadronic showers are simulated via the GFLASH algorithm [68].

Figure 7.8 shows the LAC response for events which have satisfied the PASS1 requirement and the reconstructed energy and imbalance cut. Several clear features may be seen. First, the distribution is flat and well behaved from 0.0 to 0.44 in $cos\theta$ and then from 0.48 to 0.65 in $cos\theta$. The degraded response seen at approximately 0.45 in $cos\theta$ is due to the washer, where the central and two end sections of the barrel

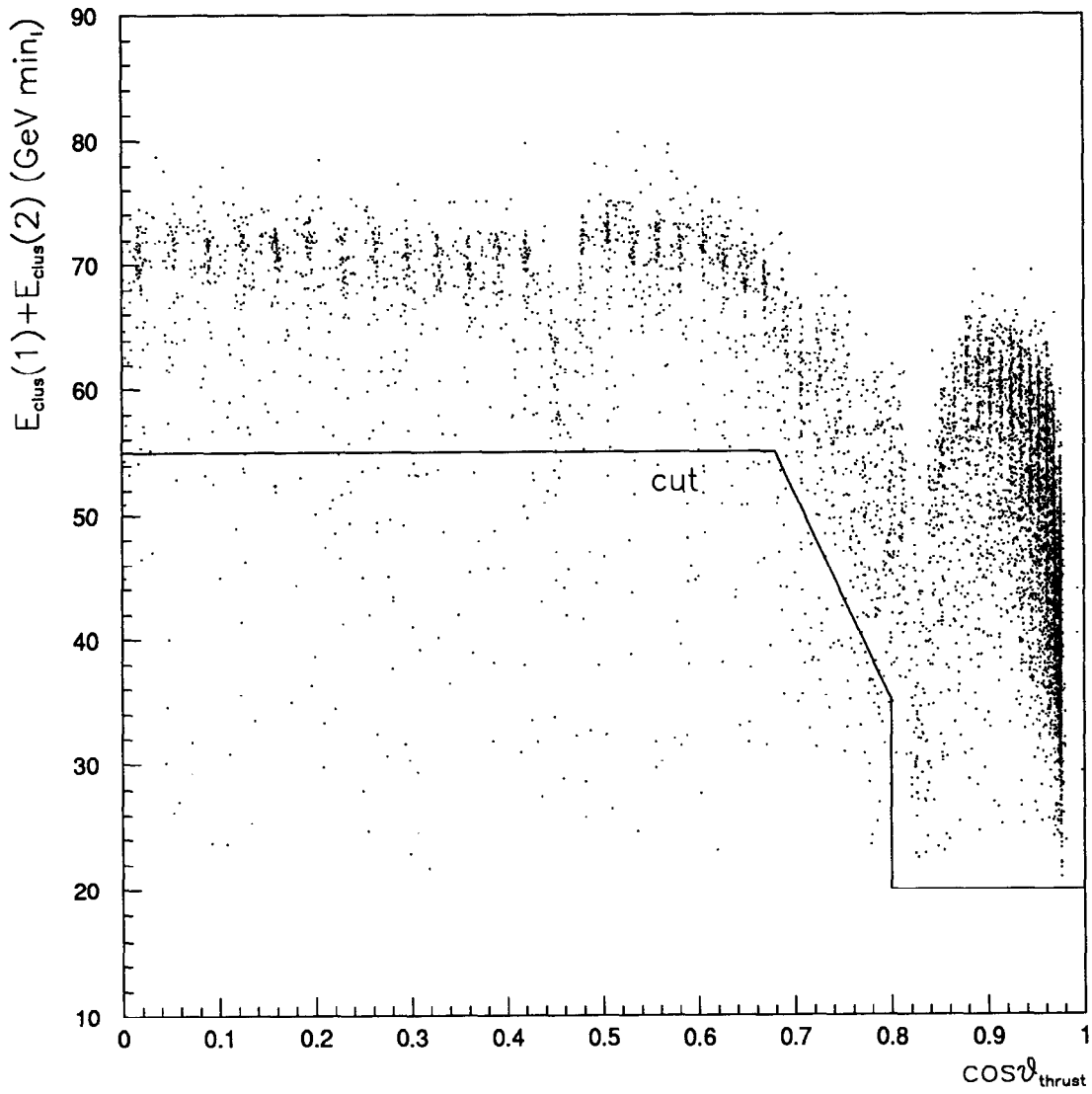

Figure 7.7: Angle dependent energy cut. The additional cut on energy serves to cut contamination in the barrel, as well as to put the barrel and endcap onto similar energy scales. Above 0.8 in $cos\theta_{thrust}$, the de facto cut comes from the requirement that both clusters deposit more than 10 GeV each in the LAC.

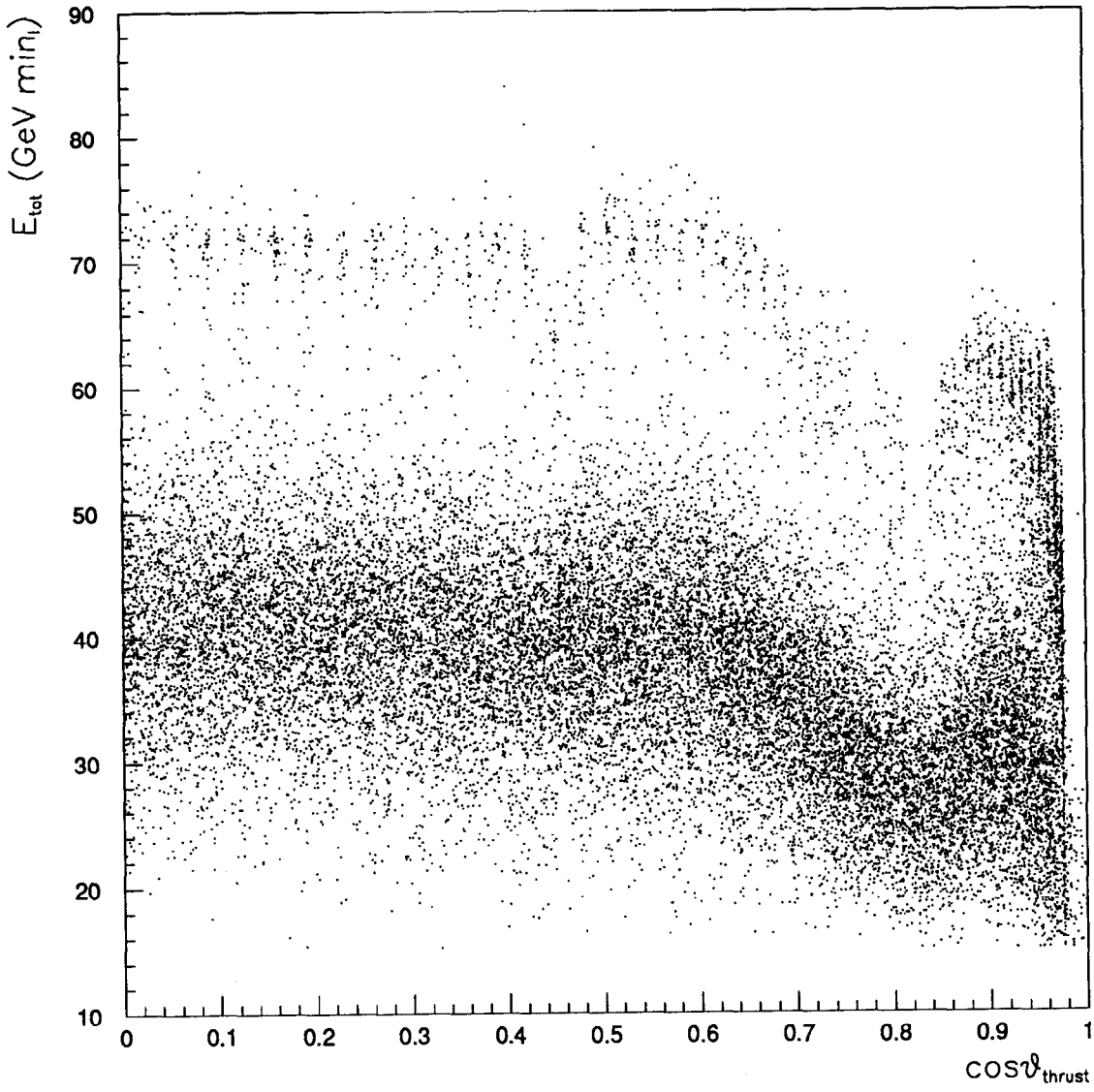

Figure 7.8: Calorimeter response as a function of angle. The events in this plot are required to satisfy PASS 1, the reconstructed energy cut and the imbalance cut. The wide band centered around 40 GeV are hadronic decays of the Z^0. The thin band around 70 GeV are Bhabha events. The degraded response may be clearly seen in the overlap region ($0.65 > cos\theta > 0.85$) and the endcap region ($cos\theta > 0.85$).

LAC come together (see Figure 4.8). Beyond 0.65 in $cos\theta$, the response is seen to fall off rapidly, due to the increase in the effective amount of aluminum dewar that particles must pass through, as well as material in front of the LAC provided by other systems.

The region between 0.76 and 0.88 in $cos\theta$ demonstrates a highly degraded response, due to the electronics, cables and plumbing necessary to operate the inner systems. The electronics and cables for the barrel CRID, the endcap CRID and endcap Drift Chambers all reside in this region. To optimize the solid angle which the inner detectors cover, the electronics follow a pattern which projects back toward the interaction point. The inclusion of all of the additional material in front of the LAC in this region causes a much larger reduction in response than does the additional dewar thickness which particles must traverse. Further into the endcap ($0.88 < cos\theta < 0.94$) the response recovers somewhat, but does not come near the response of the barrel. At smallest angles ($cos\theta > 0.95$) the cables, electronics and cryogenics of the Vertex Detector, as well as the cables and connectors serving the MASC serves to degrade the response even more.

The effect of all of this material destroys not only the resolution of the calorimeter, but also the energy scale. The cause of this apparent difference in energy scale has been investigated in great detail [89]. Based on the comparison in response to minimum ionizing particles between the barrel and endcap, systematic effects such as calibration errors and argon impurity have been ruled out.

To understand the poor response seen in the LAC at $cos\theta > 0.7$, a study of some of the materials such as electronics and cables known to be inside the detector, but not in the simulation, was undertaken. By its nature, this is a very empirical procedure, as data is preselected, then the Monte Carlo is compared to the data. However, the hope was to gain some knowledge regarding the degradation of response seen in the endcap regions. Figure 7.9 shows the original SLD Monte Carlo simulation of wide angle Bhabha events. The response in the barrel demonstrates reasonable agreement with the data. However, none of the features discussed above at larger angles are present in the original simulation. Figure 7.10 shows the approximate amount of material in radiation lengths a particle must traverse before reaching the first active layer of argon as a function of angle. The dashed line is the original SLD Monte Carlo, the solid line is the Monte Carlo after adding approximations of materials to regions where they are known to exist. The agreement between data and Monte Carlo after the material has been added shows a great deal of improvement. There is most certainly a limit to how well the agreement can become, as precise modeling of the materials contained in electronics, cables, cryogenics and mechanical support pieces would take an incredible investment in computational resources as well as manpower. However, in fitting the wide angle Bhabha distribution, the requirements on the calorimeter response are only strict enough to be able to identify e^+e^- events with high efficiency and provide the centroid of the clusters. Fortunately, this is possible even though portions of the calorimeter are stationed behind several radiation lengths of equipment.

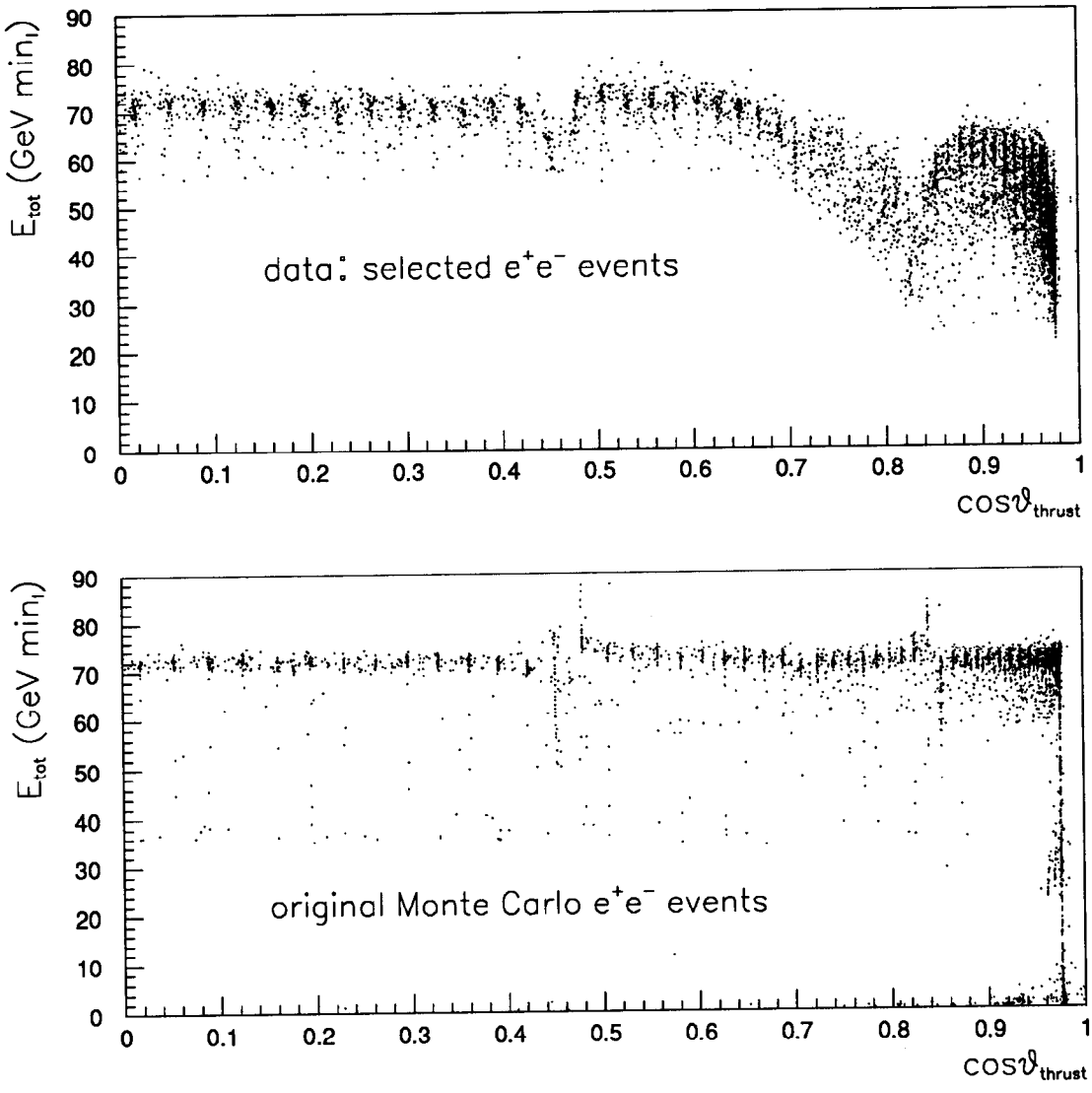

Figure 7.9: Comparison between original SLD Monte Carlo and data. The lower picture shows the reconstructed energy versus thrust angle for simulated wide angle Bhabha events before any addition materials were added to the Monte Carlo. The top picture shows reconstructed energy versus thrust angle for data.

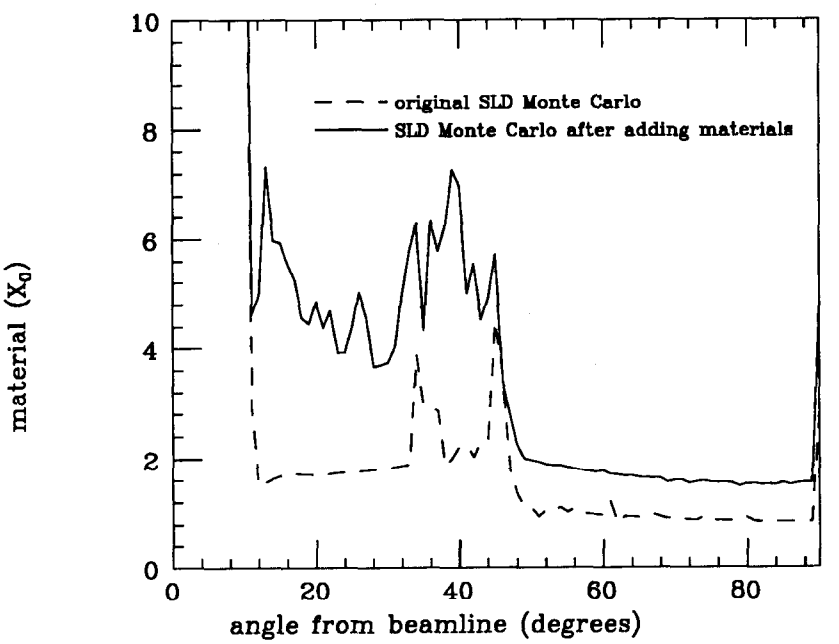

Figure 7.10: Estimation of the amount of material in front of the Liquid Argon Calorimeter as a function of angle. The solid curve shows the estimated amount of material a particle must traverse before it reaches the first argon gap. The dashed curve was the simulation before improvement.

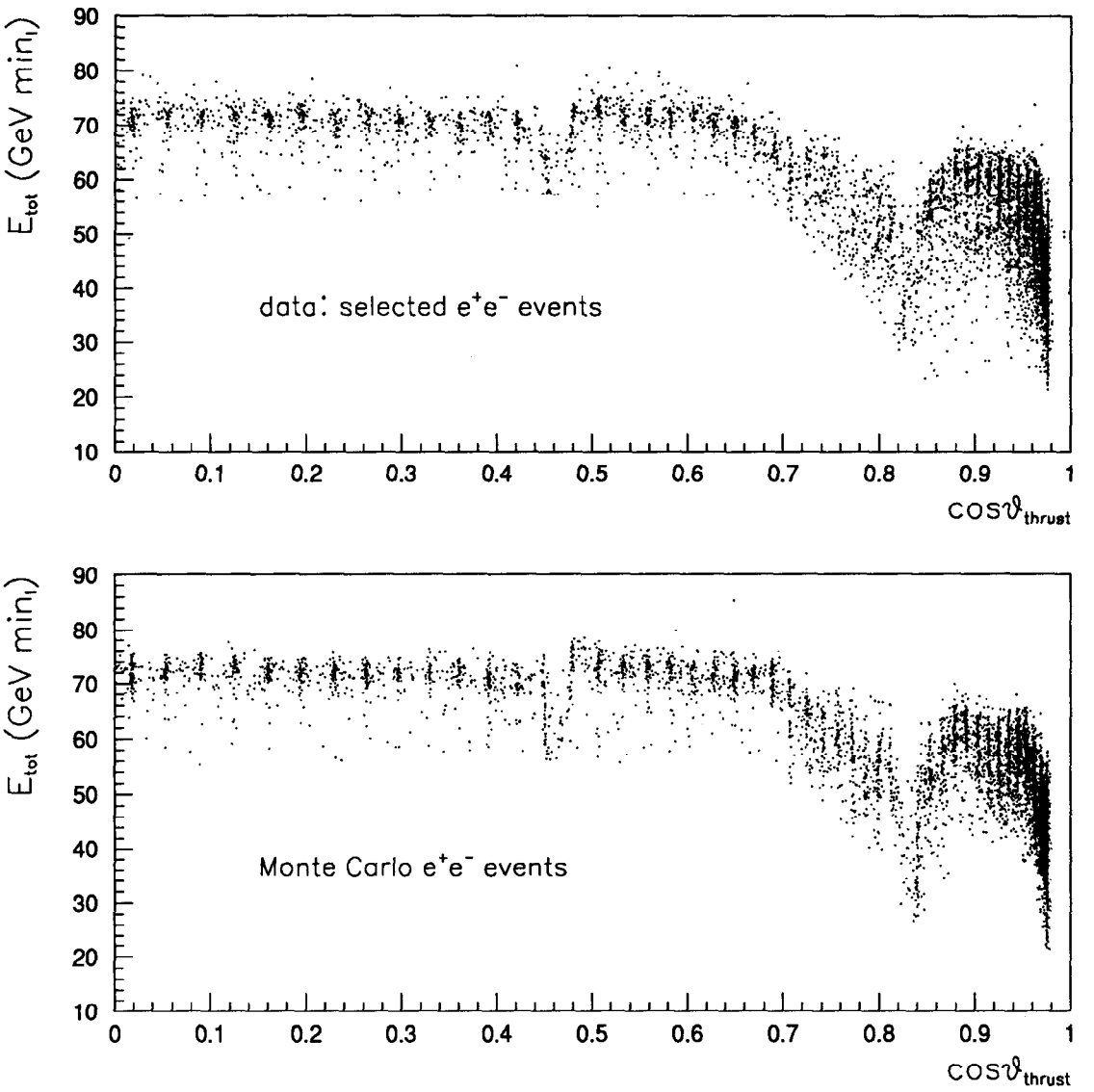

Figure 7.11: Comparison between Monte Carlo and data. The lower picture shows the reconstructed energy versus thrust angle for simulated wide angle Bhabha events. The top picture shows the same quantity for data. Although the agreement is not exact, it can be seen that many of the gross features shown in the data can be explained by means of material in front of the calorimeter.

Thanks to this poor response in the endcap, the dominant error in the axial vector coupling will come from the uncertainty in the correction factors derived from Monte Carlo. This is not the case for the vector coupling, however, as the fit is essentially (left-right)/(left+right) in nature, allowing detector effects to cancel to great degree. The sensitivity to the electron vector coupling to the Z^0 enters effectively by way of the left-right asymmetry (see Section 2.2 and equation 3.12). The response at any given location in the detector is the same for a left-handed electron beam as it is for a right-handed electron beam. Therefore, the uncertainty in the response largely cancels when the event rate asymmetry is measured. Detector correction factors do come in to the vector coupling at a small level, though, through its correlation with the axial vector coupling.

7.5.2 Efficiency

The efficiency for tagging wide angle Bhabha events may be defined as the probability that an e^+e^- final state will be properly identified. From Figure 7.8 it is clear that this function will depend on the scattering angle, with inefficiencies arising from the energy cuts.

The Monte Carlo event generator used to simulate the physics of the $e^+e^- \rightarrow e^+e^-$ process is the Caffo-Remiddi-Czyż generator, BHAGEN, which utilizes the collinear approximation, allowing initial state radiation to boost the center of mass along the beam axis [90]. The final state e^+e^- are defined as the energy summed over a cone of size 0.001 radians. This is a very good approximation for calorimetric measurement e^+e^- events, where the typical cluster size is of order the size of the cone. Radiation at this level can not be distinguished from the primary particle and is included within the cluster. To improve MC statistics, the efficiency factors are calculated with uneven bins in $cos\theta$. The first bin spans from 0.0 to 0.4, where the response is very nearly uniform across the barrel. Smaller bins of size 0.25 are employed from 0.4 to 0.6 in $cos\theta$, then the bins are again reduced to 0.125 from 0.6 to 0.8 in $cos\theta$. Finally, the bins are reduced a third time to 0.02 from 0.8 to 0.98 in $cos\theta$. This way, bins are continually made smaller while the $e^+e^- \rightarrow e^+e^-$ cross section is rising, giving similar statistical weight to each bin, while continually improving the resolution to detector inefficiencies at smaller angles. Although the likelihood fits are of varying bin sizes in $cos\theta$, the efficiency and response factors are always applied by bin.

After the events are passed through the GEANT simulation, they are superimposed on a set of luminosity-weighted random triggers to accurately simulate the backgrounds produced by the SLC. The random events are actually beam crossings on which a small angle Bhabha was tagged in the luminosity monitor. Deposition of energy from the Bhabha event in the LAC is possible but not likely. The events are processed identically to the data after they have been simulated and overlayed onto a random event.

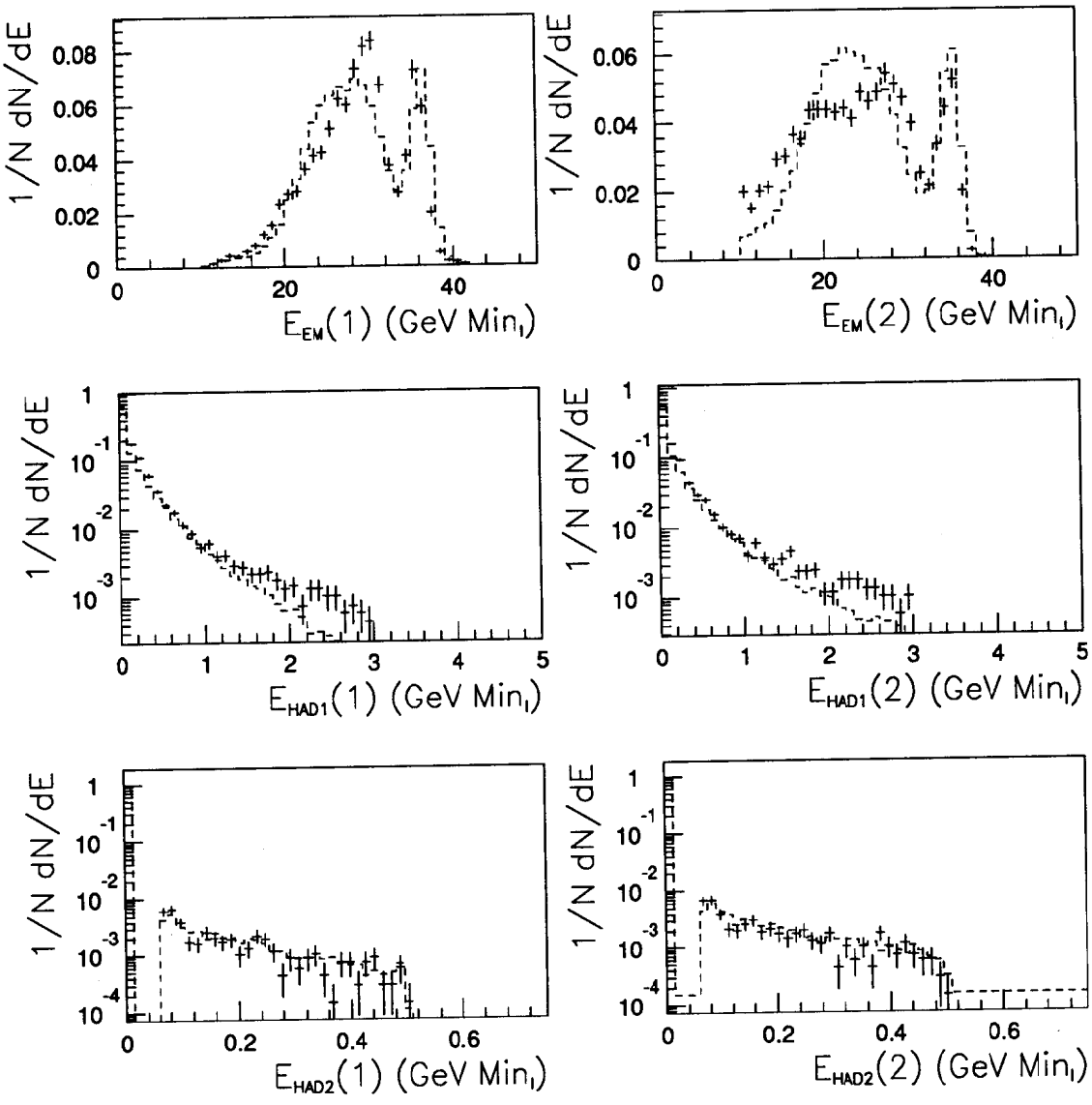

Figure 7.12: Cluster energy comparison between Monte Carlo and data. The largest discrepancy is seen to be in the electromagnetic energy of the second cluster. This effect again comes from the highly degraded response at smaller angles.

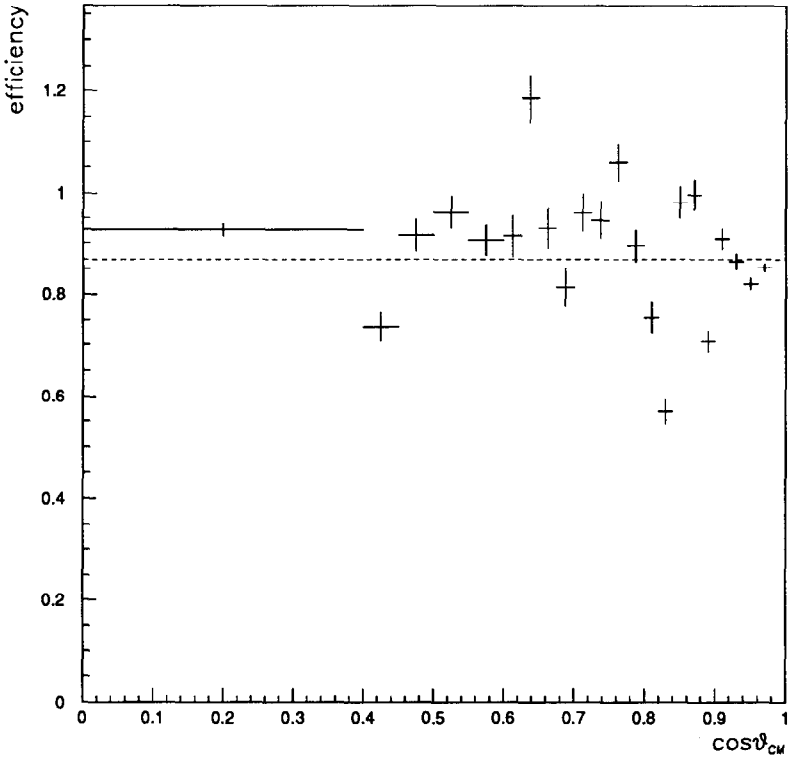

Figure 7.13: Efficiency for wide angle Bhabha events as a function of angle. The different sized bins are utilized to exploit Monte Carlo statistics and regions of the calorimeter where the response is uniform. The dashed line shows the overall average efficiency (for $0. < cos\theta_{CM} < 0.98$) to be 86.7%.

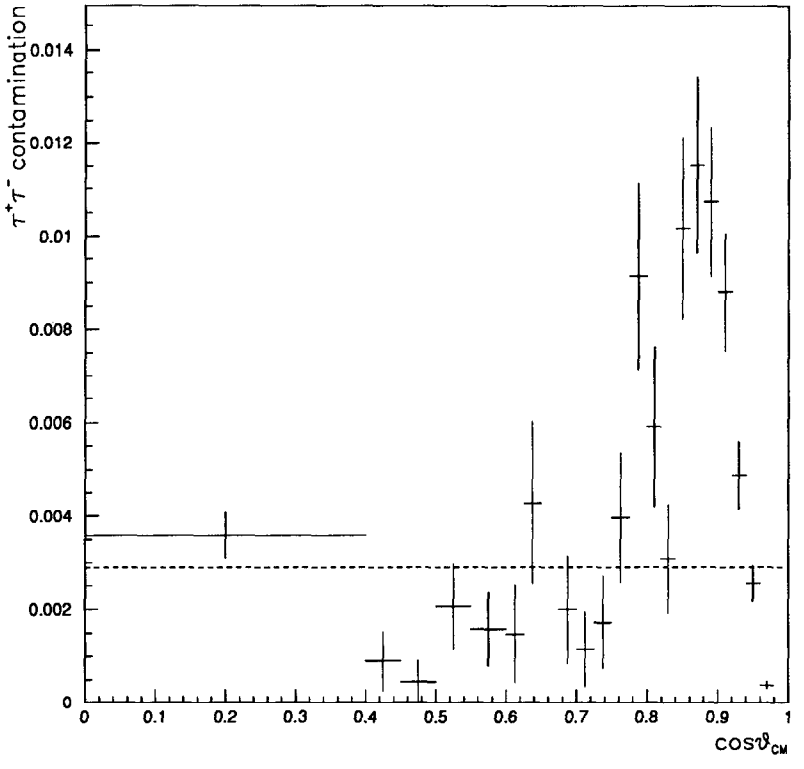

Figure 7.14: Contamination from the $Z^0 \rightarrow \tau^+\tau^-$ process relative to the expected e^+e^- yield as a function of angle. The binning is the same used in the efficiency calculation. The dashed line shows the overall average contamination from $Z^0 \rightarrow \tau^+\tau^-$ (for $0. < cos\theta_{CM} < 0.98$) to be 0.28%.

7.5.3 Contamination

Primary sources of contamination are the decays of the Z^0 into τ leptons and the QED process $e^+e^- \rightarrow \gamma\gamma$. Monte Carlo generators were used to generate physics events of each type. The events were then simulated and overlayed onto luminosity-weighted random events in the manner described in the previous section.

To verify that the hadronic decays of the Z^0 do not present any problem with the event selection scheme listed in Section 6.4.2, 17,069 HERWIG MC [91] events were passed through the detector simulation and selection algorithm. The contamination from this process (summed over all bins) was found to be less than 0.1% of the expected e^+e^- yield and will be neglected throughout the remainder of the analysis.

The $Z^0 \rightarrow \tau^+\tau^-$ process is a source of contamination when the taus decay into electrons. This contamination further complicates the polarized beam fits by contributing a different factor for left and right handed polarized beams, as the left-right asymmetry for $Z^0 \rightarrow \tau^+\tau^-$ is A_e.

Monte Carlo $\tau^+\tau^-$ events are created with the KORALZ generator of Jadach and

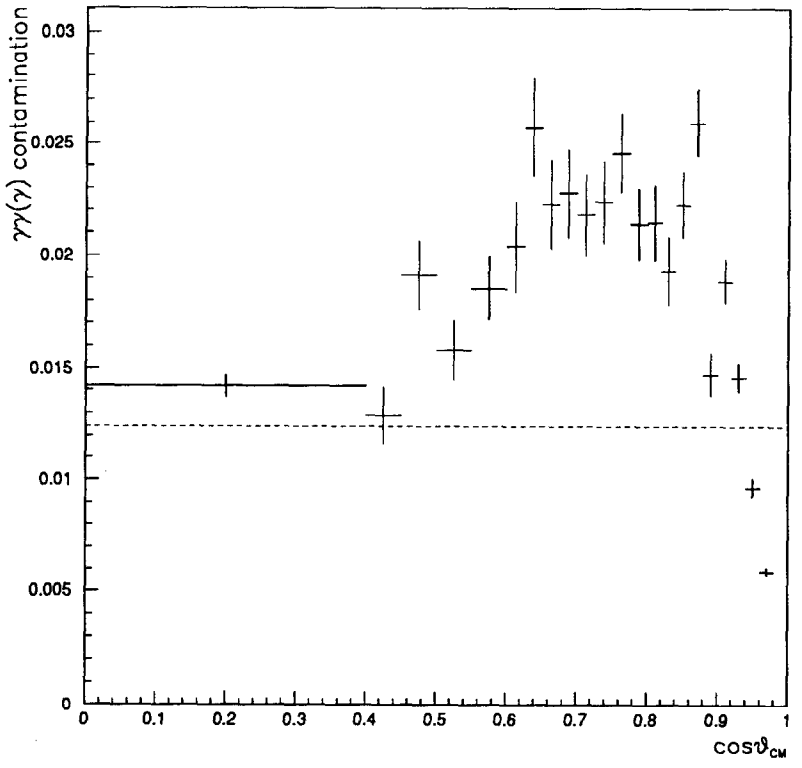

Figure 7.15: Contamination from the $e^+e^- \rightarrow \gamma\gamma$ process relative to the expected e^+e^- yield as a function of angle. The binning is the same used in the efficiency calculation. The dashed line shows the overall average contamination from $e^+e^- \rightarrow \gamma\gamma$ (for $0. < cos\theta_{CM} < 0.98$) to be 1.25%.

Ward [92]. These events are passed through the simulation and selection criteria. Of 48681 events generated, 381 passed the selection criteria overall. The contamination from the $Z^0 \rightarrow \tau^+\tau^-$ process as a function of angle may be seen in Figure 7.14. The contamination fraction is defined to be the fractional yield of contaminating events relative to the expected signal. The contamination falls at small angles due to the large number of e^+e^- events in that region, while the distribution of τ events is proportional to $1 + cos^2\theta$.

The other important contaminating fraction is the $e^+e^- \rightarrow \gamma\gamma$ process. This is a pure QED process, which preserves parity and shows no asymmetry for polarized beams. Monte Carlo $\gamma\gamma$ events were generated with the RADCOR generator of Berends and Kleiss [74]. Figure 7.15 shows the contamination from $\gamma\gamma$ events as a function of angle. The size of the contamination is determined by the overall $e^+e^- \rightarrow \gamma\gamma$ cross section, as roughly 60-75% of the events pass the cuts due to the similar calorimetric response to high energy electrons and photons. Inclusion of information from the tracking systems could be utilized to greatly reduce this contamination fraction. However, since the cross section is small and well known, it can be corrected in the fits with adequate accuracy.

Other potential sources of contamination are primarily due to beam background and cosmic ray events. Both of these have been investigated and are concluded to be negligible.

7.5.4 Summary of Correction Factors

The corrections to the data may be summarized by saying that the efficiency for finding Bhabha events is very high in the barrel region of the calorimeter with little contamination. Although the efficiency falls in the endcap region, a pure sample of Bhabha events is identified with an efficiency of over 80%. Figure 7.16 shows the effect of the corrections on the data. Most of the correction factors do not deviate wildly from one, indicating that the efficiency is good for finding Bhabha events with little background throughout the entire calorimeter.

7.6 Center of Mass Energy

The energy of both beams is measured on a pulse-by-pulse basis by the WISRD (see Section 4.2.4). The SLC ran at slightly different center of mass energies for the 1992 and 1993 runs. However, there was no change in the nominal beam energy during either of the two runs. The luminosity-weighted beam energy for each run is extracted by using the WISRD measurements from pulses which a small angle Bhabha event was tagged. Unfortunately, the acquisition of data for the WISRD is one beam crossing out of synchronization with the SLD readout. Therefore, the measured beam energy comes from the pulse immediately following that which produced the Bhabha event. This method will still yield a valid beam energy measurement, as the machine

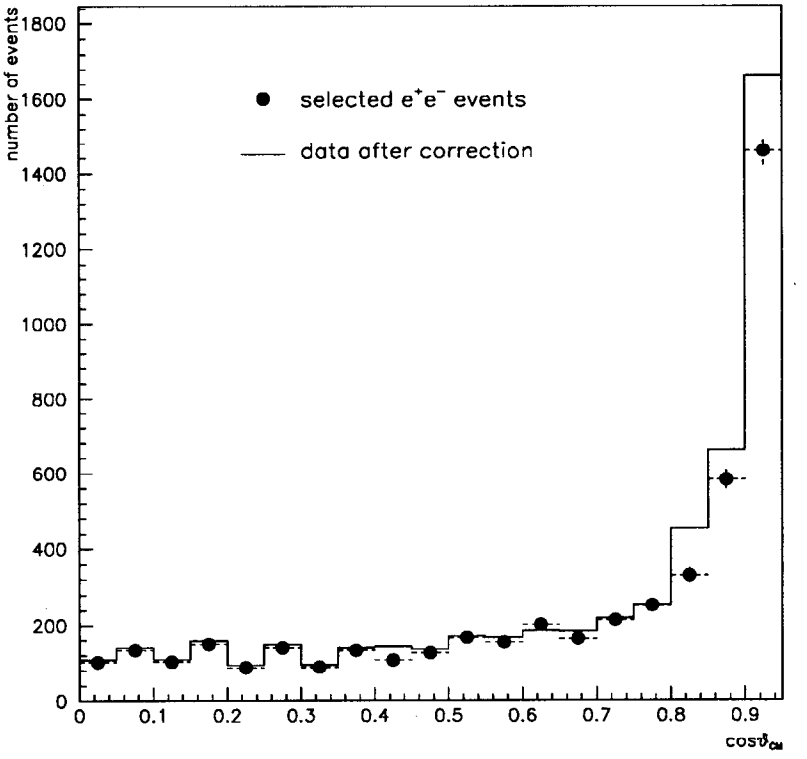

Figure 7.16: Accepted and corrected data sample. The points are the number of event which pass the cuts from the SLD 1992 and 1993 runs. The curve is the data sample after the correction factors for efficiency and contamination are applied. The largest corrections are seen to be at high $cos\theta$, as expected.

conditions and hence the beam energy can not vary wildly from pulse to pulse or else a stable luminosity could not be delivered. Figure 7.17 shows the center of mass energy distribution for small angle Bhabha events from the 1993 run, as well as the energy distributions for the electron and positron beams. The width of these distributions is approximately 0.1% and dominated by the pulse-to-pulse jitter.

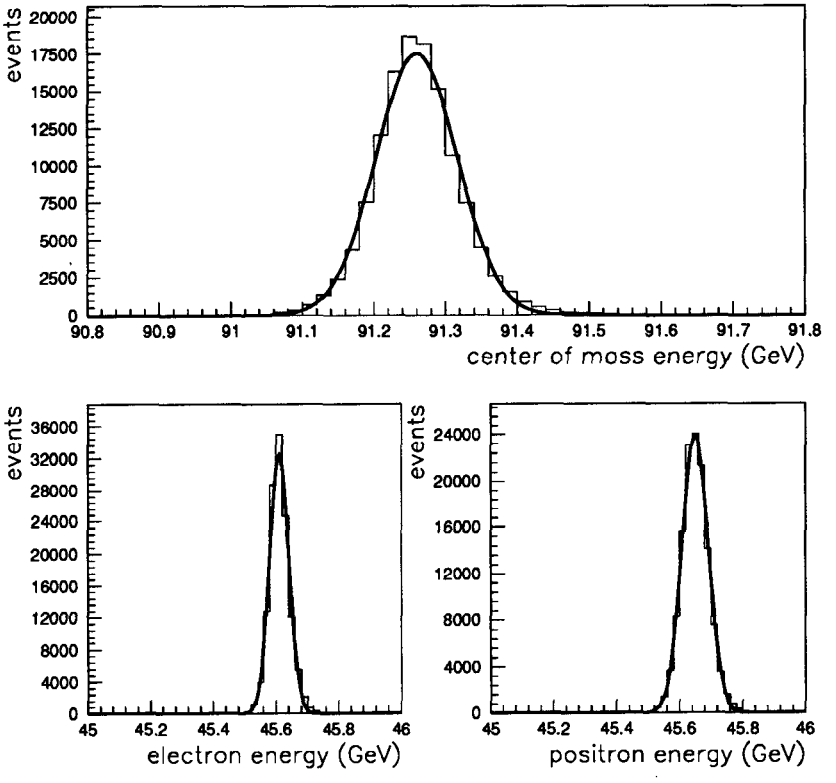

Figure 7.17: Beam energy distribution for the 1993 run. The top plot shows the center of mass energy for 128809 small angle Bhabha events. The lower two plots show the electron and positron beam energies. The widths of the distributions are about 1% and dominated by pulse-to-pulse jitter.

The center of mass energy was 91.55 ± 0.02 GeV for the 1992 run and 91.26 ± 0.02 GeV for the 1993 run. The 20 MeV error is the systematic error on the WISRD measurement [93]. Additionally, the beam energy rms was estimated to be 0.25% for the electron beam and 0.2% for the positron beam [94]. The shape and spread of the beams is not known to a high degree of accuracy.

7.7 Beam Polarization

As stated in Section 4.3, the Compton polarimeter provides the measurement of the beam polarization at the interaction point. Typical polarimeter runs take 3-5 min-

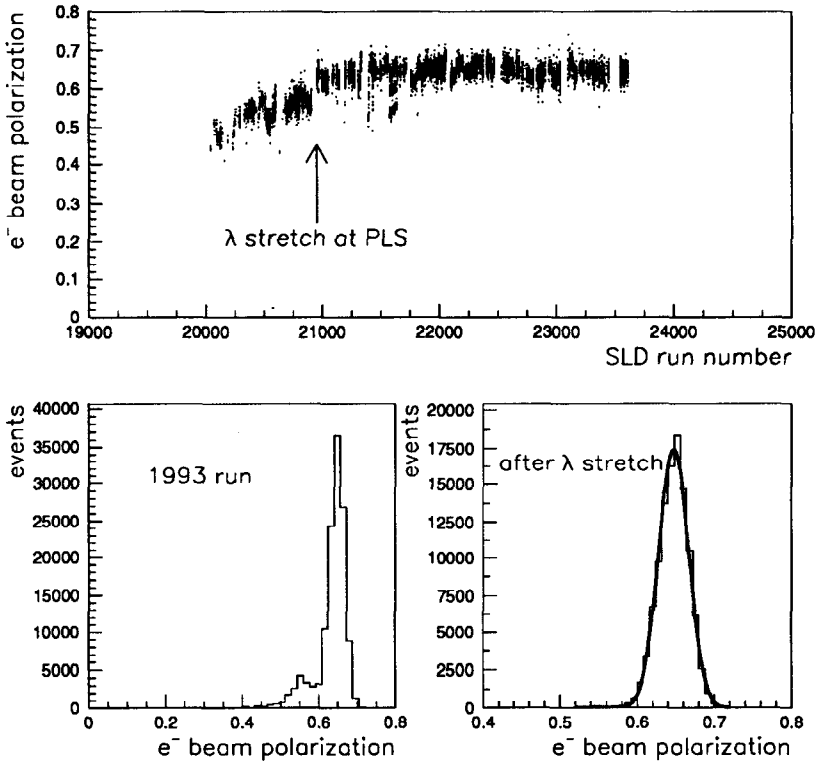

Figure 7.18: Electron beam polarization for the 1993 run. The top plot shows polarization vs. run number. The lower left plot shows the polarization for the entire run, while the lower right plot shows the polarization after the wavelength was increased at the polarized light source.

utes. For each event in the 1993 data sample, the Compton measurement associated most closely in time is attached to that event. Events that do not have a Compton measurement within one hour are assigned zero polarization, and included in the fits. This affects about 6% of the data. In the case of the 1992 data, the only information available is the mean luminosity weighted beam polarization which will be used for each event. Although it is not the optimal way to include the polarization, only 15% of the data sample will be handled in this manner and the low polarization relative to the bulk of the data sample makes the effect negligible. The mean polarization for the 1992 run was $22.4 \pm 0.7\%$.

Figure 7.18 shows the polarization versus run number for the 1993 run. For reference, run 20,100 took place on March 1 and run 23,400 took place on July 31. Notable is the jump in polarization seen around run 20948. This is associated with an increase in laser wavelength at the polarized light source from 850 nm to 865 nm (see Section 4.1.1). The lower left plot shows the polarization for the entire 1993 run. The lower right plot shows the polarization after run 20948. The rms of the distribution is

approximately 2% and dominated by changing source and machine conditions. The mean polarization after the laser wavelength was 64.7%. The preliminary relative error on the 1993 Compton polarimeter measurement (see Section 8.4.3) is $\delta\mathcal{P}_e/\mathcal{P}_e = 1.6\%$.

CHAPTER VIII

EXTRACTING THE ELECTRON VECTOR AND AXIAL-VECTOR COUPLINGS TO THE Z^0 FROM BHABHA SCATTERING

8.1 Method

As discussed in chapter II, the SLD measurement of the left-right asymmetry excludes the e^+e^- final state due to the t-channel dilution. The following chapter will utilize the $e^+e^- \rightarrow e^+e^-$ process to extract the electron vector coupling to the Z^0 and, hence, the weak mixing angle. This will be done by fitting the polarized e^+e^- distribution, which will also allow us to extract the electron axial vector coupling to the Z^0.

For each event tagged as a wide angle Bhabha, the beam energy, helicity and polarization is known, as well as the laboratory scattering angle of the electron and positron, $cos\theta_+$ and $cos\theta_-$.[1] To utilize this information to its fullest, the data, which has been corrected for detector inefficiency and contamination from other physics processes, will be fit with a likelihood function, defined as:

$$\mathcal{L} = \prod_{i \ events} p_i, \tag{8.1}$$

where p_i is the probability for event i. The maximum likelihood principle states that the best estimator of the unknown parameters will render the likelihood as large as possible [95]. The likelihood utilized here is a function of all parameters of the Standard Model, but depends most strongly in this case upon $\overline{g}_v^e$, $\overline{g}_a^e$, and m_{top}. In terms of $sin^2\theta_W$, which defines $\overline{g}_v^e$, the strongest dependence is on the mass of the top quark, m_{top}, which enters through initial vertex and oblique radiative corrections (see Section 2.4). In this analysis, the likelihood will be unbinned in polarization and will

[1]Since this analysis utilizes calorimetry only, the laboratory scattering angle of the electron and positron can be measured, but which angle is associated with which of the two particles remains ambiguous. In other words, θ_+ and θ_- are the laboratory scattering angles of the electron and positron, but it is not known which is which.

utilize small bins in $cos\theta$.[2] This is especially advantageous with beam polarization because the magnitude of the beam polarization is relatively sensitive to SLC machine parameters and therefore time-dependent. Special care and additional complication would also arise in combining the data from the 1992 and 1993 SLD runs, as the beam polarization was $\sim 23\%$ in 1992 and $\sim 63\%$ in 1993. The unbinned method allows for inclusion of all data in a simple manner, while preserving the maximal amount of information regarding each tagged event.

The probability for event i is the differential cross section normalized to the total cross section:

$$p_i = (\frac{1}{\sigma_{tot}^{e^+e^-}})\frac{d\sigma^{e^+e^-}}{dcos\theta}. \tag{8.2}$$

Fitting the differential Bhabha distribution in this manner leaves the free parameters sensitive to the shape of the distribution, but not the overall normalization. In this case, the fit may be thought of as having two parts: one polarized and one unpolarized. The polarized portion of the fit is essentially a fit to the $A_{LR}^{e^+e^-}$ function and is sensitive to the electron vector coupling. The unpolarized fit measures the number of events at low $cos\theta$ ($cos\theta \leq 0.6$) relative to the number of events at high $cos\theta$ ($cos\theta \geq 0.7$). In other words the high $cos\theta$ contribution performs the normalization, since it is primarily t-channel photon exchange, while the the low $cos\theta$ is sensitive to the partial width.

It should also be pointed out that experiments typically extract Γ_{ee} by measuring the total e^+e^- cross section integrated over the central region of the detector, where the Z^0 decay dominates. Fitting the differential cross section as a function of angle allows for sensitivity to the shape of the distribution at intermediate ($30° < \theta < 10°$) angles which can not be achieved by measuring the total e^+e^- cross section at large angles.

8.2 Fitting the e^+e^- Distribution

Two Standard Model "fitters"[3] are used to extract $\overline{g}_v^e$ and $\overline{g}_a^e$: EXPOSTAR and DMIBA. EXPOSTAR, the work of Levinthal, Kennedy, Lynn et al., is a multipurpose program which calculates a number of observables based upon the Standard Model [9, 96]. EXPOSTAR calculates cross sections in terms of helicity amplitudes, so it is very well suited for fitting polarization asymmetry measurements. DMIBA, written by Martinez and Comas, calculates the differential cross section for $e^+e^- \rightarrow e^+e^-$ in a model independent manner [97]. The DMIBA fitter is not currently configured for polarized beams, and is therefore not optimal for extracting $\overline{g}_v^e$.

[2]The fits are binned in $cos\theta$ simply to save cpu time. The bin sizes are set to be much smaller than the angular resolution of the calorimeter, to insure no bias in the binning.

[3]The programs discussed here have no implicit mechanisms for performing fits, but are instead routines to calculate cross sections for specific processes. However, since these programs are almost exclusively used to fit experimental data, they are referred to as "fitters".

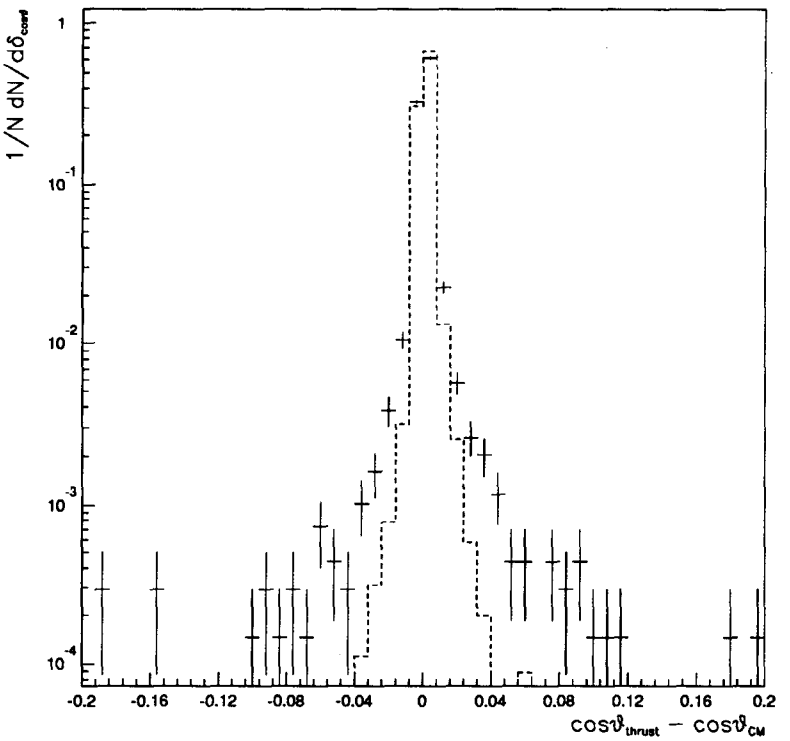

Figure 8.1: Difference between center of mass scattering angle and thrust axis for e^+e^- events. Since LAC towers cover 0.02 in $cos\theta$ typically, the difference is small between the thrust axis and center of mass scattering angle. The shape of this distribution is sensitive to both initial and final state radiation. The dashed curve is e^+e^- Monte Carlo.

The fitters are used to calculate the differential and total $e^+e^- \rightarrow e^+e^-$ cross section at each angle, center of mass energy and (in the case of EXPOSTAR) polarization. The maximum likelihood value is found by minimizing the negative log of the likelihood function, which may be written in the following manner:

$$max\mathcal{L} \rightarrow min(-ln\mathcal{L}) = -\sum_{i\ events} ln(p_i). \tag{8.3}$$

The minimization is performed with the program MINUIT [98].

Both programs calculate the differential scattering distributions in the collision frame, which is the center of mass frame for the e^+e^- after initial state radiation. The scattering angle in the collision frame may be related to the laboratory frame angles of the outgoing electron and positron in the following manner:

$$sin^2\theta_{CM} = \frac{2sin\theta_+ sin\theta_-}{1 - cos(\theta_+ + \theta_-)}, \tag{8.4}$$

where (CM) denotes the collision frame, which may be thought of as the center of mass frame between the electron and positron after initial state radiation has taken

place. In the limit of no radiation and beams of equal energy (see Figure 7.17), the lab frame and the center of mass frame are identical. Figure 8.1 shows the difference between the cosine of the thrust axis calculated in the laboratory frame and the collision frame scattering angle for tagged e^+e^- events. The deviation from zero is caused primarily by initial state radiation.

8.2.1 EXPOSTAR

The EXPOSTAR program provides routines to calculate differential and total cross sections for a variety of electroweak processes at an e^+e^- collider. Included in the calculations are initial state QED radiation and vertex corrections, oblique and initial weak corrections and box diagrams. Inclusion of these corrections allows for high precision calculations of observables which may be compared directly with experimental data.

The collinear radiation approximation is utilized in EXPOSTAR, allowing for calculation of the cross sections in terms of a convolution integral of two electron structure functions with invariant collision-frame cross sections evaluated at reduced energy. The rapidity cut introduced earlier (equation 7.4) allows the integral over the structure functions to be cut off and integrated numerically to high accuracy. In addition, a cut is made on the total amount of energy lost through initial state radiation. This is effectively a cut on the amount of visible energy in the final state.

8.2.2 DMIBA

The second fitter, DMIBA (Differential Model Independent Bhabha Approximation), assumes only very basic theoretical concepts in calculating the differential $e^+e^- \rightarrow e^+e^-$ distribution in order to minimize bias introduced in assuming more than necessary about the Standard Model. The basic formulation of DMIBA is very similar to EXPOSTAR in that the initial state radiation functions are used to compute the reduced center of mass energy and then the scattering angle in the center of mass frame. The DMIBA calculation is performed at the leading log level of accuracy.

To maintain generality, explicit Standard Model parameters such as the top and Higgs boson masses are not explicitly utilized. Instead, the fit is simply performed for the partial width of a generalized resonance of mass M_Z and width Γ_Z.

8.2.3 Fitting Formulas

In the case of EXPOSTAR, the differential cross section for a left and right handed beam, as well as an unpolarized beam may be calculated. In the general case, the probability for event i takes on the following form:[4]

[4]This method will be referred to as the "direct fit" to the data.

Table 8.1: Summary of types of fits performed.

fit name	program	description	fit for
direct	EXPOSTAR	direct fit for $\overline{g}_v^e$ and $\overline{g}_a^e$	A_e,Γ_{ee}
wide angle	DMIBA	unpolarized wide angle only	Γ_{ee}
LUM constrained	DMIBA	unpolarized + luminosity constraint	Γ_{ee}
helicity	DMIBA	separate helicities + LUM constraint	A_e

$$p_i = \frac{2\frac{d\sigma}{dz}|_{unpol} + \mathcal{P}_e(\frac{d\sigma}{dz}|_{left} - \frac{d\sigma}{dz}|_{right})}{2\sigma_{total}}, \tag{8.5}$$

where $z \equiv cos\theta_{CM}$. (For a derivation and discussion of equation 8.5, see Appendix A.) The differential cross sections are evaluated at the proper center of mass scattering angle and center of mass energy. This form allows for all data to be included into a single fit. The fit can then be performed for m_{top}, m_{Higgs}, $\overline{g}_v^e$, $\overline{g}_a^e$, or a general lepton factor, $\overline{g}_l^e$, which is equivalent to fitting an unpolarized distribution for Γ_{ee}. The procedure used here is as follows: first, the distribution is fit for m_{top} to find a preferred value for the mass of the top quark. Next, the preferred top quark mass is input into EXPOSTAR and the data is fit for $\overline{g}_v^e$ and $\overline{g}_a^e$ simultaneously. In both fits, the mass of Z^0 and mass of the Higgs boson are input parameters. Once the fit has been performed for the top mass, the Standard Model is completely defined. Therefore, in the simultaneous direct fit for $\overline{g}_v^e$ and $\overline{g}_a^e$, significant deviations of the couplings from the value defined by the input parameters would be an indication of physics beyond the Standard Model.

Since the DMIBA fitter does not allow explicitly for beam polarization, the fit must be performed in two stages. First, Γ_{ee} can be extracted fitting a simplified version of the above equation:

$$p_i = \frac{\frac{d\sigma}{dz}|_{unpol}}{\sigma_{tot}}, \tag{8.6}$$

where the data is simply treated as unpolarized.[5]

To extract A_e with DMIBA, the data must be fit exclusively for each helicity, yielding an "effective" Γ_{ee}^{left} and Γ_{ee}^{right}. Utilizing equations 2.13 and 2.14 the asymmetry A_e may be written as:[6]

$$A_e = \frac{1}{\mathcal{P}_e} \times \frac{\Gamma_{ee}^{left^2} - \Gamma_{ee}^{right^2}}{\Gamma_{ee}^{left^2} + \Gamma_{ee}^{right^2}}. \tag{8.7}$$

This method is complimentary to the direct fit for the couplings. By explicitly fitting for the partial width and then forming the left-right asymmetry, the systematic errors

[5]This method will be referred to as the "wide angle" fit for Γ_{ee}.

[6]This method will be referred to as the "helicity fit" to the data.

introduced in the partial width fits will not be the same as those from the direct fit. A drawback to this method is that all events of each helicity must be treated on equal footing, since the polarization is not explicitly included in the fit. Therefore, data must be discarded when the polarization varies wildly from the mean. Realistically, this means that the data from the 1992 run, as well as the data from the 1993 run before the increased source laser wavelength (see Section 7.7) may not be included in this method.

An alternative method for extracting the partial width will also be used. This will utilize the same data as the unbinned method, but also include the normalization provided by the small angle Luminosity Monitor.[7] This improves the error on Γ_{ee} quite dramatically because the statistical and systematic error on the normalization are greatly reduced. To perform the luminosity-constrained fit a Poisson log-likelihood will be used:

$$\chi^2 = -2\sum_{i,j}(N_{ij}^{seen} ln\big(\frac{N_{ij}^{exp}}{N_{ij}^{seen}}\big) + N_{ij}^{seen} - N_{ij}^{exp}\big), \tag{8.8}$$

where i denotes the bin in $cos\theta_{CM}$, and j denotes the center of mass energy. N_{ij}^{seen} is the number of tagged events within a bin and $N_{ij}^{exp} = \Delta_z \frac{d\sigma}{dz}\mathcal{L}\delta_i$ is the expected number of events in a bin of width Δ_z, where the calculated differential cross section is $\frac{d\sigma}{dz}$, $\mathcal{L}_j$ is the luminosity measured at energy j and δ_i are the correction factors discussed in Section 7.5.

8.3 Results

For the 1992 data sample, 1337 events satisfy the wide angle Bhabha selection criteria and display a $cos\theta_{CM} < 0.98$. The number of events passing the same cuts from the 1993 data sample is 6596. Table 8.2 lists the number of events by helicity for different angular regions for the data from the 1992 run. The results for the 1993 run are tabulated in Table 8.3. The raw asymmetry for each bin is simply $A_{LR}^{e^+e^-}(raw) = (N_L - N_R)/(N_L + N_R)$, therefore the beam polarization is not included in the table. The errors on the raw asymmetries are statistical only.

The data from Table 8.3 are plotted in Figure 8.2, showing the raw Bhabha left-right asymmetry for the 1993 selected Bhabha events. The large bin running from 0 to 0.7 in $cos\theta_{CM}$ contains approximately an 88% contribution from the s-channel Z^0 exchange and therefore demonstrates virtually the full left-right asymmetry. As the t-channel contribution increases, the asymmetry is pulled toward zero. The rightmost bin in Figure 8.2 is the contribution from small angle Bhabha events tagged in the Luminosity Monitor.

The fit to the unpolarized differential distribution using DMIBA yields

$$\Gamma_{ee} = 83.47 \pm 1.34 \text{ (stat)} \pm 5.18 \text{ (sys) MeV},$$

[7]This method will be referred to as the "LUM constrained fit" to Γ_{ee}.

Table 8.2: Bhabha raw asymmetry for the 1992 run.

region	left handed	right handed	$A_{LR}^{e^+e^-}(raw)$
$0.0 < cos\theta_{CM} < 0.70$	157	137	0.068 ± 0.058
$0.70 < cos\theta_{CM} < 0.94$	208	205	0.0073 ± 0.049
$0.94 < cos\theta_{CM} < 0.98$	305	318	-0.021 ± 0.040
$0.998 < cos\theta_{CM} < 0.9994$	12,395	12,353	0.0017 ± 0.0064

Table 8.3: Bhabha raw asymmetry for the 1993 run.

region	left handed	right handed	$A_{LR}^{e^+e^-}(raw)$
$0.0 < cos\theta_{CM} < 0.70$	864	702	0.103 ± 0.025
$0.70 < cos\theta_{CM} < 0.94$	1,039	946	0.047 ± 0.022
$0.94 < cos\theta_{CM} < 0.98$	1,566	1,479	0.029 ± 0.018
$0.998 < cos\theta_{CM} < 0.9996$	93,727	94,319	-0.0032 ± 0.0023

which is shown in Figure 8.3. The log of the likelihood function for the wide angle fit is show in Figure 8.4. This likelihood function is well-behaved and representative of all of the fits discussed in this section.

When the distribution is constrained by the luminosity measurement, the errors are reduced:

$$\Gamma_{ee} = 83.14 \pm 1.04 \text{ (stat)} \pm 2.16 \text{ (sys) MeV}.$$

This fit is shown in Figure 8.5. The upper plot in the picture shows the fit to the corrected data. The lower plot shows the residuals. The systematic uncertainty in the correction factors are included in this plot. The inclusion of the luminosity constraint lessens the dependence of the fit on the behavior of the corrected data at smaller angles ($0.98 > cos\theta > 0.7$) and therefore reduces the error.

In the case of the direct fit to the differential distribution, the result from EXPOSTAR agrees with that of DMIBA. However, in the case of the luminosity constrained fit, EXPOSTAR shows a systematic offset which yields results for the partial width which are approximately 5% below those of DMIBA. Comparing the two fitting programs with one another, as well as with the BHAGEN Monte Carlo and the semi-analytic program ALIBABA [99], it was determined that the shape of the differential distributions calculated by DMIBA and EXPOSTAR agree to 1%, while the normalization from EXPOSTAR is low.

The fit to the polarized differential distribution using EXPOSTAR yields

$$A_e = 0.197 \pm 0.038 \text{ (stat)} \pm 0.011 \text{ (sys)}.$$

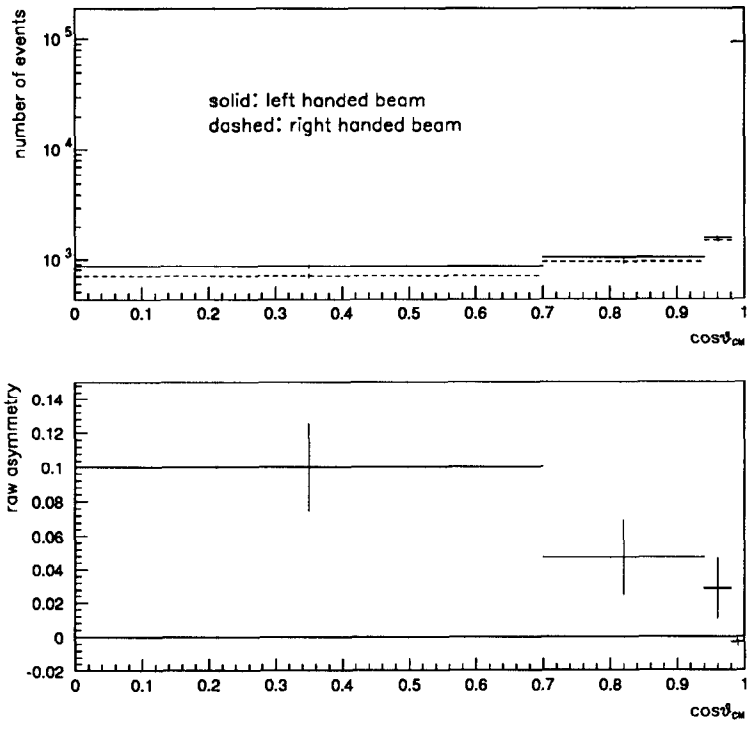

Figure 8.2: Raw Bhabha left-right asymmetry for the 1993 data. The bins sizes are selected to emphasize the features of the distribution. The first three bins show events contained within the acceptance of the LAC, which covers to $cos\theta = 0.98$. The far right bin includes Bhabha events tagged in the SLD luminosity monitor within an angular region of 28 to 68 mrad from the beam line. The bin is expanded to cover a larger region of $cos\theta$ so that it may be seen.

This fit is shown in Figure 8.6.

The fit using a subset of the 1993 data (see Section 7.7) fitting first the left-handed distribution and then the right-handed distribution using DMIBA includes the constraint of the integrated luminosity. The fit results for each helicity are $\Gamma_{ee}^{left} = 89.15$ MeV and $\Gamma_{ee}^{right} = 77.68$ MeV with a mean polarization of 64.7%. From equation 8.7, this yields:

$$A_e = 0.206 \pm 0.047 \text{ (stat)} \pm 0.009 \text{ (sys)}.$$

The helicity fits to the left- and right-handed data are shown in Figures 8.7 and 8.8. To compare the helicity fit to the direct fit, the direct fit was performed on the same subset of data which is used in the helicity fit. The result for the direct fit to that data sample is $A_e = 0.205 \pm 0.040$ (stat) ± 0.011 (sys), in good agreement with the helicity fit.

Table 8.4 shows a summary of the results for the partial width, Γ_{ee}, and the parity violation parameter, A_e. Systematic errors will be discussed in detail in the

Table 8.4: Results for Γ_{ee} and A_e.

Parameter	type of fit	result
Γ_{ee}	wide angle	83.47 ± 1.34 (stat) ± 5.18 (sys) MeV
Γ_{ee}	LUM constrained	83.14 ± 1.04 (stat) ± 2.16 (sys) MeV
A_e	direct	0.197 ± 0.038 (stat) ± 0.011 (sys)
A_e	helicity	0.206 ± 0.047 (stat) ± 0.009 (sys)

following section.

8.4 Systematic Errors

This section will discuss the systematic uncertainties involved in the measurements. Even though all of the fits are of the same e^+e^- distribution, the different systematic errors effect Γ_{ee} and A_e in different ways.

8.4.1 Correction Factors

The uncertainty in the correction factors arises from two main sources: the physics of the Monte Carlo generators and the accuracy of the simulation.

The accuracy of the BHAGEN Monte Carlo is estimated to be 1%, which will be included in the uncertainty in the efficiency factors discussed below. Unlike the small angle Bhabha analysis, the cross section calculated by the generator is not directly used in the extraction of the partial width. Therefore, the inaccuracy of the Monte Carlo translates directly into an uncertainty in the efficiency factors. The uncertainty in the Bhabha Monte Carlo arises primarily from the omission of hard radiation in the final state.

The uncertainty in the $\tau^+\tau^-$ and $\gamma\gamma$ background fractions are dominated by Monte Carlo statistics and calculated to be 0.1% of the event yield, which translates into an uncertainty of 0.1% in Γ_{ee} and an uncertainty of 0.07% in A_e.

The largest uncertainty comes from the accuracy of the detector simulation. This affects the different fits in different ways. The error from the simulation is estimated for three distinct regions of the calorimeter: the barrel region ($cos\theta < 0.6$), the intermediate region ($0.6 < cos\theta < 0.85$), and the endcap region ($cos\theta > 0.85$).

For the barrel region, the simulation is very accurate, with uncertainties arising from the description of the LAC inter-module gap, material in front of the calorimeter, and the shower simulation. The error due to these effects in the barrel is estimated to be 0.7% [87].

In both the intermediate and endcap regions, the dominant uncertainty arises from the material in front of the endcap. As discussed in Section 7.5.1, material

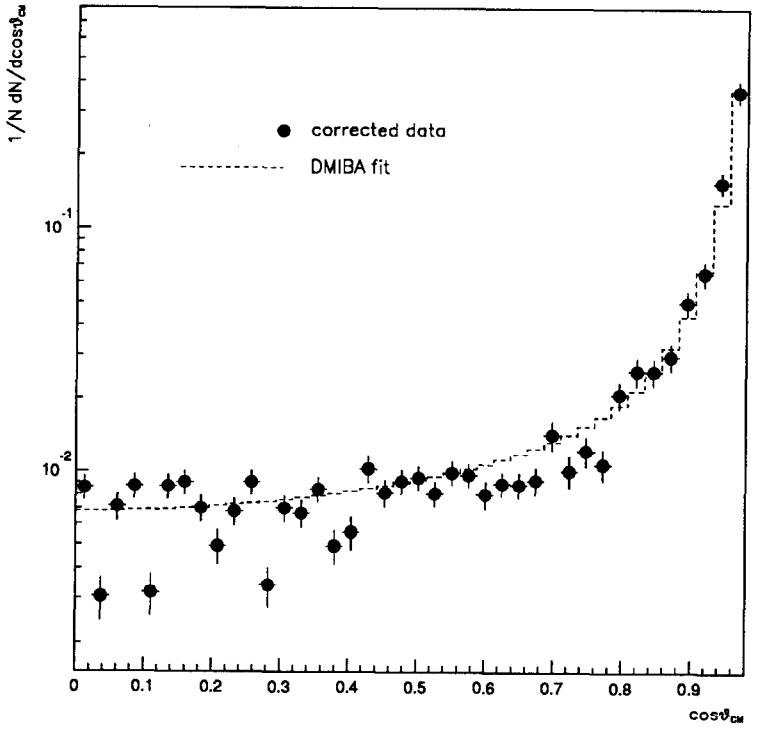

Figure 8.3: Wide angle DMIBA fit to the unpolarized $e^+e^- \rightarrow e^+e^-$ distribution.

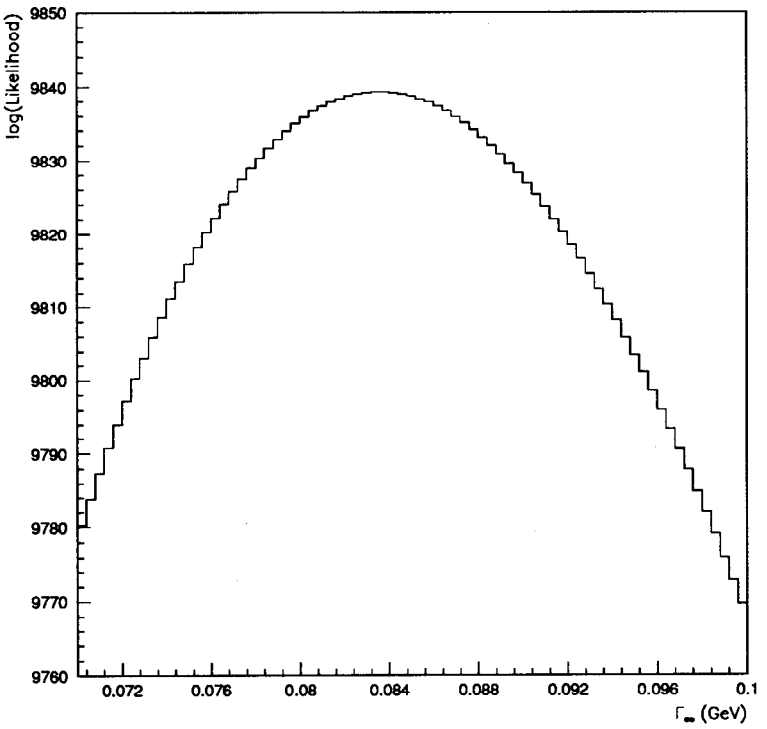

Figure 8.4: Likelihood function for wide angle fit. This likelihood function corresponds to the fit shown in Figure 8.3.

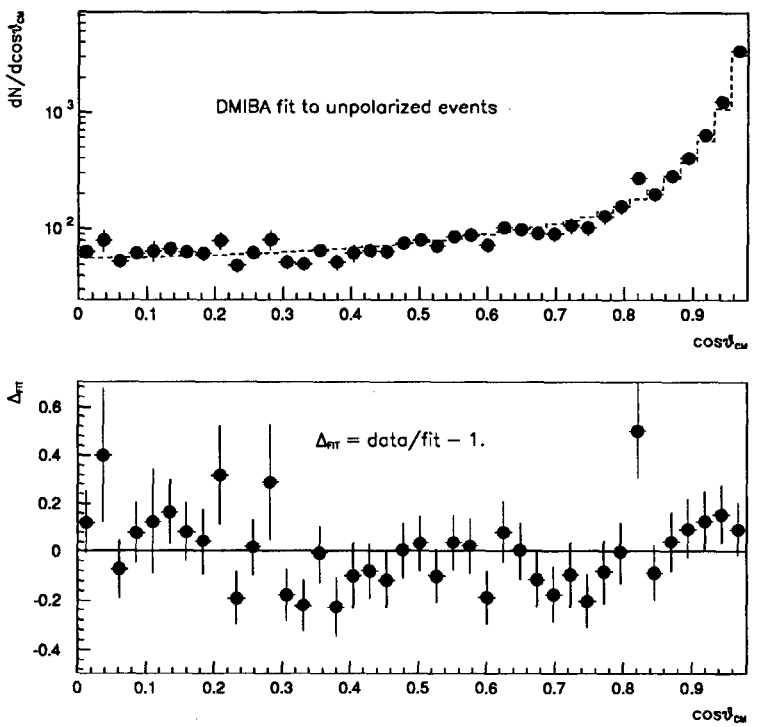

Figure 8.5: DMIBA LUM constrained fit to the corrected wide angle Bhabha distribution. The points are the corrected data, the curve is the fit. The errors on the corrected data include the systematic uncertainty of the correction factors.

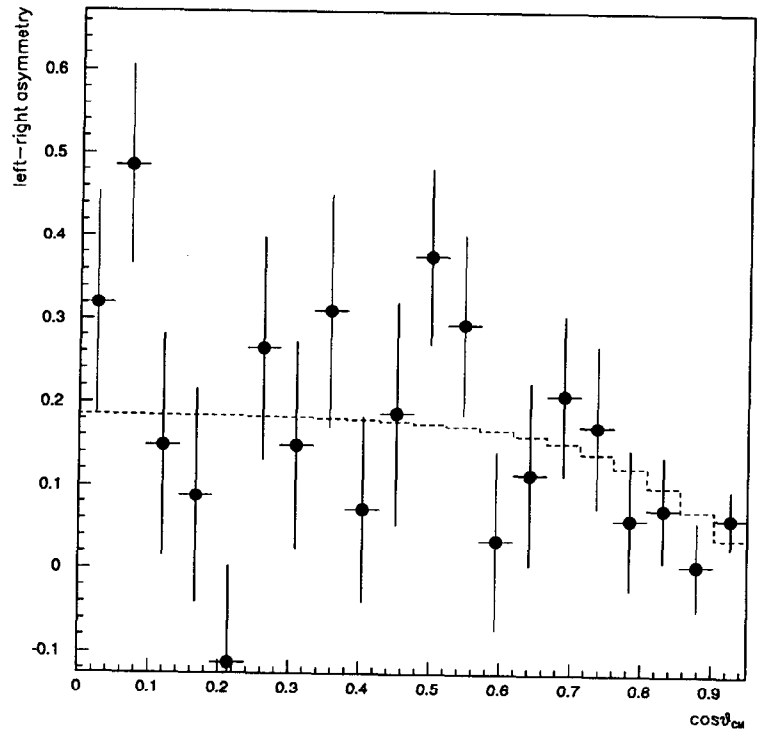

Figure 8.6: EXPOSTAR wide angle fit to the corrected wide angle Bhabha asymmetry. The points are the corrected data, the curve is the fit. The errors on the corrected data are statistical only.

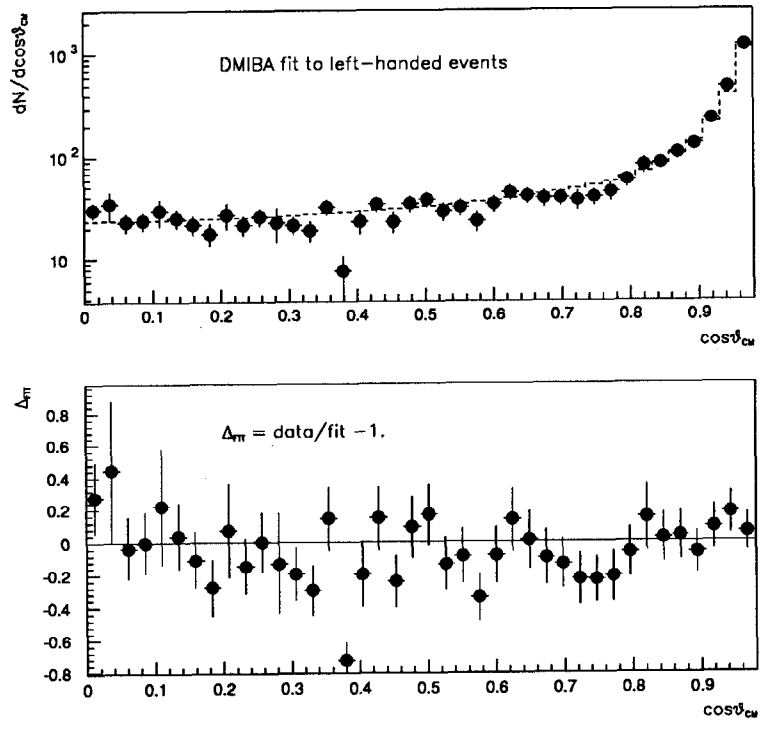

Figure 8.7: DMIBA LUM constrained fit to the corrected left-handed wide angle Bhabha distribution. The points are the corrected data, the curve is the fit. The errors on the corrected data include the systematic uncertainty of the correction factors.

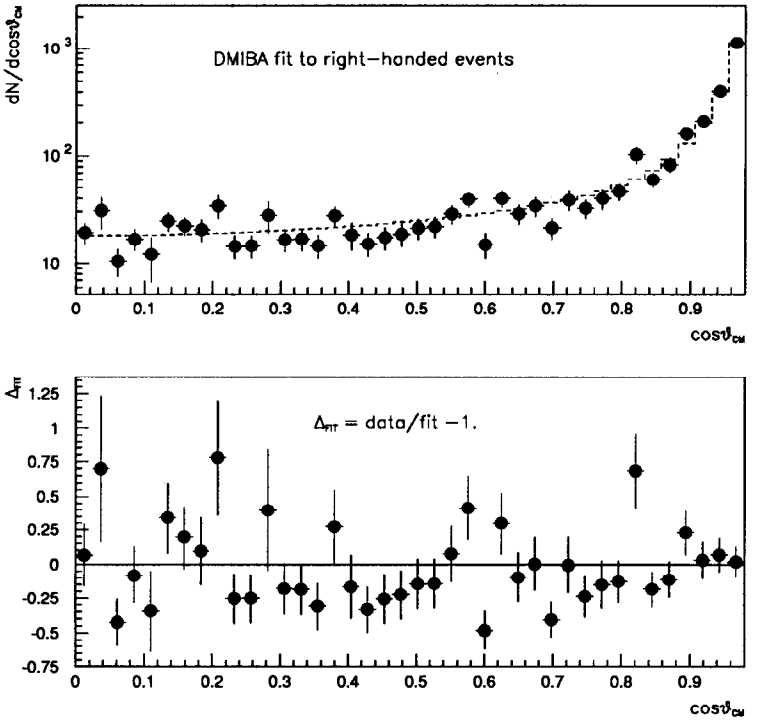

Figure 8.8: DMIBA LUM constrained fit to the corrected right handed wide angle Bhabha distribution. The points are the corrected data, the curve is the fit. The errors on the corrected data include the systematic uncertainty of the correction factors.

representing plumbing, cables and electronics are in the simulation in an average fashion. Inaccurate simulation of the module gaps exists in these regions as well, but are overwhelmed by the preshowering caused by the material in front of the calorimeter. For the intermediate region, the cluster multiplicity cut is the dominant source of uncertainty. This arises from inaccurate modeling of the location and density of the material in front of the calorimeter. The Monte Carlo demonstrates a much broader cluster multiplicity distribution than does the data, which means that a much larger correction is applied than should be. For the region from 0.6-0.7 in $cos\theta$ the simulation uncertainty is set to 5%. Further into the intermediate region, the cluster multiplicity and energy cut modeling become poorer and the uncertainty is raised to 10%.

In the case of the endcap, material again is by far the most dominant uncertainty. The quantity most poorly modeled in this region is the energy distribution. The cluster energy cut upon the energy of the second most energetic cluster leads to the largest uncertainty in that region, which is estimated to be approximately 10%.

For the wide angle fit to Γ_{ee}, the uncertainties in the endcap and intermediate regions lead to a large systematic error. This is because events in this region are providing the normalization for the distribution. In the case of the LUM-constrained fit, the measurement of Γ_{ee} depends most heavily on the luminosity and the barrel region, where the s-channel events dominate. In the case of the asymmetry fit, the correction factors largely cancel due to the left minus right nature of the fit. The corrections enter into A_e through the correlation with Γ_{ee}, which is at about the 10% level.

To estimate the effects of the efficiency uncertainties, the correction factors were varied in the fits by the size of these uncertainties. In addition, different bin sizes for the correction factors were used to verify that the staggered bins discussed in Section 7.5 do not bias the fits. For the case of the wide angle fit, the uncertainty in the efficiency corrections leads to an error of 6.0% in Γ_{ee}. For the LUM constrained fit, the uncertainty on Γ_{ee} arising from the correction factors is 2.1%. In the case of A_e in the direct fit, the uncertainty introduced from the efficiency uncertainty is 3.2%. Finally, for the helicity fit, the uncertainty in A_e arising from the efficiency factors is 3.2%.

8.4.2 Beam Energy

Two uncertainties arise pertaining to the energy of the colliding beams. First, the uncertainty on the mean center mass energy as measured by the WISRD is 20 MeV. The effect of this uncertainty is estimated by varying the center of mass energy in the fits by this amount. The uncertainty on Γ_{ee} is 0.51% in the wide-angle fit and 0.40% in the LUM constrained fit. The uncertainty on A_e from the error in the beam energy measurement is 1.5% for the direct fit, 1.4% for the helicity fit. The relative size of the two contributions maybe somewhat surprising, as the cross section is less sensitive to the center of mass energy than is the asymmetry. This arises from the

different energy dependence of the contributing terms to the differential cross section. It should be noted, however, that $A_{LR}^{e^+e^-}$ is much more sensitive to the center of mass energy than is A_{LR}, due to the energy dependence of the different e^+e^- contributions.

Secondly, the finite energy spread of the beams convolutes the cross section and asymmetry with a distribution of finite width. To estimate the magnitude of this effect, the unpolarized, left and right handed differential cross sections are calculated for many energies around the mean center of mass energy at several different angles. The convolution of the beam energy spread is then calculated, assuming a 0.2% width gaussian energy distribution for the positron beam and a 0.25% width gaussian distribution for the electron beam [87].

The effect of the beam energy spread is to lower the effective cross section by about 1.1% at $cos\theta = 0.1$, while lowering it 0.1% at $cos\theta = 0.9$. The effect on the partial width, Γ_{ee}, varies from 0.5% at large angles to 0.05% at small angles. The effect of the beam energy spread on the asymmetry raises it by 0.08% at large angles and by 0.7% at small angles. For simplicity, the maximum displacement at any angle will be taken as the size of the error due to this effect. It should be noted that the structure function approach of both DMIBA and EXPOSTAR should render it possible to include the effects of the beam energy spread directly into the differential cross section calculations of the fitters. This would allow for a straightforward method to correct for the finite beam energy spread.

8.4.3 Polarization

The systematic uncertainty on the electron beam polarization measurement are described elsewhere [101, 102] and summarized here.[8] The uncertainty in the magnitude of the electron beam polarization arises from the systematic uncertainties of the Compton polarimeter, as well as the uncertainty in the luminosity-weighted polarization.

The two dominant sources of uncertainty from the Compton polarimeter are the laser polarization and the detector linearity. The uncertainty in the laser polarization translates directly into an uncertainty on the electron beam polarization because the measured Compton scattering asymmetry is a product of the electron beam polarization and the photon beam polarization. Since the Compton polarimeter measures an asymmetry in counting rates for different electron-photon helicity combinations, any detector non-linearity translates into an uncertainty in the counting rate and, hence, the Compton asymmetry. The systematic uncertainties are listed in the top portion of Table 8.5. The total relative systematic error arising from the Compton polarimeter is 1.6%.

[8]The systematic errors listed here are preliminary results for the 1993 SLD run as reported in Reference [101]. The final results will differ very little (if any) and may be found in References [100] and [102]. Slight changes in the final results will have virtually no effect on the results presented here.

Table 8.5: Uncertainty on electron beam polarization.

Systematic uncertainty	$\delta\mathcal{P}_e/\mathcal{P}_e$
Laser polarization	1.0%
Detector linearity	1.0%
Interchannel consistency	0.5%
Electronic pickup/noise	0.2%
Spectrometer calibration	0.5%
Polarimeter total	1.6%
Energy/Polarization correlation uncertainty	1.1%
Total polarization uncertainty	1.9%

The uncertainty in the luminosity-weighted electron beam polarization may be summarized by saying that the polarization sampled by the positron beam (and therefore the luminosity-weighted polarization) is different than the polarization sampled by the photon beam at the Compton interaction point. The Compton laser is much larger in the transverse plane than the extracted electron beam, therefore the polarization is effectively a measure of the average polarization of the entire bunch. Most of the luminosity arises from the core of the beam. Since the beam tails are somewhat off-momentum, they have a polarization which is different than that of the core, which could bias the measurement of the Compton polarimeter [94]. The relative uncertainty arising from this effect is estimated to be 1.1%.

The total uncertainty on the beam polarization is 1.9%. Contributions to this uncertainty are summarized in Table 8.5.

8.4.4 Asymmetry Factors

Since the fit to A_e is a measure of the left-right asymmetry for the e^+e^- final state, systematic uncertainties arise from any underlying asymmetries due to detection efficiency and accelerator parameters. When these factors are included, the left-right asymmetry is written as follows [1, 103]:

$$A_{LR}^{e^+e^-} = \frac{A_m^{e^+e^-}}{\mathcal{P}_e} + \frac{1}{\mathcal{P}_e}\left[A_m^{e^+e^-} f_b + A_m^{e^+e^-2} A_{\mathcal{P}} - \sqrt{s}\frac{\sigma'(\sqrt{s})}{\sigma(\sqrt{s})} A_E - A_\epsilon - A_{\mathcal{L}}\right], \qquad (8.9)$$

where $A_m^{e^+e^-}$ is the measured asymmetry, f_b is the fraction of background events, $\sigma(\sqrt{s})$ is the cross section at center of mass energy $\sqrt{s}$, $\sigma'(\sqrt{s})$ is the derivative of

the cross section with respect to $\sqrt{s}$ and $A_{\mathcal{P}}$, A_E, A_ϵ, and $A_{\mathcal{L}}$ are the left-right asymmetries of the beam polarization, the center-of-mass energy, the product of detector acceptance and efficiency, and the integrated luminosity. The first term of the equation is the lowest order asymmetry and the terms which follow are correction factors. All of these factors are small, so no correction will be applied and the magnitude of the factors will be included as systematic errors.

Since the 1993 data sample dominates the fit for A_e, the following error estimations are made based on the 1993 SLD data sample. In all cases, the magnitude of the error is comparable or smaller for the 1992 contribution to the data sample. The term regarding background contamination was handled explicitly in Section 8.4.1 and will not be discussed here.

The polarization asymmetry is measured directly by the Compton polarimeter to be $A_{\mathcal{P}} = -3.5 \times 10^{-4}$ [100, 101].

The center-of-mass energy asymmetry is measured by the WISRD to be $A_E = 6 \times 10^{-6}$ [100, 101].[9] The multiplicative factor, $\sqrt{s}\frac{\sigma'(\sqrt{s})}{\sigma(\sqrt{s})}$, varies as a function of both energy and angle for the case of $A_{LR}^{e^+e^-}$. This term was calculated with EXPOSTAR for a number of different energies and angles. The maximum contribution arises at $cos\theta \simeq 0.7$ and is approximately equal to -42. Over the entire angular and energy range of the data sample, the factor ranges from -10 to -42. For simplicity, the maximum magnitude will be used to calculate the systematic error.

The A_ϵ term is the product of the detector acceptance times the efficiency, and can only be nonzero if the efficiency for detecting an electron at a given polar angle is different than the efficiency for detecting a positron at the same angle. The uniformity of the SLD calorimeter along with the azimuthally symmetric solenoidal magnetic field insures that this term does not contribute to the asymmetry.

The left-right luminosity asymmetry is measured directly by counting small angle Bhabhas detected in the luminosity monitor (see Sections 6.5.5 and 6.8). For the 1993 run, the asymmetry is measured to be $A_{\mathcal{L}} = A_{LR}^{exp}(LUM) = -0.0032 \pm 0.0023$. Since the luminosity asymmetry is slightly greater than one standard deviation from zero, the magnitude of the asymmetry itself will be taken as the error.[10]

To calculate the relative contribution to A_e, a measured asymmetry, $A_m^{e^+e^-}$ is assumed to be 0.10. The total systematic contribution to the measurement of A_e is 3.2%, dominated by the luminosity asymmetry. The systematic error contributions to A_e are summarized in Table 8.6.

[9] As with the systematic errors on the polarization measurement, the numbers listed here for $A_{\mathcal{P}}$ and A_E are 1993 SLD preliminary results as reported in [101]. The final results may differ from these preliminary numbers by a small amount and may be found in [100]. As may be seen from the text, these numbers have little or no effect on the results presented here.

[10] The systematic uncertainty on $A_{\mathcal{L}}$ may be improved through indirect measurement [1, 100]. However, the precision utilizing the direct result remains much smaller than the statistical error for this analysis.

Table 8.6: Asymmetry errors.

term	asymmetry	error factor	$\frac{\delta A_e}{A_e}$
$A_{\mathcal{P}}$	polarization	$A_m^{e^+e^-} A_{\mathcal{P}}$	0.04%
A_E	energy	$\sqrt{s}\frac{\sigma'(\sqrt{s})}{\sigma(\sqrt{s})}\frac{A_E}{A_m^{e^+e^-}}$	0.3%
A_ϵ	efficiency	$\frac{A_\epsilon}{A_m^{e^+e^-}}$	0
$A_{\mathcal{L}}$	luminosity	$\frac{A_{\mathcal{L}}}{A_m^{e^+e^-}}$	3.2%
total			3.2%

8.4.5 Fitting Programs

The uncertainty in the calculations performed by the fitting programs depends upon the level of accuracy of the calculations, as well as the degree of implementation of the fits. For DMIBA, the authors estimate the leading log calculation to be accurate to within 1% [97]. Comparison with the full second order calculation of provided by the program ALIBABA [99] agrees with this assessment.

The uncertainty of the EXPOSTAR calculation of the differential $e^+e^- \rightarrow e^+e^-$ cross section is estimated to be less than 0.5%. For this analysis, however, this estimate must be relaxed because an approximation is utilized in the calculation of the structure functions. Since the structure functions are dependent upon scattering angle in the e^+e^- process, proper handling of the structure functions would be to recalculate them at each angle. This, however, is not practical, therefore the structure functions are calculated of bins of approximately 0.1 in $cos\theta$ and the value of the structure function of the nearest bin is used. In comparing the shape of the distribution with DMIBA and ALIBABA, this approximation introduces an additional uncertainty of order 1%.

8.4.6 Inputs

Both fitters require information about the Z^0 resonance as input. DMIBA requires the mass of the Z^0, M_Z, and the total width, Γ_Z, as inputs to properly describe the resonance. EXPOSTAR requires the Z^0 mass and the mass of the Higgs boson, m_{Higgs} and the mass of the top quark, m_t.

The values used here to describe the resonance are the LEP average values: $M_Z = 91.187 \pm 0.007$ GeV and $\Gamma_Z = 2.489 \pm 0.007$ GeV [6]. For DMIBA, these input parameters were varied by the size of their errors in the fits to estimate the

uncertainty due to the inputs. The uncertainty in Γ_{ee} from the wide-angle fit is 0.43% from the Z^0 mass uncertainty and 0.20% due to the uncertainty in the total width. The uncertainty in Γ_{ee} in the LUM constrained fit is 0.13% from the Z^0 mass uncertainty and 0.30% due to the uncertainty in the total width. This translates into an uncertainty of 0.15% for the Z^0 mass and 0.18% from the total width in the helicity fit for A_e.

In the case of EXPOSTAR, the polarized wide angle Bhabha distribution was first fit for the top quark mass, m_t to find a preferred value. This was found to be $m_t = 238^{+87}_{-133}$ GeV, where the uncertainty is fit-statistical only. For the remaining fits, the top mass was set to this value. In theory, the same process should be followed for the mass of the Higgs boson. However, the dependence upon the Higgs mass is so weak, a reliable fit value can not be extracted from the current data.[11] Consequently, the Higgs boson mass was set to 300 GeV.

The Z^0 mass and top quark mass were then varied by their uncertainties to ascertain the effect on Γ_{ee} and $A_{LR}^{e^+e^-}$. Also, the Higgs boson mass was varied from 100 to 1000 GeV. The uncertainty in A_e is 0.10% from the mass of the Z^0, 0.70% from the top quark mass and 0.16% from the Higgs boson mass.

8.4.7 Luminosity

The error on the absolute luminosity enters into the measurement of Γ_{ee} and A_e when the fits are constrained by the luminosity measurement. As discussed in chapter VI, the systematic error on the luminosity measurement is 1.0%. The statistical error on the measurement is 0.61% for 1992 and 0.28% for 1993. The normalization was varied by the above factors in the luminosity constrained fit to the partial width and the magnitude found to be 0.80%.

The systematic error in the absolute luminosity determination also leads to an uncertainty in A_e in the helicity fits. This uncertainty actually enters through Γ_{ee}. The uncertainty in the luminosity leads to an uncertainty in the partial width. The uncertainty on the partial width then leads to a (small) uncertainty in A_e. The uncertainty in A_e in the helicity fit is found to be 0.29%. It should be noted that the uncertainty in A_e arising from the systematic error in the absolute luminosity measurement is different from the uncertainty from the left-right luminosity asymmetry, which was addressed in Section 8.4.4. The uncertainty addressed here arises from the error in the magnitude of the luminosity which is used to constrain the left- and right-handed fits.

[11] When the data sample presented here is fit for the Higgs boson mass, the fit returns $M_H = 0^{+2000}_{-0}$ GeV, indicating the data prefers a light Higgs boson, with enormous uncertainty.

Table 8.7: Summary of systematic errors. See Table 8.1 for fit definitions.

systematic (%)	Γ_{ee} wide angle	Γ_{ee} LUM constrained	A_e direct	A_e helicity
correction factors	6.0%	2.1%	3.2%	1.4%
beam energy	0.75	0.68	1.6	1.7
Polarization	-	-	1.9	1.9
Asymmetry Factors	-	-	3.2	3.2
fitting programs	1.0	1.0	1.0	1.0
inputs (M_Z,Γ_Z)	0.47	0.33	0.72	0.23
luminosity	-	0.80	-	0.29
total systematic	6.2%	2.6%	5.4%	4.6%

8.4.8 Summary of Systematic Errors

The systematic errors are summarized in Table 8.7. There are two different fits for Γ_{ee} and two different fits for A_e (as defined in Section 8.2.3). The systematic errors are not necessarily common for any of the fits and are therefore listed separately. In the case of Γ_{ee}, the LUM constrained fit provides a much smaller systematic uncertainty than does the wide angle fit. In the case of A_e, the systematic errors from the two methods are similar in origin and magnitude.

8.5 Measurement of $\overline{g}_v^e$ and $\overline{g}_a^e$

The results for Γ_{ee} and A_e from the previous section may now be used in equations 2.13 and 2.14 to extract the effective vector and axial vector couplings to the Z^0:

$$\overline{g}_v^e = -0.0495 \pm 0.0096 \text{ (stat)} \pm 0.0030 \text{ (sys)}$$

$$\overline{g}_a^e = -0.4977 \pm 0.0035 \text{ (stat)} \pm 0.0064 \text{ (sys)}.$$

For this result, the Γ_{ee} result from the LUM constrained fit is combined with the A_e result from the direct fit, as those results provide the smallest errors.[12]

The vector and axial vector couplings to the Z^0 may then be used through equation 2.21 to calculate the effective electroweak mixing angle:

$$sin^2\theta_W^{eff} = 0.2251 \pm 0.0049 \text{ (stat)} \pm 0.0015 \text{ (sys)}.$$

[12]Although the helicity fit yields a smaller systematic uncertainty for A_e, the increased statistical sample included in the direct fit provides a smaller overall error for A_e.

Figure 8.9 shows the 1 sigma (68%) contour for the electron vector and axial vector coupling to the Z^0. (This figure is a "zoom-in" of Figure 3.5.) The hatched region demonstrates the expected values for the couplings as calculated by the program ZFITTER [104], demonstrating the sensitivity of $\overline{g}_v^e$ on the mass of the top quark. The width of the hatched region corresponds to varying the minimal Standard Model Higgs boson mass from 50 to 1000 GeV. Figure 8.10 is the same as Figure 8.9, but includes the 68% contour when the left-right asymmetry measurement is included with the result presented here.

8.6 Comparison with Other Experiments

Figures 8.11 and 8.12 show the comparison between the results presented here for the effective electron vector and axial vector couplings and the results from the LEP experiments [6, 105]. Without the assumption of lepton universality, the electron vector and axial vector coupling may be extracted in an experiment with unpolarized beams by measuring Γ_{ee} and either the forward-backward asymmetry for electrons or the electron forward-backward asymmetry in τ decays. Both Figure 8.11 and 8.12 show the LEP averages for the effective electron vector and axial couplings to the Z^0 without the assumption of lepton universality. In both Figures, the top entry is the result presented here from fitting the polarized $e^+e^- \rightarrow e^+e^-$ distribution. The second entry in each figure shows the couplings extracted with the measurement of Γ_{ee} presented here with the SLD measurement of the left-right asymmetry [100].[13]

As can be seen from the figures, the error on the electron vector coupling to the Z^0 presented here compares favorably with the results from the LEP experiments, which have far greater statistics. This demonstrates the statistical gain from electron beam polarization. For the axial vector coupling to the Z^0, the result presented here agrees with the LEP experiments and shows far larger errors. These larger errors arise from both statistical and systematic considerations. The method utilized here poses larger systematic errors, but offers the reward of the extraction of both vector coupling as well as sensitivity to the entire $e^+e^- \rightarrow e^+e^-$ distribution.

The effective electroweak mixing angle, $sin^2\theta_W^{eff}$, is shown in Figure 8.13. The top entry is the result presented here. The second entry is the left-right asymmetry measurement from SLD. The entries from the LEP experiments are averages over all measurements of each quantity. (In the case of A_{fb}(leptons) and A_τ, the measurements from each experiment have errors which are about a factor of two larger than the error on the average value.) Included in Figure 8.13 are all of the LEP measurements for leptons. When measurements from hadronic final states are included (the forward-backward asymmetry for b and c quarks and the forward-backward jet charge measurement) the average remains at 0.2321 and the error is reduced to 0.0006 [6].

[13] As stated previously in this chapter, the SLD measurement of the left-right asymmetry shown here is preliminary. See reference [100] for the final result.

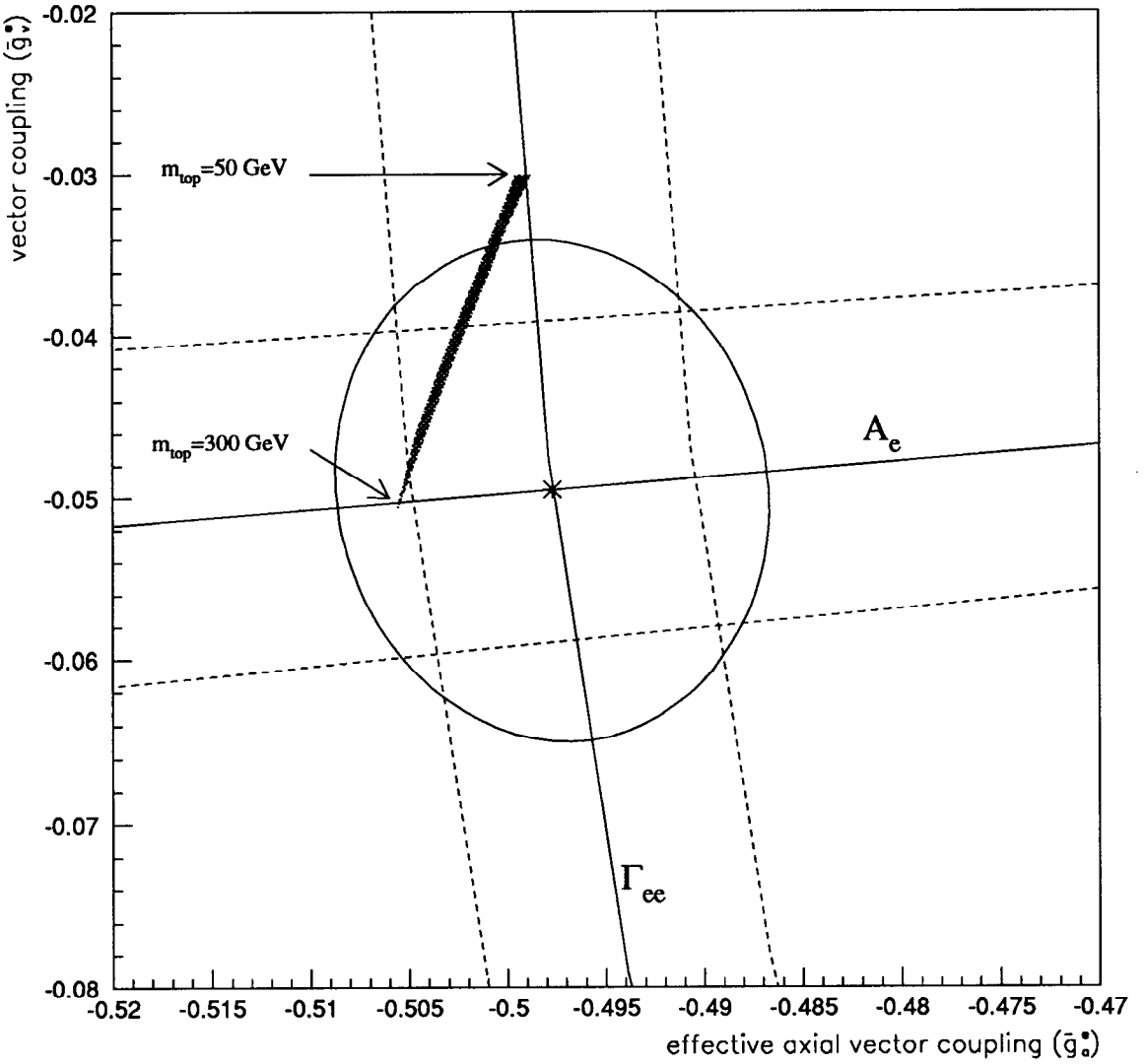

Figure 8.9: One standard deviation (68%) contour for $\overline{g}_v^e$ and $\overline{g}_a^e$. The hatched region indicates the Standard Model calculation as a function of the mass of the top quark and the Higgs boson. The width of the hatched region is the variation due to the uncertainty in the Higgs mass.

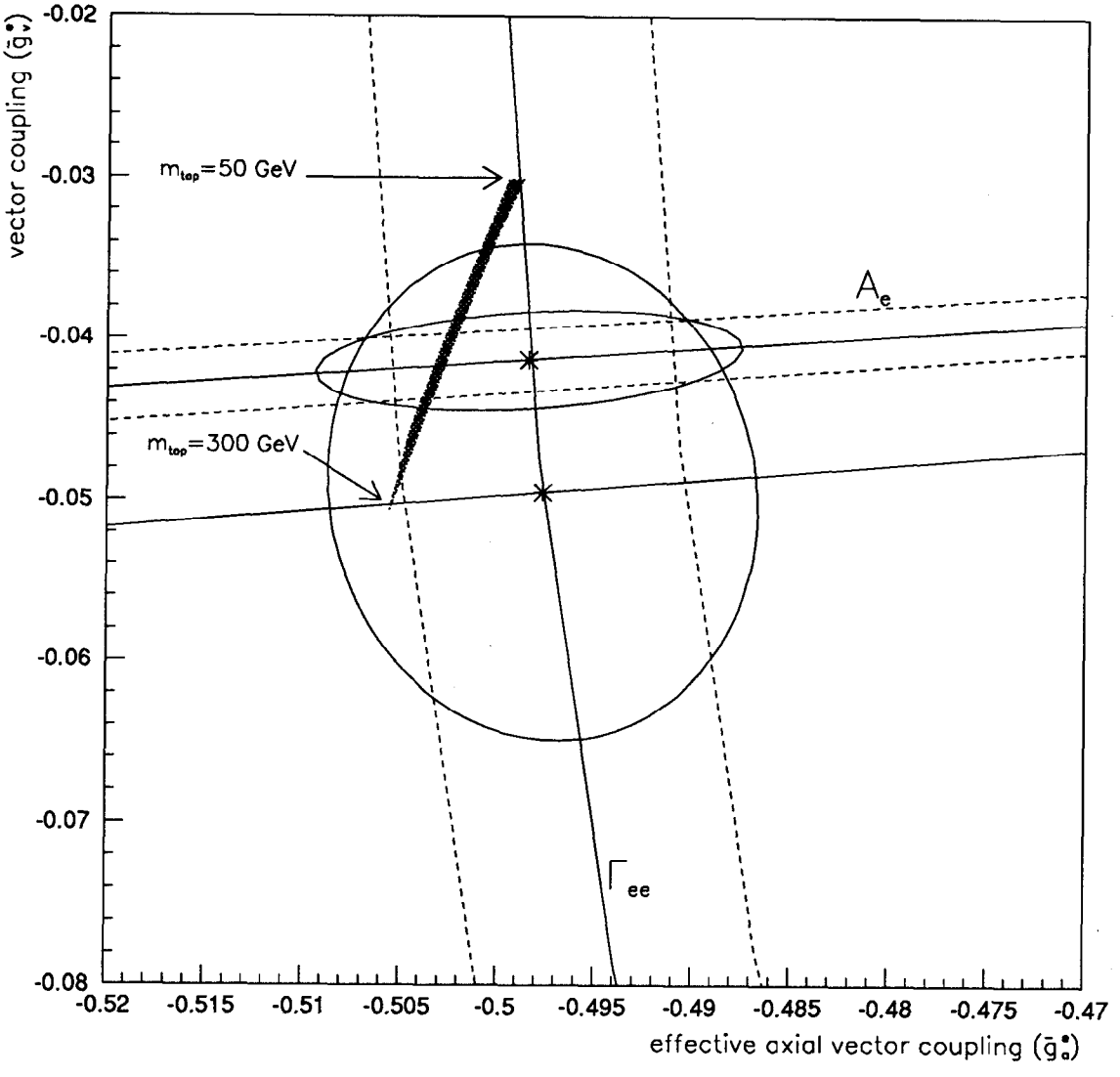

Figure 8.10: One standard deviation (68%) contours for $\overline{g}_v^e$ and $\overline{g}_a^e$. The large curve summarizes the results presented here and is identical to Figure 8.9. The smaller ellipse includes the preliminary measurement of the left-right asymmetry [100] with the results for Γ_{ee} and A_e presented here. The small statistical error of A_{LR} greatly improves the sensitivity to $\overline{g}_v^e$. The hatched region indicates the Standard Model calculation as a function of the mass of the top quark and the Higgs boson. The width of the hatched region is the variation due to the uncertainty in the Higgs mass.

The sensitivity to the electroweak mixing angle comes exclusively from the measurement of the electron vector coupling. It is interesting to note that the results from SLD agree with the LEP average electron vector coupling at a level of 1.2 standard deviations or less yet disagree with the LEP lepton average by much more. This arises from the LEP measurements of the muon forward-backward asymmetry and the tau polarization asymmetry, which pull the effective lepton vector coupling towards larger values.

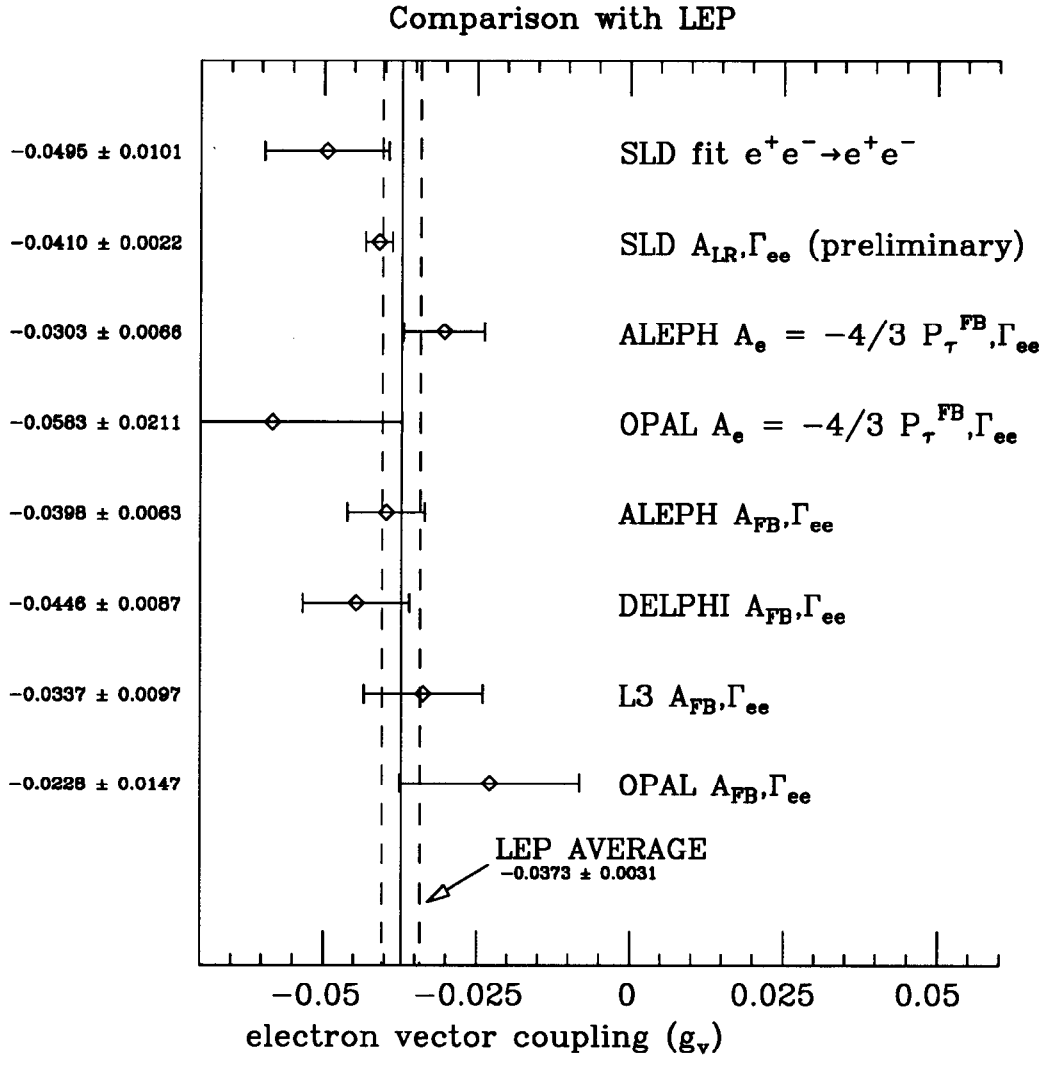

Figure 8.11: Comparison of the electron vector coupling with other experiments.

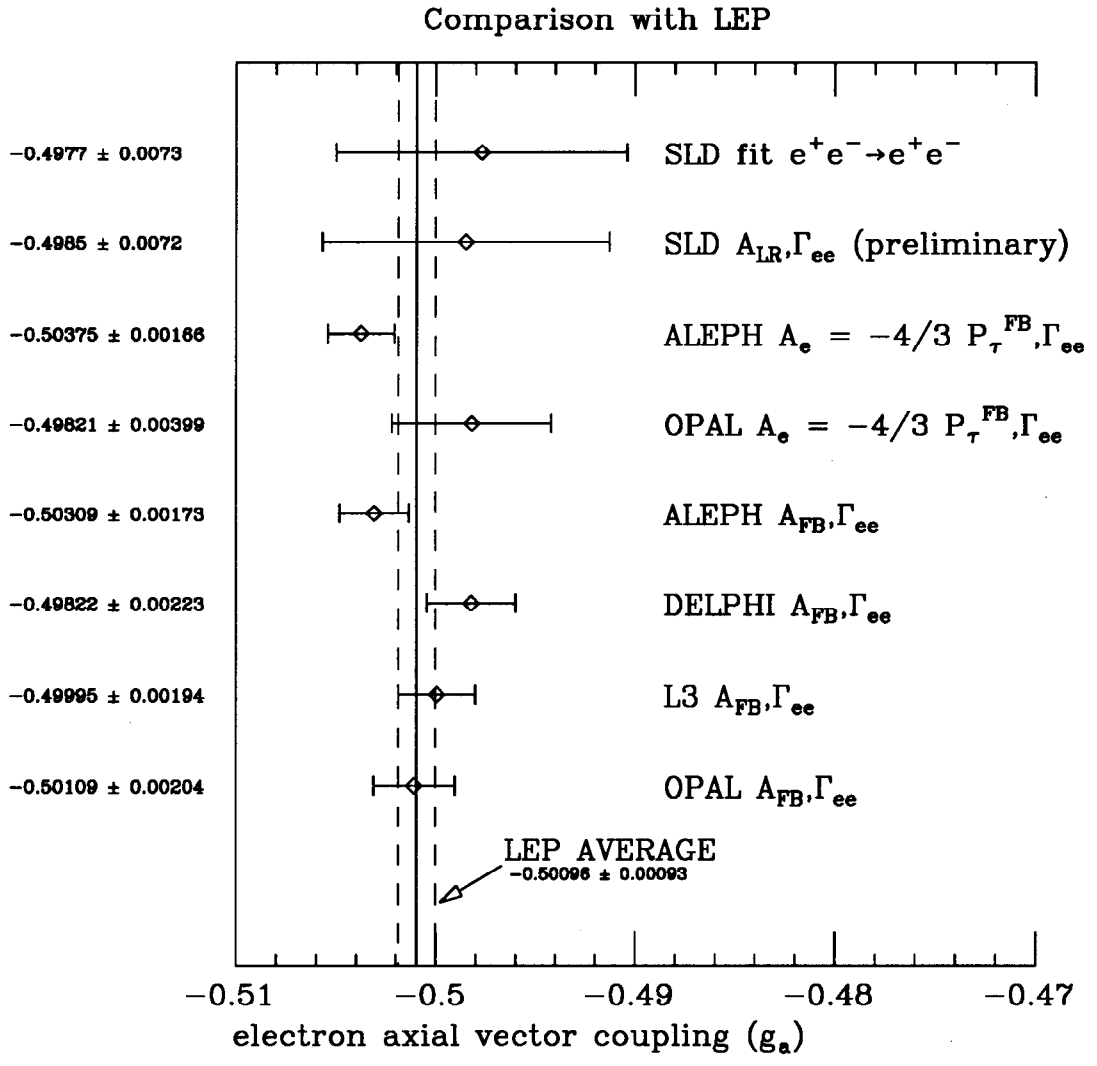

Figure 8.12: Comparison of the electron axial vector coupling with other experiments.

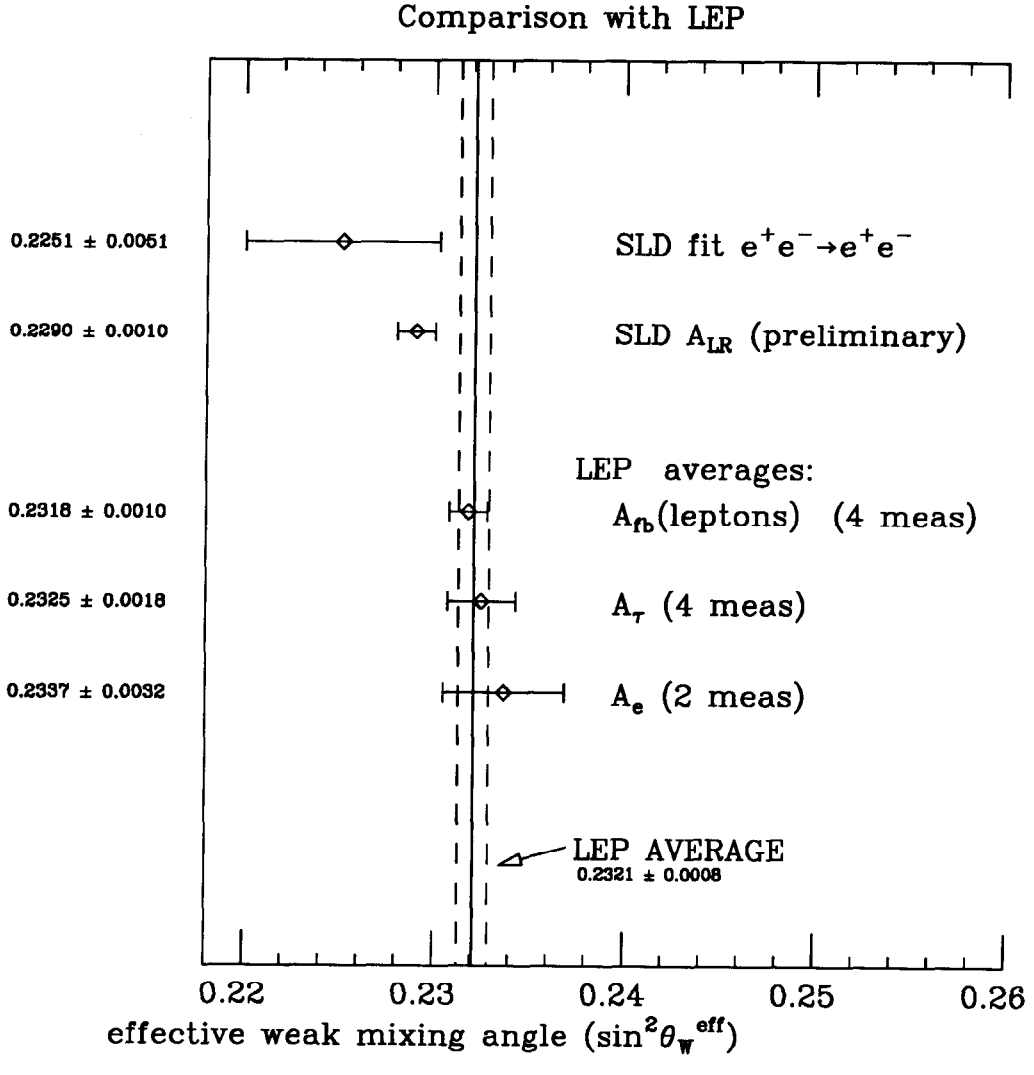

Figure 8.13: Comparison of $sin^2\theta_W^{eff}$ with other experiments.

8.7 Discussion

In comparison with the LEP results from the lepton forward-backward asymmetries (assuming universality) at the Z^0 peak, the A_e result presented here is slightly greater than one standard deviation above the LEP average. This result becomes more compelling when considered in conjunction with the measurement of A_{LR}, which, with much smaller errors, shows a 2.4 standard deviation with the LEP average value for the weak mixing angle.[14]

Taken by themselves within the framework of the minimal Standard Model the measurements of A_e from the left-right cross section asymmetry indicate a large top quark mass ($m_{top} \sim 230$ GeV). The global fits to LEP data yield an expected top quark mass of 166 GeV. When the LEP data is subdivided, the Z^0 mass and width data seems to prefer a lower top quark mass than does the asymmetry data [106].

Once the top quark is discovered (hopefully very soon at the TeVatron) the precision measurements at the Z^0 resonance can be analyzed in terms of the mass of the Higgs boson and/or physics beyond the Standard Model. If the mass of top quark is measured to be in the 150-175 GeV range, then the small values of $sin^2\theta_W^{eff}$ measured at SLC may well be an indication of physics beyond the Standard Model.

The types of new physics processes which may explain the results from LEP and SLC[15] are those in which new particles which do not couple directly to the fermions of the Standard Model. These additional particles enter measurements at the Z^0 resonance through oblique radiative corrections. The particles could be supersymmetric, massive Majorana particles or dileptons [24, 107].

A second possible explanation of these results is existence of an additional gauge boson. As described in Section 3.3.1, an additional neutral gauge boson (Z') would mix with the Z^0. Since the Z' couplings to left- and right-handed fermions are not necessarily the same as those of the Z^0, the mixing between the two bosons could modify the magnitude of the left-right asymmetry. This effect would also modify the differential Bhabha scattering distribution, but the largest interference term is of order 10^{-4} times the Standard Model cross section for $m_{Z'} \sim 500$ GeV. Therefore, an additional gauge boson could manifest itself by means of a modification of the left-right asymmetry without showing up in the differential $e^+e^- \rightarrow e^+e^-$ distribution [24].

Upon the discovery of the top quark, it may also become possible to rule out some Standard Model extensions. First, the left-right asymmetry (as well as the LEP results) do not appear to be consistent with the predictions of most technicolor theories. Secondly, although the measurements do not rule out fourth generation fermions, their existence is not sufficient (regardless of the mass splitting of the isospin doublet) to explain the results discussed above [32].

[14]The discrepancy grows to 2.7 standard deviations when the LEP hadronic asymmetries are included.

[15]In terms of the S,T,U formalism of Peskin and Takeuchi [32] the left-right asymmetry results as well as the LEP results lead to negative S.

Continued improvement of the precision electroweak measurements from LEP and SLC, as well as the discovery of the top quark at TeVatron will most likely be the first glimpse into the true nature of electroweak symmetry breaking and possibly physics beyond the Standard Model. The results achieved so far are very impressive. Further improvements will insure that the near future is an exiting time.

8.8 Conclusion

From the Bhabha scattering at the Z^0 resonance with a polarized electron beam, we have measured the parity violating parameter, A_e, to be $A_e = 0.197 \pm 0.038$ (stat)$\pm$ 0.011 (sys) and the partial width for the Z^0 decaying to electrons to be $\Gamma_{ee} = 83.14 \pm$ 1.04 (stat) $\pm$ 2.16 (sys) MeV. These results are then used extract effective electron vector and axial vector couplings: $\overline{g}_v^e = -0.0495 \pm 0.0096 \pm 0.0030$, and $\overline{g}_a^e = -0.4977 \pm$ 0.0035 $\pm$ 0.0064. The effective weak mixing angle is measured to be $sin^2\theta_W^{eff} =$ 0.2251 $\pm$ 0.0049 $\pm$ 0.0015.

If the top quark is discovered soon at the TeVatron in the mass range 150-175 GeV, then the polarized beam A_e measurements could point to physics beyond the Standard Model. Further improvements in both measurements would clarify this. It should be noted that A_{LR} will always be statistically and systematically more powerful than the measurement of A_e presented in this thesis. The measurement does, however, provide an important cross check, as well as a way to isolate the electron couplings to the neutral current.

There are several ways in which this analysis may be improved. As stated in Section 2.3, the statistical error in A_e improves as $\sqrt{\mathcal{L}\mathcal{P}_e^2}$. Therefore, an increase in beam polarization would give each event a greater weight, effectively improving the statistics. The A_e measurement is statistically limited. If we assume that the systematic error does not change and the polarization remains constant at 65%, a factor of 13 in statistics is required for the statistical error to reach the current systematic error. However, if the beam polarization becomes 80% for subsequent SLD runs, then a factor of 8.5 in statistics is required.

The prospects for improved polarization in subsequent SLD runs is very good. The latest generation of cathodes have been shown to produce electron polarizations above 80% [108].

Additionally, the inclusion of tracking information into the analysis would allow a fit to the forward and backward angular region. More information is available in the form of the polarized forward-backward asymmetry. This essentially allows the isolation of A_e from the final state $Z^0e^+e^-$ vertex. This avenue would be particularly compelling if the SLD A_{LR} result continues to show a discrepancy with the LEP forward-backward asymmetry results. Fitting the polarized differential Bhabha distribution with the forward-backward asymmetry included would allow for simultaneous extraction of $A_e^{initial}$ and A_e^{final} which are identical parameters within the Standard Model.

For the measurement of the partial width, Γ_{ee}, the results presented here are systematics limited. This is primarily a function of the fitting method utilized in this analysis with the primary focus on extracting A_e. It is most certainly possible to obtain smaller systematic errors on the partial width by measuring the cross section over the central region of the detector. This is the preferred method at LEP and has also been done with the 1992 SLD data [87]. Ideally, both methods should be incorporated to measure the partial width as precisely as possible, while still fitting the entire angular distribution to maintain sensitivity to potential physics beyond the Standard Model.

CHAPTER IX

CONCLUSION

Bhabha scattering, $e^+e^- \rightarrow e^+e^-$, at the Z^0 resonance has been utilized to extract the electron electroweak parameters. We have measured the parity violating parameter, A_e, to be $A_e = 0.197 \pm 0.038$ (stat) $\pm$ 0.011 (sys) and the partial width for the Z^0 decaying to electrons to be $\Gamma_{ee} = 83.14 \pm 1.04$ (stat) $\pm$ 2.16 (sys) MeV. These results are then used extract effective electron vector and axial vector couplings, $\overline{g}_v^e = -0.0495 \pm 0.0096 \pm 0.0030$, and $\overline{g}_a^e = -0.4977 \pm 0.0035 \pm 0.0064$ respectively. The effective weak mixing angle is measured to be $sin^2\theta_W^{eff} = 0.2251 \pm 0.0049 \pm 0.0015$.

Also presented here was a detailed description of the design, construction, testing, installation and commissioning of the SLD Silicon/Tungsten Luminosity Monitor. Utilizing this device, we have measured the luminosity for the 1992 SLD run to be 35.51 $\pm$ 0.68 (stat) $\pm$ 0.36 (sys) nb^{-1} for unpolarized running and 385.37 $\pm$ 2.47 (stat) $\pm$ 3.89 (sys) nb^{-1} for polarized running. The systematic error of 1.01% is comprised of 0.88% experimental error and 0.5% theoretical uncertainty.

For both the physics measurements and the luminosity measurement presented here the future looks promising. With continued improvement in SLC luminosity and electron beam polarization, the $e^+e^- \rightarrow e^+e^-$ process at wide angles should provide a world competitive measurement of the electron vector and axial vector couplings to the Z^0. The systematic error on the luminosity measurement will improve as well and will continue to play an important roll in future measurements made with the SLD.

APPENDIX A

PROBABILITY FUNCTION FOR POLARIZED SCATTERING

For the case of unpolarized scattering, the probability function is the differential cross section normalized to the total cross section:

$$p_i = \frac{\frac{d\sigma}{dz}|_{unpol}}{\sigma_{tot}}, \tag{A.1}$$

where $z \equiv cos\theta$. Since the differential cross section is simply the average of the left- and right-handed differential cross section, equation A.1 can be recast:

$$p_i = \frac{\frac{d\sigma}{dz}|_{left} + \frac{d\sigma}{dz}|_{right}}{2\sigma_{tot}}. \tag{A.2}$$

When the electron beam polarization is less than 100%, the left- and right-handed differential cross sections must be rewritten:

$$\begin{aligned} \frac{d\sigma}{dz}|_{left} &\rightarrow (\frac{1}{2} + \frac{\mathcal{P}_e}{2})\frac{d\sigma}{dz}|_{left} \\ \frac{d\sigma}{dz}|_{right} &\rightarrow (\frac{1}{2} - \frac{\mathcal{P}_e}{2})\frac{d\sigma}{dz}|_{right}, \end{aligned} \tag{A.3}$$

which accounts for the fraction of left-(right-)handed electrons in a beam which is right-(left-)handed. As an example, for the case where the polarization is $\mathcal{P}_e = +50\%$, the relationships in A.3 show that the ratio will be 75% left-handed and 25% right-handed, as expected. When the polarization is $\mathcal{P}_e = -50\%$, the ratio is 25% left-handed and 75% right-handed.

Substituting equation A.3 into equation A.2:

$$p_i = \frac{(\frac{1}{2} + \frac{\mathcal{P}_e}{2})\frac{d\sigma}{dz}|_{left} + (\frac{1}{2} - \frac{\mathcal{P}_e}{2})\frac{d\sigma}{dz}|_{right}}{2\sigma_{tot}}, \tag{A.4}$$

which reduces to:

$$p_i = \frac{2\frac{d\sigma}{dz}|_{unpol} + \mathcal{P}_e(\frac{d\sigma}{dz}|_{left} - \frac{d\sigma}{dz}|_{right})}{4\sigma_{total}}, \tag{A.5}$$

which is equation 8.5.

In fitting the differential distributions for Bhabha scattering, the experimentally accessible quantities are the number of events and the luminosity. Substituting $\frac{dn}{dz} = \mathcal{L}\frac{d\sigma}{dz}$ into equation A.4:

$$p_i = \frac{\frac{1}{\mathcal{L}_{left}}(\frac{1}{2} + \frac{\mathcal{P}_e}{2})\frac{dn}{dz}|_{left} + \frac{1}{\mathcal{L}_{right}}(\frac{1}{2} - \frac{\mathcal{P}_e}{2})\frac{dn}{dz}|_{right}}{\frac{2n_{tot}}{\mathcal{L}_{tot}}}, \tag{A.6}$$

where $\mathcal{L}_{left}(\mathcal{L}_{right})$ is the left-(right-)handed luminosity. The total luminosity, $\mathcal{L}_{tot}$, is the sum of the left- and right-handed luminosities.

Assuming that the left- and right-handed luminosities are equal, equation A.6 reduces to:

$$p_i = \frac{2\frac{dn}{dz}|_{unpol} + \mathcal{P}_e(\frac{dn}{dz}|_{left} - \frac{dn}{dz}|_{right})}{2n_{total}}, \tag{A.7}$$

which is functionally identical to equation A.5. Therefore, the differential event distributions ($\frac{dn}{dz}$) for polarized beams may be directly compared to the differential cross sections. The overall factor of two difference does not affect the maximum likelihood fit, as multiplication by a constant does not change the location of the maxima or the error.

APPENDIX B

THE SLD COLLABORATION

K. Abe,[18] I. Abt,[25] W.W. Ash,[17] D. Aston,[17] N. Bacchetta,[9]
K.G. Baird,[15] C. Baltay,[34] H.R. Band,[32] M.B. Barakat,[34]
G. Baranko,[23] O. Bardon,[13] R. Battiston,[10] A.O. Bazarko,[5]
A. Bean,[20] R.J. Belcinski,[26] R. Ben-David,[34] A.C. Benvenuti,[7]
M. Biasini,[10] T. Bienz,[17] G.M. Bilei,[10] D. Bisello,[9] G. Blaylock,[21]
J. R. Bogart,[17] T. Bolton,[5] G.R. Bower,[17] J. E. Brau,[27]
M. Breidenbach,[17] W.M. Bugg,[29] D. Burke,[17] T.H. Burnett,[31]
P.N. Burrows,[13] W. Busza,[13] A. Calcaterra,[6] D.O. Caldwell,[20]
D. Calloway,[17] B. Camanzi,[8] M. Carpinelli,[11] J. Carr,[23] R. Cassell,[17]
R. Castaldi,[11] [24] A. Castro,[9] M. Cavalli-Sforza,[21] G.B. Chadwick,[17]
L. Chen,[33] E. Church,[31] R. Claus,[17] H.O. Cohn,[29] J.A. Coller,[2]
V. Cook,[31] R. Cotton,[3] R.F. Cowan,[13] P.A. Coyle,[21] D.G. Coyne,[21]
A. D'Oliveira,[22] C.J.S. Damerell,[16] S. Dasu,[17] R. De Sangro,[6]
P. De Simone,[6] S. De Simone,[6] R. Dell'Orso,[11] P.Y.C. Du,[29]
R. Dubois,[17] J.E. Duboscq,[20] B.I. Eisenstein,[25] R. Elia,[17] E. Erdos,[23]
C. Fan,[23] B. Farhat,[13] M.J. Fero,[13] R. Frey,[27] J.I. Friedman,[13]
K. Furuno,[27] M. Gallinaro,[6] A. Gillman,[16] G. Gladding,[25]
S. Gonzalez,[13] G.D. Hallewell,[17] T. Hansl-Kozanecka,[13] E.L. Hart,[29]
K. Hasegawa,[18] Y. Hasegawa,[18] S. Hedges,[3] S.S. Hertzbach,[26]
M.D. Hildreth,[17] D.G. Hitlin,[4] A. Honma,[30] J. Huber,[27] M.E. Huffer,[17]
E.W. Hughes,[17] H. Hwang,[27] Y. Iwasaki,[18] J.M. Izen,[25] P. Jacques,[15]
A.S. Johnson,[2] J.R. Johnson,[32] R.A. Johnson,[22] T. Junk,[17]
R. Kajikawa,[14] M. Kalelkar,[15] I. Karliner,[25] H. Kawahara,[17]
M.H. Kelsey,[4] H.W. Kendall,[13] H.Y. Kim,[31] M.E. King,[17] R. King,[17]
R.R. Kofler,[26] N.M. Krishna,[23] R.S. Kroeger,[29] Y. Kwon,[17]
J.F. Labs,[17] M. Langston,[27] A. Lath,[13] J.A. Lauber,[23] D.W.G. Leith,[17]
X. Liu,[21] M. Loreti,[9] A. Lu,[20] H.L. Lynch,[17] J. Ma,[31] W.A. Majid,[25]
G. Mancinelli,[10] S. Manly,[34] G. Mantovani,[10] T.W. Markiewicz,[17]
T. Maruyama,[17] H. Masuda,[17] E. Mazzucato,[8] J.F. McGowan,[25]
S. McHugh,[20] A.K. McKemey,[3] B.T. Meadows,[22] D.J. Mellor,[25]
R. Messner,[17] P.M. Mockett,[31] K.C. Moffeit,[17] B. Mours,[17]

G. Müller,[17] D. Muller,[17] T. Nagamine,[17] U. Nauenberg,[23] H. Neal,[17]
M. Nussbaum,[22] L.S. Osborne,[13] R.S. Panvini,[33] H. Park,[27]
M. Pauluzzi,[10] T.J. Pavel,[17] F. Perrier,[17] I. Peruzzi,[6] [28] L. Pescara,[9]
M. Petradza,[17] M. Piccolo,[6] L. Piemontese,[8] E. Pieroni,[11] K.T. Pitts,[27]
R.J. Plano,[15] R. Prepost,[32] C.Y. Prescott,[17] G.D. Punkar,[17]
J. Quigley,[13] B.N. Ratcliff,[17] T.W. Reeves,[33] P.E. Rensing,[17]
J.D. Richman,[20] L.S. Rochester,[17] L. Rosenson,[13] J.E. Rothberg,[31]
S. Rousakov,[33] P.C. Rowson,[5] J.J. Russell,[17] P. Saez,[17]
O.H. Saxton,[17] T. Schalk,[21] R.H. Schindler,[17] U. Schneekloth,[13]
D. Schultz,[17] B.A. Schumm,[12] A. Seiden,[21] S. Sen,[34] L. Servoli,[10]
M.H. Shaevitz,[5] J.T. Shank,[2] G. Shapiro,[12] S.L. Shapiro,[17]
D.J. Sherden,[17] R.L. Shypit,[19] C. Simopoulos,[17] S.R. Smith,[17]
J.A. Snyder,[34] M.D. Sokoloff,[22] P. Stamer,[15] H. Steiner,[12] R. Steiner,[1]
I.E. Stockdale,[22] M.G. Strauss,[26] D. Su,[16] F. Suekane,[18] A. Sugiyama,[14]
S. Suzuki,[14] M. Swartz,[17] A. Szumilo,[31] T. Takahashi,[17] F.E. Taylor,[13]
J.J. Thaler,[25] N. Toge,[17] E. Torrence,[13] M. Turcotte,[30] J.D. Turk,[34]
T. Usher,[17] J. Va'vra,[17] C. Vannini,[11] E. Vella,[17] J.P. Venuti,[33]
R. Verdier,[13] P.G. Verdini,[11] S. Wagner,[17] A.P. Waite,[17] S.J. Watts,[3]
A.W. Weidemann,[29] J.S. Whitaker,[2] S.L. White,[29] F.J. Wickens,[16]
D.A. Williams,[21] D.C. Williams,[13] S.H. Williams,[17] S. Willocq,[34]
R.J. Wilson,[2] W.J. Wisniewski,[4] M.S. Witherell,[20] M. Woods,[17]
G.B. Word,[15] J. Wyss,[9] R.K. Yamamoto,[13] J.M. Yamartino,[13]
S.J. Yellin,[20] C.C. Young,[17] H. Yuta,[18] G. Zapalac,[32] R.W. Zdarko,[17]
C. Zeitlin,[27] J. Zhou,[27] M. Zolotorev,[17] and P. Zucchelli[8]

[1] Adelphi University
[2] Boston University
[3] Brunel University
[4] California Institute of Technology
[5] Columbia University
[6] INFN Lab. Nazionali di Frascati
[7] INFN Sezione di Bologna
[8] INFN Sezione di Ferrara and Universitá di Ferrara
[9] INFN Sezione di Padova and Universitá di Padova
[10] INFN Sezione di Perugia and Universitá Perugia
[11] INFN Sezione di Pisa and Universitá di Pisa
[12] Lawrence Berkeley Laboratory, University of California
[13] Massachusetts Institute of Technology
[14] Nagoya University
[15] Rutgers University
[16] Rutherford Appleton Laboratory
[17] Stanford Linear Accelerator Center

[18] Tohoku University
[19] University of British Columbia
[20] University of California, Santa Barbara
[21] University of California, Santa Cruz
[22] University of Cincinnati
[23] University of Colorado
[24] Universitá di Genova
[25] University of Illinois
[26] University of Massachusetts
[27] University of Oregon
[28] Universitá di Perugia
[29] University of Tennessee
[30] University of Victoria
[31] University of Washington
[32] University of Wisconsin
[33] Vanderbilt University
[34] Yale University

Bibliography

[1] SLD Collaboration, K. Abe *et al.*, Phys. Rev. Lett. **70**, 2515 (1993).

[2] S.L. Glashow, Nucl. Phys. **22**, 519 (1961); S. Weinberg, Phys. Rev. Lett. **19**, 1264 (1967); A. Salam, in *Elementary Particle Theory*, edited by N. Svartholm (Almqvist and Wiksell, Stockholm, 1968).

[3] D.H. Perkins, *Introduction to High Energy Physics*, (Addison-Wesley, Reading, MA, 1982); F. Halzen and A.D. Marten, *Quarks and Leptons: An Introductory Course in Modern Particle Physics*, (Wiley, New York, 1984).

[4] M. Aguilar-Benitez *et al.*, Phys. Rev. D **45**, S1 (1992).

[5] UA1 Collaboration, G. Arnison *et al.*, Phys. Lett. B **122**, 77 (1983); UA1 Collaboration, G. Arnison *et al.*, Phys. Lett. B **126**, 298 (1983).

[6] The LEP Collaborations and The LEP Electroweak Working Group, Report No. CERN-PPE-93-157, August, 1993.

[7] T. Hansl-Kozanecki, SLAC-Report-354, 50 (1989).

[8] M.L. Swartz, Report No. SLAC-PUB-5219, March 1990.

[9] D.C. Kennedy *et al.*, Nucl. Phys. **B321**, 83 (1989).

[10] M. Böhm and W. Hollik, Nucl. Phys. **B204**, 45 (1982).

[11] B. Lynn *et al.*, Report No. CERN 86-02, Volume 1, 90 (1986).

[12] J.P. Alexander, G. Bonvicini, P.S. Drell and R. Frey, Phys. Rev. D **37**, 56 (1988).

[13] This follows the convention used by the LEP Collaborations in Phys. Lett. B **276**, 247 (1992).

[14] H.J. Bhabha, Proc. Roy. Soc. A **154**, 159 (1935).

[15] M. Consoli, S. Lo Presti, and M. Greco, Phys. Lett B **113**, 415 (1982); M. Greco, Nucl. Phys. **B177**, 97 (1986).

[16] R. Battiston *et al.*, Z. Phys. C **46**, 329 (1990).

[17] M. Cacciari, G. Montagna, O. Nicrosini and G. Passarino, Phys. Lett. B **279**, 384 (1992); D. Bardin, W. Hollik and T. Riemann, Z. Phys. C **49**, 485 (1991); S. Jadach, E. Richter-Waş, B.F.L. Ward and Z. Waş, Phys. Lett. B **253**, 469 (1991); M. Cacciari *et al.*, Phys. Lett. B **268**, 441 (1991); F. Aversa, M. Greco, G. Montagna and O. Nicrosini, Phys. Lett. B **247**, 93 (1990); M. Caffo and E. Remiddi, Report No. CERN 89-08, Volume 1, 171 (1989).

[18] ALEPH Collaboration, D. Decamp *et al.*, Z. Phys. C **60**, 71 (1993); DELPHI Collaboration, P. Abreu *et al.*, Phys. Lett. B 241, 425 (1990); L3 Collaboration, B. Adeva *et al.*, Phys. Lett. B **238**, 122 (1990); OPAL Collaboration, R. Akers *et al.*, Z. Phys. C **61**, 19 (1994).

[19] U. Amaldi *et al.*, Phys. Rev. D **36**, 1385 (1987); J. Dorenbosch *et al.*, Z. Phys. C **41**, 567 (1989).

[20] R. Gatto *et al.*, Report No. CERN 89-08, Volume 2, 147 (1989); G. Belanger and S. Godfrey, Phys. Rev. D **34**, 1309 (1986).

[21] CDF Collaboration, F. Abe *et al.*, Phys. Rev. Lett. **68**, 1463 (1992).

[22] L3 Collaboration, O. Adriane *et al.*, Report No. CERN-PPE-93-44, March 1993.

[23] T.G. Rizzo, Phys. Rev. D **34**, 2699 (1986).

[24] J.L. Hewett and T.G.Rizzo, Z. Phys. C **36**, 209 (1987); J.L. Hewett and T.G.Rizzo, Phys. Rept. **183**, 193 (1989).

[25] J. Pati and A. Salam, Phys. Rev. D **10**, 275 (1974).

[26] F. Boudjema *et al.*, Report No. CERN 89-08, Volume 2, 185 (1989).

[27] E.J. Eichten, K.D. Lane and M.E. Peskin, Phys. Rev. Lett. **50**, 811 (1983); I. Bars, J.F. Gunion and M. Kwan, Phys. Rev. D **34**, 122 (1986).

[28] ZEUS Collaboration, M. Derrick *et al.*, Phys. Lett B **316**, 207 (1993).

[29] B. Schrempp *et al.*, Nucl. Phys. B **296**, 1 (1988); ALEPH Collaboration, D. Buskulic, *et al.*, Z. Phys. C **59**, 215 (1993).

[30] ALEPH Collaboration, D. Decamp *et al.*, Phys. Lett. B **236**, 511 (1990); DELPHI Collaboration, P. Abreu *et al.*, Phys. Lett. B **274**, 230 (1992); L3 Collaboration, B. Adeva *et al.*, Phys. Lett. B **251**, 321 (1990); OPAL Collaboration, M. Akrawy *et al.*, Phys. Lett. B **240**, 250 (1990); MARK II Collaboration, P. Burchat *et al.*, Phys. Rev. D **41**, 3542 (1990).

[31] CDF Collaboration, F. Abe *et al.*, Phys. Rev. Lett. **64**, 147 (1990).

[32] M.E. Peskin and T. Takeuchi, Phys. Rev. D **46**, 381 (1992).

[33] The SLC Design Report, SLAC Report 229, 1980.

[34] D. Blockus *et al.*, Proposal for Polarization at the SLC, April 1986.

[35] T. Maruyama *et al.*, Phys. Rev. Lett. **66**, 2351 (1991); T. Nakanishi *et al.*, Nagoya University Preprint DPNU-91-23, (1991).

[36] C. Adolphson *et al.*, Report No. SLAC-PUB-6118, May 1993.

[37] T. Limberg, P. Emma and R. Rossmanith, Report No. SLAC-PUB-6210, May 1993.

[38] The SLD Design Report, SLAC Report 273, 1984.

[39] G. Agnew *et al.*, Report No. SLAC-PUB-5906, in *Dallas HEP 1992*, 1862 (QCD161:I41:1992).

[40] M. Cavalli-Sforza *et al.*, IEEE Trans. Nucl. Sci. **37**, 1132 (1990); K. Abe *et al.*, Report No. SLAC-PUB-6399, November 1993.

[41] D. Axen *et al.*, Nucl. Inst. Meth. **A328**, 472 (1993); E. Vella *et al.*, Report No. SLAC-PUB-5953, October 1992.

[42] J.E. Brau and T.A. Gabriel, Nucl. Instr. Meth. **A279**, 40 (1989).

[43] A.C. Benvenuti *et al.*, Nucl.Instr.Meth. **A276**, 94(1989).

[44] J.A. Nash, Ph. D. Thesis, SLAC-Report-356, 1990.

[45] O. Chamberlain *et al.*, Report No. SLCPOL Note #3, September 1985.

[46] M.J. Fero *et al.*, Report No. SLAC-PUB-6026, December 1992.

[47] S.C. Berridge *et al.*, IEEE Trans. Nucl. Sci. **39**, 1242 (1992).

[48] U. Amaldi, Physica Scripta **23**, 409 (1981).

[49] S.C. Berridge *et al.*, IEEE Trans. Nucl. Sci. **36**, 339 (1989).

[50] G. Haller *et al.*, IEEE Trans. Nucl. Sci. **34**, 170 (1987); G. Haller *et al.*, IEEE Trans. Nucl. Sci. **36**, 675 (1988); E. Vella *et al.*, IEEE Trans. Nucl. Sci. **36**, 822 (1988); J.D. Fox *et al.*, Nucl. Phys. **B23** (Proc. Suppl.), 227 (1991).

[51] K. Einsweiler *et al.*, IEEE Trans. Nucl. Sci. **35**, 316 (1988).

[52] D.J. Sherden, Report No. SLAC-PUB-4297, April 1987.

[53] J. Bogart, M. Huffer and J.J. Russell, Report No. SLAC-PUB-6243, April 1993.

[54] J.J. Russell, private communication.

[55] J. Bogart, J.S. Huber and J.J. Russell, SLD-LUM-NOTE #94-01 (March, 1994).

[56] S.C. Berridge *et al.*, IEEE Trans. Nucl. Sci. **37**, 1191 (1990).

[57] J.E. Brau and X.Q. Yang, SLD-LUM-NOTE #91-13 (July, 1991).

[58] K.T. Pitts, SLD Physics Note #20, April 1993.

[59] C.J.S. Damerall, Lectures given at the 1984 SLAC Summer Institute, RAL-84-123, December 1984.

[60] M. Campanella *et al.*, Nucl. Inst. Meth. **A243**, 93 (1986).

[61] M. Langston, SLD Physics Note #28 (document in preparation).

[62] Y. B. Bushnin *et al.*, Nucl. Instr. Meth. **106**, 493 (1973).

[63] G. Barbiellini *et al.*, Nucl. Instr. and Meth **123**, 125 (1975); J.F. Crawford *et al.*, Nucl. Instr. and Meth. **127**, 173 (1975); L. H. O'Neill *et al.*, Phys. Rev. Lett. **37**, 395 (1976); U. Amaldi *et al.*, Nucl. Phys. **B145**, 367 (1978); B.K. Heltsley, Ph.D. Thesis, WISC-EX-83/233 (1983).

[64] J. S. Huber and K. T. Pitts, SLD Note #230 (March 1993).

[65] S. Jadach and B.F.L. Ward, Phys. Rev. D **40**, 3582 (1989); S. Jadach *et al.*, Phys. Lett. B **268**, 253 (1991).

[66] F.A. Berends *et al.*, Nucl. Phys. **B304**, 712 (1988).

[67] R. Brun *et al.*, CERN-DD/78/2 (1978).

[68] G. Grindhammer *et al.*, Nucl. Inst. Meth. **A290**,469(1990).

[69] R. Ford *et al.*, Report No. SLAC-0210 (1978).

[70] A. Angelis *et al.*, Phys. Lett. B **242**, 293 (1990).

[71] H. Park *et al.*, SLD Physics Note #17 (March 1993).

[72] P.N. Burrows *et al.*, SLD Note #229, January 1993.

[73] TPC/Two-Gamma Collaboration, H. Aihara *et al.*, Z. Phys. C **34**, 1 (1987).

[74] F.A. Berends and R. Kleiss, Nucl.Phys. **B186**, 22 (1981).

[75] G.S. Abrams *et al.*, Phys.Rev.Lett. **63**, 2173 (1989).

[76] P. Raimondi, Minutes of the Electroweak Group, February 3, 1993.

[77] ALEPH Collaboration, D. Decamp *et al.*, Z. Phys. C **48**, 375 (1992).

[78] DELPHI Collaboration, P. Abreu *et al.*, Nucl. Phys. **B367**, 511 (1991).

[79] L3 Collaboration, B. Adeva *et al.*, Z. Phys. C **51**, 179 (1991).

[80] OPAL Collaboration, P.D. Acton *et al.*, Z. Phys. C **58**, 219 (1993).

[81] MARK II Collaboration, J. Hylen *et al.*, Nucl. Instr. and Meth. **A317**, 453 (1992).

[82] W.W. Ash, private communication.

[83] D.M. Strom, Report No. OITS-504 (1993).

[84] E. Vella and J.M. Yamartino, SLD Note #213 (February 1992).

[85] J.M. Yamartino, SLD Physics Note #14 (November 1992).

[86] S. Youssef, Comput. Phys. Commun. **45**, 423 (1987).

[87] J.M. Yamartino, Massachusetts Institute of Technology Ph. D. Thesis, February 1994.

[88] S. González, SLD Note #214 (January 1992).

[89] S. González, SLD Physics Note #24 (October 1993).

[90] M. Caffo, H. Czyż and E. Remiddi, Nuovo Cim. **105A**, 277 (1992).

[91] G. Marchesini and B.R. Webber, Report No. Cavendish-HEP-87/9, December 1987; G. Marchesini *et al.*, Comp. Phys. Commun. **67**, 465 (1992).

[92] S. Jadach, B.F.L. Ward and Z. Waş, Comp. Phys. Commun. **66**, 276 (1991).

[93] G. Blaylock, SLD Physics Note #22 (June, 1993).

[94] F.-J. Decker *et al.*, SLD Note #238, January 1994.

[95] A.G. Frodesen *et al.*, *Probability and Statistics in Particle Physics*, (Universitetsforlaget, Oslo, 1979).

[96] D. Levinthal, F. Bird, R.G. Stuart and B.W. Lynn, Z. Phys. C **53**, 617 (1992).

[97] P. Comas and M. Martinez, Z. Phys. C **58**, 15 (1993); M. Martinez and R. Miquel, Z. Phys. C **53**, 115 (1992).

[98] F. James and M. Roos, CERN Report D506 (1989).

[99] W. Beenakker, F.A. Berends and S.C. van der Marck, Nucl. Phys. **B349**, 323 (1991).

[100] SLD Collaboration, K. Abe *et al.*, Report No. SLAC-PUB-6456, March 1994 (to be published).

[101] B.A. Schumm, talk delivered at the Aspen Winter Physics Conference, Aspen, Colorado, January 17, 1994; P.C. Rowson, talk delivered at CERN, February 24, 1994.

[102] M.J. Fero *et al.*, Report No. SLAC-PUB-6423, February 1994 (to be published).

[103] P.C. Rowson, T. Bolton and M. Shaevitz, SLD-Note #176 (April 1990).

[104] D. Bardin *et al.*, Report No. CERN-TH-6443-92, May 1992.

[105] M.L. Swartz, Report No. SLAC-PUB-6384, November 1993.

[106] J. Ellis, G.L. Fogli and E. Lisi, Phys. Lett. B **318**, 148 (1993).

[107] G. Altarelli *et al.*, Phys. Lett. B **318**, 139 (1993); J.T. Liu and D. Ng, Report No. IFP-460-UNC and Report No. TRI-PP-93-11, June 1993; E. Ma and P. Roy, Phys. Rev. Lett. **68**, 2879 (1992); E. Gates and J. Terning, Phys. Rev. Lett. **67**, 1840 (1991).

[108] T. Maruyama *et al.*, Report No. SLAC-PUB-6033, January 1993; E.L. Garwin and T. Maruyama, Report No. SLAC-PUB-5751, February 1992.